

Copyright  
by  
Matthew Earl Colburn  
2001

**Step and Flash Imprint Lithography:  
A Low-Pressure, Room-Temperature Nanoimprint Lithography**

**by**

**Matthew Earl Colburn, B.S., M.S.**

**Dissertation**

Presented to the Faculty of the Graduate School of

The University of Texas at Austin

in Partial Fulfillment

of the Requirements

for the Degree of

**Doctor of Philosophy**

**The University of Texas at Austin**

**August, 2001**

The Dissertation Committee for Matthew Earl Colburn  
Certifies that this is the approved version of the following dissertation:

**Step and Flash Imprint Lithography:  
A Low-Pressure, Room-Temperature Nanoimprint Lithography**

**Committee:**

---

C. Grant Willson, Supervisor

---

Isaac C. Sanchez

---

Roger T. Bonnecaze

---

Peter F. Green

---

Walter R. Romanko

## **Dedication**

To my parents and my loving wife.

## **Acknowledgements**

The work presented in this dissertation could not have been completed without the assistance of many people. First, I would like to thank my wife, Jenny, for being so patient and supportive for the past seven years. I couldn't have done it without you! I would also like to thank my parents, family, and friends for supporting me throughout my 27 years.

I would like to name a few that have contributed directly to the research throughout the course of my graduate studies. I have been fortunate to have worked with a wonderful set of undergraduate students during my tenure at The University of Texas. I appreciate the hard work of Michael Wedlake, Angela Guerry, Tim Michaelson, Ravin Singh, Mario Meissl, and Itai Suez. I am grateful for the experience I gained at Agilent Technologies and would like to thank Dr. Annette Grot for making my experience there a wonderful one. I appreciate all the interesting and thought-provoking discussions with my fellow graduate students and am grateful to them. I would like to thank Kathleen Sparks for her assistance throughout the past four years. I express thanks to Steve Johnson and Todd Bailey for their dedication to the Step and Flash research program that helped make it a success. I appreciate the guidance and advice of Professors S.V. Sreenivasan and John. G. Ekerdt. To Dr. Byung Jin Choi with whom I have

enjoyed working with over the past few years, I extend my sincerest gratitude for all his patience and insightful suggestions. While many have contributed to my graduate experience, the knowledge and experience I gained in graduate school is due to my advisor, Professor C. Grant Willson, to whom I will be forever indebted; I cannot imagine having studied under another.

Matthew Earl Colburn

**Step and Flash Imprint Lithography:  
A Low-Pressure, Room-Temperature Nanoimprint Lithography**

Publication No. \_\_\_\_\_

Matthew Earl Colburn, Ph.D.  
The University of Texas at Austin, 2001

Supervisor: C. Grant Willson

Step and Flash Imprint Lithography (SFIL) is a technique that has the potential to replace photolithography for patterning resist with *sub*-100 nm features. SFIL is a bilayer lithographic scheme that utilizes the *in situ* photopolymerization of a low viscosity organosilicon monomeric fluid to replicate the topography of a template on an organic-coated substrate. The silylated relief structure is then etch transferred through the organic layer, which then can be used for subsequent processing such as additive metalization or device etch.

Several key aspects of the SFIL process have been investigated. Several means of fluid delivery have been evaluated and compression of multiple droplets has been determined to be the most consistent with high volume manufacturing requirements. The surface energies of the SFIL materials have been tailored to

allow for preferential separation at the template-photopolymer interface. The mechanical properties and densification induced by photopolymerization have been studied as a function of photopolymer composition. The current photopolymer shrinks 9.3% (v/v) and has an elastic modulus of 4.2 MPa. Based on these experimentally determined properties and finite element simulation, the in-plane motion of replicated patterns was determined to be insignificant and that the effect of the densification manifests itself mainly in the direction normal to the substrate surface.

The photopolymer has been tailored to provide an O<sub>2</sub> reactive ion etch selectivity greater than 10:1 with respect to an underlying organic film. Exploiting this selectivity, features with an aspect ratio of 14:1 were produced and high aspect ratio features have been printed over non-flat surfaces. The SFIL process has been successfully applied to optoelectronic structures such as micropolarizer arrays, and its resolution appears to be limited only by the size of the structures that can be created on the template. The Step and Flash Imprint Lithography process has been proven to be a high-resolution technique capable of patterning a wide variety of substrate at room temperature under low applied pressure in a fashion consistent with high volume manufacturing requirements.

## Table of Contents

List of Tables.....	xiii
List of Figures .....	xiv
List of Figures .....	xiv
1 Introduction .....	1
1.1 Transistor Process Flow .....	2
1.2 Semiconductor Microlithography .....	5
1.3 Thermal Imprint Lithography.....	9
1.4 Step and Squish Imprint Lithography .....	11
1.5 Conclusion.....	17
2 Step and Flash Imprint Lithography.....	21
2.1 Process Description .....	21
2.2 Agilent-UT SFIL Process.....	23
2.3 SFIL Single Imprint Machine .....	25
2.4 SFIL Imprint Stepper .....	26
2.5 Illumination Sub-system for Single-Imprint Apparatus and Multi-Imprint Stepper.....	29
2.6 Template Fabrication Process .....	30
2.7 Surface Treatment .....	34
2.8 Summary .....	37
3 Fluid Dynamics Evaluation.....	40
3.1 Capillary Action .....	40
3.2 Application by spincoating.....	43
3.3 Single Droplet Compression .....	43
3.4 Multi-droplet Compression .....	55
3.5 Experimental Observation.....	59

3.6	Conclusions .....	60
4	Surface Energy Characterization.....	63
4.1	Surface Energy Models .....	65
4.2	Rame-Hart m100 Contact Angle Goniometer.....	68
4.3	Liquid Surface Tension by Pendant Drop.....	71
4.4	Surface energy characterization of SFIL components .....	74
4.5	Conclusion.....	82
4.6	Future work .....	83
5	Characterization of the Elastic Modulus of Photopolymer Films by Nanoindentation .....	87
5.1	Introduction .....	87
5.2	Background .....	88
5.3	Contact Mechanic Models for Nanoindentation .....	89
5.4	Atomic Force Microscope in Force-Distance Mode .....	92
5.5	Film Preparation .....	95
5.6	Results .....	96
5.7	Conclusions .....	103
5.8	Future Work .....	103
6	Volumetric Contraction of Photopolymers .....	105
6.1	Introduction .....	105
6.2	Background .....	106
6.3	Procedure.....	108
6.4	Results .....	110
6.5	Conclusions .....	120
6.6	Future Work .....	120
7	Finite Element Modeling of SFIL Photopolymer Replicated Features.....	123
7.1	Introduction .....	123
7.2	Finite Element Modeling Background .....	123

7.3	FEM Implementation .....	129
7.4	Results .....	130
7.5	Conclusions .....	154
7.6	Future Work .....	155
8	Reactive Ion Etching .....	157
8.1	Background .....	158
8.2	Equipment .....	163
8.3	Results .....	166
8.4	Conclusions .....	179
8.5	Future Work .....	180
9	Spectral Reflectometry for <i>Real-time</i> Gap Sensing and Other Applications .....	184
9.1	Introduction .....	184
9.2	Spectral Reflection .....	188
9.3	Background .....	191
9.4	Application of Spectral Reflectivity to Gap Sensing .....	192
9.5	Fourier Transform .....	194
9.6	Experimental Setup .....	196
9.7	FFT Analysis Simulation .....	198
9.8	Effect of Dispersion on FFT Analysis.....	202
9.9	Effect of FFT Parameters on Analysis .....	205
9.10	Inflection-Maximum-Minimum Analysis (IMMA) .....	206
9.11	Phase Angle Calculation (PAC) .....	210
9.12	Experimental Results.....	211
9.13	Conclusions .....	216
9.14	Future Work .....	217
10	Patterning Results and Conclusions .....	221
10.1	Patterning Results.....	221

10.2 Curved surface patterning .....	230
10.3 Conclusion.....	232
Appendix .....	235
Appendix A: SFIL Stepper Operation .....	235
Appendix B: Power Meter Design.....	238
Appendix C: Multiangle Spectral Reflectometry .....	243
Appendix D: Primary Etch Barrier Formulations .....	246
Bibliography .....	247
Vita .....	251

## List of Tables

Table 4.1. Surface energy components of fluids.....	67
Table 4.2. Surface tension of prospective etch barrier components measured by pendant drop.....	74
Table 4.3. Surface tension of several organic polymer films.....	75
Table 4.4. Surface energies of several transfer layer, etch barrier formulations, and untreated template and a treated template measured by Acid-Base method.....	76
Table 4.5. Etch barrier compositions (by mass (g)).....	76
Table 4.6. Work of Adhesion between SFIL Interfaces.....	77
Table 4.7. Surface energy properties of the etch barrier, transfer layer, and template unless otherwise stated for the simulation.....	79
Table 5.1. High $T_g$ Polymers that may be suitable for the current etch barrier formulation.....	101
Table 6.1. Densification for free radical polymerization.....	105
Table 6.2. Densification for addition polymerization.....	106
Table 6.3. Chemical name, commercial name, and volumetric shrinkage for solutions with 1% (w/w) SIB 1402 and 3% (w/w) free radical generator (1:1 mixture of Irgacure 184 and Irgacure 819) added.....	119
Table 8.1. Screening of Transfer Layer Candidates.....	172
Table 9.1. Error Associated with FFT analysis using different estimates of indices.....	204
Table 9.3. Error associated with the $n(\lambda)/\lambda$ sampling method for a range of Cauchy coefficients.....	205
Table 9.4. Logic used to calculate optical path (nD).....	209
Table 9.5. Static film thicknesses (nm) measured by FFT-IMMA combined algorithm.....	213
Table 9.6. Optical Path (nD) over which each algorithm is utilized if the index is constant.....	216
Table 9.7. Optical Path (nD) over which each algorithm is utilized if the film exhibits dispersion.....	217
Table B.1. Amplifier components.....	240
Table D.1. Primary Etch Barrier Formulations.....	246

## List of Figures

Figure 1.1. MOS FET.....	2
Figure 1.2. Summarized MOS-FET fabrication flow. ....	4
Figure 1.3. The semiconductor microlithographic process.....	5
Figure 1.4. Historic cost of lithography tools.....	7
Figure 1.5. Step and Squish Imprint Lithography.....	12
Figure 1.6. Optical micrograph of a 2 $\mu\text{m}$ grating structure created at 150 $^{\circ}\text{C}$ at a pressure of 40 psi (left), and a partial displacement of polymer in a pattern with irregular pattern density (right). ....	13
Figure 1.7. Pattern density effects were found during SSIL. ....	13
Figure 1.8. Phillips 2-P Process .....	15
Figure 2.1. Step and Flash Imprint Lithography process flow diagram for both a) UT equipment and b) UT-Agilent Technologies imprint equipment.....	22
Figure 2.2. SFIL Single Imprint Apparatus (left) and the passive wafer stage (right) based on a three ring flexure that allows motion in the $\alpha$ , $\beta$ , and $Z$ directions. ....	26
Figure 2.3. Multi-imprint SFIL Stepper. ....	28
Figure 2.4. Template stage housing. ....	28
Figure 2.5. SFIL illumination sub-systems. ....	30
Figure 2.6. Template Fabrication Process.....	33
Figure 2.7. Template Generation. After patterning, the mask is cut into template pieces. The chromium is removed and the transparent template is surface treated with a fluorinated self-assembly monolayer. ....	34
Figure 3.1. The etch barrier wicks the cavity between the template and the transfer layer by capillary action as it is being delivered by a micropipette. ....	40
Figure 3.2. The time to fill a gap that is 2.54 cm long with a fluid the wets both gap surfaces is shown as a function of $\mu/H$ . ....	42
Figure 3.3. The template and substrate approach each other with a velocity, $2V$ , and displace the fluid between them in a radial manner. The gap height is $2H$ and the meniscus of the fluid has a meniscus radius, $H_{curv}$ . ....	44
Figure 3.4. The time required to compress a filled gap starting at a height ( $2H_o$ ) of 1 micron to a height ( $2H_f$ ) of 100 nm with a fixed pressure for a 1 cP fluid and a 100 cP fluid. ....	48
Figure 3.5. Comparison of pressure as a function of base layer ( $2H$ ) for constant pressure (Case 1) and constant velocity (Case 2) actuation schemes. The imprint time is 1 second. (Left) The corresponding base layer during the time of actuation. ....	49
Figure 3.6. Comparison of pressure generated as a template expels fluid from the gap for Case 2 and Case 3 fill methods ( $2V = 0.9 \mu\text{m/s}$ ). ....	50
Figure 3.7. Time required to achieve a certain base layer with a fixed volume (31.4 nl) with a 100 N applied force. ....	52

Figure 3.8. The gap height ( $2H$ ) in time compared for cases 3-5. ....	53
Figure 3.9. Pressure as a function of gap height for cases 3-5. ....	54
Figure 3.10. Imprint pressure required to achieve a 100 nm gap height in 1 second for a single drop in a multi-drop compression. The viscosity is 1 cP. .....	56
Figure 3.11. Force required to compress a fixed volume of 31.4 nl to a gap height of 100 nm in 1 second as a function of the number of droplets ( $n$ ).....	58
Figure 3.12. a) 138 nm base layer thickness remains and is uniform over nearly the entire 1” x 1” template. The total imprint and exposure time was ~30 seconds. Further improvement may come from improved filtration techniques. b) 55 nm base layer measured by tilt-SEM. The imprint time was approximately 1 second. The pressure is not monitored on the Agilent imprint equipment. ....	60
Figure 4.1. Cohesive failure (bottom) and adhesive failure (top) .....	64
Figure 4.2. Depending on the surface properties, SFIL replication can lead to a) defects or b) faithful replication. ....	65
Figure 4.3. Contact angle of three liquids required for surface energy characterization using Acid-base theory. ....	67
Figure 4.4. Rame-Hart m100 Goniometer with computer capture system. ....	68
Figure 4.5. Environmental chamber for the Rame-Hart goniometer rests on the gimbal stage. The sample is illuminated and imaged through the two view ports. The heater-chiller block is attached to the bottom of the chamber. ....	69
Figure 4.6. Characteristic dimensions, $D_s$ and $D_e$ , are shown on a pendant drop.	72
Figure 4.7. Trilayer stack indicating the interfaces of interest. ....	78
Figure 4.8. The ratio of the etch barrier-transfer layer work of adhesion to the etch barrier-template work of adhesion when the etch barrier’s $\gamma^{p+}$ and $\gamma^{p-}$ range from 0 to 20 dyne/cm. The treated template has a $\gamma^{p+}$ and $\gamma^{p-}$ of ~0.2 and ~6 dyne/cm which is highlighted on the plot by the star. ....	79
Figure 4.9. The ratio of the etch barrier-transfer layer work of adhesion to the etch barrier-template work of adhesion when the template’s $\gamma^{p+}$ and $\gamma^{p-}$ range from 0 to 20 dyne/cm. The treated template has a $\gamma^{p+}$ and $\gamma^{p-}$ of 1 and 44.2 dyne/cm. ....	80
Figure 4.10. The ratio of the etch barrier-transfer layer work of adhesion to the etch barrier-template work of adhesion when the transfer layers’ $\gamma^{p+}$ and $\gamma^{p-}$ range from 0 to 20 dyne/cm. The transfer layer has a $\gamma^{p+}$ and $\gamma^{p-}$ of 0.23 and 13.3 dyne/cm. ....	82
Figure 5.1. Hertzian model system: a spherical tip penetrating a flat surface. ....	89
Figure 5.2. Sneddon’s flat-end cylindrical tip (flat-punch) model: a cylindrical tip penetrating a flat surface. ....	91
Figure 5.3. Sneddon’s conical tip model: a conical tip penetrating a flat surface. .....	91

Figure 5.4. Sampling frequencies greater than 1 Hz results in digitation of the force data. Note: the dashed line represents the surface of the film and the forces are adjusted vertically for display. The horizontal portion of the force represents a cantilever experiencing no attraction or repulsion from the surface. ....	94
Figure 5.5. Force- $\delta$ showing the effect of the substrate observed at a depth of approximately 200 nm. ....	95
Figure 5.6. Regression of force- $\delta^{3/2}$ for the Hertzian model ....	96
Figure 5.7. Regression of force- $\delta^2$ for the Sneddon conical model. ....	97
Figure 5.8. Regression of force- $\delta$ for the Sneddon flat-punch model. ....	97
Figure 5.9. Force-vs.-deflection depth data of poly((n-butyl)-co-(3-acryloxypropyltristrimethylsiloxane)silane) with overlaid Hertzian, Sneddon conical model, and Sneddon flat-punch model. ....	98
Figure 5.10. Force-vs.-deflection depth data of poly((3-acryloxypropyl-tristrimethylsiloxane)silane) with overlaid Hertzian, Sneddon conical model, and Sneddon flat-punch model. ....	99
Figure 5.11. Moduli of lightly crosslinked homopolymer films. ....	100
Figure 6.1. UV exposure chamber with N <sub>2</sub> purge used to cure photopolymer samples. ....	109
Figure 6.2. Volume contraction of n-alkyl acrylates measured by Archimedes' principle plotted versus the pendant group length. The SFIL etch barrier is plotted for reference. ....	111
Figure 6.3. Silylated Monomer Densification. ....	113
Figure 6.4. Hyperchem <sup>®</sup> model of (3-acryloxypropyltristrimethylsiloxane)silane. ....	114
Figure 6.5. Volumetric contraction as a function of pendant group volume percent (simulated in HyperChem <sup>®</sup> ). R <sup>2</sup> = 0.92. ....	115
Figure 6.6. Effect of crosslinker concentration on the volumetric change of 3-acryloxypropyltristrimethylsiloxane silane. ....	116
Figure 6.7. Densification of (3-acryloxypropyltristrimethylsiloxane)silane and butyl acrylate copolymers ....	117
Figure 7.1. Two examples of a continuum digitized into elements defined by their nodes. (Left) Uniform grid. (Right) Customized grid designed to increase accuracy of simulation within the feature and at the vertices. ....	124
Figure 7.2. Calculated relative displacement of two points on opposing surfaces of a constrained film (■) and a free film (□). ....	131
Figure 7.3. Pro/E models of 200 nm tall wide isolated lines, gratings, and L-structures on 100 nm thick base layer and 1000 nm thick transfer layer. The images on the right are enlargements of the patterned region of interest....	133
Figure 7.4. Cross-section of an isolated line with color indicating the total displacement resulting from a 27.1% volumetric shrinkage (10% linear	

shrinkage) on a constrained film. The total displacement magnitude is displayed in microns.....	134
Figure 7.5. 200 nm tall equal line-space grating on a 200 nm pitch. 27.1 % volumetric shrinkage. The top is an X-Y plane cross section. The bottom is an X-Z plane cross section. The total displacement magnitude is displayed in microns.....	136
Figure 7.6. The vertical component of the displacement for a grating densified by 27.1% (v/v) in its undeformed state. The vertical displacement is displayed in microns.....	137
Figure 7.7. Isometric view of L-structures shown in their deformed state after 27.1% (v/v) shrinkage. Note the slope at the corners of the "L" features. The total displacement magnitude is displayed in microns.....	138
Figure 7.8. Cross-section of the vertical component of the displacement for L-structure with 100 nm square pillars (shown in the undeformed state). The vertical displacement is displayed in microns.....	138
Figure 7.9. Pattern placement model.....	140
Figure 7.10. In-plane pattern motion measured just above the base layer predicts less than 1 nm displacement for the 100 nm wide line running parallel to the edge of the two $\mu\text{m} \times 2 \mu\text{m}$ square features (color scale units are in $\mu\text{m}$ ). .....	141
Figure 7.11. Parametric model used for densification simulations.....	142
Figure 7.12. Vertical Shrinkage of etch barrier features.....	144
Figure 7.13. The ratio of the vertical shrinkage for a Poisson's ratio of 0.3 and 0.4 relative to the vertical shrinkage for a Poisson's ratio of 0.5 is independent of densification but is aspect ratio dependant.....	145
Figure 7.14. Effect of densification on line width at the top of the features.....	147
Figure 7.15. Effect of densification on line width at the bottom of the features. .....	148
Figure 7.16. Effect of densification and Poisson's ratio on sidewall angle.....	149
Figure 7.17. (Top) Top length shrinkage of etch barrier features as a function of aspect ratio and volumetric shrinkage. (Bottom) Top length shrinkage of etch barrier features as a function of aspect ratio, and volumetric shrinkage. .....	151
Figure 7.18. Top-down SEM of line width measured using oblique overlay to determine line edge position.....	153
Figure 7.19. Line width measured by SEM for the template and the replicated features.....	154
Figure 8.1. Parallel plate capacitively coupled etcher.....	159
Figure 8.2. Time-averaged potential across the electrode gap with an applied RF voltage ( $V_{\text{RF}}$ ).....	161
Figure 8.3. HeNe interferometry signal taken during $\text{O}_2$ RIE process.....	164

Figure 8.4. Effect of silicon content on O <sub>2</sub> etch selectivity between the etch barrier and a polystyrene film. ....	167
Figure 8.5. The variation in base layer thickness (A) across the imprint must be less than the feature height (B) if the RIE transfers function properly. ....	168
Figure 8.6. a) SEM of 55+nm base layer using polycarbonate template. b) Base layer across a 1" x 1" patterned region measured with ellipsometry. ....	169
Figure 8.7. Etch Rate of 467k MW PMMA in O <sub>2</sub> RIE .....	170
Figure 8.8. Undercut at 40 mTorr and 150 V (left), and 10 mTorr and 250 V (right). ....	171
Figure 8.9. (a) 80 nm features etched 300 nm into the PMMA transfer layer, (b) 80 nm features etched through 1.4 μm of PMMA. ....	173
Figure 8.10. 70 nm features etch transferred through 300 nm of PMMA. ....	174
Figure 8.11. (Top) Schematic of wafer deflection under vacuum. (Bottom) Thickness of an imprinted film on a poor quality wafer chuck. ....	175
Figure 8.12. 138 nm base layer imprinted with a quartz template in the SFIL Stepper. ....	176
Figure 8.14. Comparison of Template (top), the replicated features (middle), and the etched features (bottom). ....	178
Figure 8.15. Top-Down and Tilt SEM of features etch transferred with the μ80 etcher. ....	179
Figure 9.1. Plot of cos(Σ) and cos(Δ) for optical path lengths ( <i>nD</i> ) ranging from 0 nm to 3000 nm for wavelengths of 500 nm and 600 nm. ....	186
Figure 9.2. Simplified SFIL system consisting of a template, gap, and substrate. ....	188
Figure 9.3. <i>In situ</i> Spectral Reflectometry System. ....	197
Figure 9.4. Gap Sensing Orientation Measurement. ....	198
Figure 9.5. Example of Simulated Signal for (a) relative intensity vs wavelength, (b) relative intensity vs wavenumber, and (c) FFT of (b). ....	199
Figure 9.6. Error associated with calculated thin film for a set of ideal films. ...	201
Figure 9.7. Film Thickness of a dissolving film calculated by FFT analysis alone. ....	202
Figure 9.8. Thickness of a dissolving film was calculated <i>in situ</i> analysis. ....	212
Figure 9.9. Gap measurement through a transparent template. a) Air Gap, b) Water Gap, and c) Overlay of measured force and gap height. ....	215
Figure 9.10. FFT of the spectral reflection from a bilayer film stack. ....	219
Figure 10.1. Replication resolution demonstration. (A) 135 nm wide feature replicated in the etch barrier. (B) Lower resolution of (A) shown the repeating stitching error that demonstrate sub-25 nm fidelity of the replication process. (C) 60 nm feature that is ~190 nm tall replicated in the etch barrier. All samples were coated with Au for imaging by SEM. ....	222

Figure 10.2. (A) Top-down SEM of 14:1 aspect ratio features etch transferred through 1.4 micron thick PMMA. (B) Tilt SEM of a defect region that shows the aspect ratio more clearly.....	223
Figure 10.3. Cross-section of the GaAs template.....	224
Figure 10.4. Cross-section of the transferred structure. ....	224
Figure 10.5. Additive metalization process.....	225
Figure 10.6. Micropolarizer array consisting of orthogonal 100 nm lines and spaces shown illuminated with non-polarized light (left) and polarized light (right).....	226
Figure 10.7. Photonic crystal fabricated by SFIL at Agilent Technologies. ....	227
Figure 10.8. A schematic of an SFIL non-flat patterned cross section (top) prior to etch transfer and (bottom) after etch transfer .....	228
Figure 10.9. (A) Top-down SEM of non-flat patterning process. The lines are part of a 700 nm tall Fresnel lens. (B) 250+ nm features were transferred through 1.1 mm of PMMA and the planarization layer over the 700 nm tall Fresnel lens. (C) Cross-section SEM shown the silicon substrate, the spincoated PMMA layer, the planarization layer, and the etch barrier .....	229
Figure 10.10. Curved surface replication process flow.....	231
Figure 10.11. (a) Optical micrograph shows features etched into the template generated by ion-proximity lithography. (b) Optical micrograph shows a relief pattern in the etch barrier. (c) AFM image of topography patterned in etch barrier.....	232
Figure A.1. SFIL Stepper Graphic User Interface. ....	237
Figure B.1 Power meter and inline instrumentational amplifier. ....	238
Figure B.2. Instrumentational Amplifier Circuit Diagram. ....	239
Figure B.3. PowerMeter.vi Front End.....	240
Figure B.4. Power meter algorithm (Steps 1 through 3) .....	242
Figure C.1. Path length of the probe light is increased by non-normal illuminations.....	243
Figure C.2 Effect of Incident Angle and Spectral Range on the Minimum Detectable Thickness for a) FFT algorithm, and b) the IMMA algorithm. ....	244

# 1 Introduction

The semiconductor industry has grown at the astonishing rate that was predicted by Gordon Moore [1] in the 1965. Moore's law, as it became known, states that the number of transistors per chip will double every 18 months. This doubling has become a "self-fulfilling" prophecy that, to a large degree, can be attributed to the advancements in microlithography.

To understand the driving force behind this growth, one must understand the devices that are fabricated by these manufacturing techniques. A semiconductor microprocessor is composed of millions of transistors. While there are many variations on the design of a transistor, an example of the most common device, a Metal-Oxide-Semiconductor Field Effect Transistor (MOS FET), is shown in Figure 1.1 [2,3]. When a voltage is applied across the gate oxide in the transistor, the vacancies (holes) in the valence band are depleted in the channel that is represented by region above the dashed line and below the gate oxide making that area conducting [2]. An electrical connection forms between the source and the drain that allows current to flow. For short channel transistors, the current is proportional to  $V_D/L^3$ , where  $V_D$  is the drain voltage, and  $L$  is the channel length [2]. This current is one major factor that affects transistor switching speed and overall system performance. Accordingly, the channel length, or the critical dimension (CD), has been the focus of much of the semiconductor industry's attention.

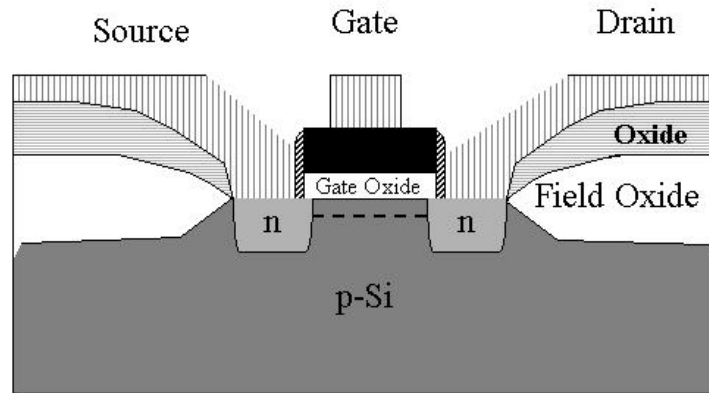


Figure 1.1. MOS FET.

### 1.1 TRANSISTOR PROCESS FLOW

The process flow for the semiconductor MOS fabrication is detailed by Plummer *et al.* and summarized briefly in Figure 1.2 [3]. A) Starting with a silicon wafer covered with field oxide with regions of silicon exposed, a well is doped with a group III or group V element such as boron or phosphorus. This creates a region of either depleted electron population in the valence band (p-type) or enhanced electron population in the valence band (n-type). For this example, boron was used to create a p-type well. B) A shallow ion implantation into the well forms a region near the surface where the vacancy population in the substrate's valence band is larger than in the p-type well. This region is referred to as  $p^+$ -type silicon. A thin film of silicon oxide (gate oxide) is grown on the substrate and polysilicon is deposited over it. The polysilicon is doped with phosphorus rendering it more conductive than pure polysilicon. Photoresist is

patterned over the well to define the width of the gate. C) The pattern in the photoresist is used as a etch mask for removing exposed polysilicon. The source and drain are then generated by ion implantation of a column V element, such as arsenic, that form two n-type regions in the silicon lattice; the polysilicon gate blocks dopants from contaminating the p-channel during this implantation. A layer of silicon dioxide is deposited over the substrate and then etched isotropically to create a sidewall spacer between the polysilicon gate and what will be the source and drain contacts. The substrate is annealed at elevated temperatures to “drive-in” the ion implanted elements. D) Once this is complete the contacts to the source and to the drain must be made. An isotropic oxide etch removes the oxide from the source and drain regions of the device. Metal is then deposited over the substrate and lithography is used to isolate the regions where metal is to be removed. Once the source and drain contacts are formed, a conformal silicon dioxide isolation layer is deposited over the substrate and is patterned using lithography. A gap is etched in the oxide above the polysilicon gate and the spacer oxide and metal is deposited into the gap to make contact to the gate. Once the contacts are made, contact vias are etched through an interlayer dielectric (ILD) that separates the transistors from the intra-chip wiring and connect the transistor to the external environment.

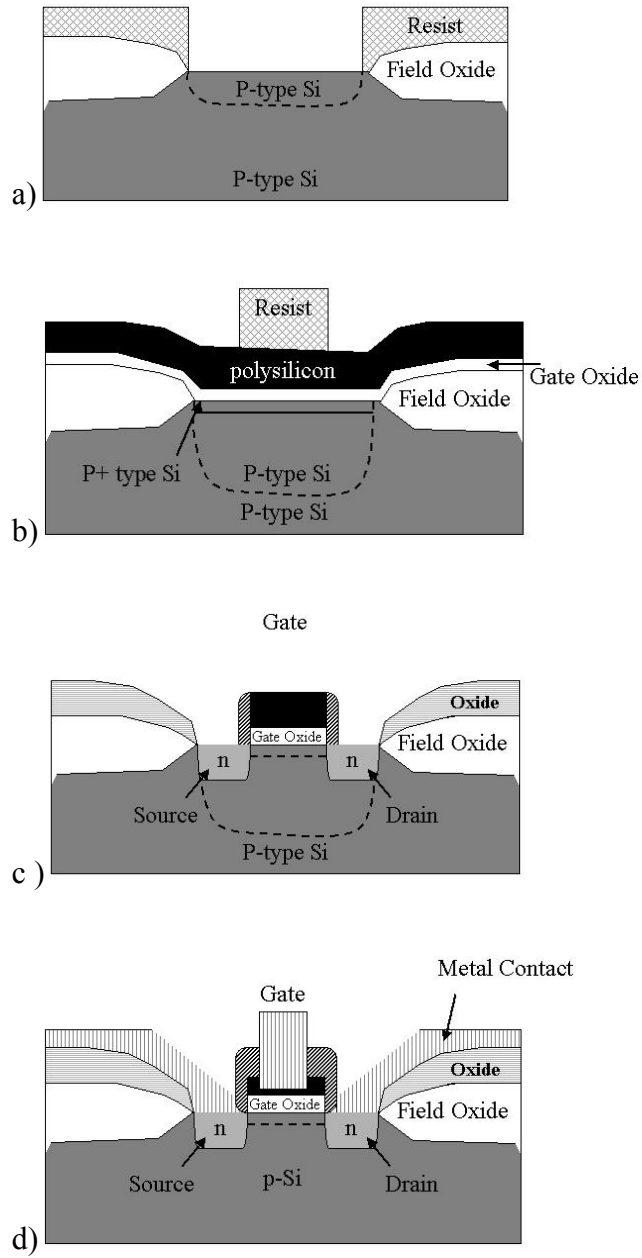


Figure 1.2. Summarized MOS-FET fabrication flow.

## 1.2 SEMICONDUCTOR MICROLITHOGRAPHY

As shown above, the lithography step is a critical process that defines the circuit layout as well as the critical dimension of the gate. The conventional lithographic process used in semiconductor manufacturing is shown schematically in Figure 1.3. In this process, a substrate is spincoated with a photosensitive polymer, known as a photoresist. This film is then baked at around 100 °C to evaporate the casting solvent. Energy is deposited into the film by illumination through a mask that contains the circuit pattern. Depending on the chemistry, the resist can react to this energy deposition by becoming soluble (positive tone) or insoluble (negative tone) in a developer. For many photoresists, a post-exposure bake is required for this reaction to occur in the activated region. Once developed, the pattern in the resist is a relief image of the pattern on the mask. This pattern is transferred into the substrate and residual resist stripped from the substrate.

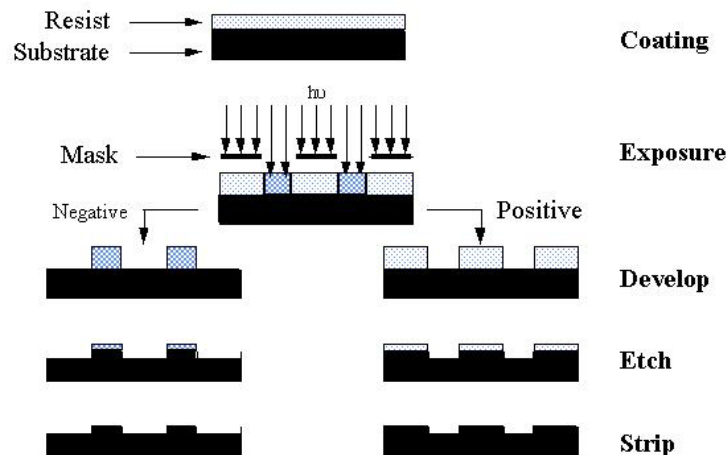


Figure 1.3. The semiconductor microlithographic process.

The resolution,  $R$ , of conventional projection lithography is governed by the laws of diffraction and can be simplified to the Raleigh Equation [4]:

$$\text{Equation 1.1} \quad R = \frac{k\lambda}{NA}$$

where  $k$  is a system dependent parameter that includes resist material properties,  $\lambda$  is the wavelength of the light, and  $NA$  is the numerical aperture of the lens. The  $k$ -parameter is affected by lens aberrations, lens design, type of illumination, and photoresist materials; among others. The  $k$ -parameter approaches  $\frac{1}{2}$  in the theoretical limit of diffraction.

Another parameter that affects image quality is the depth of focus ( $DOF$ ). There is always some error in the location of the substrate relative to the focal plane of the imaging system. As the position of the substrate deviates from the focal plane the quality of aerial image suffers; adversely affecting the resolution of the process. It is desirable to have a large  $DOF$  in order to compensate for the errors in focal position. Unfortunately, this requires either larger wavelengths or lower numerical aperture.

$$\text{Equation 1.2} \quad DOF = \frac{\lambda}{2NA^2}$$

In fact, driven by the need to increase the speed of transistors, the industry has lowered the exposure wavelength, increased the  $NA$  of the lens, and tailored photoresist properties to improve the resolution of the lithography. For nearly a decade, experts have been predicting the end of optical microlithography. While there are many technological challenges with advanced optical lithography, the

limit of optical lithography may not be technical but economical. The combination of improved optics, shorter exposure wavelengths, and introduction of more complex masks and processes has enabled printing features smaller than 100 nm [5] at the expense of exponential increases in costs [6]. Beyond optical lithography, the Semiconductor Industry Association (SIA) Roadmap [6] lists several alternative “next generation lithography” (NGL) techniques capable of sub-50 nm resolution based on ionizing radiation: X-ray, extreme ultraviolet (EUV), electron projection lithography (EPL), and direct-write electron beam. Each approach has its advantages and disadvantages, but all are systematically more expensive than the current lithography tools. At the current rate, the price of lithography equipment will make new fabrication facilities cost-prohibitive [6].

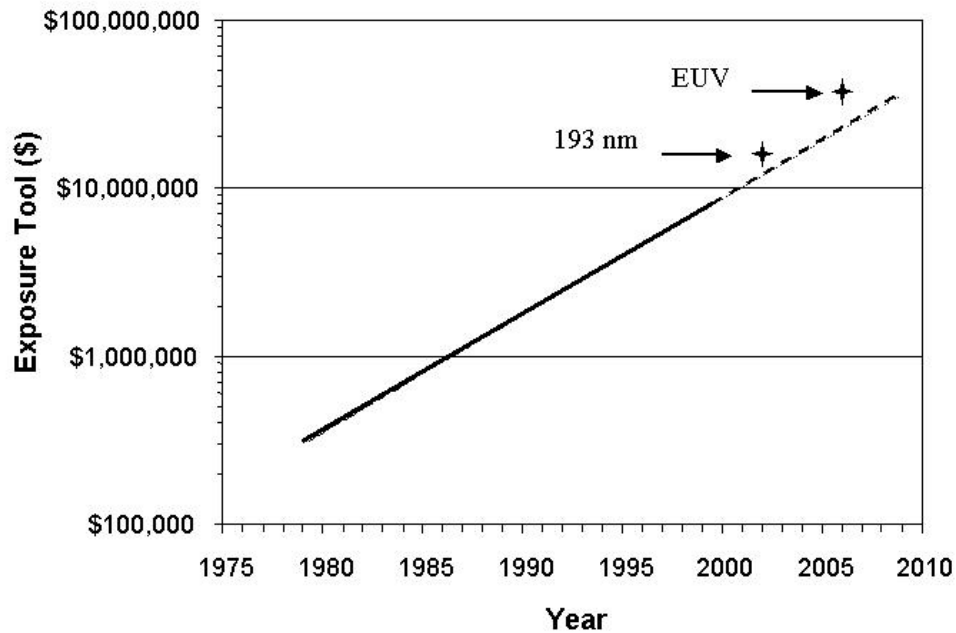


Figure 1.4. Historic cost of lithography tools.

Consequently, many researchers are exploring inexpensive methods for pattern generation capable of sub-100 nm resolution on substrates, silicon or otherwise. If such a method is to be significantly cheaper than proposed NGLs, it must, by necessity, be very different from those now contemplated. One such method is imprint lithography which was first proposed as a means of semiconductor patterning by Stephen Chou *et al.* of the University of Minnesota [7].

Imprint lithography has several important advantages over conventional optical lithography and NGLs. The parameters in Equation 1.1 are not relevant to imprint lithography because the technology does not use reduction lenses. The resolution of imprint techniques in the sub-100 nm regime is well documented [7-12] and appears to be limited only by the resolution of structures that can be generated in the template or mold. Imprint templates are typically fabricated using imaging tools such as electron beam writers that provide high resolution but lack the throughput required for mass production. Imprint lithography, therefore, takes advantage of the resolution offered by direct-write electron beam technology without compromising throughput goals required for high volume manufacturing.

There are many imprint lithography techniques, all of which are variations on a common theme. The basic premise is that a template with a prefabricated topography is pressed into a resist material. This material conforms to the shape of the master pattern defined in the template, and the shaped material is cured into a solid. The process is a contact printing process that transfers patterns without

reduction. The foremost challenges of such processes are the dependence on 1- $X$  template fabrication (current lithography utilizes 4:1 reduction), and defect susceptibility.

### 1.3 THERMAL IMPRINT LITHOGRAPHY

Researchers systematically studied imprint lithography techniques in the 1990's [7-12]. The research is divided into two techniques; one based on imprinting into a thermoplastic or thermoset polymer at elevated temperature, and the other imprinting into a low viscosity curable material. Chou *et al.* [5], Schultz *et al.* [9], Scheer *et al.* [10], and Jaszewski *et al.* [12] fall into the former category of thermal imprint technology in which a polymer heated above its glass transition temperature ( $T_g$ ) is imprinted with a mold with pressure on the order of 10 to 100 MPa. The imprint time is usually greater than 15 minutes per imprint. The system is cooled to below the  $T_g$  of the polymer while the mold is in contact, thus fixing the shape of the imprint. The mold is then removed from the substrate. Thermal imprint lithography has demonstrated remarkable resolution with features as small as 10 nm [5]. Chou *et al.* has demonstrated the first functional devices with imprint lithography as well as course overlay on the order of 1  $\mu\text{m}$  [13,14].

The thermal imprint lithography techniques all have been demonstrated on silicon substrates with silicon templates in order to address thermal expansion mismatch between the template and substrate. The imprinted material is typically PMMA or a PMMA derivative. Three issues must be addressed with this technique. First, if overlay is to be obtained the template must be transparent to a light source; for silicon templates, this is in the infrared region. Given

conventional overlay techniques based on Moiré patterns or box-in-square methods, this technique, at best, is limited to ~100 nm due to the long wavelength of infrared light. The reactive ion etch selectivity of PMMA with respect to silicon, polysilicon, or silicon dioxide is at best 1:1 in a Cl etch [15]. Therefore, high aspect ratio features with a height greater than the desired etch depth are required. Lastly, the force required to displace a high modulus (high Tg) material such as PMMA over relatively long distances is quite large.

More recently, Chou, *et al.* [16], and Russell, *et al.* [17] have demonstrated an alternative to the high temperature, high pressure imprint process. Both processes rely on instabilities generated by surface forces acting on a thin film that is heated above its glass transition temperature. Van der Waals' and electrostatic forces acting among the template, the film, and the substrate govern the formation of periodic micropillar arrays in the Lithography Induced Self-Assembly (*LISA*) process [16,18]. Russel *et al.* expanded on this technique taking advantage of electrostatic forces, that can act over a longer range than Van der Waals', by applying an electric field to the template-substrate gap. Both techniques, however, are very sensitive to the gap size and material properties [18]. Each technique will also be limited to certain feature sizes that will be linked to the nature of the forces causing the thin film instability [18]. Both are elegant techniques that may be well suited for applications in periodic photonic devices but inadequate for non-periodic patterning of semiconductor devices.

#### 1.4 STEP AND SQUISH IMPRINT LITHOGRAPHY

Early in our research program, we investigated the prospect of imprinting a silylated thermoplastic at elevated temperatures and pressures [19]. Our goal was to generate a bi-layer structure analogous to that produced by bi-layer or tri-layer lithographic processes [20]. This process, named “Step and Squish Imprint Lithography”, is shown in Figure 1.5. In this process, a silicon substrate was spin coated with an organic thermoset or a negative tone photoresist, such as Olin HR100, that crosslinks upon ultraviolet (UV) illumination. A second film of poly(trimethylsilylmethyl methacrylate) with a glass transition temperature ( $T_g$ ) of 108°C [21] was spin coated to a thickness of 100 nm to 200 nm depending on the etch depth and duty cycle of the template topography. A template containing a defined topography was placed with the topography laying on top of the bi-layer coated substrate. The template was treated with a fluorinated self-assembled monolayer that produced a surface with a surface energy of 19-24 dynes/cm [19]. This stack was then placed in a press that was preheated to 150°C (above the  $T_g$  of the silicone film). The entire assembly was placed in a oven and pressure up to 40 atm was applied. The system was removed from the oven after 15 minutes and allowed to cool. The template was then separated from the substrate. The substrate was then exposed to a short halogen reactive ion etch (RIE) that removed any undisplaced silicone polymer from the base of the features. An oxygen etch transferred the pattern in the silicon polymer film through the organic film. This pattern could then be used for additive metalization or further etch transfer into the substrate. An advantage of this process over other imprint

lithography schemes is that one needs only to generate low aspect ratio features in the silylated film. The O<sub>2</sub> reactive ion etch amplifies the low aspect ratio relief structure in the silylated resist into a high aspect ratio feature in the organic layer.

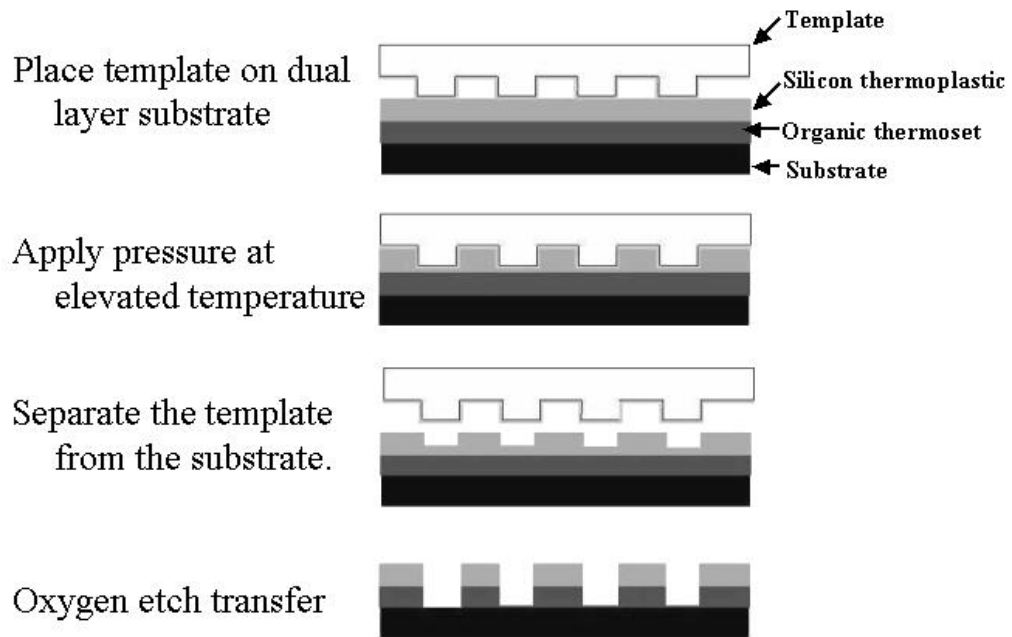


Figure 1.5. Step and Squish Imprint Lithography.

Some results from this compression molding process are shown in Figure 1.6. The micrograph on the left demonstrates the transfer of 2 μm grating with 1:1 line-to-space pitch in the silicone rubber layer over a large area. The image on the right, however, illustrates a serious problem with this approach. Imprinting with varying pattern density results in incomplete displacement of the thermoplastic even when high temperature and pressure were applied for long times. A simple depiction of this result is illustrated in Figure 1.7. Periodic

patterns and isolated protruding features are replicated relatively easily. Isolated recessed patterns are difficult to imprint successfully.

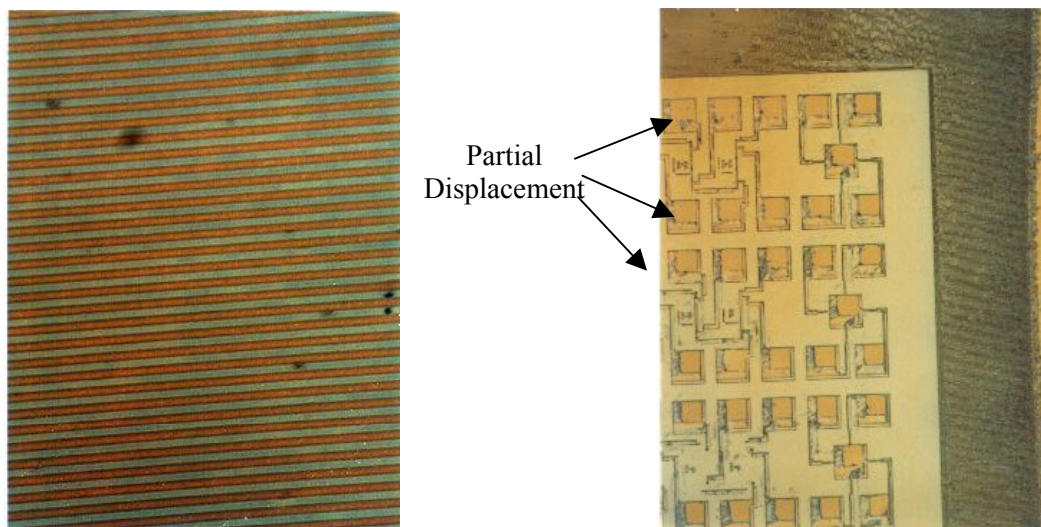


Figure 1.6. Optical micrograph of a 2  $\mu\text{m}$  grating structure created at 150  $^{\circ}\text{C}$  at a pressure of 40 psi (left), and a partial displacement of polymer in a pattern with irregular pattern density (right).

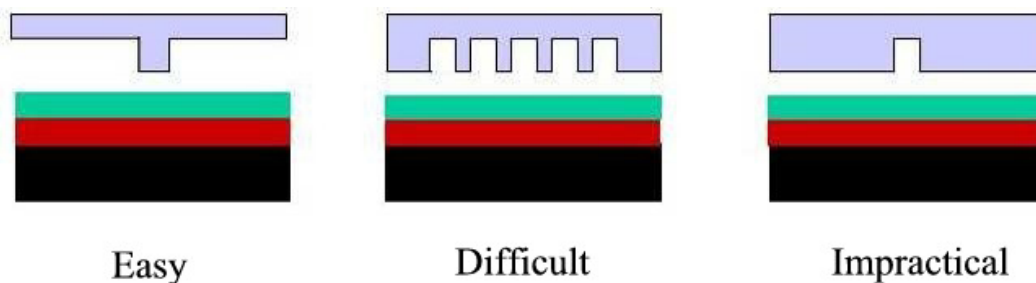


Figure 1.7. Pattern density effects were found during SSIL.

Partial pattern transfer, failure to displace material completely, release difficulties, and harsh process conditions seem to limit the potential of this approach. H.C. Scheer *et al.* also have documented these problems with

compression molding of PMMA derivatives [10]. An additional disadvantage of the thermal imprint technique is that the use of high temperatures and high pressures that compromise precise alignment and overlay required for microelectronic device fabrication.

#### **1.4.1 Soft Imprint Lithography**

The second route to imprint lithography relies on curing a low viscosity, photosensitive material with ultraviolet light. A similar method has been used in the production of optical disks [22]. Philips Research has demonstrated a photopolymer process (2P process) of this sort, which produces high-resolution polymer features [8].

In this process, shown in Figure 1.8, a liquid acrylate formulation was photopolymerized in a glass template to generate the required topographical features. The photopolymerizable solution consisted of 1,6-hexanediol-diacrylate and bis(hydroxyethyl)bisphenol-A dimethacrylate for photopolymer precursors and 2,2-Dimethoxy-1,2-diphenylethan-1-one for the free radical initiator. The dose required to cure this solution was  $\sim 1000$  mJ/cm<sup>2</sup>. It took 25 seconds with 10 kPa (75 torr) pressure applied to a 30 mm x 30 mm substrate to displace the material. The residual amount of film remaining at the base of the features was less than 40 nm after 5 minutes at 10 kPa. The uniformity of the film across 30 mm substrates was 50 nm. For 100 mm templates, however, the uniformity was greater than 500 nm. The smallest feature replicated on the 30 mm substrate was 37.5 nm [8].

While the Phillips process produced high-resolution images, it did not produce high aspect-ratio images; the narrowest having an aspect ratio of 3:1. Also, the patterned acrylate photopolymer film lack the etch resistance required for semiconductor manufacturing. However, this work does demonstrate sub-50 nm resolution for replication via photopolymerization.

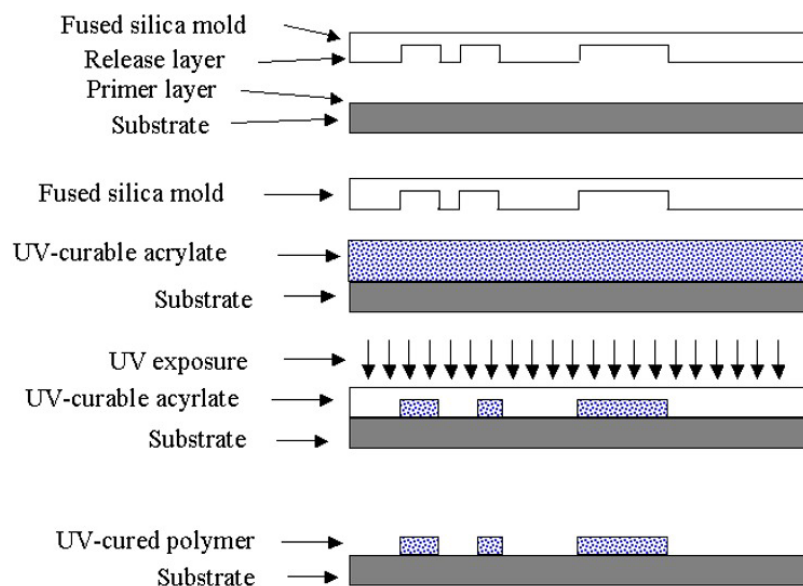


Figure 1.8. Phillips 2-P Process

Other soft imprint lithography techniques have been developed by Whitesides, *et. al.* at Harvard that generate patterns on curved surfaces as well as selective placement of self-assembly monolayers [11]. These processes differ from the above techniques in that the mold is not rigid but quite compliant. Three of the techniques developed were microcontact printing ( $\mu$ CP) [23], micromolding in capillaries (MIMIC) [24], and solvent-assisted micromolding (SAMIM) [25].

Microcontact printing has become an extensively utilized method of patterning substrates without the aid of photolithography. In  $\mu$ CP, a self-assembly monolayer (SAM) is patterned on a substrate by placing a poly(dimethylsiloxane) (PDMS) mold in contact with a substrate. The PDMS mold is first dipped in a solution of monomers that are capable of forming a SAM. Typically, this has been used for patterning either thiol on gold or chlorosilane on silicon dioxide. A contact time of 10-20 seconds is usually used [26]. The selective pattern of these SAMs allow for further functionalization of the surface or provides a means of selectively etching the unprotected surface.

Micromolding in capillaries and SAMIM both are based on a similar principle. A PDMS mold containing a topography is used to pattern a substrate. In  $\mu$ CP, the drop of photopolymer precursor is placed along side the edge of the PDMS template and the fluid is wicked into the capillary. The photopolymer precursor is then cured under ultraviolet illumination. The mold is removed and the pattern remains on the substrate. In SAMIM, a substrate coated with a polymer film was exposed to a solvent placed on a PDMS mold. The solvent plasticizes the polymer film. Under pressure, the topography of the template is imprinted into the polymer film. All these techniques require a flexible PDMS mold that is easily distorted. While these techniques are well suited for specific applications, they do not address the issue of generating sub-100nm without distortion.

## **1.5 CONCLUSION**

The cost of lithography has been growing at an exponential rate that parallels Moore's Law and the projected costs of NGL equipment may be prohibitive. Radical new patterning methods offer the possibility of a disruptive shift in patterning technology. Imprint lithography is a technique that is gaining credibility as a viable alternative to NGLs but still requires substantial research and development to meet the stringent demands of high volume semiconductor manufacturing.

References:

---

- 1 Moore, G.; "Cramming More Components Onto Integrated Circuits," *Electronics*, **38**(8), 114-117. (1965)
- 2 Streetman, B. G.; *Solid State Electronic Devices, 4th Ed.* Prentice, NJ. (1995)
- 3 Plummer, J. D.; M.D. Deal, P.B. Griffin. *Silicon VLSI Technology: Fundamentals, Practice, and Modeling.* Prentice, NJ (2000).
- 4 Okazaki. S.; *J. Vac. Sci. Technol. B*, **9**, 2829-2833 (1991)
- 5 Patterson, K.; U. Okoroanyanwu, T. Shimokawa, S. Cho, J. Byers, C. G. Willson. "Improving Performance of 193 nm Photoresists Based on Alicyclic Polymers," *Proc. SPIE*. 3333, 425-437 (1998).
- 6 *3rd International SEMATECH Next Generation Lithography Workshop.* Semiconductor Industry Association, Colorado. (1999)
- 7 Chou, S.Y; P.R.Krauss, P.R. Renstrom. *J. Vac. Sci. Technol. B*, **14**(6), 4129-33 (1996)
- 8 Haisma, J.; M. Verheijen, K. van der Huevel, J. van den Berg. "Template-assisted nanolithography: A process for reliable pattern replication," *J. Vac. Sci. Technol. B*. **14**(6), 4124-29 (1996)
- 9 Schulz, H.; H.-C. Scheer, T. Hoffmann, C. M. Sotomayor Torres, K. Pfeiffer, G. Bleidiessel, G. Grützner, Ch. Cardinaud, F. Gaboriau, M.-C. Peignon, J. Ahopelto, and B. Heidari. *J. Vac. Sci. Technol. B*. **18**(4), 1861 (2000)
- 10 Scheer, H-C; H. Schults, F. Gottschalch, T. Hoffmann, C.M. Sotomayor Torres. "Problems of the Nanoimprint Technique for nm-scale Pattern Definition," *J. Vac. Sci. and Technol. B*. **16**(6), 3917-3921 (1998)
- 11 Xia, Y.; G.M. Whitesides. "Soft Lithography," *Angew. Chem. Int.* **37**, 550-575. (1998)
- 12 Jaszewski, R. W.; H. Schiff, J. Gobrecht and P. Smith. *Microelectronic Engin.* **41/42**, 575-578 (1998)

- 
- 13 Guo, L.L.; P.R. Krauss, S. Y. Chou. "Nanoscale silicon field effect transistors fabricated using imprint lithography," *Appl. Phys. Lett.* **71**(13), 1881-1883 (1997)
  - 14 Zhang, W.; S. Y. Chou. "Multilevel nanoimprint lithography with submicron alignment on 4" wafers," *EIPBN*. Palm Springs, CA (2000)
  - 15 Constantine, C.; L. Heckerd. "ICP quartz etch uniformity improvement for phase-shift mask fabrication," *Proc. SPIE.* 3412, 220-227(1998)
  - 16 Chou, S.Y.; L. Zhuang. "Lithographically induced self-assembly of periodic polymer micropillar arrays," *J. Vac. Sci. Technol. B.* 17(6) 3197-3202 (1999)
  - 17 Thurn-Albrecht, T.; J. Schotter, G.A. Kastel, N. Emley, T. Shibauchi, L. Krusin-Elbaum, K. Guarini, C.T. Black, M. T. Tuominen, T. P. Russell. "Ultrahigh-Density Nanowire Arrays Grown in Self-Assembled Diblock Copolymer Templates," *Science.* 290, 2126-2129 (2000)
  - 18 Zhuang, L.; Personal Communication. May (2001)
  - 19 Colburn, M.; S. Johnson, M. Stewart, S. Damle, B. J. Jin, T. Bailey, M. Wedlake, T. Michaelson, S.V. Sreenivasan, J. Ekerdt, C.G. Willson. "Step and Flash Imprint Lithography: An alternative approach to high resolution patterning." *Proc. SPIE.* 3676, 379-389 (1999)
  - 20 Shaw, J.; E. Babich, M. Hatzakis, J. Paraszczak. *Solid State Technology.* **30**(6), 83-89 (1987)
  - 21 Reichmanis, E.; G. Smolinsky. "Oxygen RIE-Resistant Deep-UV Positive Resists: Poly trimethylsilylmethyl methacrylate) and Poly (trimethylsilylmethyl methacrylate-co-3-oximo-2-butanone methacrylate," *J. Electrochem. Soc.* **132**(5) (1985)
  - 22 Bouwhuis, G.; J. Braat, A. Huijser, J. Pasman, G. van Rosmalen, K.S. Immink. *Principles of optical disc systems.* Adam Hilger, Bristol, UK. (1985)
  - 23 Kumar, A.; G. M. Whitesides. *Appl. Physics Lett.* 63, 2002-2004 (1993)
  - 24 Kim, E.; Y. Xia, G. M. Whitesides. *Adv. Mater.* 376, 581-584 (1995)

---

25 Kim, E.; Y. Xia, G. M. Whitesides. *Adv. Mater.* 9, 651-654 (1997)

26 Wilbur, J.L.; E. Kim, G. M. Whitesides. *Adv. Mater.* 6, 600-604 (1994)

## **2 Step and Flash Imprint Lithography**

Imprint lithography has demonstrated extraordinary resolution but still lacks the process conditions suitable for semiconductor manufacturing. The imprint pressure and time must be drastically reduced to enable precision overlay and materials must be utilized that are consistent with reactive ion etching. The design of Step and Flash imprint lithography technique incorporates the advantages of imprint lithography but offers the opportunity to achieve the precision and reliability of conventional semiconductor processes.

### **2.1 PROCESS DESCRIPTION**

Step and Flash Imprint Lithography (SFIL) is a low pressure, room temperature technique utilizing a rigid quartz template as is shown in Figure 2.1. A substrate is coated with an organic planarization layer, known as the “transfer layer,” and brought in close proximity to a low surface energy template bearing low aspect-ratio topography. A low viscosity, UV-sensitive organosilicon solution, called the etch barrier, is deposited between the template and coated substrate. The template is brought into contact with the substrate using minimal pressure to trap the photopolymerizable etch barrier solution in the topography of the template. Then, the template is illuminated with UV through its backside thereby crosslinking the organosilicon solution at room temperature. The low viscosity acrylic photopolymer etch barrier formulation requires a dose of approximately  $20 \text{ mJ/cm}^2$  which is comparable to that of the chemically amplified resists used in high volume manufacturing today [1,2]. The template is then

separated from the substrate leaving a polymer replica of its relief image on the substrate. This patterned substrate is first etched with a short halogen break-through reactive ion etch (RIE) to remove any undisplaced silylated films, and then by an O<sub>2</sub> RIE to form a high-resolution, high aspect-ratio features in the organic layer.

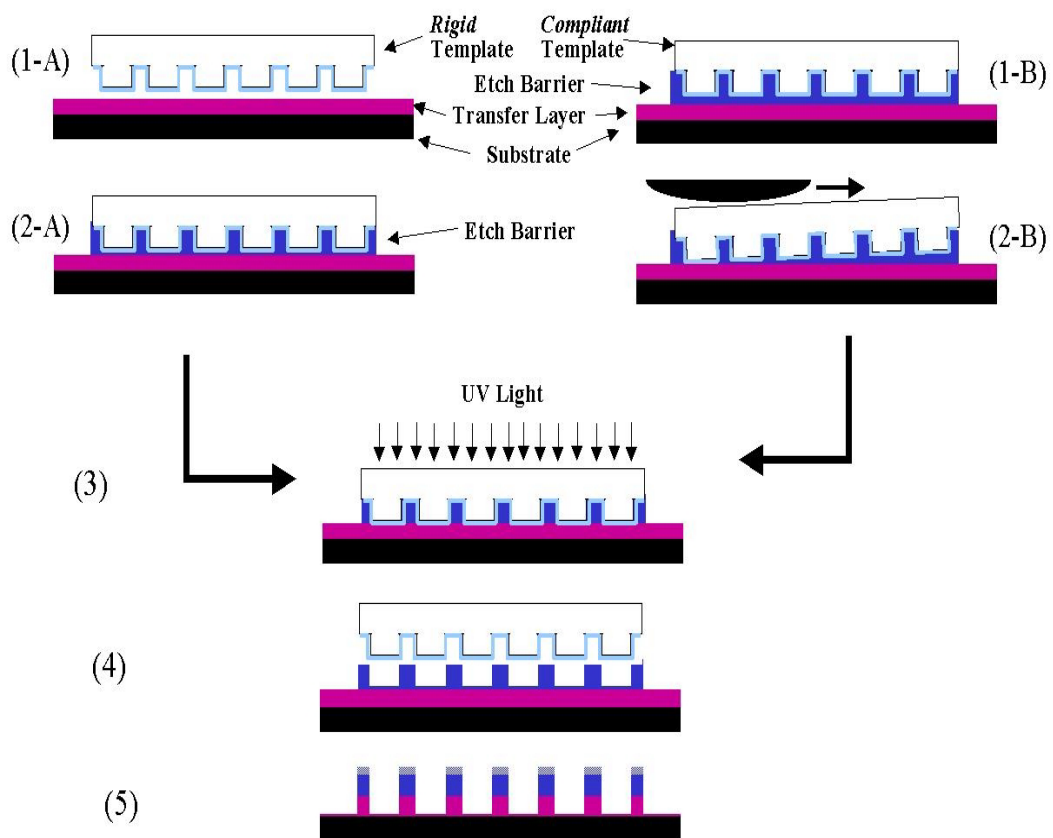


Figure 2.1. Step and Flash Imprint Lithography process flow diagram for both a) UT equipment and b) UT-Agilent Technologies imprint equipment.

The SFIL process consists of four principle components: the template, the etch barrier, the transfer layer, and the substrate. Each has material properties that

can be tailored for the purposes of high-resolution patterning. Each material has some principle properties that are desirable from a high-level standpoint.

The template should be transparent to UV light to allow for backside illumination and rigid to minimize distortion of the pattern when pressure is applied. It must also release from the etch barrier without generating particles. The substrate will be dictated by the device that is being created but may be treated with surface modifiers such as hexamethyldisilazane (HMDS) to render its surface similar to the transfer layer. The transfer layer must remain adhered to the substrate and etch barrier during the separation process while being immiscible in the etch barrier solution. The transfer layer also must have sufficient reactive ion etch selectivity relative to the substrate in order to act as an etch mask. The etch barrier must easily displaced from the gap between the template and transfer layer. Upon illumination, it must polymerize quickly and completely. After curing, it must release reliably and cleanly from the template and remain firmly adhered to the substrate. The following chapters detail work that pertains to the development of the SFIL process as a whole but will focus mainly on the etch barrier formulation. Several machines and processes used throughout the course of SFIL development are described below.

## **2.2 AGILENT-UT SFIL PROCESS**

The SFIL development program has proceeded down two parallel paths. At the University of Texas at Austin, a multi-imprint Stepper was developed to conduct a statistical defect susceptibility study on 200 mm wafers and a single imprint apparatus was constructed for preliminary resolution demonstrations. A

collaboration with Agilent Technologies was established to develop the reactive ion etch transfer process [3,4]. The SFIL process implemented at Agilent Technologies was performed using on a roller-press imprint system [3,4].

The Agilent equipment is a two-stage system consisting of a laminator capable of applying pressure to a substrate and an illumination system that crosslinks the etch barrier once the pressure is removed. A 3” diameter GaAs substrate was first coated with an organic layer. PMMA was typically used as an additive metalization mask. Then, a solution of etch barrier was spincoated onto the PMMA-coated substrate. The flexible polycarbonate-based template, treated with a fluorinated film, was applied to the surface of the substrate. The template-substrate was loaded onto the roller press and pressure was applied for no more than 2 seconds. The substrate-template was then brought to the illumination system where it was exposed to the output of a broadband 1000-Watt Hg Arc lamp. Due to the high absorbance of the polycarbonate sheet in the UV wavelengths, exposures typically took 10+ minutes. Once cured, the template was removed and the relief structure of the template topography remained on the substrate. After a short 20-second halogen break-through etch was completed, this pattern then was transferred through the transfer layer using the oxygen RIE. Further processing such as RIE transfer into the substrate and metalization was also performed.

### 2.3 SFIL SINGLE IMPRINT MACHINE (ADAPTED FROM M. COLBURN *ET AL.* [1])

Unless otherwise stated, the replication resolution demonstrations were performed on a custom-designed single imprint apparatus detailed in the master's thesis of Steve Johnson [5]. Briefly, the single imprint machines shown in Figure 2.2. The base of the press consists of two steel parallel plates fixed by four 1" diameter Steel posts. A three-ring flexure stage (Figure 2.2) mounted on the base plate was kinematically designed to allow motion in the  $z$ ,  $\alpha$ , and  $\beta$  direction but eliminates shearing motion that would result from  $x$ - $y$  translation or rotation in the  $\gamma$ -direction. It holds a 4" ceramic vacuum wafer chuck (Kyrocera) with a surface uniformity of  $\frac{1}{4}$  wave. Force transducers (Sensotec), which are mounted in the bottom of the vacuum chuck, are capable of measuring forces up to 50  $lb_f$  during the imprint step. A linear actuator consisting of a brushless DC servo motor (MicroMo), a harmonic drive gear reducer, and a precision ground ball screw slowly lowers the template along the length of linear bearings attached to the top plate and positions the template directly above the silicon wafer. The servomotor, harmonic drive, and ball screw combination offers motion resolution on the order of 10  $\mu m$  over a range of up to 6". The use of a preloaded ball screw nut and harmonic drive eliminates backlash that may cause problems with the SFIL replication process. The template is mounted facedown onto the mount plate with a dovetail fixture. A hole in the surface of the mount plate and the fixture allows for backside illumination through the template. The entire system is controlled and monitored with Labview 5.0.

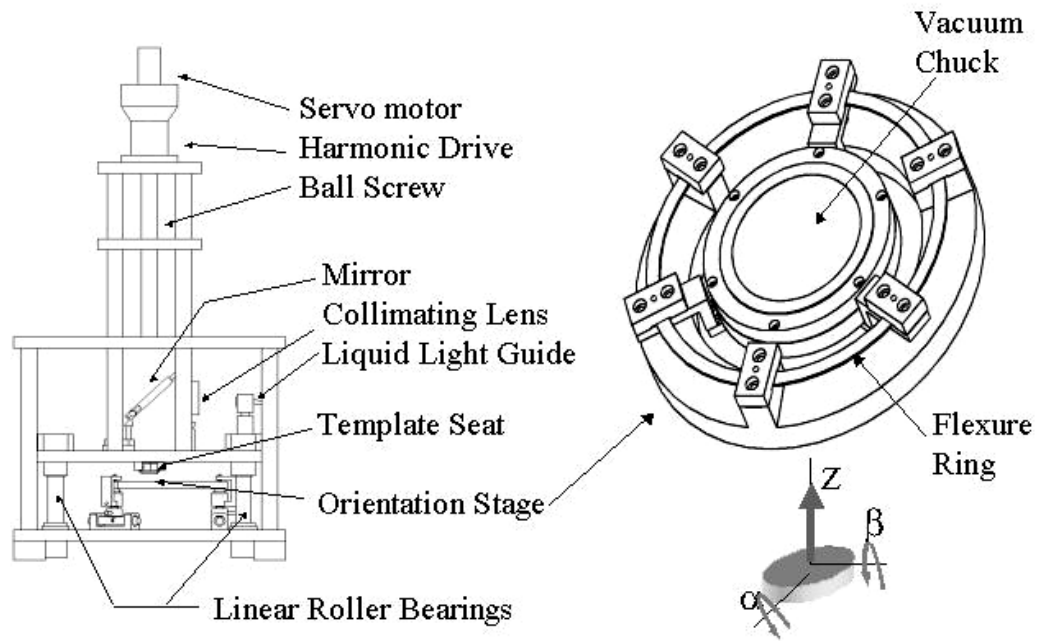


Figure 2.2. SFIL Single Imprint Apparatus (left) and the passive wafer stage (right) based on a three ring flexure that allows motion in the  $\alpha$ ,  $\beta$ , and  $Z$  directions.

#### 2.4 SFIL IMPRINT STEPPER (Adapted from Choi, et al. [6])

The multi-imprint Step and Flash Lithography machine that can perform repeated imprints on 200 mm wafers was developed for the purpose of defect susceptibility analysis, and is shown in Figure 2.3. This machine can imprint high-resolution (sub-100 nm) features from quartz templates using a step-and-repeat process. The major machine components include the following: (i) a micro-resolution  $Z$ -stage that controls the average distance between the template and substrate and the imprinting force; (ii) an automated  $X$ - $Y$  stage (Ultratech) for step and repeat positioning; (iii) a pre-calibration stage that enables parallel

alignment between the template and substrate by compensating for orientation errors introduced during template installation; (iv) a fine-orientation flexure stage that provides a highly accurate, passive parallel alignment of the template and wafer to the order of tens of nanometers across an inch [6]; (v) a flexure-based wafer calibration stage that orients the top of the wafer surface parallel with respect to the plane of the XY-stage; (vi) an exposure source that is used to cure the etch barrier; (vii) an automated fluid delivery system that accurately dispenses known amounts of the liquid etch barrier; and (viii) load cells that provide both imprinting and separation force data.

The multi-imprint apparatus is currently configured to handle 1 cm x 1 cm templates. It is used to produce more than 20 imprints on 200 mm wafers for defect studies. The installation of the template and the loading and unloading of the wafer are performed manually. The printing operations, including X-Y positioning of the wafer, dispensing of etch barrier liquid, translation of the template to close the gap between the template and wafer, UV curing of etch barrier, and controlled separation are all automated. These unit processes are controlled by a LabVIEW<sup>®</sup> interface. Detailed information about the major subcomponents of the system is available in publications by this group [6].

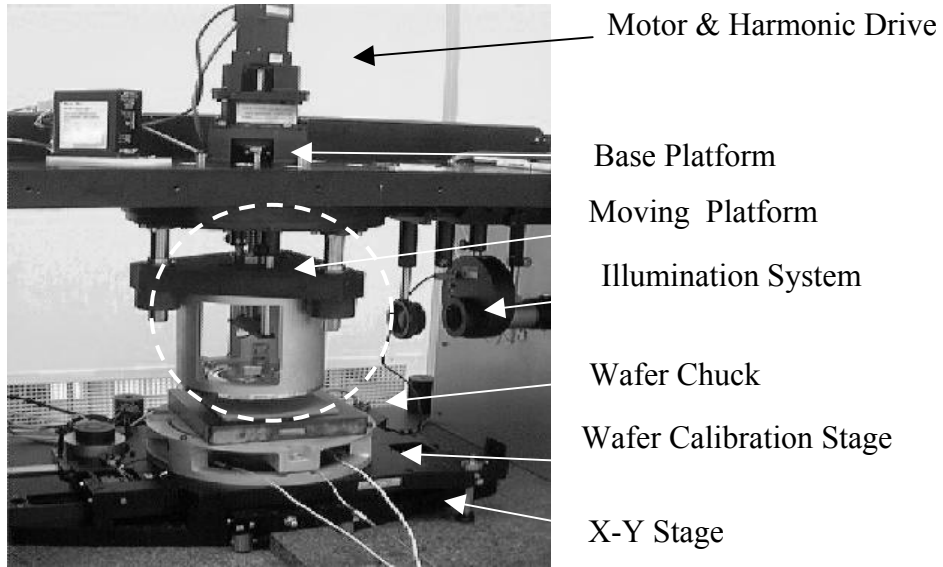


Figure 2.3. Multi-imprint SFIL Stepper.

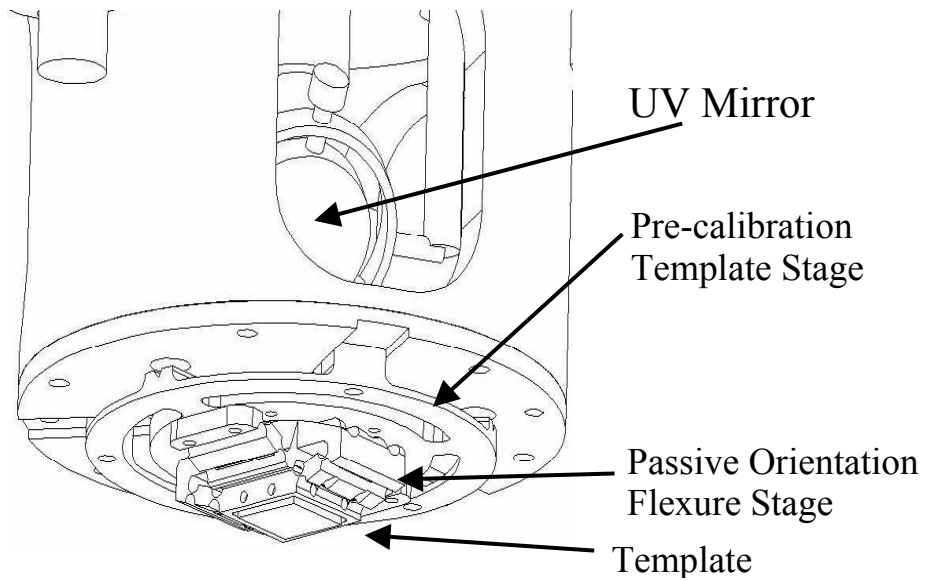


Figure 2.4. Template stage housing.

## **2.5 ILLUMINATION SUB-SYSTEM FOR SINGLE-IMPRINT APPARATUS AND MULTI-IMPRINT STEPPER.**

Two nearly identical illumination systems designed were incorporated into the SFIL multi-imprint stepper and the SFIL single imprint apparatus (Figure 2.5). For both systems, the illumination source is a 500-Watt Hg arc lamp (Oriel, 66142) with a maximum output at the 365 nm Hg-line. The light is focused with a parabolic mirror within the lamp housing (Oriel, 66033) through the 1.5" diameter exit optics. An electronically controlled shutter passes or blocks the light. If passed, an Infrared water filter (Oriel, 6117) absorbs infrared energy from the light.

For the single imprint apparatus, the light exiting the filter passes through a UV-pass filter and is focused into a liquid light guide (Oriel, 7755) using a coupling optic (Oriel, 77800). The diverging light exiting the liquid light guide is collimated and projected onto a 2" diameter 45° UV-enhanced mirror (Ed. Sci, D32,638) with the collimating optic (Ed. Sci., D8,008). The mirror reflects the light down through the hole in the mount plate, the template fixture, and the transparent template. This allows for efficient curing of the etch barrier film.

For the multi-imprint imprint apparatus, the light exiting the IR filter continues through a 1" diameter filter (Melles Griot, FCG177) that transmits wavelength from 250 nm to 400 nm. This light is then focused with a fused silica plano-convex lens (Ed. Sci., D8,008) with a focal length of 75 mm. The light is then collimated to a diameter of ~1.5" with a fused silica plano-concave lens (Ed. Sci., D8,030) which has a focal length of -75mm. The collimated light is projected onto a 45° UV-enhanced mirror and reflected down through the hole in

the mount plate, the template fixture, and the transparent template. A power meter can monitor a small region of UV light passing outside the diameter of mirror for dose control (see Appendix 2).

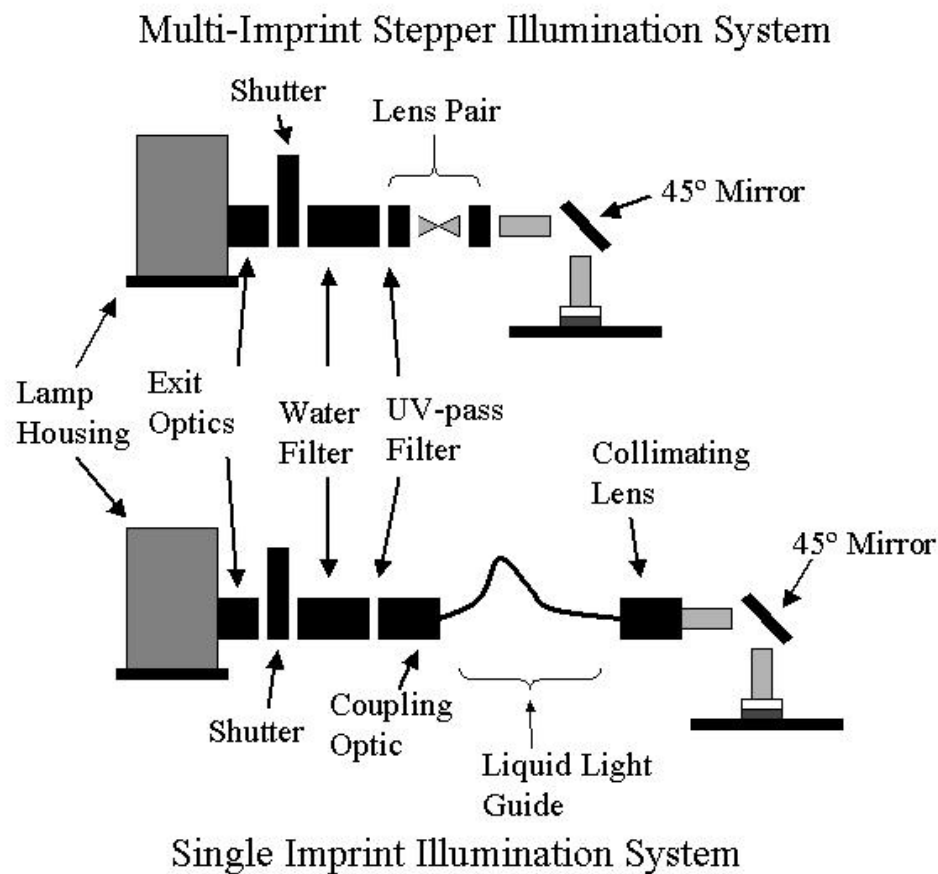


Figure 2.5. SFIL illumination sub-systems.

## 2.6 TEMPLATE FABRICATION PROCESS

The SFIL process is designed with reliable, high-resolution patterning capability in mind. The concept of layer-to-layer overlay has always been a primary consideration in the development of the materials and process. In order

to pattern a semiconductor substrate with functional devices, several layer-to-layer alignments are required as is evident from the MOS process shown in Chapter 1 [7]. As such, the process has been designed to take advantage of typical semiconductor processes such as phase-shift reticle technology for template fabrication, reactive ion etch for feature transfer, and conventional alignment schemes based on Moiré fringes, box-in-box, and veneer patterns applicable to transparent templates.

### **2.6.1 Template Pattern Generation**

The SFIL templates are fabricated using a conventional phase-shift reticle process flow that is shown in Figure 2.6. A semiconductor-standard 6"x6" reticle-grade fused silica blank coated with  $\sim 1000\text{\AA}$  of chromium is spin coated with a photoresist. The substrate is then post-application baked (PAB) to drive off excess casting solvent. In general, the resist thickness after PAB is 200 nm to 300 nm; the exact resist and bake conditions are propriety to the reticle manufacturer. The plate is then exposed by electrons in a direct-write patterning tool. Most templates have been fabricated using a direct write electron beam (e-beam) tool due to their sub-100 nm patterning capability. These tools work in a similar fashion to a scanning electron microscope (SEM) [8]. The electron beam tool consists of a source filament, an extraction piece, a condenser lens, an objective lens. The condenser and objective lenses focus electrons which are extracted from the source and raster the beam across the surface of the resist creating a latent image of a specified layout in the resist. In the case of the template manufactured at IBM-Burlington, the tool was the EL-04 electron

projection tool designed in-house by IBM. Once the pattern is written in the resist, the resist is developed. Resists respond to the irradiation in either a positive or negative tone. PMMA is a standard positive tone electron beam resist that undergoes chain scission upon exposure to an electron beam of sufficient energy. Therefore, upon development, the exposed regions of PMMA are removed leaving behind a pattern in the unexposed resist patterns. This pattern is then etched into the chromium layer by a chlorine based reactive ion etch. Again, the exact process conditions of this etch are proprietary to each reticle manufacturer. The etch selectivity between the resist and the chromium is approximately 1:1 [9]. This dictates that the spin coated resist must be 2 to 3 times as thick as the chromium in order to minimize etch related defects. Once the pattern is etched into the chromium, a fluorine based reactive ion etch transfers the image into the fused silica substrate to a depth of 100 to 200 nm depending on the minimum feature size in the pattern. The chromium acts as an etch mask for the fused silica and a conducting layer that minimizes charging effects during electron beam writing.

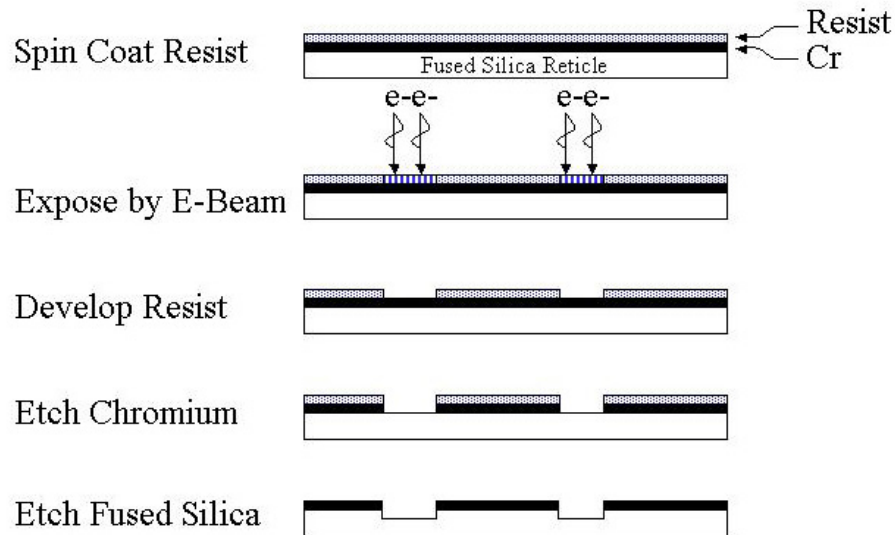


Figure 2.6. Template Fabrication Process.

### 2.6.2 Template Generation

Once the pattern is written and transferred into the reticle, it is spin coated with a protective polymeric coating. Two sets of 100  $\mu\text{m}$  wide scribe lines are cut across the 6" length of the template perpendicular to two adjacent edges. They form a rectilinear grid on a 1" x 1" spacing. A second pass cut with a thinner blade is made in each scribe line through the entire thickness template. The scribe lines minimize the chipping that may occur when cutting through the entire  $\frac{1}{4}$ " thick template. After being cut into 1"x1" templates, the protective coating is stripped in organic solvent.

The template is stripped of the chromium layer with a wet etch. The etchant is formulated by mixing 16.45 g of Cerium Ammonium Nitrate ( $\text{Ce}(\text{NH}_4)_2(\text{NO}_3)_6$ , Aldrich) into 100 mL of deionized (DI) water. The orange

Cerium Ammonium Nitrate powder remains undissolved in the water. To this mixture, 4.3 mL of perchloric acid ( $\text{HClO}_4$ , Aldrich) is added. The powder dissolves in the solution turning it a bright orange hue. The template is then placed into the well-mixed solution for 2-5 minutes or until the template appears transparent. Once the chromium is completely etched the template is removed from the solution and rinsed in DI water for 10 minutes. The template is then dried in a furnace at  $110^\circ\text{C}$ . The templates are removed and allowed to cool.

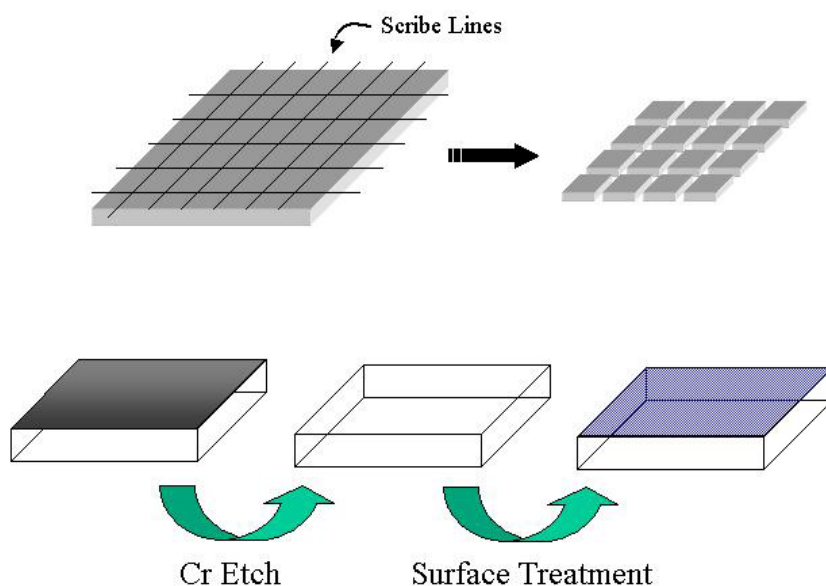


Figure 2.7. Template Generation. After patterning, the mask is cut into template pieces. The chromium is removed and the transparent template is surface treated with a fluorinated self-assembly monolayer.

## 2.7 SURFACE TREATMENT

The templates are treated with tridecafluoro-1,1,2,2-tetrahydroctyltrichlorosilane (Gelest). Two primary methods of applications were

studied: liquid phase and vapor phase. In both cases, the chlorosilane reacts with the surface silanol (SiOH) group on the template to release HCl [10]. The remaining chlorosilane bonds react with adjacent chlorosilanes releasing HCl as the by-product of the reaction. Other monomers such as the ethoxy and methoxy counterpart to the chlorosilane are available and are more stable to hydrolysis than the chlorosilane [11]. The by products of these monomers are ethanol and methanol, respectively. These can also be synthesized by reacting the chlorosilane with the corresponding alkyl alcohol [11].

#### ***2.7.1.1 Immersion Treatment***

For the liquid phase surface treatment, the clean template (with the chromium stripped) was triple rinsed in H<sub>2</sub>O:acetone:isopropanol then heated at 90°C to drive off adsorbed solvent. In a dry box, the template was submerged with the pattern side up (to prevent damage to the surface of the substrate) in a 1% (w/w) solution of tridecafluoro-1,1,2,2-tetrahydrooctyltrichlorosilane (Gelest) in an azeotropic mixture of methylnonafluoro-*n*-butyl ether and methylnonafluoro-isobutyl ether (HFE7100, 3M). The template was immersed for the desired time, typically 15 minutes. It was then removed and rinsed in pure HFE 7100 for a specific amount of time, typically 15 minutes. HFE 7100 serves as a dewetting agent for adsorbed tridecafluoro-1,1,2,2-tetrahydrooctyltrichlorosilane that is not covalently bound to the surface of the substrate. The treatment rendered the surface similar to Teflon<sup>®</sup> which has a surface energy of 18 dynes/cm [12]. After the rinse in HFE 7100, the templates were dried in a filtered air stream. The success of the surface treatment was validated by measuring the contact angle of

the template with water. If the contact angle of water with the substrate was greater than 90 then the treatment was considered to be successful.

### ***2.7.1.2 Vapor Phase Deposition***

For the vapor phase surface treatment, the template with the chromium stripped was triple rinsed in H<sub>2</sub>O:acetone:isopropanol then heated at 90°C to drive off adsorbed solvent. In a dry box, the template was placed in a sealable vessel with the pattern side up (to prevent damage to the surface of the substrate). Three drops of tridecafluoro-1,1,2,2-tetrahydroctyltrichlorosilane from a 3 mL disposable glass pipette were placed in the bottom of the vessel and the vessel sealed. The vapor pressure of tridecafluoro-1,1,2,2-tetrahydroctyltrichlorosilane is 1.6 kPa at 24.4°C. The template remained sealed in the vessel for the desired time, typically 30 min. It was then removed and rinsed in HFE 7100 for a specific amount of time, typically 15 minutes. HFE 7100 serves as a dewetting agent for adsorbed tridecafluoro-1,1,2,2-tetrahydroctyltrichlorosilane that is not bonded to the surface of the substrate. After the rinse, a filtered air stream was used to dry the templates. Again, the success of the surface treatment was then validated by measuring the contact angle of the template with water. Baker has found that the annealing promotes the crosslinking of adjacent chlorosilanes but that if left for 24 hours at room temperature the networking still occurs [11]. An adaptation of the vapor phase treatment and its durability is being studied and will be detailed in his doctoral thesis of Todd Bailey [13].

## **2.8 SUMMARY**

There are four principle components to the SFIL system: the substrate, the transfer layer, the etch barrier, and the template. The properties of each component can be tailored to optimize the process. The following chapters detail work that pertains to the development of the SFIL process as a whole but will focus mainly on the etch barrier formulation. The processes and equipment detailed above have been routinely used throughout the course of development to explore the influence of surface energy, fluid dynamics, etch resistance, and mechanical properties on SFIL.

## References:

---

- 1 Colburn, M.; S. Johnson, M. Stewart, S. Damle, B. J. Jin, T. Bailey, M. Wedlake, T. Michaelson, S.V. Sreenivasan, J. Ekerdt, C.G. Willson, *Proc. SPIE*. 3676, 379-389 (1999)
- 2 Mack, C. A.; M. Ercken, M. Moelants. "Matching Simulation and Experiment for Chemically Amplified Resists," *Proc. SPIE*. 3679, (1999)
- 3 Colburn, M.; A. Grot, M. N. Amistoso, B. J. Choi, T. C. Bailey, J. G. Ekerdt, S.V. Sreenivasan, J. Hollenhorst, C.G. Willson. *Proc. SPIE*. 3997, 453-457 (2000)
- 4 Colburn, M.; A. Grot, B. J. Choi, M. Amistoso, T. Bailey, S.V. Sreenivasan, J. G. Ekerdt, C. G. Willson. "Patterning non-flat substrates with a low pressure, room temperature imprint lithography process," *J. Vac. Sci. Technol. B*. (2001) [submitted]
- 5 Johnson, S; "Selectively Compliant Orientation Stages for Imprint Lithography." MS Thesis, The University of Texas at Austin. (1999)
- 6 Choi, B. J.; S. Johnson, M. Colburn, S.V. Sreenivasan, C. G. Willson. "Design of Orientation Stages for Step and Flash Imprint Lithography." *J. Precision Engineering*. [accepted]
- 7 Choi, B. J.; M. Meissl, M. Colburn, T. Bailey, P. Ruchhoeft, S.V. Sreenivasan, F. Prins, S. Banerjee, J.G. Ekerdt and C.G. Willson. "Layer-to-Layer Alignment for Step and Flash Imprint Lithography", *Proc. SPIE: Emerging Lithographic Technologies*. (2001) [accepted]
- 8 Goldstein, J. I.; D.E. Newbury, P. Echlin, D.C. Joy, A.D. Romig, C.E. Lyman, C. F. and E. Lifshin. *Scanning Electron Microscopy and X-Ray Microanalysis: A text for biologist, material scientists, and geologists*. Plenum, NY (1992)
- 9 Constantine, C.; L. Hecker. "ICP quartz etch uniformity improvement for phase-shift mask fabrication," *Proc. SPIE*. 3412, 220-227(1998)
- 10 Plueddemann, E. P.; Silane Coupling Agents. Plenum, NY (1982)
- 11 Arkles, B.; "Tailoring surfaces with silanes," *Chemtech*, 7, 766-778 (1977)

- 
- 12 Wu, S.; ed. "Surface and interfacial energies of polymers," *Polymer Handbook*. Wiley, 411-432 (1989)
- 13 Bailey, T.; B. J. Choi, M. Colburn, M. Meissl, S. Shaya, J. G. Ekerdt, S.V. Sreenivasan, C. G. Willson. "Step and Flash Imprint Lithography: Template Surface Treatment and Defect Analysis," *J. Vac. Sci. Technol. B*, **18**(6), 3572-3577 (2000).

### 3 Fluid Dynamics Evaluation

Two of the primary issues affecting the manufacturability of SFIL are throughput and replication reliability. The rate limiting step in the SFIL replication process is the application of the etch barrier to the imprint field. Spin coating, capillary action, and compression fill techniques have been investigated in an effort to match the theoretical SFIL throughput to that of conventional semiconductor lithographic systems, which print approximately 1-3 cm<sup>2</sup> per second.

#### 3.1 CAPILLARY ACTION

Capillary action was the first method of etch barrier application that was investigated. In this approach shown schematically in Figure 3.1, the template and substrate are brought into close proximity (1-100 μm); a drop of etch barrier is dispensed on the substrate at the edge of template; and the fluid is drawn into the gap by surface tension of the etch barrier that forms a contact angle with the template ( $\theta_1$ ), and with the substrate ( $\theta_2$ ).

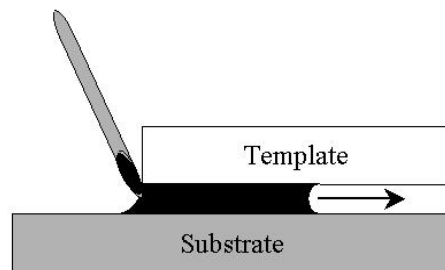


Figure 3.1. The etch barrier wicks the cavity between the template and the transfer layer by capillary action as it is being delivered by a micropipette.

The rate that the etch barrier fills the gap between the template and substrate,  $H$ , can be described by the Washburn equation [1]:

**Equation 3.1** 
$$\frac{dx}{dt} = \frac{(H^2 \gamma_{EB} / H_{curv})}{24 \mu x}$$

which accounts for the effects of viscosity,  $\mu$ , surface tension,  $\gamma_{EB}$ , and the radius of the meniscus,  $H_{curv}$ , of the etch barrier and the distance of the meniscus along the length of the capillary,  $x$ . The rate of fill is maximized for a given gap height and surface tension when the radius of meniscus is minimized, which occurs when the etch barrier completely wets both the template and the transfer layer.

If the etch barrier is delivered along the entire length of one side of the template, it fills in a rectilinear fashion and the fill time can be calculated by integrating Equation 3.1 which results in the following equation:

**Equation 3.2.** 
$$t_{fill} = \frac{12 \mu L^2}{(H^2 \gamma_{EB} / H_{curv})}$$

where  $t_{fill}$  is the time required for the etch barrier to traverse the length of the template,  $L$ .

In Figure 3.2, the time required to fill a 2.54 cm long template with a fluid with a surface tension of 30 dyne/cm that is assumed to wet both the template and the substrate ( $H=H_{curv}$ ) is shown as a function of the quantity  $(\mu/H)$ . From this plot, the time for a 1 cP fluid to fill a 1  $\mu\text{m}$  gap is 129 seconds. Similarly, the gap height that will fill in 1 second is 129 microns. If a fill time of 1 second is

imposed, the gap height must be quite large and would require 99.9% of the fluid that filled the gap to be expelled from the gap into the area surrounding the template before photopolymerization. This would cause manufacturing problems and demonstrates that employing capillary action alone to fill the gap is not consistent with semiconductor manufacturing requirements.

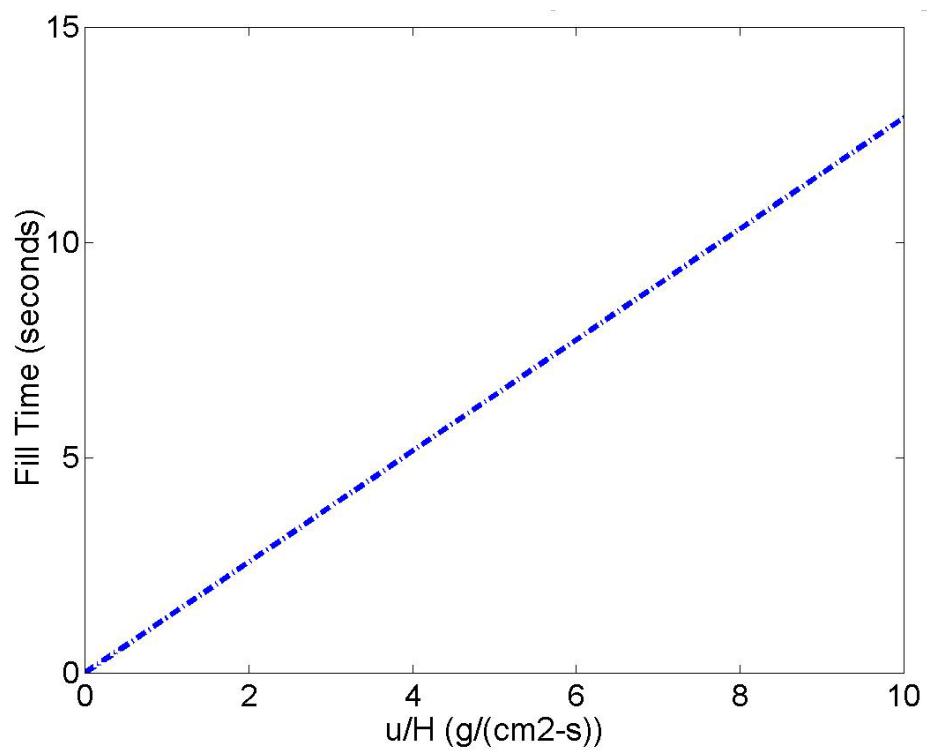


Figure 3.2. The time to fill a gap that is 2.54 cm long with a fluid the wets both gap surfaces is shown as a function of  $\mu/H$ .

### 3.2 APPLICATION BY SPINCOATING

Spincoating is the conventional means of dispensing a photoresist onto a substrate. However, this process is used with high glass transition temperature polymers that form stable films as the casting solvent evaporates. The thermodynamic criterion for a stable thin film is:

**Equation 3.3** 
$$A_{Ham} L^2 < 8\pi^3 h^4 \gamma$$

where  $A_{Ham}$  is the Hamaker constant,  $L$  is the wavelength of dewetting,  $h$  is the thickness, and  $\gamma$  is the surface energy [2].

Given that  $A_{Ham}$  is usually  $10^{-20}$  J, the  $\gamma$  of the etch barrier is  $\sim 30$  dyne/cm, the maximum diameter of the substrate would be 0.1 mm for a 200 nm thick stable film [2]; thus, the low viscosity etch barrier films are predicted to dewet the substrate. This is observed experimentally. Even if a stable film were to be cast, the spontaneous and stochastic snap of the etch barrier meniscus to the surface of the quartz template as it approaches the substrate results in bubble formation and, consequently, a high density of defects during the imprint process.

### 3.3 SINGLE DROPLET COMPRESSION

The application of the etch barrier by droplet-compression is quite different in nature from capillary fill or spin coating. In the droplet-compression method, the etch barrier acts as a damping fluid between the template and the etch barrier and its behavior can be analyzed by lubrication theory since the template width is much larger than the template-substrate gap [3,4].

The analysis below assumes that a flat template is parallel to a flat substrate, that both are cylindrically symmetric, and that the template and the substrate are infinitely rigid with respect to the forces generated as a result of the fluid compression. The fluid (or etch barrier) is assumed to exhibit Newtonian behavior and obey no slip boundary conditions at the template and substrate surfaces. Based on scaling arguments, the pressure gradient is also assumed to be much greater in the radial direction than in the vertical direction. The coordinate system is symmetric between the two surfaces and is shown schematically in Figure 3.3. The gap height,  $2H$ , is compressed with a force,  $F$ , while the plates approach the center of the fluid with a velocity,  $V$ . The velocity of the template relative to the substrate is therefore  $2V$ .

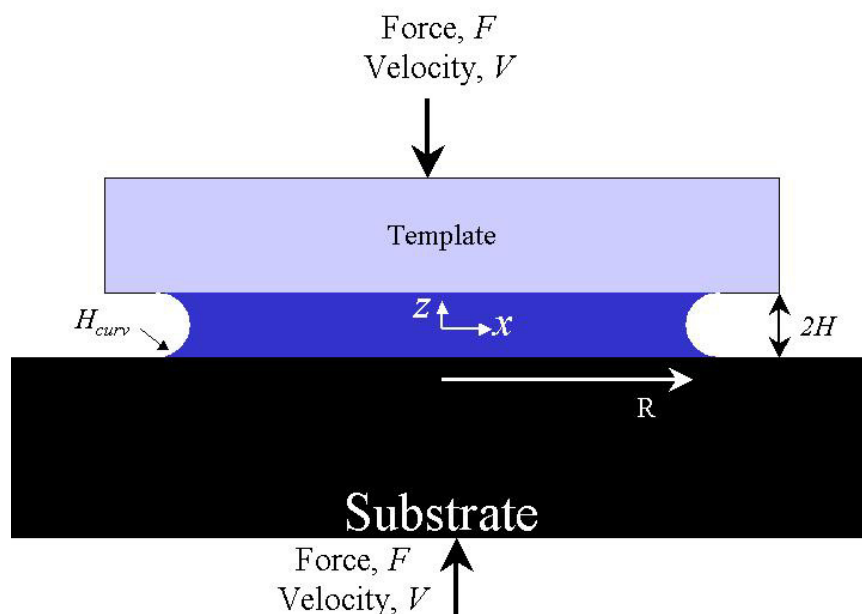


Figure 3.3. The template and substrate approach each other with a velocity,  $2V$ , and displace the fluid between them in a radial manner. The gap height is  $2H$  and the meniscus of the fluid has a meniscus radius,  $H_{curv}$ .

With these assumptions, the continuity equation simplifies to:

$$\text{Equation 3.4} \quad \frac{1}{r} \frac{\partial}{\partial r} (ru_r) = -\frac{\partial u_z}{\partial z}$$

where  $u_r$  is the velocity of the fluid in the radial direction and  $u_z$  is the velocity of the fluid in the z-direction and the radial component of the momentum balance simplifies to:

$$\text{Equation 3.5} \quad \frac{\partial p}{\partial r} + \mu \frac{\partial^2 u_r}{\partial z^2} = 0$$

where  $\mu$  is viscosity of the fluid and  $p$  is the pressure in fluid. Solving Equation 3.5 for  $u_r(z)$  yields:

$$\text{Equation 3.6} \quad u_r(z) = \frac{H^2}{2\mu} \frac{\partial p}{\partial r} \left[ 1 - \left( \frac{z}{H} \right)^2 \right]$$

where  $H$  is equal to  $\frac{1}{2}$  the gap height. Substituting Equation 3.6 into Equation 3.4 and applying the boundary condition that the vertical velocity at the template,  $V$ , is equal to  $\frac{1}{2}$  the absolute velocity that the template and substrate approach each other, produces:

$$\text{Equation 3.7} \quad V = \frac{H^3}{3\mu r} \left[ \frac{\partial p}{\partial r} + r \frac{\partial^2 p}{\partial r^2} \right]$$

Integrating Equation 3.7 defines the radial pressure distribution under a template approaching a substrate with a velocity,  $2V$ , through a gap,  $2H$ , filled with a fluid that has a viscosity,  $\mu$ , surface tension,  $\gamma$ , and meniscus with a radius of curvature,  $H_{curv}$ .

**Equation 3.8** 
$$p = \left( P_{atm} - \frac{\gamma}{H_{curv}} \right) + \frac{3\mu VR^2}{4H^3} \left[ 1 - \left( \frac{r}{R} \right)^2 \right]$$

The capillary boundary condition effectively lowers the pressure required to achieve a certain gap relative to the condition where the capillary forces are absent. The pressure required to displace a fluid of radius,  $R$ , at a velocity,  $V$ , can be calculated by integrating the pressure distribution function across the contact radius to yield:

**Equation 3.9** 
$$P = \left( P_{atm} - \frac{\gamma}{H_{curv}} \right) + \frac{3\mu VR^2}{8H^3}$$

Several features of Equation 3.9 are worth noting. This relationship does not include any assumptions about the relationship between the gap height and the radius of the drop but is a generalized case including the effect of capillary pressure. The meniscus radius,  $H_{curv}$ , is dictated by the contact angle that the fluid makes with the two surfaces:

**Equation 3.10** 
$$H_{curv} = \frac{H}{(\cos \theta_1 + \cos \theta_2)}$$

where  $\theta_1$  and  $\theta_2$  are the contact angles that the fluid makes with the surface of the template and with the substrate separated by a distance,  $H$ . The pressure scales linearly with velocity and viscosity but is more strongly dependent on the radius of the displaced fluid ( $R^2$ ), and the gap height ( $H^3$ ). Therefore, the force required to imprint will increase parabolically with the imprinted area and cubically with the inverse of the film thickness.

### 3.3.1 Film Time Analysis

Several control methodologies can be applied to the imprint system. Five cases are detailed below based on displacement of a constant volume, displacement at a fixed velocity, displacement at a fixed pressure, and displacement with a constant applied force.

#### 3.3.1.1 Case 1: Filled Gap, Constant Pressure

If the fluid being displaced initially fills the gap to the radius of the template and is displaced for set time,  $t_{fill}$ , a fixed applied pressure,  $P$ , required to achieve a thickness,  $2H_f$ , can be simplified to:

$$\text{Equation 3.11} \quad P_{gauge} = \frac{3\mu R_{Template}^2}{16t_{fill} H_f^2} \left[ 1 - \left( \frac{H_f}{H_o} \right)^2 \right]$$

where  $2H_f$  is the final gap height and is equivalent to the desired base layer thickness,  $H_o$  is  $\frac{1}{2}$  of the initial gap height, and  $R_{template}$  is the radius of the template. The capillary effect disappears due to a lack of a fluid meniscus at the edge of the template. Figure 3.4 shows the fill time required to compress a 1 cP fluid and 100 cP fluid from an initial thickness of 1 micron to a base layer of 100 nm using a template of radius 1 cm. It can be seen that for reasonable imprint times, the viscosity must be minimized.

### Compression with Fixed Applied Pressure with Two Fluids of Different Viscosities

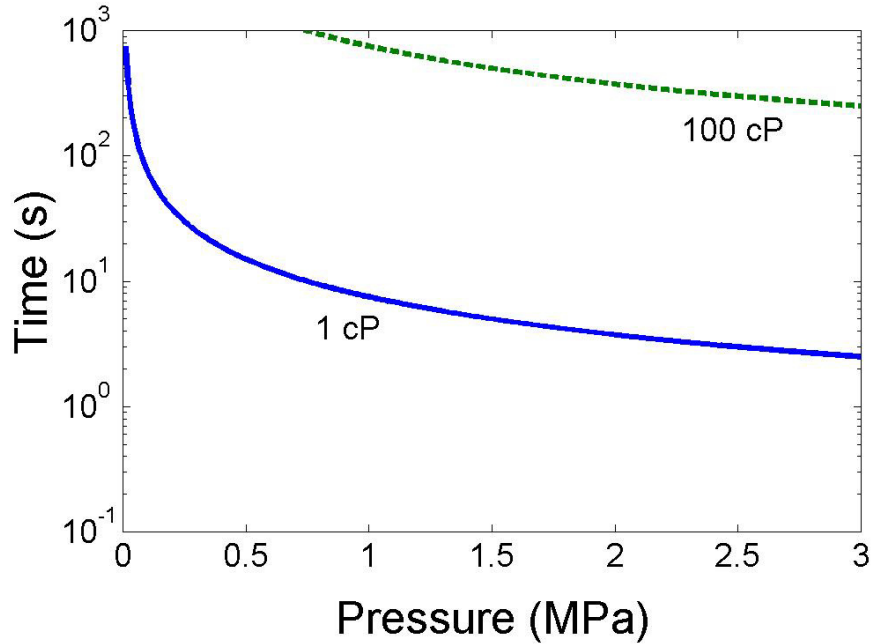


Figure 3.4. The time required to compress a filled gap starting at a height ( $2H_o$ ) of 1 micron to a height ( $2H_f$ ) of 100 nm with a fixed pressure for a 1 cP fluid and a 100 cP fluid.

#### 3.3.1.2 Case 2: Filled Gap, Constant Velocity

Alternatively, the velocity can be held constant and the pressure as a function of the gap height,  $H$ , can be obtained as follows when the velocity is defined as  $V = \frac{H_o - H_f}{t_{fill}}$ :

**Equation 3.12**

$$P_{gauge} = \frac{3\mu R_{template}^2}{8t_{fill}H^3}(H_o - H_f)$$

A comparison of the pressures used in cases 1 and 2 can be drawn if the imprint time is fixed. Figure 3.5 shows the pressure as a function of gap height for the constant velocity case (Case 1) and the constant pressure case (Case 2) with a 1 second imprint time. The constant velocity method generates very little resisting pressure initially but as the base layer becomes thin the pressure begins to increase dramatically.

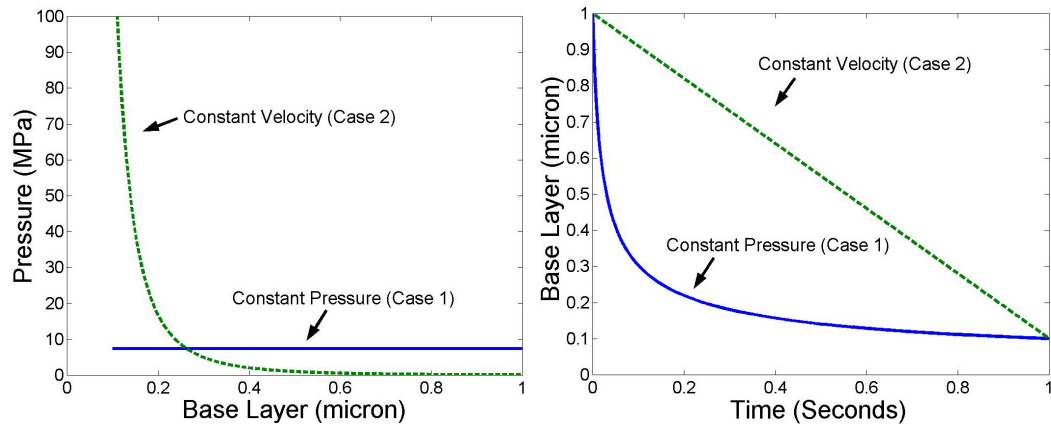


Figure 3.5. Comparison of pressure as a function of base layer ( $2H$ ) for constant pressure (Case 1) and constant velocity (Case 2) actuation schemes. The imprint time is 1 second. (Left) The corresponding base layer during the time of actuation.

### 3.3.1.3 Case 3: Fixed Volume, Constant Velocity

In both of the cases described above, the radius of the template defined the limits of the pressure distribution. If, however, the volume of the fluid is fixed and defined as  $K = \pi R_{template}^2 L$  where  $L$  is the final desired gap height, then the displacing pressure,  $P$ , can be defined in terms of the vertical gap height,  $H$ , and the velocity,  $V$ , as shown below:

**Equation 3.13** 
$$P_{gauge} = \frac{3\mu K(H_o - H_f)}{8\pi r_{fill}} \left( \frac{1}{H^4} \right) - \frac{\gamma}{H_{curv}}$$

The time to fill the cavity under these circumstances is defined by the  $(H_o - H_f) / V$ . The force changes drastically through the course of the displacement as the gap height gets smaller just as in Case 2. Figure 3.6 demonstrates the effect of compressing a constant volume on the total pressure exerted on the substrate during compression. The fixed volume (case 3) method exhibits significantly less pressure than the Case 2 method at identical gap heights.

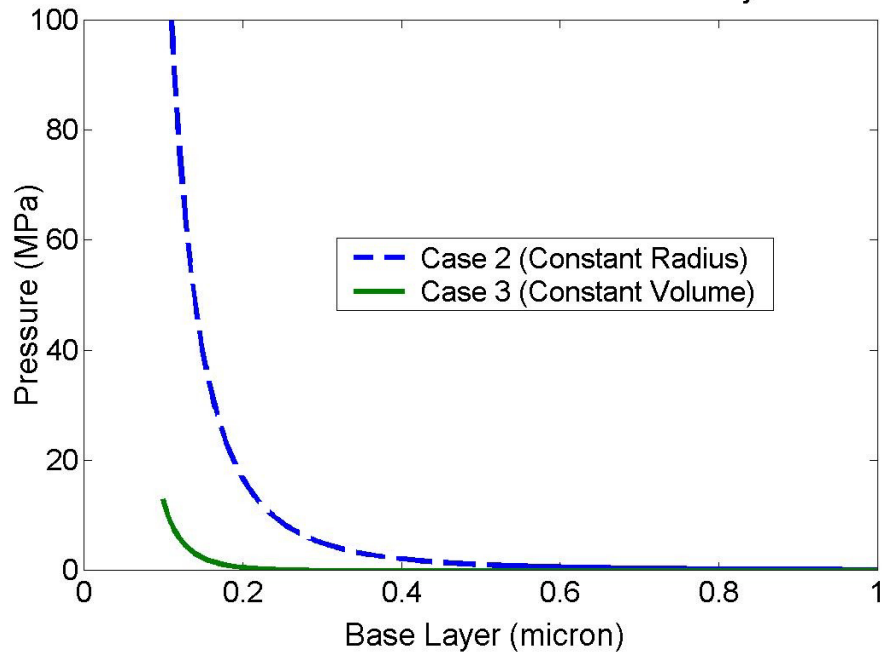


Figure 3.6. Comparison of pressure generated as a template expels fluid from the gap for Case 2 and Case 3 fill methods ( $2V = 0.9 \mu\text{m/s}$ ).

### 3.3.1.4 Case 4: Fixed Volume Constant Pressure

As with case 1, if the pressure,  $P$ , is held constant and a fixed volume,  $K$ , is being displaced, the time required to achieve a final thickness,  $2H_f$ , can be calculated by substituting  $V = dH/dt$  into Equation 3.13 and integrating by partial fraction expansion to yield the following relationship:

$$\text{Equation 3.14} \quad t_{fill} = \frac{3\mu K}{8\pi P} \int_{H_o}^{H_f} \frac{dH}{H^3 \left( H + \gamma/P \right)}$$

### 3.3.1.5 Case 5: Fixed Volume, Fixed Force

In this scheme, a fixed force,  $F$ , is applied to the template through the course of template actuation. Given a fixed volume, the contact area that defines the pressure exerted on the fluid is quite small initially and then expands to a larger diameter. Thus, the applied pressure decreases during the actuation. The time to displace the fluid is shown below as a function of applied force, fluid volume, and gap height.

$$\text{Equation 3.15} \quad t_{fill} = \frac{3\mu K^2}{8\pi F} \int_{H_o}^{H_f} \frac{dH}{H^3 \left( H^2 + \gamma K/F \right)}$$

If the base layer final is assumed to be 100 nm, the volume is defined as the base layer times the template area ( $\pi \text{ cm}^2$ ), the viscosity of the etch barrier is 1 cP, the surface tension of the fluid is 30 dyne/cm, then the time required to fill the gap for applied loads of 10 N, 100 N, and 1000 N is 10.51 seconds, 5.47 seconds,

and 1.04 seconds; respectively. If the desired base layer is 150 nm, then 100 N (22 lb<sub>f</sub>) will displace the material in 2.9 seconds.

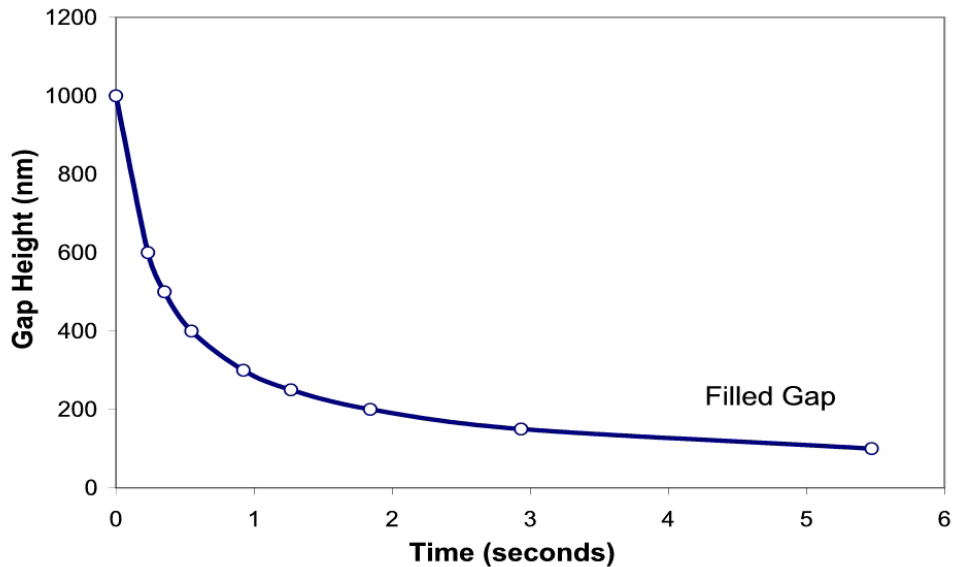


Figure 3.7. Time required to achieve a certain base layer with a fixed volume (31.4 nl) with a 100 N applied force.

### 3.3.1.6 Fixed Volume Case Comparisons

The time to reach a certain base layer was calculated to compare the three fixed volume cases. Figure 3.8 compares the gap height during the actuation of a 1 cm-radius template through a 1 cP fluid with a volume of 31.4 nl. For case 3, the velocity was fixed at 0.9  $\mu\text{m/s}$ ; for case 4, the pressure was fixed at 4.7 MPa; and for case 5, the force was fixed at 1050 N. All cases have a fill time of 1 second. The template approaches the substrate quite quickly in the first 0.1 seconds for both constant pressure (case 4) and constant force (case 5) and then becomes exceedingly slow.

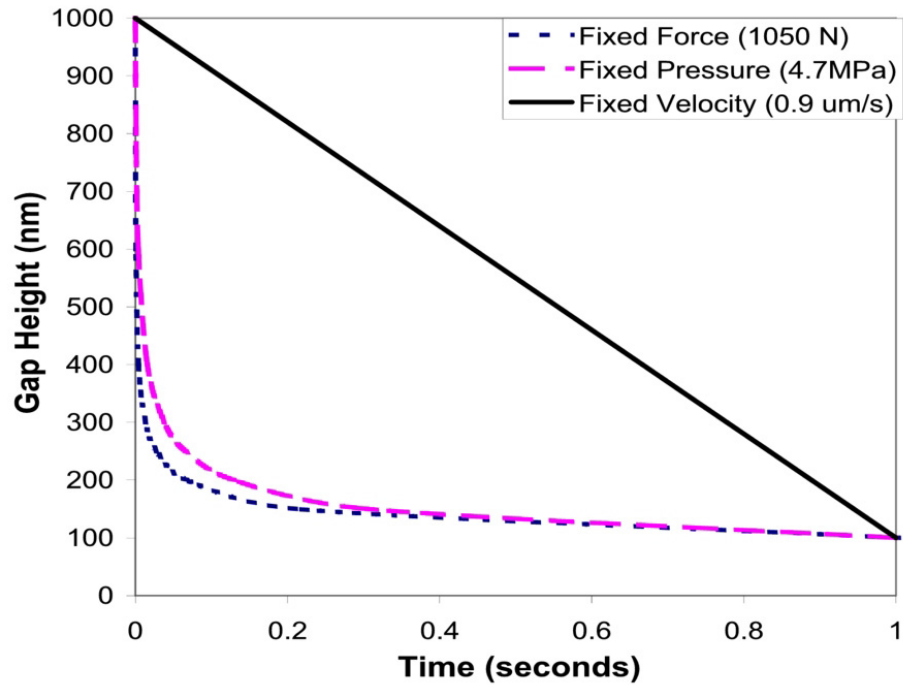


Figure 3.8. The gap height ( $2H$ ) in time compared for cases 3-5.

To understand the gap-time relationship it is also useful to understand how the pressure during the course of template actuation. Figure 3.9 shows the pressure as a function of template position for the three cases in Figure 3.8. The above plot shows that the constant pressure and constant force methods approach rapidly then slow. This is a result of the viscous resistance encountered at high approach velocities in thin gaps. The constant velocity exerts little pressure on the substrate until the gap ( $2H$ ) approaches 200 nm at which point the predicted pressure climbs rapidly.

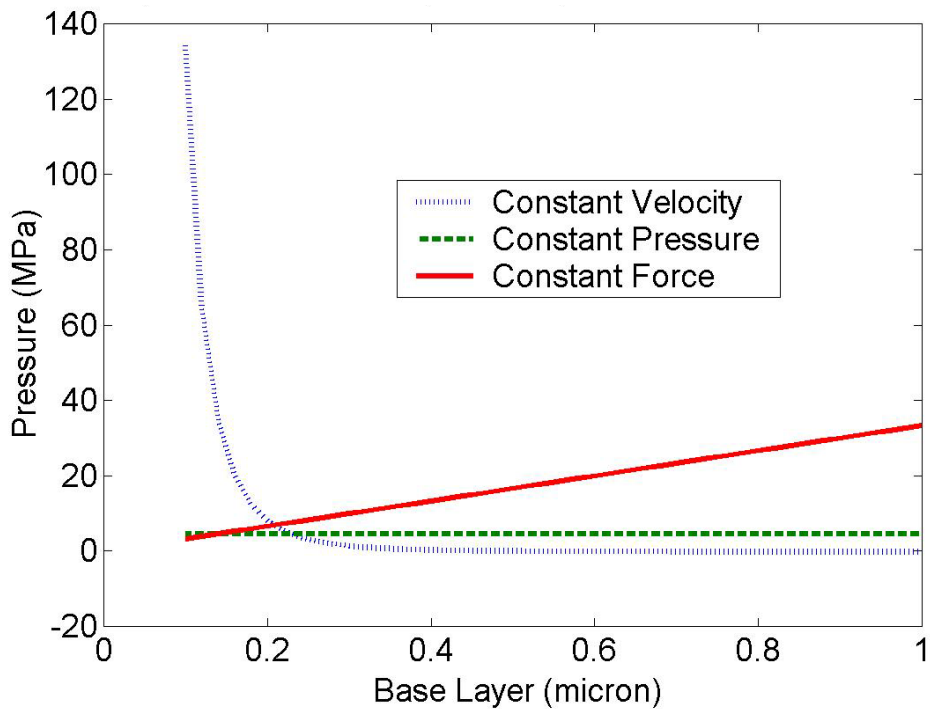


Figure 3.9. Pressure as a function of gap height for cases 3-5.

### 3.3.1.7 *Single Droplet Compression Summary*

For the five compression cases, the viscosity is proportional to the imprint time and therefore the viscosity of the etch barrier fluid must be minimized to maximize the throughput. The original etch barrier formulation was a 50-50 blend of a 100 cP oligimer and 1 cP monomers. Currently, the low viscosity etch barrier is comprised of monomers with viscosities of ~1 cP. From Equation 3.13, the pressure required to displace a wetting fluid to a desired thickness in a fixed time is less than that of a non-wetting fluid. The sensitivity of the applied pressure to the gap height is strong in all cases and thus provides a mechanism for passive base layer control in which the base layer is nearly constant once the

threshold condition is met. Also, since the pressure is so sensitive to the gap height, any difference in base layer thickness across a template surface will result in a substantial difference in local pressure and will provide a mechanism for correcting template-substrate orientation errors in the passive orientation stage. The fixed velocity methods generate large applied pressures during the last part of the imprint when displacement is difficult due to viscous force becoming dominant while the fixed force method applies the largest pressure initially when viscous forces do not hinder fluid displacement significantly. Therefore, case 5 compression reaches thinner films more quickly but the change in film thickness slows dramatically as viscous forces increase at a base layer of ~100 nm.

Of the five methods of imprinting, the fixed force approach appears to be the most appropriate since the current SFIL system can monitor applied force and control template actuation speed. For a  $\pi$  cm<sup>2</sup> template, a 100 N force will displace the etch barrier to a base layer of 150 nm in just under 3 second. For this template the “apparent” pressure,  $P_{apparent} = \frac{F_{fixed}}{A_{Template}}$ , during the imprint is 0.3 MPa which is roughly 100 times less pressure than thermal imprint lithography typically uses.

### 3.4 MULTI-DROPLET COMPRESSION

As shown in Cases 1-5, the imprint pressure is sensitive to the contact radius and gap height. Unfortunately, the base layer (or gap height) required by subsequent reactive ion etch steps is ~100 nm or less. Utilizing any of the five approaches requires relatively high pressures in order to compress a single droplet in a manufacturable time period. However, one might consider the compression

of multiple smaller droplets. If the volume of the single droplet is divided in two, the total contact area of the two droplets equals the contact area of the single droplet but the radius associated with each of the two smaller droplets is smaller than the single droplet by 30% ( $1-1/\sqrt{2}$ ). Thus, if everything else is held constant, the imprint pressure is also reduced according to Equation 3.9.

This analogy has been extended to 15 droplets with a total volume equal to the original single droplet dispense case. Figure 3.10 shows the fixed pressure required to compress a single droplet in a multi-droplet dispense approach starting from 10  $\mu\text{m}$ . The viscosity of the fluid is 1 cP and the volume of displaced material defined by  $\pi R^2(2H_f)$  where  $2H_f$  is 100 nm. The pressure and the individual droplet contact areas decrease as the number of droplets increases.

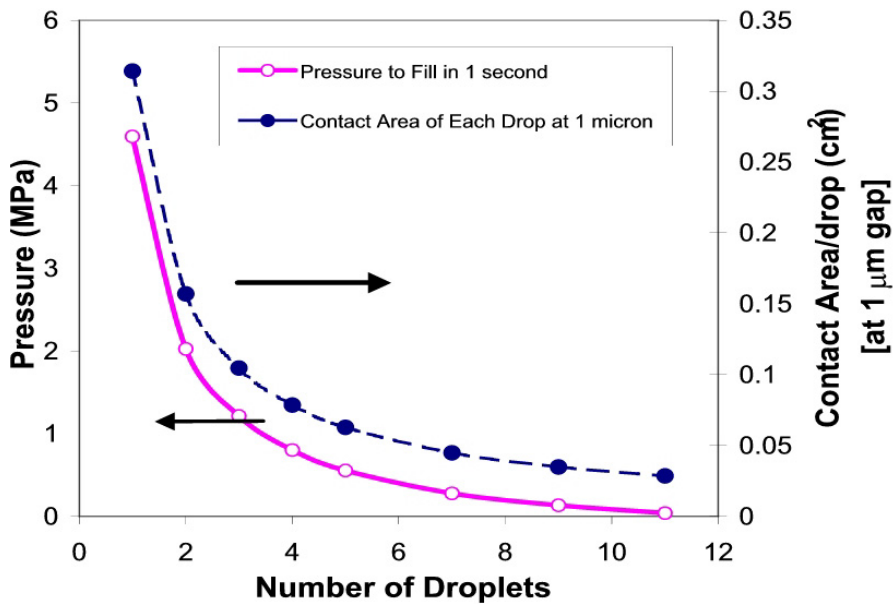


Figure 3.10. Imprint pressure required to achieve a 100 nm gap height in 1 second for a single drop in a multi-drop compression. The viscosity is 1 cP.

The relationships between the imprint force, the applied pressure, and the contact area for a single droplet, two-droplet, and  $n$ -droplet approach are shown below:

**Equation 3.16**  $F_1 = P_1 A_1$

**Equation 3.17**  $F_2 = 2P_2 A_2 = P_2 A_1$

**Equation 3.18**  $F_n = nP_n A_n = P_n A_1$

where  $A_1$  is the contact area of a single droplet,  $A_2$  is the contact area of each of the two droplets,  $A_n$  is the contact area of each of  $n$ -droplets,  $P_1$  is the pressure required to imprint a single droplet,  $P_2$  is the pressure required to imprint each of the two droplets,  $P_n$  is the pressure required to imprint each of the  $n$ -droplets,  $F_1$  is the force required to imprint a single droplet,  $F_2$  is the force required to imprint the two droplets,  $F_n$  is the force required to imprint the  $n$ -droplets.

Since the sum of the contact areas for the  $n$  equal-sized droplets,  $nA_n$ , equals the contact area of the single droplet,  $A_1$ , and the imprint pressure,  $P_n$ , is drastically reduced as the number of droplets increase (see Figure 3.10), the total force (and pressure) required to imprint in a fixed time is dramatically reduced. For example, for an 11-droplet approach with an initial height of 10  $\mu\text{m}$ , the pressure required to achieve a 100 nm base layer in 1 second over an area equal to a single droplet of the same total volume reduces from 4.7 MPa (single drop case) to 40 kPa or a 99% reduction!

The constant applied force approach (case 5) can also be applied to the multi-droplet scheme. For a fixed volume,  $K_1$  (which is equal to the volume of the single droplet case), the total force applied to  $n$ -droplets is  $nF_n$  where  $F_n$  is the

force required to displace an individual droplet with volume of  $K_I/n$  to a gap height of 100 nm in 1 second. The total force required to compress a 1cP fluid with a total volume,  $K_I$ , to a thickness of 100 nm in 1 second is shown in Figure 3.11.

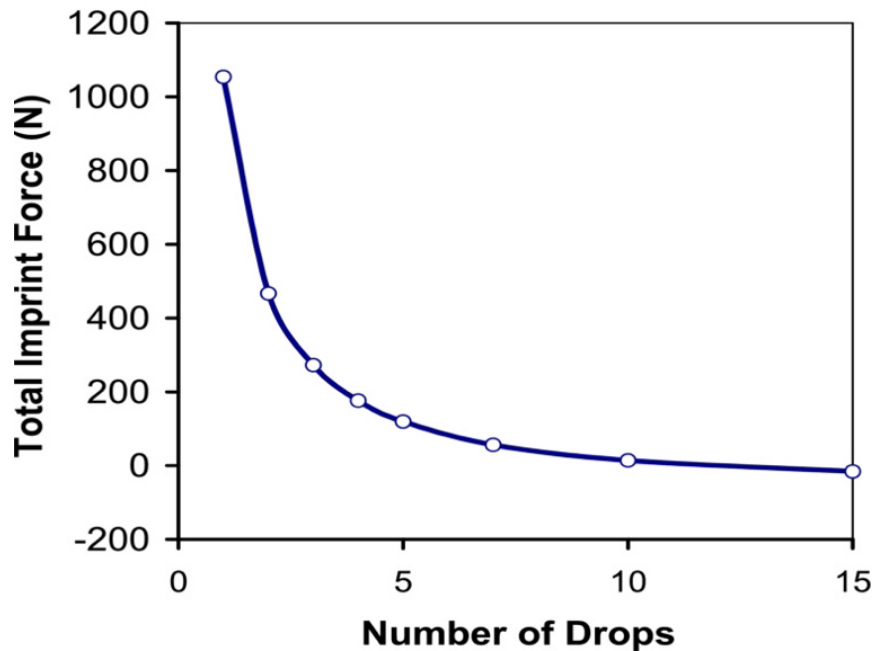


Figure 3.11. Force required to compress a fixed volume of 31.4 nl to a gap height of 100 nm in 1 second as a function of the number of droplets ( $n$ ).

Based on the two schemes presented above, the multi-droplet approach is vastly more effective than the single droplet methodology since the imprint pressure and imprint force are proportional to the inverse number of droplets ( $1/n$ ) and have a lower limit less than 0 N due to the effect of capillary pressure. However, it should be noted that the benefits of the multi-droplet approach are eliminated as soon as the droplets coalesce. Therefore, the fluid dispensing pattern is critical to the etch barrier fill rate.

### 3.5 EXPERIMENTAL OBSERVATION

During the course of fluid delivery experimental evaluation, it was discovered that several patterns of fluid placement are preferable to a single droplet located at the center of the template [5]. The fluid delivery pattern affects both the imprint uniformity and processing time. A volume of etch barrier between 0.1  $\mu\text{l}$  and 1.0  $\mu\text{l}$  is typically dropped onto a wafer prior to the template being brought into proximity of the substrate. Non-symmetric pressure applied to the template generated by asymmetric fluid deposition (i.e.: single drop placed off center) generates rotation in the template about the tilt axis causing an edge of the template to prematurely touch the template making capillary action the predominant means to fill the gap near that edge.

Due to the symmetry of the system and the fluid dynamics described above that govern the behavior of fluid displacement in capillaries, it is desirable to dispense the fluid in a pattern that causes zero effective moment about the tilt axes of the fine orientation template stage. By using symmetric patterns, such as H, V, X, W, N, Z, M, or  $\perp$ , it has been determined experimentally that the fluid fills the gap more evenly and quickly by minimizing any rotation of the template about the tilt axes of the fine orientation flexure. Alternatively, an array of precisely positioned droplets can be dispensed.

An example of a 138 nm uniform base layer printed by the SFIL stepper is shown in Figure 3.12. More recently, a set of closely controlled and positioned droplets have been used to dispense the etch barrier and resulted in a very uniform base layer over the entire 1" square patterned region. Care was taken to place

more fluid in the central droplet so as to minimize the potential of coalescence of three mutually adjacent droplets that results in bubble formation.

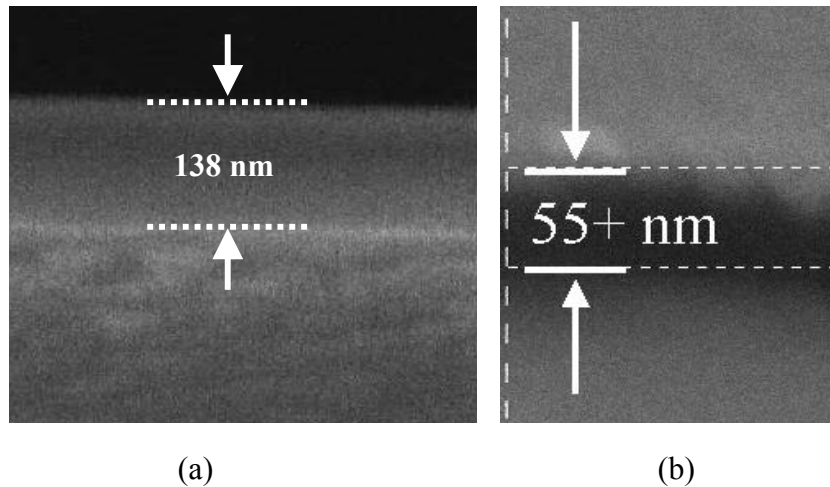


Figure 3.12. a) 138 nm base layer thickness remains and is uniform over nearly the entire 1" x 1" template. The total imprint and exposure time was ~30 seconds. Further improvement may come from improved filtration techniques. b) 55 nm base layer measured by tilt-SEM. The imprint time was approximately 1 second. The pressure is not monitored on the Agilent imprint equipment.

### 3.6 CONCLUSIONS

Three methods of fluid delivery have been evaluated theoretically and experimentally. Capillary action has been proven to be insufficient from a manufacturing throughput standpoint and spin-coating the low viscosity etch barrier has the potential for thin film dewetting that manifests itself in bubble formation during imprinting on the SFIL stepper. Spincoating is applicable to roller-press imprint equipment that eliminates bubble defects. The imprint pressure has been evaluated for five cases of single-drop compression. Of the five cases, the compression of a fixed volume of a wetting fluid benefits from capillary

force that augments the applied pressure as well as a contact area that is initially quite small. This method also minimizes excess fluid expelled from underneath the template. The fixed force and fixed velocity cases are the most applicable to the current SFIL stepper design since the stepper can control velocity and monitor applied force.

The single drop compression requires relatively large pressures in order to achieve a 100 nm base layer in 1 second. However, the multi-droplet approach appears to have a significant advantage over the other methods. For a template with an area of  $\pi \text{ cm}^2$ , and a fluid with a viscosity of 1 cP, and a surface tension of 30 dynes/cm, a constant applied pressure of 40 kPa should achieve a 100 nm base layer in 1 second while a constant applied force of  $\sim 14 \text{ N}$  will also achieve the same base layer in 1 second. Thus, the throughput constraints of semiconductor manufacturing can be met by applying the multi-droplet approach to the SFIL etch barrier delivery.

References:

---

- 1 Paul, D.R., D.W. Fowler, "Surface Impregnation of Concrete Bridge Decks with Polymers", *J. Applied Polymer Sci.* 19, 281-301 (1975)
- 2 Isrealichvili. J.; Intermolecular & Surface Forces, 2<sup>nd</sup>. Academic Press, San Diego (1991)
- 3 Ruchhoeft, P.; M. Colburn, B. J. Choi, H. Nounu, S. Johnson, T. Bailey, S. Damle, M. Stewart, J. Ekerdt, S.V. Sreenivasan, J. C. Wolfe, C. G. Willson, *J. Vac. Sci. Technol. B.*, **17**(6), 2965-2969 (1999)
- 4 Deen, W. M. Analysis of Transport Phenomena, Oxford Press, NY (1998)
- 5 Colburn, M.; A. Grot, B. J. Choi, M. Amistoso, T. Bailey, S.V. Sreenivasan, J. G. Ekerdt, C. G. Willson, "Patterning non-flat substrates with a low pressure, room temperature imprint lithography process," *J. Vac. Sci. Technol. B.* [submitted 2001]

## 4 Surface Energy Characterization

By the nature of imprint lithography, two surfaces come into intimate contact and then must be separated. As such, ramifications of surface phenomena are inevitable. Both the fluid delivery and the separation process are affected by the surface properties of the SFIL materials. As shown in Chapter 3, the surface tension plays a critical role in three proposed modes of delivery: capillary fill, spin coating, and droplet compression.

Surface energies also play a critical role in how two materials separate. For the SFIL process to be manufacturable, the separation must occur adhesively at the interface between the template and the etch barrier. The detailed mechanism of separation depends not only on interfacial energies but also on mechanical properties [1]. The thermodynamic criteria for adhesive separation must be met first. The work of cohesion is defined as follows:

**Equation 4.1** 
$$W_{Coh} = 2\gamma_{1V}$$

where  $\gamma_{1V}$  is the surface energy of material 1 in air [2]. The work of adhesion is defined as follows:

**Equation 4.2** 
$$W_{Adh} = \gamma_{1V} + \gamma_{2V} - 2\gamma_{12}$$

where  $\gamma_{1V}$  is the surface energy of surface 1,  $\gamma_{2V}$  is the surface energy of surface 2, and  $\gamma_{12}$  is the interfacial energy of the 1-2 interface. These surfaces are defined in Figure 4.1.

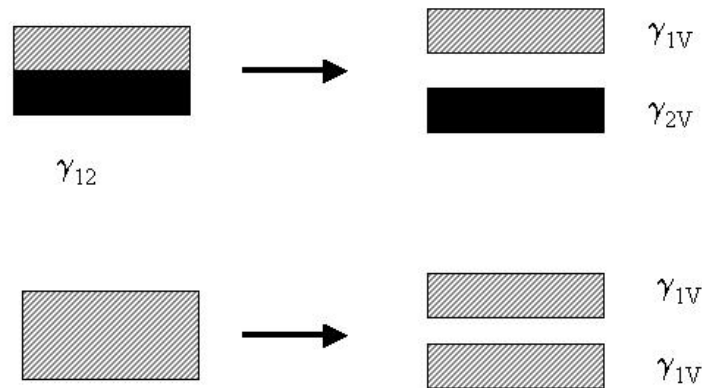


Figure 4.1. Cohesive failure (bottom) and adhesive failure (top)

For separation to occur at an interface rather than within a material the work of cohesion must be greater than the work of adhesion. For the SFIL system, there are 4 materials and 3 interfaces to consider. Therefore, the work of adhesion at the template-etch barrier interface must be less than the work of cohesion for the template, the transfer layer, and the substrate, and less than the work of adhesion for the other interfaces (etch barrier-transfer layer and transfer layer-substrate). Once these constraints are met, unique separation at the etch barrier-template interface is thermodynamically favorable. Two examples of separation are shown in Figure 4.2 where the etch barrier has delaminated from the substrate and where the etch barrier has remained adhesively attached to the transfer layer.

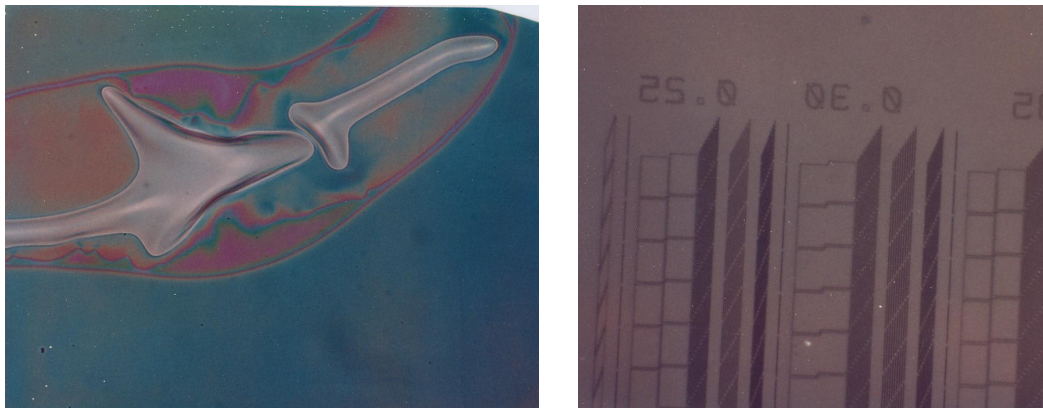


Figure 4.2. Depending on the surface properties, SFIL replication can lead to a) defects or b) faithful replication.

#### 4.1 SURFACE ENERGY MODELS

Several models for characterizing surface energy have been proposed in literature [3,4,5,6]; the application of which is dictated by the type of materials that are being modeled. There are four principle models, shown below, that permeate literature: i) the Fowkes' model [3], ii) the Owen and Wendt model, often referred to as the geometric mean model [4], iii) the Harmonic Mean Approximation [5], and iv) the Acid-Base theory [6]. The Fowkes model is the most simplistic and is only valid for non-hydrogen bonding materials such as *n*-alkanes [7]. Owens and Wendt proposed an extension of Fowkes model that incorporates materials that exhibit both dispersive (*d*) and polar (*p*) attraction such as aromatics. The harmonic mean approximation proposed by Wu *et al.* is another approximation for dispersive and polar components based on empirical analysis of data rather than a first principle's derivation of interactions [8]. The last model, proposed by van Oss, Good, and Chaudhury is a rigorous

thermodynamic model that includes dispersion ( $\gamma^{LW}$ ), Lewis acid ( $\gamma^{P+}$ ), and Lewis base ( $\gamma^{P-}$ ) components. It is by far the most inclusive and has been shown to be valid for a wide range of materials [6]. It should be noted that the acid-base interaction term ( $\gamma^{AB}$ ) is roughly equivalent to the polar term in Owens and Wendt ( $\gamma^p$ ) but is more sensitive to acid-base interactions.

**Equation 4.3**

Fowkes' 
$$\gamma_{12} = \gamma_{1V} + \gamma_{2V} - 2\sqrt{\gamma_{1V}\gamma_{2V}}$$

**Equation 4.4**

Geometric Mean 
$$\gamma_{12} = \gamma_{1V} + \gamma_{2V} - 2(\sqrt{\gamma_{1V}^P \gamma_{2V}^P} - \sqrt{\gamma_{1V}^d \gamma_{2V}^d})$$

**Equation 4.5**

Harmonic Mean 
$$\gamma_{12} = \gamma_{1V} + \gamma_{2V} - 4\left(\frac{\gamma_{1V}^P \gamma_{2V}^P}{\gamma_{1V}^P + \gamma_{2V}^P} - \frac{\gamma_{1V}^d \gamma_{2V}^d}{\gamma_{1V}^d + \gamma_{2V}^d}\right)$$

**Equation 4.6**

Acid – Base 
$$\gamma_{12} = \gamma_{12}^{LW} + \gamma_{12}^{AB}$$

$$\gamma_{12}^{LW} = (\sqrt{\gamma_{1V}^{LW}} - \sqrt{\gamma_{2V}^{LW}})^2,$$

$$\gamma_{12}^{AB} = (\sqrt{\gamma_{1V}^{P+} \gamma_{1V}^{P-}} + \sqrt{\gamma_{2V}^{P-} \gamma_{2V}^{P+}} - \sqrt{\gamma_{1V}^{P+} \gamma_{2V}^{P-}} - \sqrt{\gamma_{1V}^{P-} \gamma_{2V}^{P+}})^2$$

The surface energy of a solid can be calculated using one of the above models based on the contact angles that fluids of known surface energy make with the substrate. The contact angle of a fluid with a substrate is described by the Young-Dupre equation [7]:

**Equation 4.7**

$$\gamma_{LV} \cos \theta = \gamma_{SV} - \gamma_{SL} - \pi_{eq}$$

where  $\gamma_{LV}$  is the surface tension of the fluid,  $\gamma_{SV}$  is the surface energy of the solid vapor interface,  $\gamma_{LS}$  is the interfacial energy of the liquid-solid interface, and  $\pi_{eq}$  is the equilibrium spreading pressure. The equilibrium spreading pressure is approximately zero for normal polymeric surfaces [7].

Water, diiodomethane, and glycerol have known surface energy components that are listed in Table 4.1 and are the standard fluids used to calculate the surface energy of a solid. For the two-parameter models, only two contact angles are required to satisfy the two-equation, two-unknown system. Similarly, the acid-base method requires three contact angles to calculate the surface energy of a solid.

Table 4.1. Surface energy components of fluids.

Fluid	$\gamma^{LW}$	$\gamma^{p+}$	$\gamma^{p-}$	$\gamma^{total}$
Water	21.8	25.6	25.4	72.8
Diiodomethane	50.8	0.7	0	50.8
Glycerol	37.5	3.92	57.4	63.9

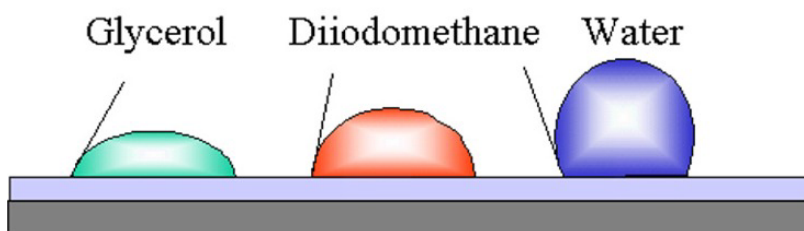


Figure 4.3. Contact angle of three liquids required for surface energy characterization using Acid-base theory.

#### 4.2 RAME-HART M100 CONTACT ANGLE GONIOMETER

Contact angles were measured on a Rame-Hart m100 Contact Angle Goniometer, shown in Figure 4.4. The RH-100 consists of a goniometer, a manually operated micropipette that is held in position above the gimbaled sample stage, an optics rail to align the diffuse-light illumination system with the CCD camera that is used to capture the image of a droplet. The captured images are analyzed by the Rame Hart software.

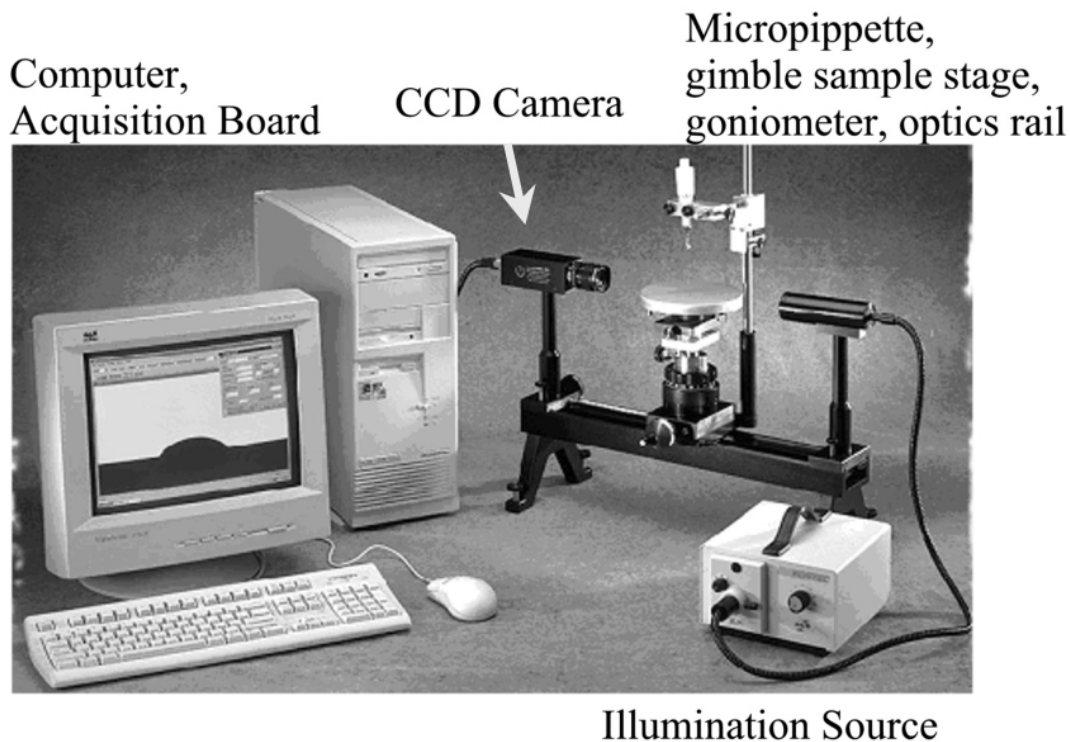


Figure 4.4. Rame-Hart m100 Goniometer with computer capture system.

The goniometer is equipped with an environmental chamber, shown in Figure 4.5, that minimizes the effect of external factors on surface

characterization. The chamber is 2" wide x 4" deep x 3" tall. Two optically flat windows allow for sample imaging. The chamber bottom has a heater-water chiller attachment that enables the chamber temperature to be controlled manually via a combination of cooling water and heat supplied by a resistive element connected to a voltage regulator. Four access ports accommodate gas purge but could be retrofitted for evacuation. All ports are sealed with Viton<sup>®</sup> O-rings. The top plate has  $\frac{3}{4}$ " diameter tapped hole that accommodates a micropipette fixture.

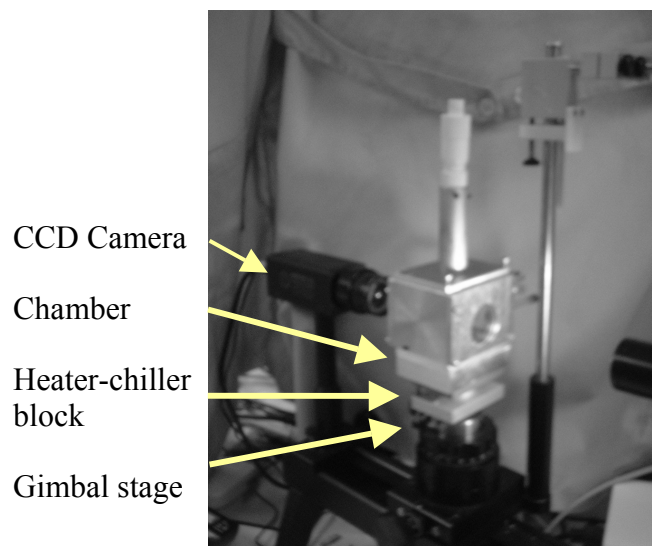


Figure 4.5. Environmental chamber for the Rame-Hart goniometer rests on the gimbal stage. The sample is illuminated and imaged through the two view ports. The heater-chiller block is attached to the bottom of the chamber.

#### 4.2.1 Rame Hart Contact Angle Procedure

An initial calibration procedure was performed with the image acquisition software according to the manufacturer's recommendation [9]. The light was

adjusted such that the range of intensity observed by the CCD was maximized. Once the lighting was adjusted, a magnetic substrate with a ball bearing of known diameter was placed in the environmental chamber that rests on the gimbal stage. A ball bearing of known diameter (in centimeters) was placed on a magnetic strip and its diameter in pixels determined by the image analysis software. This calibrated the length scale for the image analysis software. The length calibration is not required for contact angle measurements but it did provide assurance that the image analysis software is operating correctly.

Prior to performing a measurement, both the needle and glassware were cleaned using a triple rinse of Acetone-IPA-Water followed by a piranha etch for the glassware. The two parts were placed in an oven at 120 °C over night and allowed to dry to remove any organic contaminants. A dry, glass barrel and stainless steel needle were removed from the oven and allowed to cool to room temperature. Then the micropipette was assembled and the test fluid drawn into the micropipette. The three fluids were dispensed from separate pipettes sequentially. Each pipette was placed in the syringe holder and its tip lowered into the proximity of the substrate such that the tip could be seen with the CCD camera. One drop was allowed to fall gently on the surface and spread. Once motion had stopped the static drop contact angle was measured by the image analysis software. Typically, 12 measurements were taken at an interval of 5 seconds. Each measurement was performed on a 5-image averaged signal. All evaluations were performed within the environmental chamber in air saturated with the vapor of the test fluid at 72-74 °C. The measurement was repeated on

three separate drops. The procedure was repeated for diiodomethane and glycerol. Care was taken not to make measurements at identical locations in order to avoid contamination of the surface.

### 4.3 LIQUID SURFACE TENSION BY PENDANT DROP

The sections above have dealt primarily with surface energy characterization for solids. However, many of the important surfaces in SFIL are liquids. The surface tension of a fluid can be determined by analysis of the shape of a suspended drop [10]. Two opposing forces are experienced by a hanging drop: gravity and surface tension. Surface tension tries to minimize the surface area making the drop more spherical; a sphere having smallest surface area for a given volume. Gravity distorts this shape by pulling the drop downward. The shape of a static drop under the influence of gravity has a definitive relationship to its surface tension that can be described by the Young-Laplace equation:

**Equation 4.8** 
$$\gamma(\nabla \cdot n) = \Delta P = P - P_{atm} - \rho g y$$

where  $\gamma$  is the surface tension,  $g$  is gravity,  $\rho$  is the density of the fluid,  $P$  is pressure,  $y$  is position along the vertical position of the drop, and  $n$  is the unit normal to the drop surface.

The 2D case for a hanging drop has been solved [11] but the 3D case requires a numerical solution to the Young-Laplace equation. The conventional method of performing the pendant drop analysis requires the measurement of the drop diameter at its widest point,  $D_e$ , and the diameter,  $D_s$ , of the drop at a position  $D_e$  from apex of the drop [10]. Bashforth and Adams developed a table

that correlated the radius of curvature,  $H$ , to the ratio,  $S$  ( $D_e/D_s$ ) [12], which allows the surface tension to be calculated from the relationship below.

**Equation 4.9**  $\gamma_{lv} = \Delta\rho g D_e^2/H$

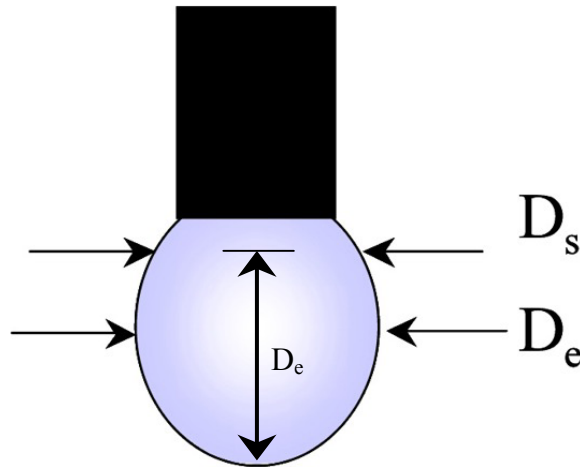


Figure 4.6. Characteristic dimensions,  $D_s$  and  $D_e$ , are shown on a pendant drop.

The measurement of surface tension by pendant drop requires careful attention to measurement conditions. The diameter measurement is accurate to 1/100" based on the characterization of a standard. The surface tension of a liquid is a function of the temperature [13] as well as humidity. Evaporation of the droplet adversely affects the drop stability. To minimize these effects, the environmental chamber was fabricated. As described for the contact angle procedure, a Kimwipe<sup>®</sup> was wetted with sufficient test fluid to saturate the air in the chamber with the monomer vapor to minimize the effect of evaporation. The chamber's main benefit is to provide a controlled environment that eliminates drafts that affect evaporation and produce temperature fluctuations.

### 4.3.1 Pendant Drop Procedure

There are benefits to performing pendant drop measurements over other compared to measurement methods. The volume of liquid required to perform the characterization is small, less than 1 ml, and changes in the surface of the syringe tip do not adversely affect the measurement. A standard protocol for the pendant drop measurements was established. Prior to performing a measurement, both the needle and glassware were cleaned using a triple rinse of Acetone-IPA-Water followed by a piranha etch for the glassware. The two were placed in an oven at 120 °C over night and allowed to dry to remove any organic contaminants. A dry, glass barrel and stainless steel needle were removed from the oven and allowed to cool to room temperature. Then the micropipette was assembled and the test fluid drawn into the micropipette. The goniometer was calibrated according to the manufacturer's direction [9]. The calibration was then verified by measuring the diameter of a standard. The stainless steel needle was placed on the pipette, installed in the pipette stand, and positioned such that the needle tip is directly above the calibration standard. The standard was removed from the chamber and a Kimwipe<sup>®</sup> was wetted with sample fluid was placed in the environmental chamber. The micrometer on the pipette was adjusted by 3 graduations (for the 2 ml barrel) to form a 60-120  $\mu$ l droplet hanging from the tip. Each sample was measured 12 times at 5 second intervals. Each measurement was performed on a 5-image averaged signal and the data stored under both a log file and a pd file for future retrieval.

#### 4.4 SURFACE ENERGY CHARACTERIZATION OF SFIL COMPONENTS

The surface tension of several silylated monomers and DMS derivatives was measured by the pendant drop method and the results are presented in Table 4.2. The surface energies of several organic polymer films taken from the literature are listed in Table 4.3 [5]. These are homopolymer films of prospective organic monomers that are candidates for etch barrier formulation. The surface tension of the silylated monomers ranges from 19 to 31 dynes/cm. The alkyl acrylate and alkyl methacrylate films range from 30 dyne/cm to 43 dyne/cm. For reference purposes, the surface energies of two fluorocarbon films are included.

Table 4.2. Surface tension of prospective etch barrier components measured by pendant drop.

Monomer	Surface tension by Pendant Drop ( $\gamma$ )	$\sigma_\gamma$
(3-acryloxypropyltris-trimethylsiloxane)silane ( <i>SIA0210</i> )	21.3	0.1
Tris(trimethylsiloxypropyl) methacrylate ( <i>SIM 6487.6</i> )	21.6	0.5
2-(trimethylsiloxyethyl)-methacrylate ( <i>SIM 6481.0</i> )	23.3	0.4
Trimethylsiloxyvinyl dimethylcarbinol ( <i>SIT 8573.0</i> )	18.9	0.9
1,3-bis(3-methacryloxypropyl) tetramethyldisiloxane ( <i>SIB 1402</i> )	27.7	1.0
1,3-bis(glycidoxypropyl)-tertramethylsiloxane ( <i>SIB 1115</i> )	28.6	1.9
Octa(dimethylsiloxypropylglycidyl ether) silsesquioxane	31.51	1.5

Table 4.3. Surface tension of several organic polymer films (from S. Wu[5])

Polymer	Surface Tension (dyne/.cm)
Poly(methyl methacrylate)	41.1
Poly(butyl methacrylate)	31.2 - 32.2
Poly(t-butyl methacrylate)	39.5
Poly(lauryl methacrylate)	32.8
Poly(methyl acrylate)	41-42.7
Poly(ethyl acrylate)	37-33.7
Poly(butyl acrylate)	30.7-33.7
Poly(heptafluoropropoxyethyl acrylate)	16
Poly(styrene)	39.5
Poly(ethylene)	35.3-36.8
Poly(hexafluoropropylene)	12.8-17
Poly(tetrafluoroethylene)	21.5 – 23.9

#### 4.4.1 Work of Adhesion

Three etch barrier formulations with the compositions listed in Table 4.5 were characterized by contact angle measurement and their surface energies calculated from Acid-Base theory (Table 4.4). The surface energies of several transfer layers, the untreated template, and the treated template are also listed. The three transfer layers have similar surface energies as do the three etch barrier films. The liquid phase surface treatment decreases the surface energy of the template by 27.4 dynes/cm to a value of 22.3 dyne/cm [5].

Table 4.4. Surface energies of several transfer layer, etch barrier formulations, and untreated template and a treated template measured by Acid-Base method.

Film	$\gamma^{p+}$	$\gamma^{p-}$	$\gamma^p$	$\gamma^d$	$\gamma^{total}$
HR100	0.29	3.47	2.01	39.7	41.7
Poly(vinyl cinnamate)	0.23	13.3	3.50	39.6	43.2
Poly(styrene)	0.74	4.31	3.57	42.3	45.9
Etch Barrier – A	0.17	6.96	2.18	27.8	30.0
Etch Barrier – D	0.03	6.50	0.848	27.9	28.7
Etch Barrier – E	0.06	5.77	1.20	29.9	31.1
Treated Template	1.00	44.2	13.3	9.09	22.3
Untreated Template	3.21	34.4	21.0	28.7	49.7

Table 4.5. Etch barrier compositions (by mass (g))

Monomer	Solution A (Preliminary Etch Barrier)	Solution D (Preliminary EB w/ adjusted initiator)	Solution E (Agilent Etch Barrier I)
SIA 0210	0.659	0.388	-
Butyl Acrylate	0.658	0.391	0.744
UMS-182	1.300	0.766	0.814
SIB 1402	-	-	0.087
Irgacure 184	0.094	0.037	0.052
Irgacure 819	0.045	0.041	0.047

The work of adhesion between the SFIL interfaces was calculated for all three etch barrier solutions (Table 4.6) [14]. The three transfer layers have similar predicted adhesion performance with a work of adhesion of 70-75 dynes/cm. The three etch barrier solutions have nearly identical properties. The etch barrier to untreated template interface has a work of adhesion of 70 dynes/cm leading to no preferential separation while the lowest work of adhesion is at the etch barrier to treated template interface. These predictions indicate a preferential release at the etch barrier to treated template interface and this is observed experimentally. It should be noted that the surface energy of these films was taken on a surface that was in contact with a treated quartz template. As such, the extrapolation of the work of adhesion to the transfer layer may include some error that would lower etch barrier-transfer layer interfacial energy. This only further increases the work of adhesion at this interface and improves the chance of selective release between the etch barrier and the template.

Table 4.6. Work of Adhesion between SFIL Interfaces.

Work of Adhesion (dyne/cm)	Solution A	Solution D	Solution E
HR100	71	70	72
Poly(vinyl cinnamate)	72	71	73
Poly(styrene)	75	75	76
Treated Template	42	40	41
Untreated template	71	69	70

#### 4.4.2 Etch Barrier Analysis

One of the benefits of analyzing the surface energy with the Acid-Base model is that it provides a fundamental understanding of what parameters in the materials may be tailored to further improve the release characteristics. For the trilayer stack shown in Figure 4.7, the ratio of the works of adhesion, defined in Equation 4.10, is a metric of the likelihood of separation at a particular interface.

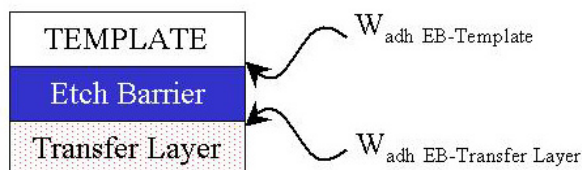


Figure 4.7. Trilayer stack indicating the interfaces of interest.

**Equation 4.10**

$$Ratio = \frac{W_{adh-EB-TL}}{W_{adh-EB-Template}}$$

An analysis of the current SFIL formulations was performed in which the transfer layer and the template have the fixed surface energy components shown in Table 4.7, the  $\gamma^d$  of the etch barrier was fixed at 27.8 dyne/cm, and the  $\gamma^{p+}$  and  $\gamma^{p-}$  parts ranged from 0 to 20 dyne/cm. The plot in Figure 4.8 details the effect of the polar components on the ratio of the works of adhesion defined in Equation 4.10. The effect of  $\gamma^{p+}$  has the more dominant effect on the ratio than the  $\gamma^{p-}$  component for this system. This leads to the conclusion that for these representative interfaces, a decrease in the  $\gamma^{p+}$  component improves the release properties more than an equivalent change in  $\gamma^{p-}$ . Further, since the current SFIL

system has a ratio of 1.7 which is designated in Figure 4.8 by the star, only a reduction in the  $\gamma^{p^-}$  from 6 dyne/cm to 0 dyne/cm would increase the ratio to the maximum of 2.08.

Table 4.7. Surface energy properties of the etch barrier, transfer layer, and template unless otherwise stated for the simulation.

Property (dyne/cm)	Etch Barrier	Transfer Layer	Template
$\gamma^{p^+}$	0.17	0.23	1
$\gamma^{p^-}$	6.97	13.3	44.2
$\gamma^d$	27.8	39.6	9.09

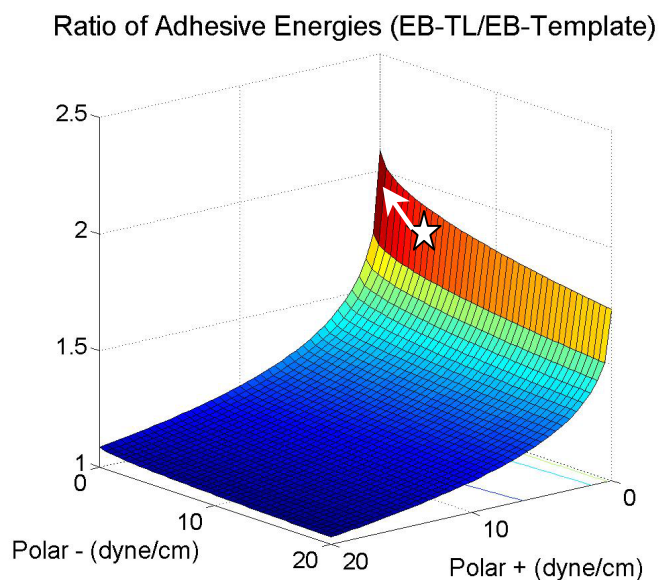


Figure 4.8. The ratio of the etch barrier-transfer layer work of adhesion to the etch barrier-template work of adhesion when the etch barrier's  $\gamma^{p^+}$  and  $\gamma^{p^-}$  range from 0 to 20 dyne/cm. The treated template has a  $\gamma^{p^+}$  and  $\gamma^{p^-}$  of  $\sim 0.2$  and  $\sim 6$  dyne/cm which is highlighted on the plot by the star.

### 4.4.3 Template Analysis

The same analysis was applied to the template surface properties. The transfer layer and etch barrier had the fixed surface properties designated in Table 4.7, the  $\gamma^d$  of the surface treatment was fixed at 9.09 dyne/cm, and the  $\gamma^{p+}$  and  $\gamma^{p-}$  of the template changed from 0 to 20 dyne/cm. The  $\gamma^{p+}$  component plays a dominant role in the ratio of works of adhesion. The current FSAM treatment produced a quartz surface with  $\gamma^{p+}$  of 1 dyne/cm and  $\gamma^{p-}$  of 44 dyne/cm; thus the system may be further improved by reducing the  $\gamma^{p-}$ . Based on these simulated surface properties, the improvement would be 34% in the ratio (2.28 from 1.70).

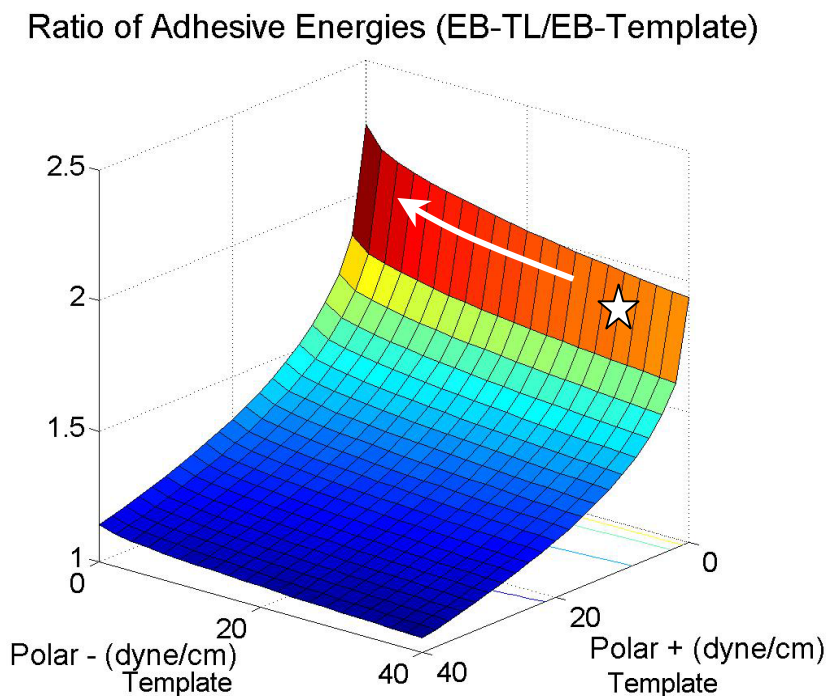


Figure 4.9. The ratio of the etch barrier-transfer layer work of adhesion to the etch barrier-template work of adhesion when the template's  $\gamma^{p+}$  and  $\gamma^{p-}$  range from 0 to 20 dyne/cm. The treated template has a  $\gamma^{p+}$  and  $\gamma^{p-}$  of 1 and 44.2 dyne/cm.

#### 4.4.4 Transfer Layer Analysis

The same analysis was applied to the transfer layer surface properties. The template and etch barrier had the fixed surface properties designated in Table 4.7, the  $\gamma^d$  of the transfer layer was fixed at 39.6 dyne/cm, and the  $\gamma^{p+}$  and  $\gamma^{p-}$  of the transfer layer changed from 0 to 20 dyne/cm. Again, the  $\gamma^{p+}$  component dominates the ratio of works of adhesion for this system of material interfaces. A representative transfer layer has a  $\gamma^{p+}$  of 0.23 dyne/cm and  $\gamma^{p-}$  of 13.3 dyne/cm; thus the system may be further improved by increasing both the  $\gamma^{p-}$  and  $\gamma^{p+}$ . Based on these simulated surface properties, the improvement would be 28% in the ratio (2.18 from 1.70). Since there is a lower bound on the dispersive component of the surface treatment, the transfer layer may be tailored more easily by incorporating both Lewis acids and Lewis bases into the transfer layer resin.

### Ratio of Adhesive Energies (EB-TL/EB-Template)

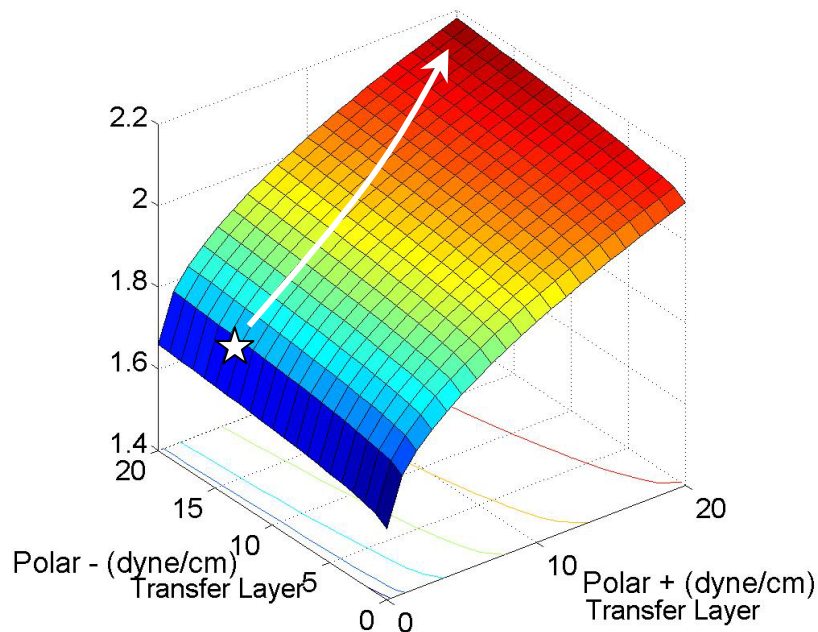


Figure 4.10. The ratio of the etch barrier-transfer layer work of adhesion to the etch barrier-template work of adhesion when the transfer layers'  $\gamma^{p+}$  and  $\gamma^{p-}$  range from 0 to 20 dyne/cm. The transfer layer has a  $\gamma^{p+}$  and  $\gamma^{p-}$  of 0.23 and 13.3 dyne/cm.

#### 4.5 CONCLUSION

The surface tension of several silylated etch barrier components has been characterized by pendant drop measurements and the surface energy of the etch barrier, transfer layer and FSAM surface treatment has been evaluated by contact angle measurements. The treatment of the template with the fluorinated self-assembly monolayer is a critical process for SFIL. Based on the work of adhesion and the cohesive energy of the four critical components, separation is predicted to occur uniquely at the etch barrier-template interface; this was observed

experimentally. For the surface properties of the SFIL components, the ratio of the work of adhesion of the etch barrier-transfer layer to the etch barrier-template is nearly maximized with respect to the etch barrier properties. Reduction of the  $\gamma^P$  of the etch barrier could improve the release properties further. However, both the transfer layer and the surface treatment offer more opportunity for improvement, especially the transfer layer since the surface energy of the treated template is close to the lowest feasible limit.

#### **4.6 FUTURE WORK**

The current design of the SFIL relies on the adhesive strength of the etch barrier to the transfer layer. While experimental evidence indicate that the current system is sufficient for reliable replication, promoting crosslinking or grafting across the interface would strengthen the interface. For example, a glycidyl methacrylate co-polymerized into an epoxide-based transfer layer resin would allow the acrylate based etch barrier to covalently bind to the transfer layer during the photopolymerization step of SFIL. The added energy required to cause separation at the transfer layer-etch barrier interface would then be increase proportionately to the crosslinker surface concentration at the interface since the energy required to break a C-C bond is 348 kJ/mole [15].

Alternatively, polarity switching monomers may also provide added functionality of the etch barrier. The Pinacol rearrangement, shown below,

transforms two adjacent alcohol groups into a nonpolar ketone. Thus the molecule transforms from polar to non-polar as a result of the reaction and may provide a mechanism for enhanced separation.

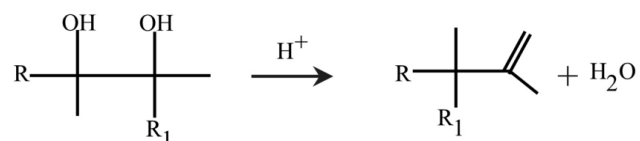


Figure 4.11. The Pinacol rearrangement [15].

Other additives such as fluorinated acrylate monomers could be introduced into the etch barrier formulation. Literature suggests that less than 1 mole percent of fluorinated monomer is required to reduce the surface tension of a material [16]. For the etch barrier, this would reduce the dispersive surface energy component that is currently ~28 dyne/cm to near that of poly(heptafluoroethylene). The breadth at which the etch barrier technology could be explored is extensive and only limited by creativity.

References:

---

- 1 Lee, L.H. ed; Fundamentals of Adhesion, Plenum, NY, 366 (1991)
- 2 Isrealachvili. J.; Intermolecular & Surface Forces, 2<sup>nd</sup>. Academic Press, San Diego (1991)
- 3 Fowkes, F.M.; *Ind. Eng. Chem.*, **55**, 28 (1964)
- 4 Owens, D.K.; R.C. Wendt, "Estimation of the Surface Free Energy of Polymers," *J. Appl. Poly. Sci.*, 13, 1741-1747 (1969)
- 5 Wu, S.; ed. "Surface and interfacial energies of polymers," *Polymer Handbook*, Wiley, 411-432 (1989)
- 6 van Oss, C. J.; R. J. Chaudury, M.K. Goode. "Additive and Nonadditive Surface Tension Components and the Interpretation of Contact Angles," *Langmuir*, 4, 884-891 (1988)
- 7 Mittle, K.L. ed. Adhesion and Wettability. 161-171
- 8 Wu. S.; *J. Adhesion*, **5**(39) (1973)
- 9 "Rame-Hart m100 Goniometer Standard Operating Procedure," Rame-Hart (1998)
- 10 Andreas, J.M.; Hauser, E.A.; Tucler, W.B., *J. Phys. Chem.*, **1938**, 42, 1001.
- 11 Pitts, E.; *J. of Fluid Mechanics*, **59**, 753-767 (1973)
- 12 Bashforth, F.; J.C. Adams, *An attempt to test the theories of capillary action*, Cambridge University Press (1883).
- 13 Wu, S; Polymer Interface and Adhesion, Marcel Dekker, NY, (1982)
- 14 Colburn, M.; S. Johnson, M. Stewart, S. Damle, B. J. Jin, T. Bailey, M. Wedlake, T. Michaelson, S.V. Sreenivasan, J. Ekerdt, C.G. Willson. "Step and Flash Imprint Lithography: An alternative approach to high resolution patterning." *Proc. SPIE*. 3676, 379-389 (1999)
- 15 Loudon, G.M.; *Organic Chemistry*, Redwood City, CA (1995)

- 
- 16 Ameduri, B.; R. Bongiovanni, G. Malucelli, A. Pollucino, A. Priola, "New Fluorinated Acrylic Monomers for surface modification of UV-curable Systems," *J. Poly. Sci. A*, 37, 77-87 (1999)

## 5 Characterization of the Elastic Modulus of Photopolymer Films by Nanoindentation

### 5.1 INTRODUCTION

The elastic modulus plays a critical role in the replication processes [1] such as SFIL. From experimental observation, the force required to separate the template from the substrate increases with glass transition temperature ( $T_g$ ) of the photopolymer adhering the two. There are many models [1] for adhesive behavior; one such model, the Barenblatt fracture model, that describes the tensile stress,  $\sigma$ , required to delaminate a film of thickness,  $t$ , is shown below:

**Equation 5.1** 
$$\sigma < \sqrt{\frac{1}{2} \frac{EW_{adh}}{t(1-\nu^2)}}$$

where  $E$  is elastic modulus,  $\nu$  is the Poisson's ratio, and  $W_{adh}$  is work of adhesion,. If the stress is defined as the tensile force at delamination,  $F_{delam}$ , divided by the area,  $A$ , over which the tensile force is applied, the equation can be rearranged to yield the tensile force required to delaminate a film.

**Equation 5.2** 
$$F_{delam} > A \sqrt{\frac{1}{2} \left( \frac{EW_{adh}}{t(1-\nu^2)} \right)}$$

As discussed in Chapter 4 on surface energy characterization, the work of adhesion between the etch barrier and the treated template has been cut in half making it the interface most susceptible to delamination. According to the Barenblatt model this will also reduce the force of separation by a factor of  $\sqrt{(1/2)}$  or ~30%. To further reduce the force required for separation, the elastic modulus

may be tailored. In fact, the modulus of the photopolymer can have a far greater effect since it can be tailored over several orders of magnitude. For example, a polymer above its  $T_g$  has a modulus on the order of 1 MPa where as a polymer below its  $T_g$  has a modulus of on the order of 1GPa. Therefore, the photopolymer's elastic modulus can be exploited to dramatically reduce the force of separation.

## 5.2 BACKGROUND

There are several methods of characterizing the elastic properties of a material. Traditionally, the elongation of a sample is measured as a function of the tensile force. The tensile modulus,  $E$ , is defined by the ratio of tensile stress,  $\sigma$ , to strain,  $\varepsilon$ :

**Equation 5.3** 
$$E = \frac{\sigma}{\varepsilon}$$

where  $\sigma$ , is the applied force divided by the cross sectional area of the sample.

However, the elastic properties of thin films often exhibit unusual behavior such as glass transition elevation or depression [2]. Since the etch barrier is present in a film, it is desirable to quantify it in this state. Nanoindentation is a relatively new technique developed to quantify the elastic properties of thin films using equipment such as atomic force microscopes (AFM), nanoindentors, and recently interfacial force microscopes (IFM) [3,4,5,6].

### 5.3 CONTACT MECHANIC MODELS FOR NANOINDENTATION

The contact mechanics of a tip impinging on a surface has been extensively studied [7,8,9]. H. J. Hertz proposed the original model in 1885. In the Hertzian model, the material is assumed to behave isotropically and have no attractive forces that distort the contact area between the tip and the substrate. The indenter is assumed to have a spherical tip of radius,  $R$ , that forms a contact area that is defined by  $\pi\delta R$  as the tip penetrates into the surface a small depth,  $\delta$ , with a force,  $F$ . This is shown schematically in Figure 5.1.

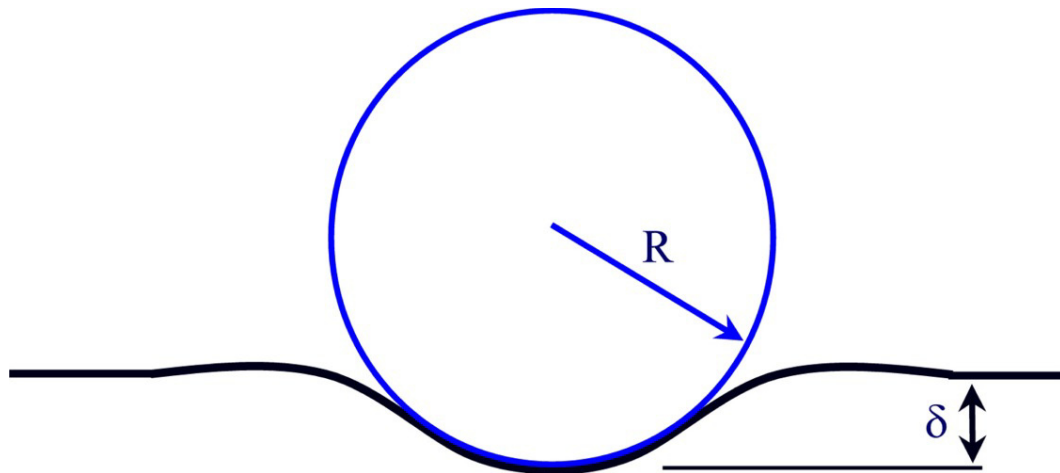


Figure 5.1. Hertzian model system: a spherical tip penetrating a flat surface.

Under these assumptions, the force,  $F$ , obeys the following equation [7]:

$$\text{Equation 5.4} \quad F = (K^2 R \delta^3)^{1/2}$$

where  $K = \frac{4}{3} \left( \frac{1-\nu_s^2}{E_s} + \frac{1-\nu_{tip}^2}{E_{tip}} \right)^{-1}$ ,  $\nu$  is the Poisson's ratio,  $E$  is the tensile

modulus. Since the modulus of the probe tip ( $E_{tip}$ ) is much greater than the modulus of the samples ( $E_s$ ), the second part of the quotient is approximately zero. Linear regression of the force against  $\delta^{3/2}$  data set yields a slope that is equal to  $\frac{4ER^{1/2}}{3(1-\nu^2)}$ . The elastic modulus can then be calculated using the tip's

radius of curvature and an approximated Poisson's ratio.

I. N. Sneddon performed a similar analysis of a tip penetrating a surface for several common tip geometries [8]. Two of which are the flat-ended cylindrical tip (flat-punch) and a conical tip shown schematically in Figure 5.2 and Figure 5.3. The flat-ended cylinder is defined by its radius,  $a$ , while the conical tip is defined by an approach angle,  $\alpha$ .

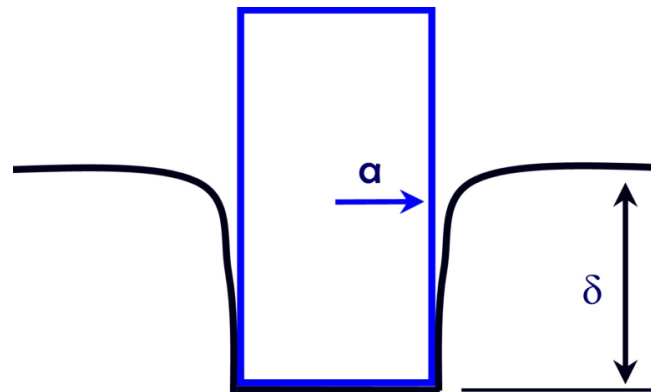


Figure 5.2. Sneddon's flat-end cylindrical tip (flat-punch) model: a cylindrical tip penetrating a flat surface.

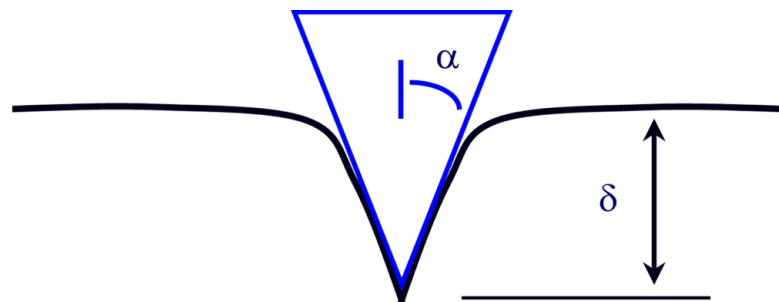


Figure 5.3. Sneddon's conical tip model: a conical tip penetrating a flat surface.

Sneddon developed analytical expressions for the force that a tip is required to exert to penetrate the surface to a depth,  $\delta$ . The results of his derivations are summarized in Equation 5.5 and Equation 5.6 [8]. Each geometry yields a different dependence on  $\delta^n$ . For the flat-punch model, the slope of the force- $\delta$  data equals  $\frac{4Ea}{(1-\nu)}$ . For the conical tip, the slope of the force- $\delta^2$  data equals  $\frac{4E \cot(\alpha)}{\pi(1-\nu)}$ .

$$\text{Equation 5.5} \quad F = \frac{4Ea\delta}{(1-\nu)} \quad \text{(Flat-punch)}$$

$$\text{Equation 5.6} \quad F = \frac{4E \cot(\alpha)}{\pi(1-\nu)} \delta^2 \quad \text{(Conical Tip)}$$

The elastic modulus of a film can be extracted from the force- $\delta^n$  curve by applying the appropriate model to the system. For the Hertzian model, the flat-punch model, and the conical tip model shown above, the slope of corresponding is analyzed by least-squares regression and set equal to  $\frac{4ER^{1/2}}{3(1-\nu^2)}$ ,  $\frac{4Ea}{(1-\nu)}$ ,  $\frac{4E \cot(\alpha)}{\pi(1-\nu)}$ , respectively [7,8]. With an approximated Poisson's ratio of 0.35 and information regarding the tip geometry, the elastic modulus can be calculated.

#### 5.4 ATOMIC FORCE MICROSCOPE IN FORCE-DISTANCE MODE

A Thermomicroscope CP Research AFM equipped with an Ultra lever B tip was run in contact mode using a 5  $\mu\text{m}$  scanner. The calibration procedure prescribed by Thermomicroscopes for the Force-Distance analysis was performed on each Ultralever B tip [10] and a small area scan was performed to ensure the location to be tested was flat and free of particles. The scanning force was set to 2 nN. The Ultralever tip has a radius of curvature of 10 nm, and an approach angle of 18°. Its cantilever has a spring constant of 0.4 N/m.

In this technique, the AFM cantilever is actuated toward the sample a distance,  $z$ , that is measured by piezo. When the tip comes in contact with the sample, the cantilever is deflected a distance,  $d$ , that is measured by a quadrapole sensor. The force imparted on the sample is directly proportional to this

deflection by the spring constant,  $k$ , of the cantilever. This force results in the indentation of the sample to a depth,  $\delta$ . The cantilever travel is equal to the deflection plus the indentation depth ( $z = d + \delta$ ).

An example of force-distance plots taken at several frequencies is shown in Figure 5.4. Before the tip comes in contact with the surface, no force is observed and results in a slope of zero. Just before the tip comes in contact with the surface, attractive forces deflect the AFM cantilever toward the sample resulting a negative force reading; this is often referred to as “snap-in”. As the tip is actuated further toward the sample, the cantilever relaxes and eventually deflects the other direction resulting in a positive force reading. The tip is actuated to a desired position and then is retracted from the sample and the process starts again.

The AFM reports the average of 10 force-distance cycles taken at a fixed frequency. The frequency of these cycles affects the quality of the measurement. Several experiments, shown in Figure 5.4, were run to determine the optimum operating frequency. The variance of the measurements improves dramatically as the indentation cycle is decreased below 1 Hz. The main source of error is related to the ability of the AFM to measure the force at scan rates greater than 1 Hz. Digitization of the force signal leads to significant errors in determination of indentation depth; thus, adversely affecting any analysis performed on the data.

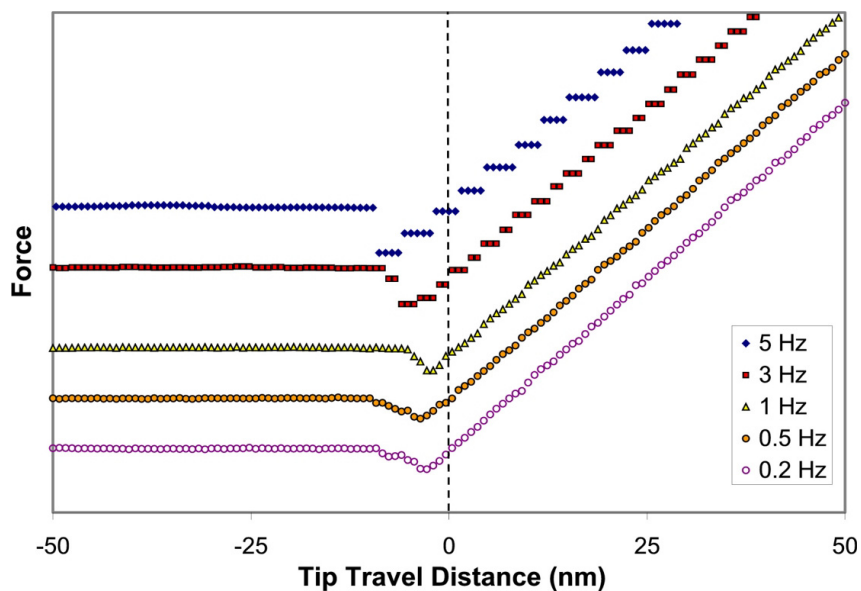


Figure 5.4. Sampling frequencies greater than 1 Hz results in digitation of the force data. Note: the dashed line represents the surface of the film and the forces are adjusted vertically for display. The horizontal portion of the force represents a cantilever experiencing no attraction or repulsion from the surface.

If the indentation depth is deep relative to the thickness of the film, the effect of the underlying substrate is observed. An example of this effect is shown in Figure 5.5 where a marked change in slope is observed at a penetration depth of approximately 200 nm. This occurs only if the substrate is more rigid than the film. Typically, the tip was extended less than 10% of the total film thickness and care taken to analyze data only up to the depth at which no effect of the substrate was evident. In most cases, this was between 100 nm and 200 nm for soft samples.

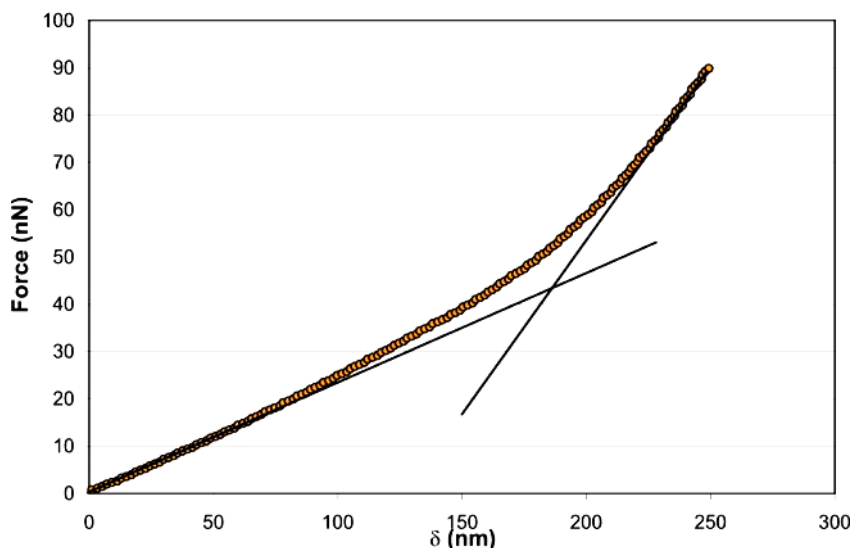


Figure 5.5. Force- $\delta$  showing the effect of the substrate observed at a depth of approximately 200 nm.

## 5.5 FILM PREPARATION

Monomer solutions formulated with 3% (w/w) of a 1:1 mixture of bis(2,4,6-trimethylbenzoyl)-phenylphosphine oxide (Irgacure 819, Ciba) and 1-benzoyl-1-hydroxycyclohexane (Irgacure 184, Ciba) and 1 % (w/w) 1,3-bis(methacryloxytetramethyl)disiloxane (SIB 1402, Gelest), for crosslinking, were cured with UV light under either a quartz template or a poly(ethylene) sheet onto a silicon substrate coated with a transfer layer to promote adhesion. The film thicknesses ranged from 1  $\mu\text{m}$  to 10  $\mu\text{m}$ . Polyethylene sheets were used for high modulus films that could not be separated from the quartz without causing damage.

## 5.6 RESULTS

In the example of a force-distance plot shown in Figure 5.5, the circles represent the force that the tip is exerting on a poly(n-butyl acrylate)-co-(3-acryloylpropyltrimethylsiloxane) silane) film as it extends into the surface of the substrate. This copolymer was a 50-50 mixture of the two monomers. The plot is an average of 10 scans taken at  $\frac{1}{2}$  Hz. Least-square regressions were applied to the force-vs- $\delta$  data for penetration depths of 30 nm to 150 nm using the Hertzian model (Figure 5.6), the conical model (Figure 5.7), and the flat punch model (Figure 5.8). All three regressions have  $R^2$  values better than 0.98.

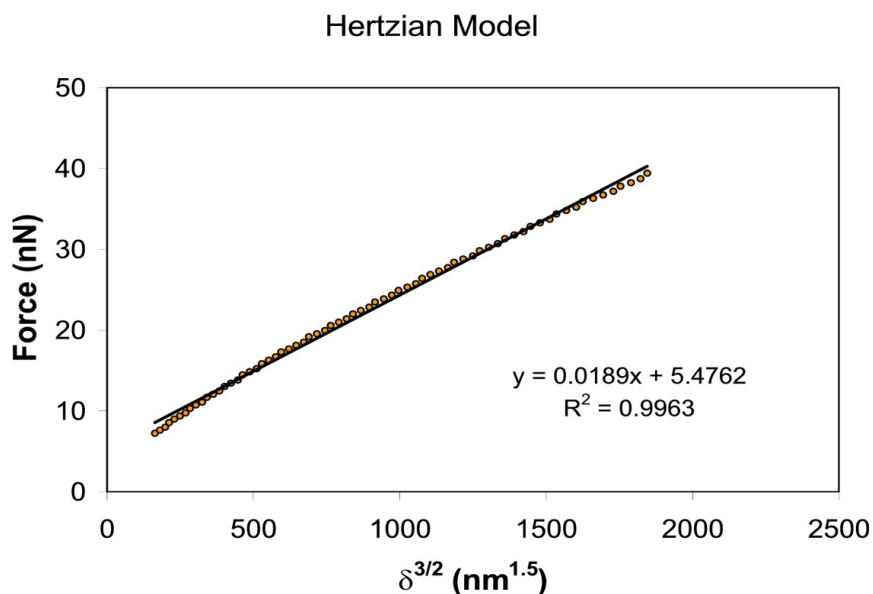


Figure 5.6. Regression of force- $\delta^{3/2}$  for the Hertzian model

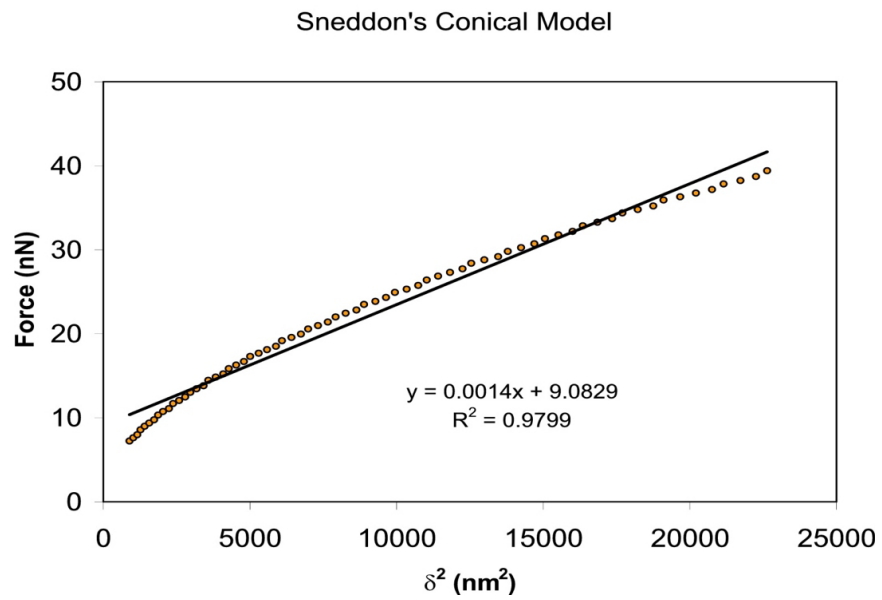


Figure 5.7. Regression of force- $\delta^2$  for the Sneddon conical model.

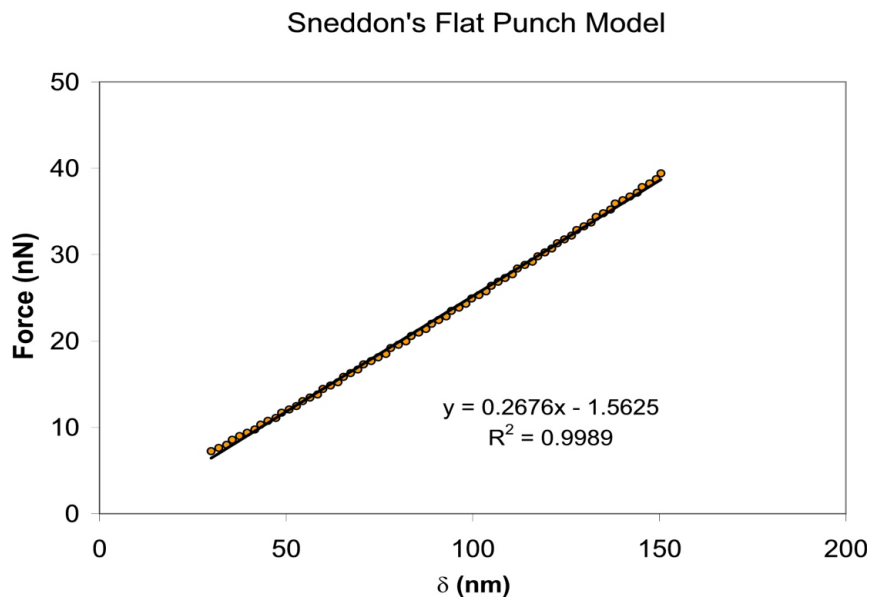


Figure 5.8. Regression of force- $\delta$  for the Sneddon flat-punch model.

The predicted forces based on these fits are plotted against the real data in Figure 5.9. The elastic modulus extracted using the Hertzian model and the flat-punch model were 3.9 MPa and the 4.4 MPa; respectively. The conical model, which did not fit the raw data well, yielded a modulus of 5.5 MPa. So, the moduli calculated from the Hertzian model and the Flat-punch model are similar even though the assumption of  $\delta < R$  is violated for the Hertzian model. Both the Hertzian model and the flat punch model fit the raw data well.

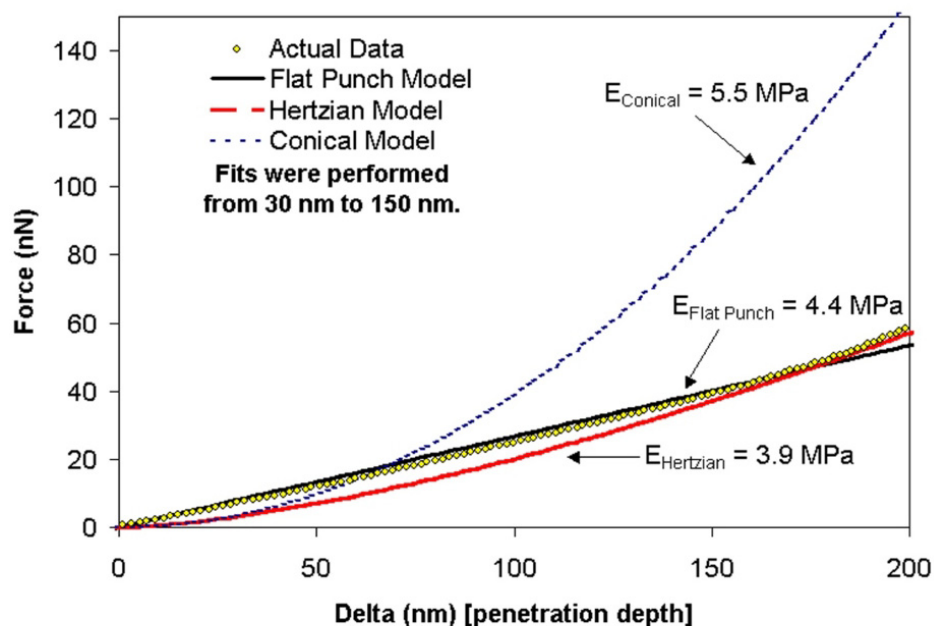


Figure 5.9. Force-vs.-deflection depth data of poly((n-butyl)-co-(3-acryloxypropyltrimethylsiloxane)silane) with overlaid Hertzian, Sneddon conical model, and Sneddon flat-punch model.

A second example of the three models overlaid on the force- $\delta$  data is shown in Figure 5.10 for a poly((3-acryloxypropyltrimethylsiloxane)silane) film. The modulus of the film according to the Hertzian model is 8.0 MPa while

it is 7.4 MPa according to the Flat-punch model. Again, the Hertzian model and the Sneddon Flat-punch model fit the data more accurately than Sneddon's conical model. In fact, both the Hertzian and Sneddon's Flat-punch model have proved quite robust for all of the samples analyzed.

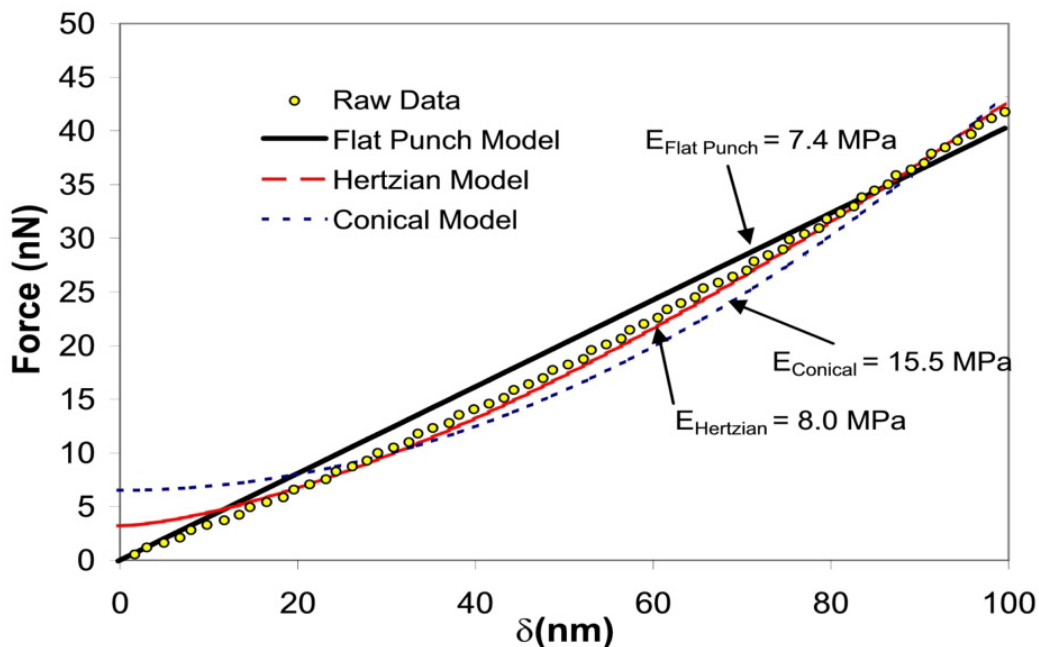


Figure 5.10. Force-vs.-deflection depth data of poly((3-acryloxypropyl-trimethylsiloxane)silane) with overlaid Hertzian, Sneddon conical model, and Sneddon flat-punch model.

### 5.6.1 Homopolymer Evaluation

A representative set of homopolymers crosslinked with 1% 1,3-bis(methacryloxytetramethyl)disiloxane were evaluated by nanoindentation at room temperature. Their force- $\delta^n$  relationship was analyzed using both the Hertzian model and the Sneddon flat-punch model. The elastic moduli of each calculated with the Flat-punch model is shown in Figure 5.11. The organic

homopolymer films have a modulus of 2 MPa while the silylated acrylate monomers (2-(acryloxyethoxy)trimethylsilane (SIA0160, Gelest)), (3-acryloxypropyl-tristrimethylsiloxane) silane (SIA0210, Gelest)) and silylated methacrylate monomers (acryloxytrimethylsilane (SIM6481, Gelest), and methacryloxypropyl (tristrimethylsiloxane)silane (SIM6487.6, Gelest)) range from 4.5 MPa to 34.5 MPa.

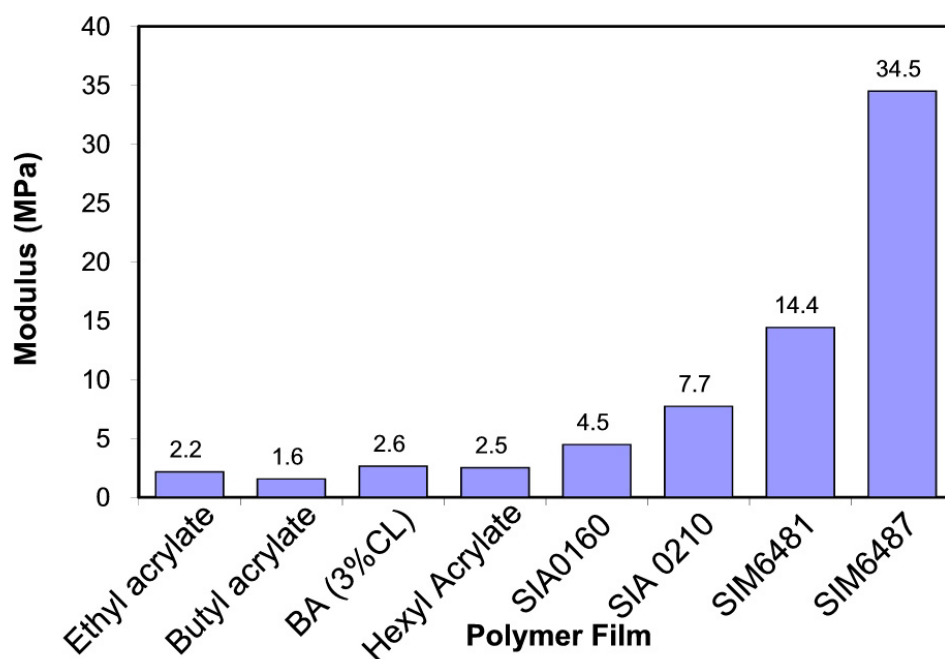


Figure 5.11. Moduli of lightly crosslinked homopolymer films.

The range of moduli for the polymers could be extended higher by incorporation of higher Tg monomers like those shown in Table 5.1. In the case of methyl methacrylate, however, this would have a negative impact on the photopolymerization rate [11]. It should be noted that nanoindentation performed

on the AFM with an Ultralever cantilever tip is limited to soft samples below 100 MPa since the cantilever is more compliant than the film. For higher  $T_g$  materials, an AFM equipped with a specialized stainless steel cantilever, a nanoindenter, or an IFM is required.

Table 5.1. High  $T_g$  Polymers [12] that may be suitable for the current etch barrier formulation.

Monomer	Glass Transition Temperature (°C)
Styrene	100
Acrylamide	165
Acrylic acid	110
Methyl methacrylate	115

### 5.6.2 Moduli of *n*-butyl acrylate – (3-acryloxypropyl-tristrimethylsiloxane)silane copolymers

A series of poly(*n*-butyl acrylate-(3-acryloxypropyl-tristrimethylsiloxane)silane) films were formulated in 25% (w/w) intervals and characterized by nanoindentation. The force- $\delta$  curves for all 5 films are shown in Figure 5.12. Qualitatively, the force required to generate identical penetration depths increases with (3-acryloxypropyltristrimethylsiloxane)silane content and consequently the modulus of the films increases with the percent of (3-acryloxypropyl-tristrimethylsiloxane)silane. Quantitatively, the modulus of the (3-acryloxypropyltristrimethylsiloxane)silane, *n*-butyl acrylate, and 50-50 copolymer films were calculated at 7.4 MPa, 1.6 MPa, and 4.4 MPa, respectively based on the Flat-punch model.

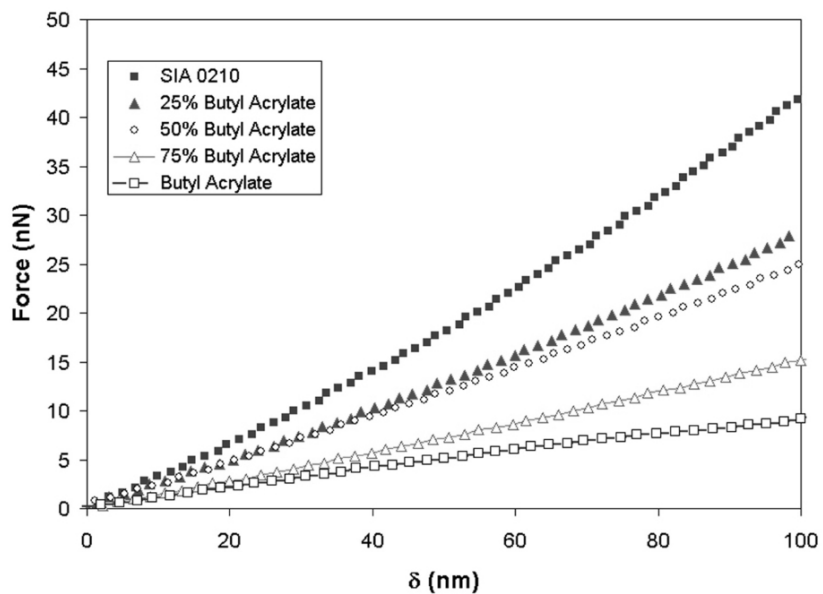


Figure 5.12. Raw force- $\delta$  data for (3-acryloxypropyl trimethylsiloxane)silane - *n*-butyl acrylate copolymer films.

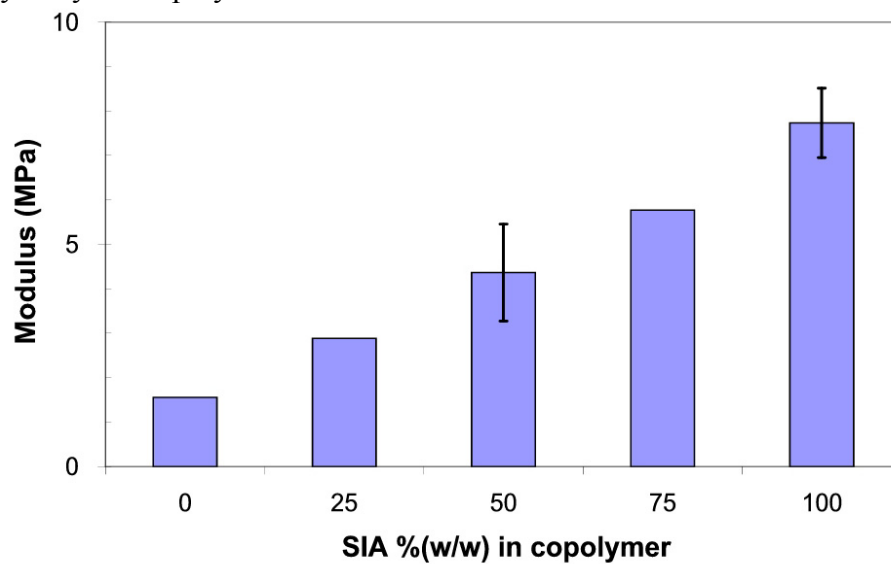


Figure 5.13. Young's modulus of (3-acryloxypropyltrimethylsiloxane)silane - *n*-butyl acrylate copolymer as calculated from Sneddon's flat-punch model. Error bars represent sample-to-sample variability in elastic modulus. Error due to regression fit was negligible.

## 5.7 CONCLUSIONS

Both the Hertzian model and the Sneddon flat-punch model proved quite robust for fitting nanoindentation data. The moduli of a variety of monomers were calculated from regression fits to force- $\delta$  data using the Sneddon flat-punch model. The moduli of several prospective etch barrier monomers were obtained and range from 2 MPa to 35 MPa with the current acrylate functionality. The current etch barrier formulation has a modulus of 4.4 MPa.

## 5.8 FUTURE WORK

In this work, Poisson's ratio was assumed to be 0.35. Typical polymers have a Poisson's ratio of 0.3 to 0.44. A perfectly elastic, isotropic material has a Poisson's ratio of 0.5. Absolute characterization of the Poisson's ratio is the next step toward a more complete understanding of the separation mechanics. However, the absolute affect of Poisson's ratio is limited to the range of 0.3 to 0.5 while the range over which the elastic modulus is tailorable is several orders of magnitude.

A collaboration has been established to allow etch barrier samples to be investigated by IFM. The design of the IFM is conducive to characterization of both soft samples (~1MPa) and hard samples on the order of 100 GPA. The IFM was developed by Sandia National labs and is described in detail in literature [4]. The IFM will be useful for characterization of a wider variety of prospective etch barrier components than is currently feasible on an AFM or nanoindenter. Consequently, new etch barrier chemistries can be investigated.

## References:

---

- 1 Lee, L.H. ed; Fundamentals of Adhesion, Plenum, NY, 366 (1991)
- 2 Van Workum, K.; J. J. de Pablo, P.F. Nealy and K. Yoshimoto, "Glass Transition and Mechanical Properties of Thin Polymer Films and Nano-scale Structures," *EIPBN*, Resists I: Properties and Processing, Washington, DC (2001)
- 3 Domke, J.; M. Radmacher, "Measuring the Elastic Properties of Thin Polymer Films with the Atomic Force Microscope," *Langmuir*, 14, 3320-3325 (1998)
- 4 Joyce, S.A.; J.E. Houston, "A new force sensor incorporating force-feedback control for interfacial force microscopy," *Rev. Sci. Instrum.* 62(3) 710-715 (1991)
- 5 Goken, M.; M. Kempf, W.D. Nix, "Hardness and Modulus of the Lamellar Microstructure in PST-TiAl studied by Nanoindentation and AFM," *Acta Mater.* 903-911 (2001)
- 6 Oliver, W.C.; G.M. Pharr, *J. Mater. Res.* 1, 601 (1992)
- 7 Hertz, H.J.; *J. Riene Angew. Mathematik*, 92, 156-171 (1882)
- 8 Sneddon, I.N.; *Int J. Eng. Sci.* 2, 47-57 (1965)
- 9 Johnson, K.L.; Contact Mechanics; University Press, Cambridge (1987)
- 10 "User's Guide to AutoProbe CP", Chapter 4. Park Scientific Instruments (1998)
- 11 Colburn, M.; S. Johnson, M. Stewart, S. Damle, B. J. Jin, T. Bailey, M. Wedlake, T. Michaelson, S.V. Sreenivasan, J. Ekerdt, C.G. Willson, *Proc. SPIE.* 3676, 379-389 (1999)
- 12 Allock, H. R.; F.W. Lampe. Contemporary Polymer Chemistry, 2<sup>nd</sup> Ed. Prentices, NJ (1990)

## 6 Volumetric Contraction of Photopolymers

### 6.1 INTRODUCTION

Step and Flash Imprint Lithography (SFIL) is a patterning process utilizing photopolymerization to replicate the topography of a template onto a substrate [1,2]. Polymerization, however, is often accompanied by densification. The interaction environment between photopolymerizable monomers that undergo free radical polymerization changes from Van der Waals' to covalent resulting in volumetric contraction. Several examples of monomers that densify upon polymerization are shown in Table 6.1 and Table 6.2. This densification has repercussions for replication processes, such as SFIL [3], that are explored in Chapter 7. As such, the extent of densification of prospective etch barrier components must be evaluated and the implications of shrinkage understood.

Table 6.1. Densification for free radical polymerization (from Bailey et al. [4])

Monomer	Densification (%)
Ethylene	66
Butadiene	36
Vinyl Chloride	34
Methyl methacrylate	21
Styrene	14

Table 6.2. Densification for addition polymerization (from Bailey et al. [4])

Monomer	Densification (%)
Ethylene Oxide	23
Tetrahydrofuran	10
Cyclooctadiene	3
Dimethylsilane oxide cyclic tetramer	2

## 6.2 BACKGROUND

Several methods are available for measuring the volume change that monomers undergo as a result of polymerization. Dilatometry is a traditional method for measuring thermal expansion coefficients as well as monitoring the extent of the polymerization reaction [4,5]. Ellipsometry and spectral interferometry are two other techniques that have been used to monitor film thickness changes during reaction [6]. Density gradient columns and the Archimedes' principle are two other methods for determining density based on buoyancy.

Initially, dilatometry was the preferred method of characterization for which the American Oil Chemists Society (AOCS) published a standard experimental procedure [7]. The procedure is based on a dilatometer that consists of a 10 ml sample bulb connected to a graduated column, which is transparent down to 350 nm in the UV spectrum. Each column is characterized for non-linearity along its length to correct for manufacturing flaws according to the AOCS method.

According to the method, a volume of mercury is drawn into an inverted dilatometer through the graduated column such that the mercury fills just over half the column when re-inverted. A sample of known volume is then charged into the sample bulb. The bulb is stoppered leaving no void volume. The samples are subjected to UV illumination that initiates free radical polymerization. The height of the mercury in the graduated column is monitored during the course of the reaction and is used to calculate the volumetric change. Based on the minimum gradation observable in the column the resolution of the dilation measurement is 0.05%.

This procedure poses several challenges to the study of silylated photopolymers. Conventional cleaning solutions such as piranha etch (2 H<sub>2</sub>SO<sub>4</sub>:1 H<sub>2</sub>O<sub>2</sub>) or methanol/HCl that oxidize organic contaminants will not remove the etch barrier due to the high silicon content of the photopolymerized etch barrier; oxidation simply forms an intractable SiO<sub>2</sub> mass. Consequently, many of the etch barrier solutions tested would be required to use a new dilation column (and its characterization) for each measurement which makes the method impractical for large scale screening experiments.

Initial work was performed to judge the validity of the measuring the dilation in real time using ellipsometry or spectral ellipsometry. In fact, the gap sensing system detailed in Chapter 9 was designed to measure the index of refraction and film thickness simultaneously. Using film stability calculations

shown in Chapter 3, it was determined that confinement of a film that 1.16  $\mu\text{m}$  or thicker would generate a stable film up to 3 mm in diameter. The confined liquid film could then be monitored while the film is exposed. However, the lack of an ellipsometer and the development time required for real time simultaneous characterization of film thickness and index of refraction was not viable. As a result, the densities of the photopolymers were measured by Archimedes' principle.

### 6.3 PROCEDURE

In Archimedes' experiments, a dry sample ( $T_1$ ) was first weighed. Then, the sample ( $T_2$ ) was weighed again while submerged in a fluid of known density ( $\rho_{liq}$ ). Equation 6.1 relates the ratio of the measured masses to the density of the sample ( $\rho_{sample}$ ). The final densities were measured and the volumetric change was calculated using Equation 6.2.

$$\text{Equation 6.1} \quad \rho_{sample} = \rho_{liq} \left( \frac{T_1}{T_2} \right)$$

$$\text{Equation 6.2} \quad \Delta V = \left( \frac{\rho_{polymer} - \rho_{monomer}}{\rho_{polymer}} \right)$$

The samples were generated by photopolymerization of the monomeric solutions in a modified 10 ml syringe. The illumination system consisted of a 500 W Hg-Arc lamp (Oriental) that focused light on a liquid light guide (Oriental). The sample was placed in a 16" x 16" x 16" UV protection chamber that was purged

with  $N_2$  flowing at  $\sim 5$  standard cubic feet per minute (scfm). The liquid light guide entered through the port in the top of the chamber and was attached to a collimating optic (Oriol) that projected the UV light onto the sample. Due to the thickness of the samples, the solutions were allowed to cure under UV illumination for  $\sim 15$  minutes. The exposure time was set by determining the time required for the density of a poly(methyl methacrylate) (PMMA) sample to become an invariant in dose.

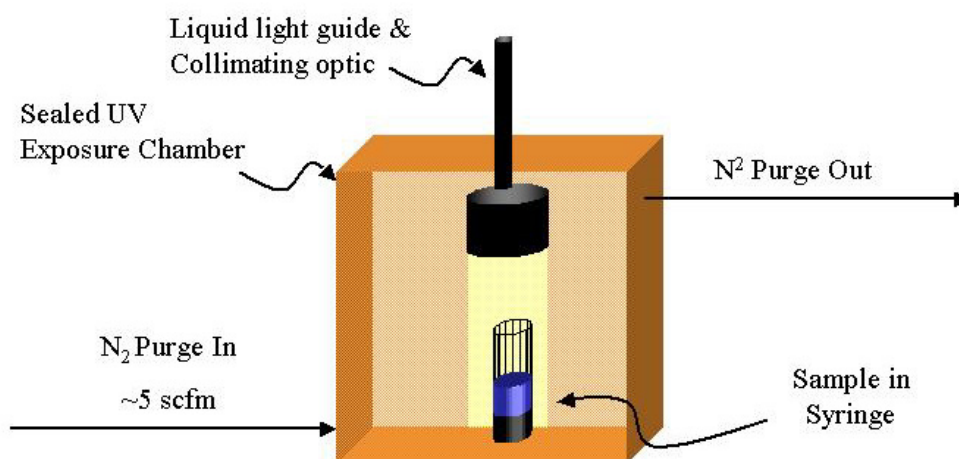


Figure 6.1. UV exposure chamber with  $N_2$  purge used to cure photopolymer samples.

Several precautions must be taken when performing this measurement. The heat of polymerization can cause a sample to boil. Therefore, illumination intensity was attenuated to allow the heat to dissipate. Bubble formation in the solution artificially decreases the density of the resulting polymer and must be eliminated. Ultrasonication of the monomer solutions was performed to minimize

these sources of error. A 5 minute degas cycle followed by a 10 minute ultrasonication was standard procedure. A third concern was the absorption of the liquid into the polymer sample during the buoyancy measurement. This was determined to be insignificant since the measured mass remained constant over the time scale of the measurement.

The accuracy of the method was validated by comparing the literature values for the density of low molecular weight PMMA to the density determined by Archimedes principle. The mean densities were statistically identical with a 95% confidence. The precision of density measurements using Archimedes principle ranges from 0.001 – 0.02 but on average was 0.005 (0.5%).

## **6.4 RESULTS**

### **6.4.1 Alkyl Acrylates**

By studying a set of model organic monomers, the effect of pendant group size on densification was investigated. Ethyl acrylate, butyl acrylate, hexyl acrylate, and lauryl acrylate solutions were formulated with 1% (w/w) of 1,3-bis(3-methacryloxypropyl)tetramethyldisiloxane (SIB 1402.0, Gelest) and 3%(w/w) of a 1:1 mixture of bis(2,4,6-trimethylbenzoyl)phenylphosphine oxide (Irgacure 819, Ciba) and 1-benzoyl-1-hydroxycyclohexane (Irgacure 184, Ciba); then cured under N<sub>2</sub> purge. The crosslinker was added to insure a solid sample that could be easily handled.

A plot of volumetric change versus monomer chain length is shown in Figure 6.2. The densification is 16.5% for ethyl acrylate and decreases linearly to

6% for lauryl acrylate. This indicates that length of the side chain plays an important role in densification of these monomers, and formulating solutions with different *n*-alkyl acrylate monomers can control that densification.

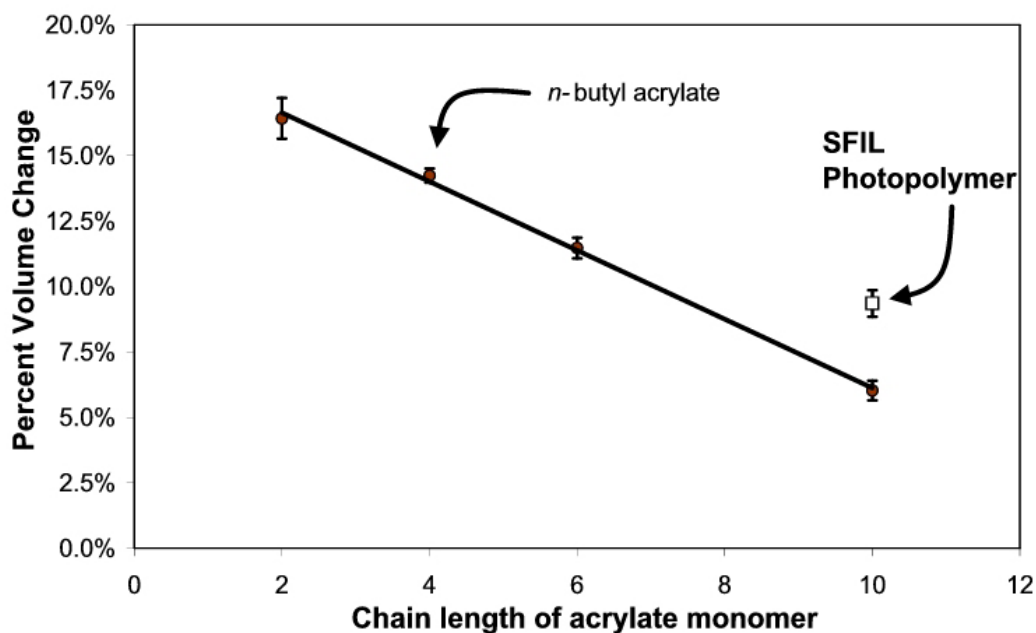


Figure 6.2. Volume contraction of *n*-alkyl acrylates measured by Archimedes' principle plotted versus the pendant group length. The SFIL etch barrier is plotted for reference.

Several other test molecules were included in the study: *t*-butyl acrylate, cyclohexyl acrylate, and cyclohexyl methacrylate. These provided some insight into the effect of the steric hindrance of the pendant group and the methyl group in methacrylate monomers on densification. All of these monomers exhibited less densification than their *n*-alkyl acrylate counterpart and are listed in Table 6.3.

## 6.4.2 Silylated Monomers

The etch barrier formulation consists of both an organic monomer and a silylated monomer and is constrained by its process performance requirements. The silicon content must be at least 15% (w/w) for etch selectivity purposes, which will be presented in Chapter 8 [2]. Consequently, the volumetric change of silylated acrylate monomers was also investigated. Due to the complexity of the pendant groups, the same analysis as that used on the organic monomers could not be applied readily.

These data were normalized by dividing the molecular weight of the monomer minus the molecular weight of the pendant group by the molecular weight of the monomer to give the weight percent of the reactive portion of the monomer. The densification of a host of silylated monomers is shown in Figure 6.3 and shows a strong correlation to the weight percent of the reactive portion. The chemical name and corresponding commercial name are tabulated below with their average volumetric shrinkage and its standard deviation.

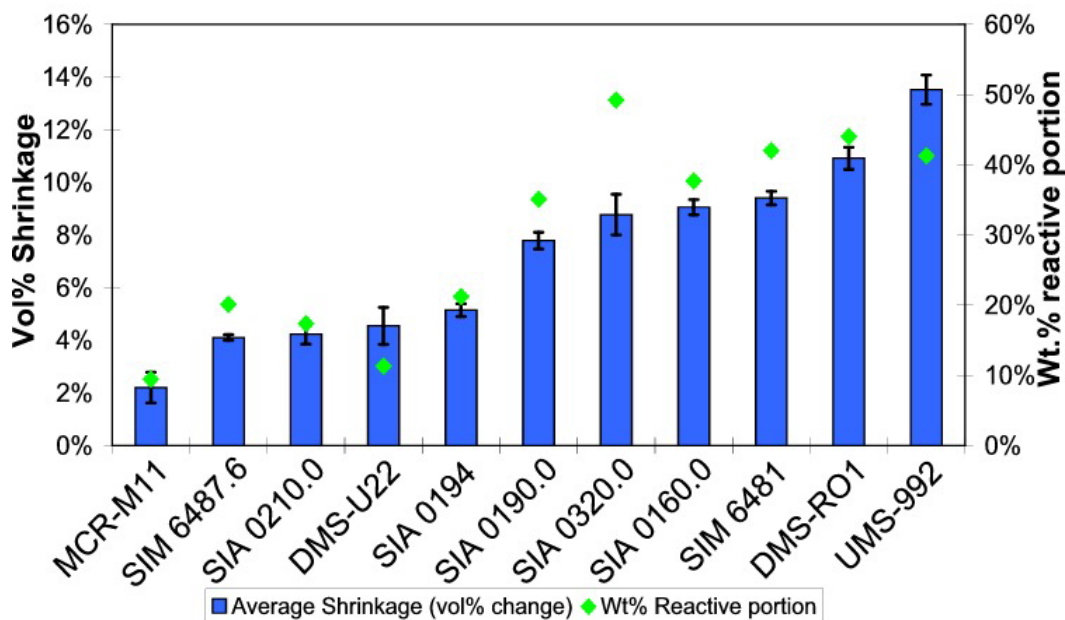


Figure 6.3. Silylated Monomer Densification.

In an attempt to further improve the predictive capability of this analysis, HyperChem® molecular dynamic simulations were utilized to determine the ratio of the monomer volume to the pendant group volume for several monomers. The pendant group volume percent was defined as the volume of the monomer minus the volume of an acrylic acid monomer. A schematic of this methodology is shown in Figure 6.4 where the blue spheres represent the atoms in the pendant group and the red and aqua spheres represent the acrylate functional group.

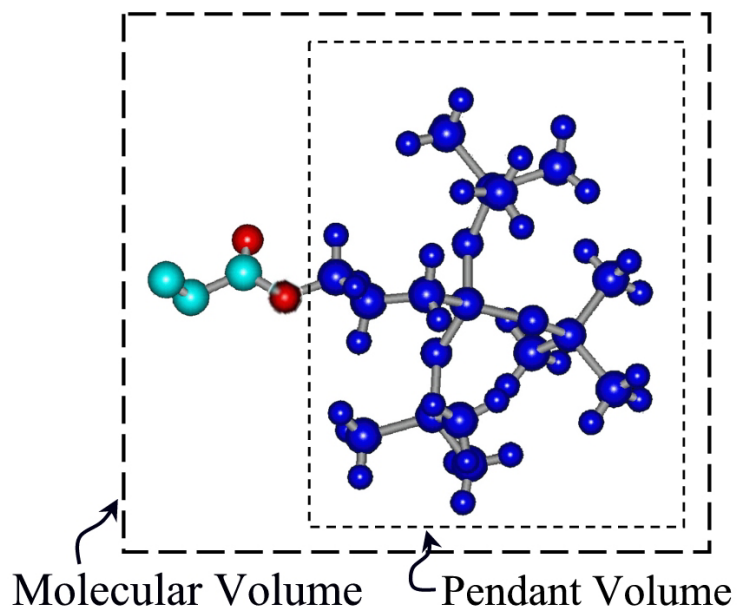


Figure 6.4. Hyperchem<sup>®</sup> model of (3-acryloxypropyltristrimethylsiloxane)silane.

A plot of the pendant group volume fraction versus densification is shown in Figure 6.5. The plot shows a relatively linear relationship that is valid for both organic and silylated monomers and may be used for estimating volume change of other prospective etch barrier candidates.

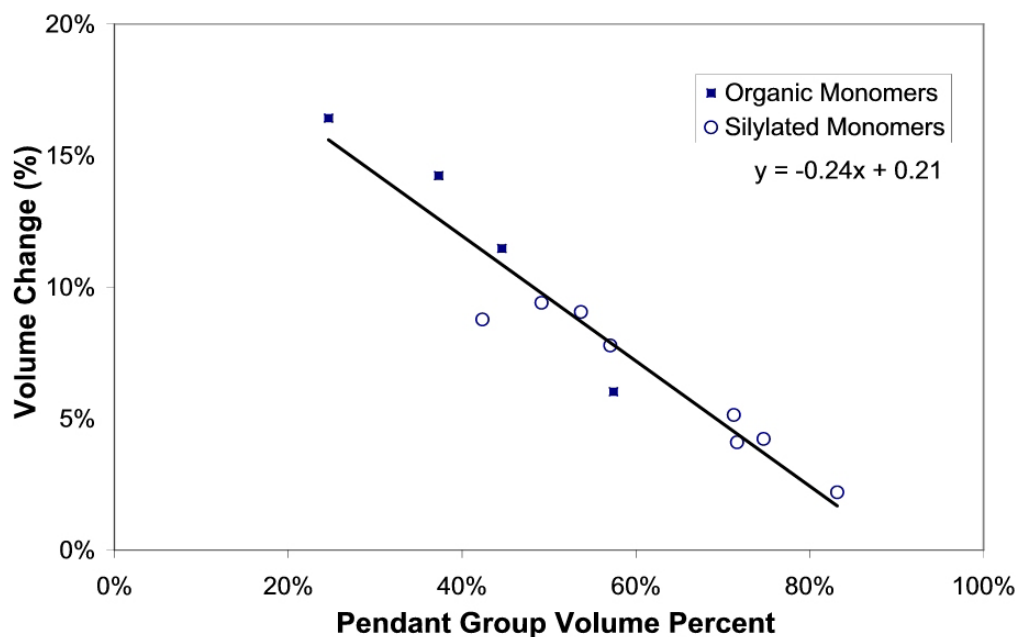


Figure 6.5. Volumetric contraction as a function of pendant group volume percent (simulated in HyperChem®).  $R^2 = 0.92$ .

#### 6.4.3 Crosslinker effect on (3-acryloxypropyl-tristrimethylsiloxane)silane

In addition to the effect of the volume of the pendant group, the amount of crosslinker may also impact on the volumetric contraction of the etch barrier. Therefore, a set of densification measurements was performed on (3-acryloxypropyl-tristrimethylsiloxane)silane (SIA 0210.0, Gelest) mixtures with the percent of 1,3-bis(3-methacryloxypropyl) tetramethyldisiloxane (SIB1402.0, Gelest) varied from 0.1% and 5% (w/w). The results show that an increase in crosslinker concentration increases the volumetric contraction. The effect is modest, however, and only changes the densification of this particular monomer a

total of 1.5% across the range of 0.5% to 5% (w/w) crosslinker. It is a small effect that was not statistically significant for other monomer solutions.

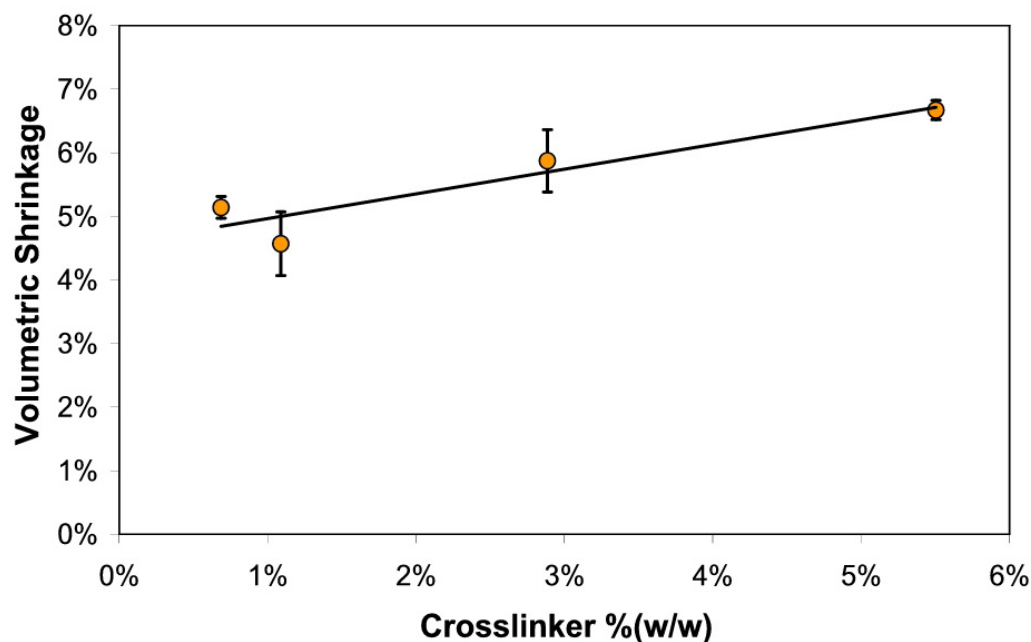


Figure 6.6. Effect of crosslinker concentration on the volumetric change of 3-acryloxypropyltrimethylsiloxane silane.

#### 6.4.4 Volumetric shrinkage of butyl acrylate-(3-acryloxypropyl-trimethylsiloxane)silane copolymers

Since the etch barrier is a blend of two principle components: butyl acrylate and (3-acryloxypropyltrimethylsiloxane)silane, it was necessary to study the effect that blending the two monomers has on the volumetric change. Butyl acrylate and (3-acryloxypropyltrimethylsiloxane)silane were mixed at 25% (w/w) intervals from 100% butyl acrylate to 100% (3-

acryloxypropyltrimethylsiloxane)silane. These mixtures were cured and their density measured. A graph of the measured densification is shown in Figure 6.7.

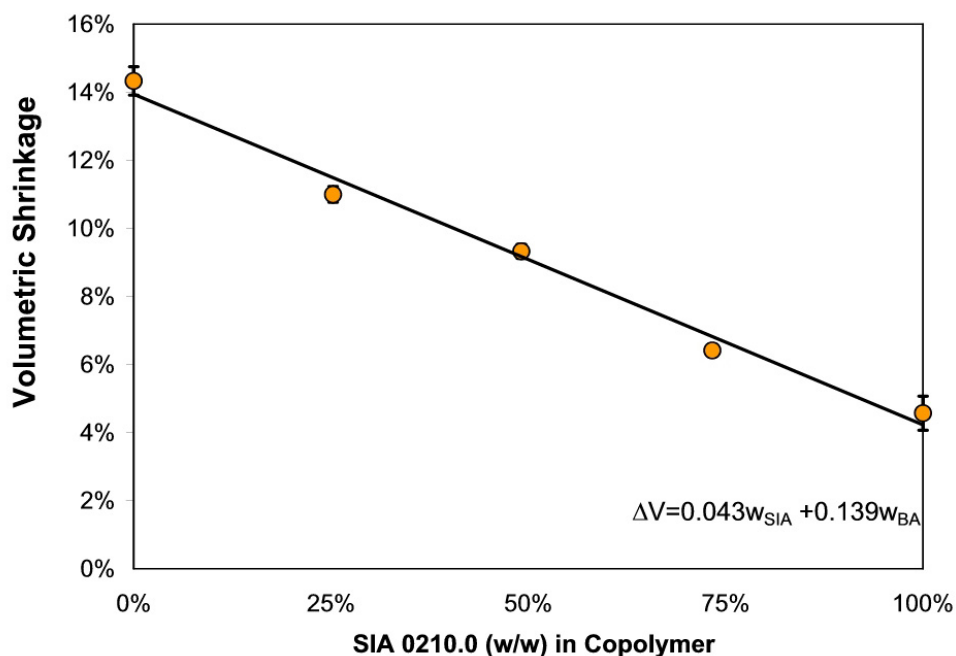


Figure 6.7. Densification of (3-acryloxypropyltrimethylsiloxane)silane and butyl acrylate copolymers

The system behaves linearly; there is no interaction present in this system. Therefore, the volumetric change of a blend of these two polymers can be predicted by Equation 6.3:

**Equation 6.3** 
$$\Delta V_{\text{total}} = 13.9\% w_{BA} + 4.3\% w_{SIA}$$

where  $w_{BA}$  and  $w_{SIA}$ , are the weight percent of the butyl acrylate and (3-acryloxypropyltrimethylsiloxane)silane, respectively, and 13.9% and 4.3% are

the predicted volumetric changes of butyl acrylate and (3-acryloxypropyltrimethylsiloxane)silane, respectively.

The densification of the etch barrier was measured at 9.3% (v/v). It consists of 50% (w/w) *n*-butyl acrylate, 50% (w/w) (3-acryloxypropyltrimethylsiloxane)silane (SIA 0210.0, Gelest), to which 5% (w/w) 1,3-bis(3-methacryloxypropyl) tetramethyldisiloxane (SIB 1402.0, Gelest), and 3% (w/w) of 1:1 mixture of bis(2,4,6-trimethylbenzoyl)-phenylphosphineoxide (Irgacure 819, Ciba) and 1-benzoyl-1-hydroxycyclohexane (Irgacure 184, Ciba) were added. A summary of the volumetric shrinkage measurements is shown in Table 6.3

Table 6.3. Chemical name, commercial name, and volumetric shrinkage for solutions with 1% (w/w) SIB 1402 and 3% (w/w) free radical generator (1:1 mixture of Irgacure 184 and Irgacure 819) added.

Monomer	Acronym / Product Name	Average Volume Change	Standard Deviation
2-(acryloxyethoxy)trimethylsilane	SIA 0160.0	9.1%	0.3%
(3-acryloxypropyl)dimethyl methoxysilane	SIA 0190.0	7.8%	0.3%
(3-acryloxypropyl)methyl(bis-(trimethylsiloxy)silane	SIA 0194	5.1%	0.2%
(3-acryloxypropyl tristrimethylsiloxane)silane	SIA 0210.0	4.6%	0.5%
Methacryloxyethoxy-Trimethylsilane	SIA 0320.0	8.8%	0.8%
Acryloxytrimethylsilane	SIM 6481	9.4%	0.3%
Methacryloxypropyl (tristrimethylsiloxane)silane	SIM 6487.6	4.1%	0.1%
Monomethacryloxypropyl terminated dimethylsilane	MCR-M11	2.2%	0.6%
Acryloxypropyl-terminated dimethyl siloxane	DMS-U22	4.6%	0.7%
Methacryloxypropyl-terminated dimethyl siloxane	DMS-RO1	10.9%	0.4%
Acryloxypropylmethylsiloxane homopolymer	UMS-992	13.5%	0.6%
Ethyl acrylate	EA	16.4%	0.8%
Butyl acrylate	BA	14.2%	0.3%
Hexyl acrylate	HA	11.5%	0.4%
Lauryl acrylate	LA	6.0%	0.4%
Cyclohexyl acrylate	CHA	8.6%	0.5%
Cyclohexyl methacrylate	CHMA	10.0%	0.6%
<i>t</i> -Butyl acrylate	TBA	10.4%	0.4%
Etch Barrier	Low- $\mu$ EB	9.4%	0.9%

## 6.5 CONCLUSIONS

Step and Flash Imprint Lithography is dependent on the process of photopolymerization that is accompanied by volumetric contraction. For acrylate formulations, the densification is structure dependent and can be tailored from 4% to 16%. A simple model based on simulated pendant group volume has been proposed and appears valid for both alkyl and silylated monomers. The effect of crosslinker concentration was determined but found to be minimal in comparison the effect of pendent group size. The blends of butyl acrylate and (3-acryloxypropyltrimethylsiloxane)silane monomers undergo a change in density that is linear in composition. The current etch barrier shrinks 9.3% (v/v).

## 6.6 FUTURE WORK

The densification of acrylate monomers has been characterized and a useful model based on simulated molecular volumes has been proposed that fits both silylated and organic monomers. However, norbornenes, styrene, or other monomers that may be added to the etch barrier may exhibit different behavior and should be characterized.

All of the monomers tested for densification underwent free radical photopolymerization. Different methods of photopolymerization may also be useful in SFIL. While free radical polymerization has been the primary focus of the etch barrier development, cationic polymerization of epoxides has also studied. One benefit of these ring-opening polymerizations is a lower degree of shrinkage, which is a consequence of the number of covalent bonds generated by

polymerization being offset by the number of covalent bonds being broken during the reaction. An additional benefit of cationic polymerization is that it is not subject to oxygen sensitivity like free radical polymerization. This oxygen sensitivity makes the photopolymerization of peripheral regions subject to atmospheric oxygen inconsequential.

Epoxides are just one class of monomers that exhibit low shrinkage upon polymerization. In fact, Bailey *et al.* has described spiro ortho esters, ketal lactones, and trioxabicyclooctanes, and spiro ortho carbonates that undergo polymerization with expansion in volume [4,8]. In principle, any method of photopolymerization is compatible with SFIL as long as the rate of polymerization, the viscosity, the surface properties, and the etch selectivity restrictions are met. The properties of the acrylate systems, however, can be tailored over a large range using existing chemistries in a manner suitable for SFIL replication so they are particularly attractive.

References:

---

- 1 Colburn, M.; S. Johnson, M. Stewart, S. Damle, B. J. Jin, T. Bailey, M. Wedlake, T. Michaelson, S.V. Sreenivasan, J. Ekerdt, C.G. Willson; "Step and Flash Imprint Lithography: An alternative approach to high resolution patterning." *Proc. SPIE*. 3676, 379-389 (1999)
- 2 Colburn, M.; A. Grot, M. Amistoso, B.J. Choi, T. Bailey, J. G. Ekerdt, S.V. Sreenivasan, J. Hollenhorst, C. G. Willson; "Step and Flash Imprint Lithography for sub-100nm Patterning." *Proc. SPIE*, 3676, 379-389 (2000)
- 3 Colburn, M.; I. Suez, B.J. Choi, M. Meissl, T. Bailey, S.V. Sreenivasan, J.G. Ekerdt, C. G. Willson. "Characterization and Modeling of Volumetric and Elastic Properties of Step and Flash Imprint Lithography Photopolymers," *J. Vac. Sci Technol. B*. [submitted]
- 4 Bailey. W. J.; "Ring opening polymerization with expansion in volume," *ACS Symp.* 59, 38-59, (1977)
- 5 Pearce, E.M.; C.E., Wright, B.K. Bordoloi, "Laboratory Experiments in Polymer Synthesis and Characterization," Educational Modulus for Material Science and Engineering Projects (1982)
- 6 Burns, S. D.; M. D. Stewart, J. Hilfiker, R. Synowicki, G. M. Schmid, and C. G. Willson. "Determining Free Volume Changes During PAB and PEB of a Chemically Amplified Resist," *Retech 12th International Conference on Photopolymers* (2000)
- 7 Official Methods and Recommended Practises of AOCS, 5<sup>th</sup> ed., AOCS (1998)
- 8 Bailey, W. J.; K. No, P.C. Yuan, K. Saigo, J. Stansbur, S.R. Tan, J. Zhou, "Recent dvances in ionic polymerizations with expansion in volume," *Polym. Prepr.* **26**(1) 50-1 (1985)

## **7 Finite Element Modeling of SFIL Photopolymer Replicated Features**

### **7.1 INTRODUCTION**

Step and Flash Imprint Lithography (SFIL) utilizes the photopolymerization of an etch barrier to replicate a topography of a template onto a substrate [1,2]. The photopolymerization is accompanied by 9.3 %(v/v) densification that may affect the size, shape, and placement of relief patterns. The length scale of the densification for high-resolution features is on the order of nanometers, so quantification is difficult. However, finite element modeling (FEM) makes it possible to explore the influence of changes in densification and mechanical properties on the replicated feature geometry. The simulations are based on the densification and the elastic modulus of the etch barrier precursors detailed in previous chapters.

### **7.2 FINITE ELEMENT MODELING BACKGROUND**

Finite element modeling (FEM) is a powerful computational method capable of solving complex systems of coupled differential equations that predict a continuum deformation in response to external forces such as applied loads or environmental changes. FEM uses a discrete representation of a continuum to model the spatial change of a model parameter such as temperature or displacement. To understand how these simulations are performed, it is useful to review the fundamental mechanics that govern stress-strain relationships and how

digitization of the continuum affects the model. The primary metric of interest for SFIL is displacement of the etch barrier.

The first step in FEM is to define the elements and their nodes. An example of a basic two-dimensional grid is shown in Figure 7.1 together with an example of a grid optimized for accuracy around the feature vertices. Many types of grids are available but a general guideline is that a variable pitch grid that is denser near large gradients in the metric makes the solution to the system of equations more accurate while maintaining computational efficiency [3]. Each element has at least as many nodes as vertices. As the number of nodes per element increases, a higher order polynomial approximation of the metric is required. Many commercial packages, such as Pro/Mechanica<sup>®</sup>, utilize self-adaptive algorithms that optimizes the grid size, the number of nodes per grid, and the polynomial order.

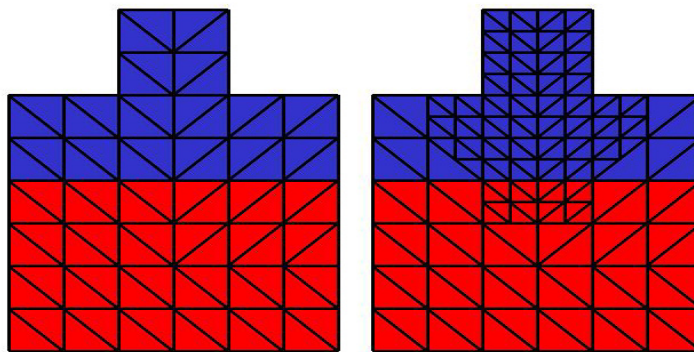


Figure 7.1. Two examples of a continuum digitized into elements defined by their nodes. (Left) Uniform grid. (Right) Customized grid designed to increase accuracy of simulation within the feature and at the vertices.

## 7.2.1 Stress-strain Relationships for Isotropic Materials

With the model and its element defined, applied loads and constraints can be applied that deform the model [4]. These deformations can be quantified by the strain. For an unconstrained three dimensional model, each node has six degrees of freedom defined by the three principle tensile strains ( $\epsilon_i$ ) and shear strains, ( $\gamma_i$ ) defined below [3]:

$$\text{Equation 7.1} \quad \epsilon_x = \frac{\partial u}{\partial x}, \quad \epsilon_y = \frac{\partial v}{\partial y}, \quad \epsilon_z = \frac{\partial w}{\partial z}$$

$$\text{Equation 7.2} \quad \gamma_{xy} = \frac{\partial v}{\partial x} + \frac{\partial u}{\partial y}, \quad \gamma_{yz} = \frac{\partial w}{\partial y} + \frac{\partial v}{\partial z}, \quad \gamma_{zx} = \frac{\partial w}{\partial x} + \frac{\partial u}{\partial z}$$

where  $u$ ,  $v$ , and  $w$  are the three components of the displacement vector in the  $x$ ,  $y$ , and  $z$  directions. The generalized Hook's relationships that relate these strains to the associated stresses,  $\sigma_i$  and  $\tau_{ij}$ , are shown below [3]:

$$\text{Equation 7.3} \quad \epsilon_x = a_{11}\sigma_x + a_{12}\sigma_y + a_{13}\sigma_z + a_{14}\tau_{xy} + a_{15}\tau_{yz} + a_{16}\tau_{zx}$$

$$\text{Equation 7.4} \quad \epsilon_y = a_{21}\sigma_x + a_{22}\sigma_y + a_{23}\sigma_z + a_{24}\tau_{xy} + a_{25}\tau_{yz} + a_{26}\tau_{zx}$$

$$\text{Equation 7.5} \quad \epsilon_z = a_{31}\sigma_x + a_{32}\sigma_y + a_{33}\sigma_z + a_{34}\tau_{xy} + a_{35}\tau_{yz} + a_{36}\tau_{zx}$$

$$\text{Equation 7.6} \quad \gamma_{xy} = a_{41}\sigma_x + a_{42}\sigma_y + a_{43}\sigma_z + a_{44}\tau_{xy} + a_{45}\tau_{yz} + a_{46}\tau_{zx}$$

$$\text{Equation 7.7} \quad \gamma_{yz} = a_{51}\sigma_x + a_{52}\sigma_y + a_{53}\sigma_z + a_{54}\tau_{xy} + a_{55}\tau_{yz} + a_{56}\tau_{zx}$$

$$\text{Equation 7.8} \quad \gamma_{zx} = a_{61}\sigma_x + a_{62}\sigma_y + a_{63}\sigma_z + a_{64}\tau_{xy} + a_{65}\tau_{yz} + a_{66}\tau_{zx}$$

where  $\varepsilon_i$  is the strain in the  $i^{\text{th}}$  direction, and  $\gamma_{ij}$  is the shear strain in the  $i^{\text{th}}$  direction acting across the plane defined by the  $j^{\text{th}}$  normal,  $\sigma_i$  is the stress, and  $\tau_{ij}$  is the shear stress. The  $a_{ij}$  coefficients for isotropic materials are shown below:

$$\text{Equation 7.9} \quad a_{11} = a_{22} = a_{33} = 1/E$$

$$\text{Equation 7.10} \quad a_{ij} = -\nu/E \quad \text{for } i, j = 1, 2, 3$$

$$a_{ij} = 0 \quad \text{if } i \text{ or } j = 4, 5, 6$$

$$\text{Equation 7.11} \quad a_{44} = a_{55} = a_{66} = 1/G$$

where  $E$  is the tensile (Young's) modulus,  $\nu$  is Poisson's ratio,  $G$  is the shear modulus.

### 7.2.2 Conditions and Constraints for Equilibrium

Since the displacement vectors define the strains, they are governed by the law of continuity that yields the following restrictions [3] that must be satisfied to eliminate voids between adjacent elements.

$$\text{Equation 7.12} \quad \frac{\partial^2 \varepsilon_x}{\partial y^2} + \frac{\partial^2 \varepsilon_y}{\partial x^2} = \frac{\partial^2 \gamma_{xy}}{\partial x \partial y}$$

$$\text{Equation 7.13} \quad \frac{\partial^2 \varepsilon_z}{\partial y^2} + \frac{\partial^2 \varepsilon_y}{\partial z^2} = \frac{\partial^2 \gamma_{yz}}{\partial z \partial y}$$

$$\text{Equation 7.14} \quad \frac{\partial^2 \varepsilon_x}{\partial z^2} + \frac{\partial^2 \varepsilon_z}{\partial x^2} = \frac{\partial^2 \gamma_{zx}}{\partial x \partial z}$$

$$\text{Equation 7.15} \quad 2 \frac{\partial^2 \varepsilon_x}{\partial y \partial z} = \frac{\partial}{\partial x} \left( -\frac{\partial \gamma_{yz}}{\partial x} + \frac{\partial \gamma_{zx}}{\partial y} + \frac{\partial \gamma_{xy}}{\partial z} \right)$$

**Equation 7.16** 
$$2 \frac{\partial^2 \varepsilon_y}{\partial x \partial z} = \frac{\partial}{\partial y} \left( \frac{\partial \gamma_{yz}}{\partial x} - \frac{\partial \gamma_{zx}}{\partial y} + \frac{\partial \gamma_{xy}}{\partial z} \right)$$

**Equation 7.17** 
$$2 \frac{\partial^2 \varepsilon_z}{\partial x \partial y} = \frac{\partial}{\partial z} \left( \frac{\partial \gamma_{yz}}{\partial x} + \frac{\partial \gamma_{zx}}{\partial y} - \frac{\partial \gamma_{xy}}{\partial z} \right)$$

For a static system, the net force and moment acting on each element must equal zero. If not, the elements are subject to rotation and translation in time. The conditions for equilibrium for a three dimensional model are listed in the equations below:

**Equation 7.18** 
$$\frac{\partial \sigma_x}{\partial x} + \frac{\partial \tau_{xy}}{\partial y} + \frac{\partial \tau_{zx}}{\partial z} + X = 0 \quad \text{[X-Force Balance]}$$

**Equation 7.19** 
$$\frac{\partial \tau_{xy}}{\partial x} + \frac{\partial \sigma_y}{\partial y} + \frac{\partial \tau_{yz}}{\partial z} + Y = 0 \quad \text{[Y-Force Balance]}$$

**Equation 7.20** 
$$\frac{\partial \tau_{xy}}{\partial x} + \frac{\partial \tau_{yz}}{\partial y} + \frac{\partial \sigma_z}{\partial z} + Z = 0 \quad \text{[Z-Force Balance]}$$

where  $X, Y, Z$  are external forces acting on each element. The moment must also be balanced and results in the conditions the  $\tau_{xy} = \tau_{yx}$ ,  $\tau_{yz} = \tau_{zy}$ , and  $\tau_{zx} = \tau_{xz}$  [3].

Unfortunately, multiple solutions to these coupled sets of differential equations often exist. However, each solution has an associated potential energy. When an applied force or constraint deforms an elastic system, strain energy ( $U_s$ ) is stored. This stored energy varies locally and is defined by the product of corresponding local strains and local stresses [3]:

**Equation 7.21**

$$dU_s = dU_\sigma + dU_\tau = \left( \int_0^{\varepsilon_i} \sigma_i d\varepsilon_i + \int_0^{\gamma_{ij}} \tau_i d\gamma_{ij} \right) dV \quad \text{for } i, j = 1, 2, 3$$

where  $U_\sigma$  and  $U_\tau$  are the components of strain energy related to tensile stress-strain and shear stress-strain. When the local strain energy is integrated over the entire volume of the system, as shown below, the result is a measure of the potential energy stored in the system [3].

$$U_s = \int_V \left( \int_0^{\varepsilon_i} \sigma_i d\varepsilon_i + \int_0^{\gamma_{ij}} \tau_i d\gamma_{ij} \right) dV \quad \text{for } i, j = 1, 2, 3$$

Thermodynamically, the real system prefers to relax into the lowest possible energy state. Therefore, FEM algorithms converge on a numerical solution for displacement that offers a minimum in the global strain energy. Convergence on local strain energy and displacement can also be imposed to improve the accuracy of the model in the critical regions of interest.

### 7.2.3 Types of Strain

The above sections detail the relationship of stress and elastic strain in a deformed material and the equilibrium achieved by strain energy minimization. However, these were generalized relations for an isotropic material and they do not dictate how the stress or strain is applied. The total strain ( $\varepsilon$ ) is comprised of three principle components: elastic strain ( $\varepsilon_E$ ), thermal strain ( $\varepsilon_T$ ), and initial strain ( $\varepsilon_I$ ).

**Equation 7.22**

$$\varepsilon = \varepsilon_E + \varepsilon_T + \varepsilon_I = C\sigma + \varepsilon_T + \varepsilon_I$$

where  $C$  is the matrix defined by the generalized Hook's relationships above and  $\varepsilon_T$  for a material is defined by [4]:

**Equation 7.23** 
$$\varepsilon_T = S_T \alpha_{Th} \Delta T$$

where  $\Delta T$  is temperature, and  $\alpha_{Th}$  is a matrix of coefficients of thermal expansion, and  $S_T$  is  $[1\ 1\ 1\ 0\ 0\ 0]^T$ . For an isotropic material,  $\alpha_{Th}$  is constant. It should also be noted that thermal strain related does not result in elastic stress but a change in the size of the material.

For the simulations performed in this chapter, the model had no external applied force nor were the materials pre-stressed. Thus, the initial strain was zero. However, an adhesive constraint on the bottom surface of the model was applied that required the displacement vector at this surface to be zero throughout the simulation. Therefore, if the material is subjected to a change in temperature, the elastic strain,  $\varepsilon_E$ , at the bottom surface is equal to the opposite of the thermal strain,  $\varepsilon_T$ .

### 7.3 FEM IMPLEMENTATION

Solid models developed using Pro/E<sup>®</sup>, a commercially available computer aided design (CAD) package, were analyzed using FEM techniques in Pro/E Mechanical<sup>®</sup>. The isotropic densification of the etch barrier was simulated using psuedo-coefficients of thermal expansion (CTE). The percent volumetric shrinkage of the etch barrier was divided by 1°C. This results in units of CTE. A model was defined and assigned physical properties ( $E$ ,  $\nu$ ,  $CTE$ ). Reference points placed in the model were used to monitor the film thickness, sidewall angles, and pattern motion.

The temperature was then subjected to a uniform reduction of 1°C, which resulted in the defined isotropic volumetric contraction of the etch barrier. The simulations were solved by minimization of the global strain energy and convergence of local displacements and strain energies at the reference points and boundaries. All simulations converged to less than 5% and in general less than 1% for all reference points and strain energy.

## **7.4 RESULTS**

### **7.4.1 Free-standing and Constrained Film Simulation**

In order to validate the accuracy of the FEM analysis on thin structures, a simple model of a 1 cm diameter, 12.7  $\mu\text{m}$  thick free-standing film was densified 27.1% (10% linearly in each direction). A tensile modulus of 1.6 MPa and a Poisson's ratio of 0.3 were applied to the model. Two reference points were placed in the center of opposing surfaces of the film used to monitor the relative displacement of the two surfaces.

A second simulation was performed on the film in which the sides of the film and the bottom surface of the film were fixed. This replicates the conditions of a thin film resting on a silicon substrate and confined within the borders of a 12.7  $\mu\text{m}$  thick, high-modulus film. Again, two points at the center on opposing sides of the film were used to measure the displacement.

Figure 3 shows the thickness of a 12.7  $\mu\text{m}$  freestanding film and a 12.7  $\mu\text{m}$  film constrained on its edges and bottom surface as a function of densification. The change in thickness of the unconstrained film experiencing 27.1% volumetric contraction (10% linear shrinkage) is 1.27  $\mu\text{m}$  or 10% of the

original thickness; while that of the constrained film is 2.36  $\mu\text{m}$  or 18.6% of the original thickness. Therefore, the simulation accurately predicted the film thickness change of a freestanding thin film and it indicates that the presence of the rigid constraint such as a substrate dramatically affects the deformation of the cured film.

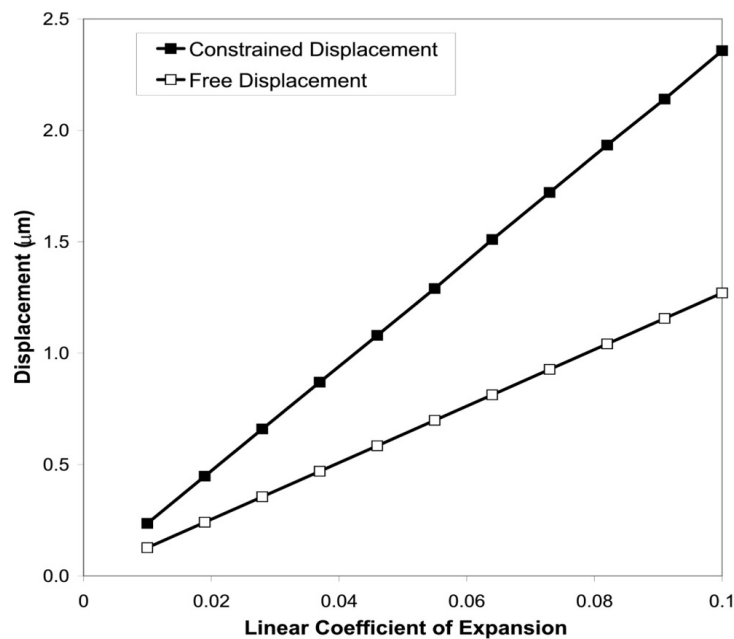


Figure 7.2. Calculated relative displacement of two points on opposing surfaces of a constrained film (■) and a free film (□).

#### 7.4.2 Preliminary Patterned Film Simulation

Preliminary simulations were performed on isolated lines, gratings, and L-structures that are representative of structures used in the semiconductor industry (see Figure 7.3). In all three simulations, the structure was composed of a rigid

substrate (silicon), a high-modulus polymer (transfer layer), and a low-modulus polymer (etch barrier). The thickness of the transfer layer was 1000 nm. The base layer was 100 nm thick. The feature height was initially 200nm. The silicon substrate was modeled as a rigid substrate since the modulus of silicon is 115 GPa which is 5 orders of magnitude greater than the etch barrier. The transfer layer was modeled with a 1 GPa modulus, similar to PMMA and a Poisson's ratio of 0.3. These structures were densified 27.1% (or 10% linearly) using a psuedo-coefficient of thermal expansion. This simulation is an estimate a worst-case densification scenario. The displacement magnitude and strain energy of the densified structures were characterized by cross-sectional analysis of the features.

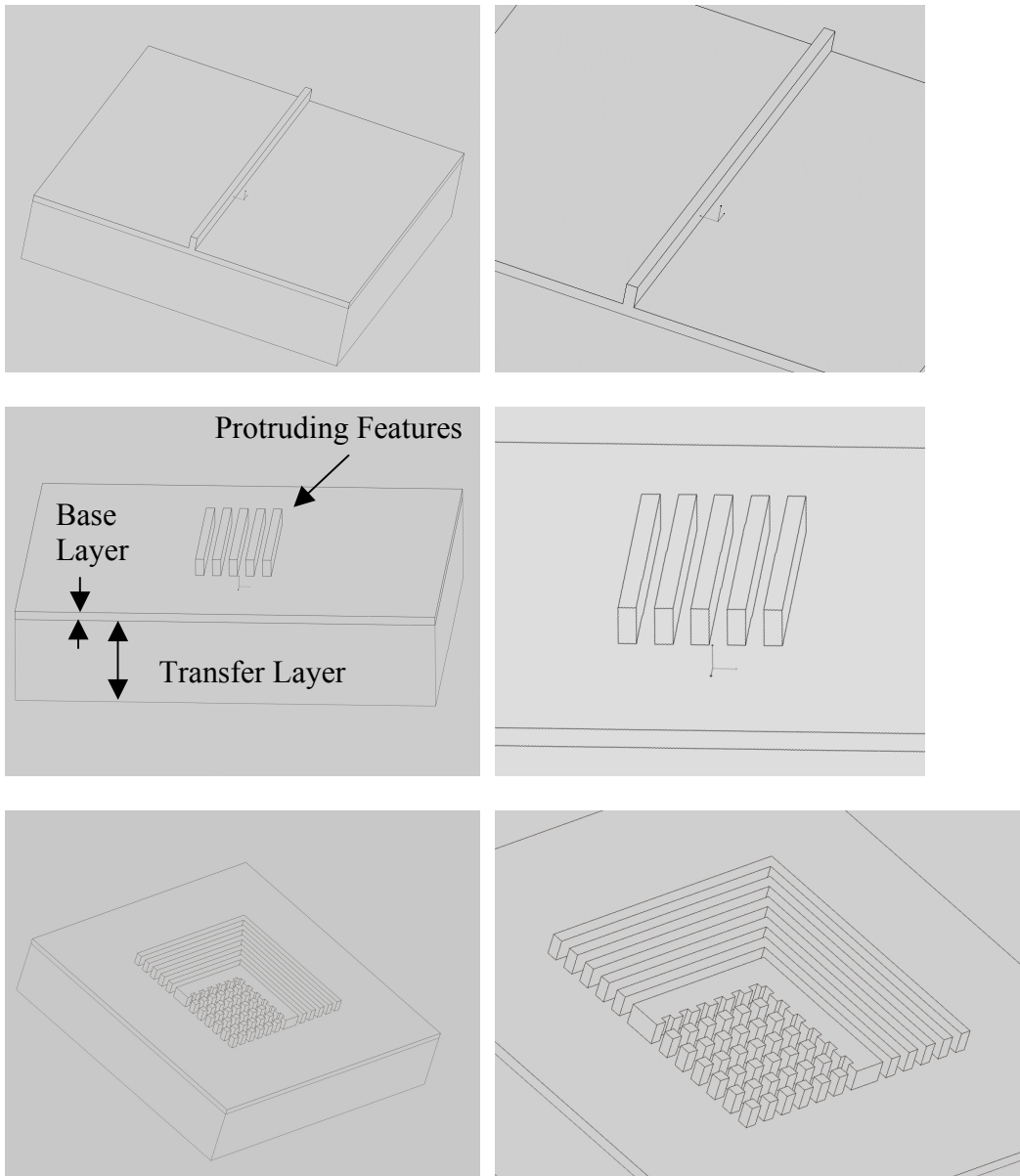


Figure 7.3. Pro/E models of 200 nm tall wide isolated lines, gratings, and L-structures on 100 nm thick base layer and 1000 nm thick transfer layer. The images on the right are enlargements of the patterned region of interest.

An isolated 100 nm wide, 200 nm tall feature on a 100 nm thick base layer is shown in Figure 7.4. Qualitatively, the feature cross-section narrowed at the top and the top of the line ends were pulling back toward the center of the feature. The base layer displacement was uniform in the planes parallel to the transfer layer surface indicating that most shrinkage is independent of the position across the surface of the transfer layer. Quantitatively, the displacement at the top of the feature shrank 47-50 nm with the feature ends displacing 53.6 nm.

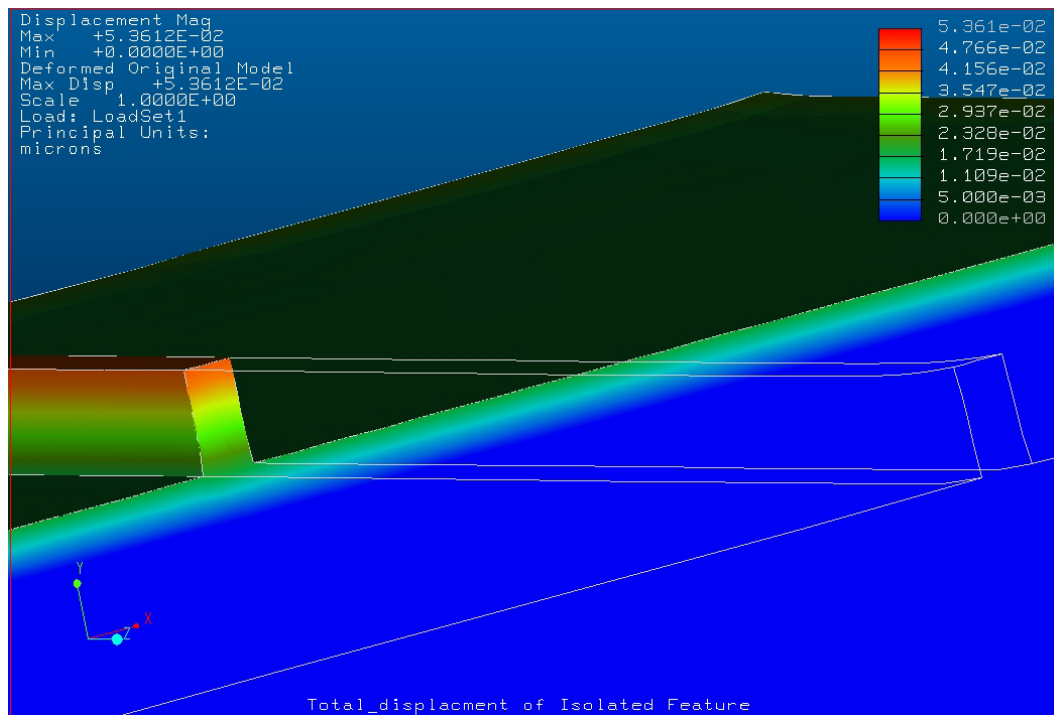


Figure 7.4. Cross-section of an isolated line with color indicating the total displacement resulting from a 27.1% volumetric shrinkage (10% linear shrinkage) on a constrained film. The total displacement magnitude is displayed in microns.

As with the 100 nm-isolated lines, the 200 nm tall, 200 nm pitch grating exhibited some line end pull back as shown in the bottom image of Figure 7.5. The top image is a cross-section of the grating that indicates nearly uniform vertical shrinkage across the base layer and a slight narrowing of the features at the top of relief. The base layer shrank ~20 nm in the vertical direction and was uniform across the plane of the surface, which indicates that only vertical shrinkage is experienced. The vertical component of the displacement is shown below in Figure 7.6. The transfer layer experienced no displacements and is represented in blue in Figure 7.4 and red in Figure 7.5. The side of the protruding features in Figure 7.5 shows that the top of the features shrank 46 nm (15.5%) vertically and that this shrinkage was nearly uniform along  $\frac{3}{4}$  of the feature length. A maximum displacement of 50 nm occurred at the top of the line ends as they pulled back toward the middle of the line, which shrank vertically 46 nm.

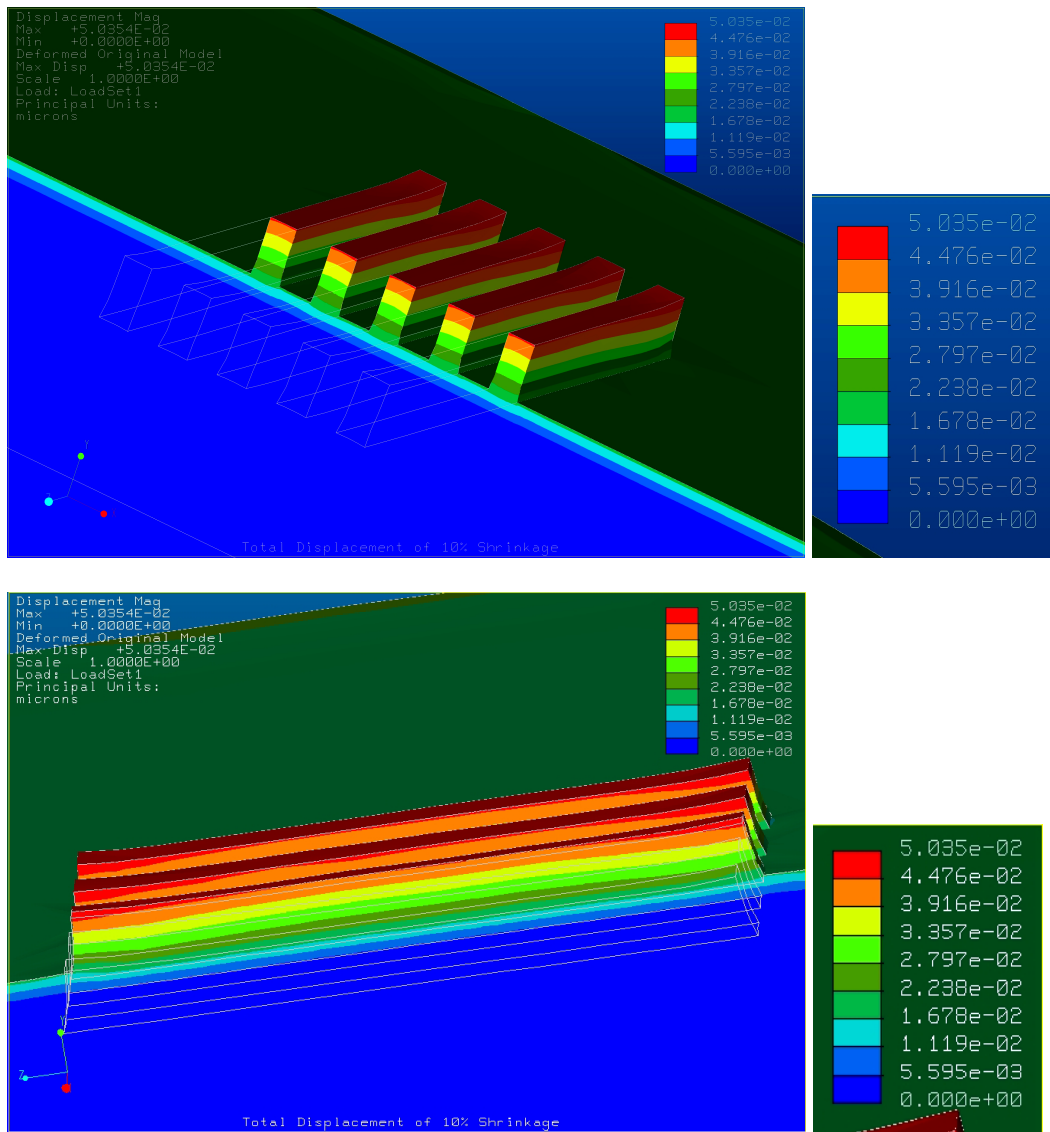


Figure 7.5. 200 nm tall equal line-space grating on a 200 nm pitch. 27.1 % volumetric shrinkage. The top is an X-Y plane cross section. The bottom is an X-Z plane cross section. The total displacement magnitude is displayed in microns.

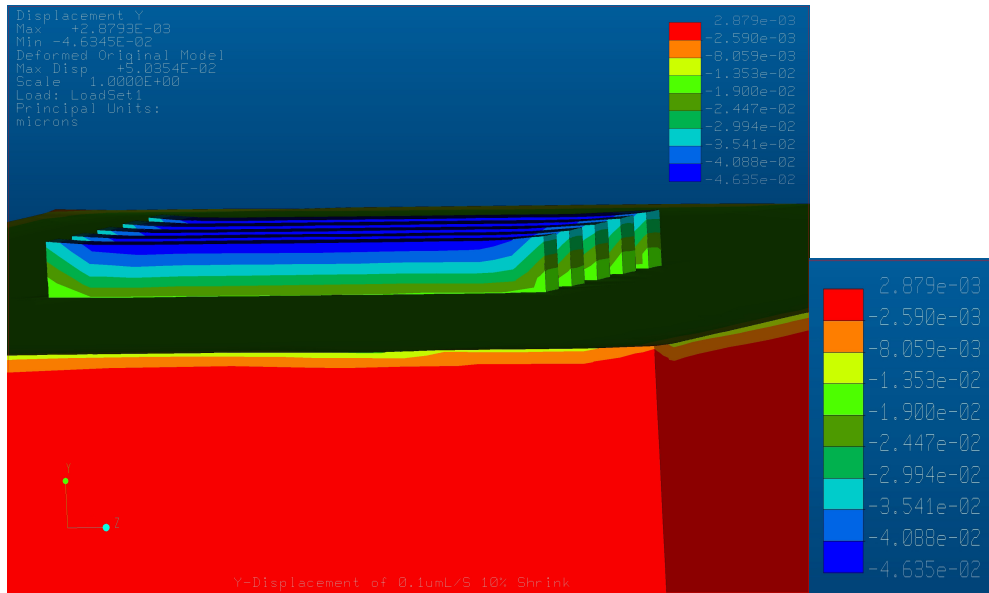


Figure 7.6. The vertical component of the displacement for a grating densified by 27.1% (v/v) in its undeformed state. The vertical displacement is displayed in microns.

The etch barrier in the *L*-structure was densified 27.1% and evaluated in cross-section (see Figure 7.7). Several observations can be made from this cross-section. The base layer shrank ~20 nm vertically and is uniform in the plane of the surface. The transfer layer again was unaffected by the densification of the low modulus etch barrier and is represented by the bright blue volume that has zero displacement. Also, the vertex of the *L*-structure appears to have pulled inward toward the central *L*. The maximum displacement (57.7 nm) was at the top of the vertex of the *L*. The vertical shrinkage is evaluated in more detail in Figure 7.8. The maximum vertical displacement was 51.3 nm for the *L*-lines but the narrow pillars only shrank approximately 40 nm.

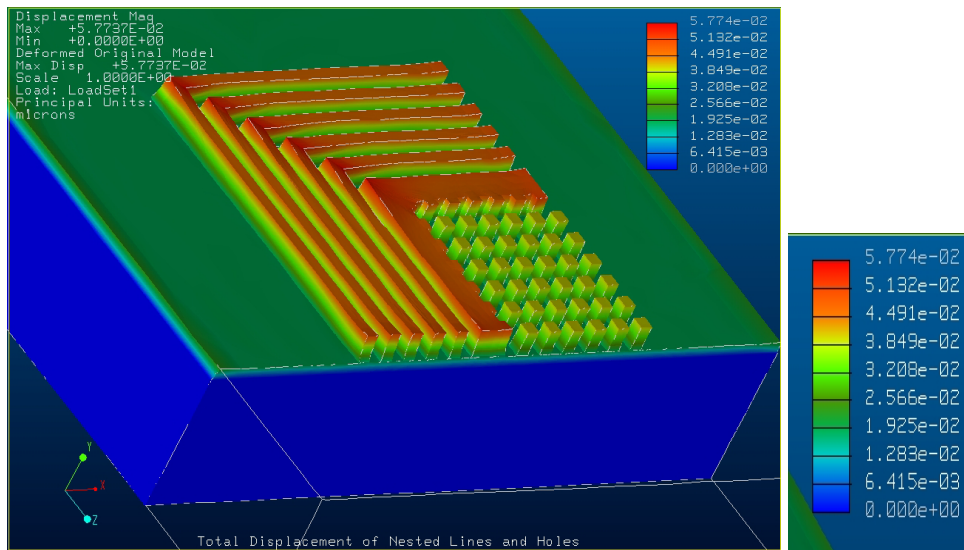


Figure 7.7. Isometric view of L-structures shown in their deformed state after 27.1% (v/v) shrinkage. Note the slope at the corners of the "L" features. The total displacement magnitude is displayed in microns.

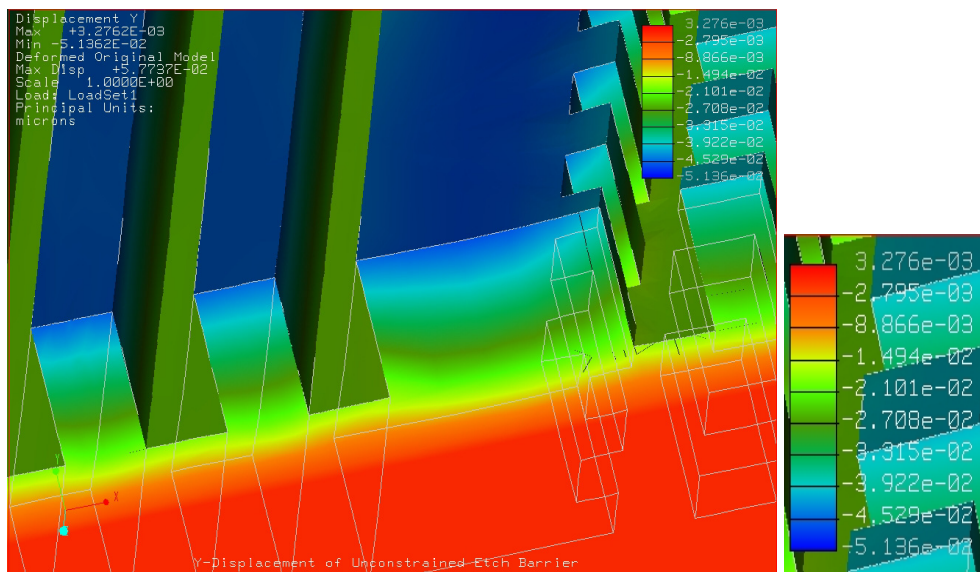


Figure 7.8. Cross-section of the vertical component of the displacement for L-structure with 100 nm square pillars (shown in the undeformed state). The vertical displacement is displayed in microns.

### 7.4.3 Pattern placement study

The pattern placement study was performed on the pattern shown in top down view in Figure 7.9. In the reference state, the features were 200 nm tall. The lines and boxes were separated by 100 nm. The boxes were 2  $\mu\text{m}$  by 2  $\mu\text{m}$  squares. The length of the central line that runs along the boxes was 7.6 microns long. The line that is perpendicular to the central line was 2.5  $\mu\text{m}$  long. The base layer was 100 nm thick and rigid boundary condition fixed the bottom of the base layer. The top of the etch barrier was free. The modulus of the etch barrier was 1.6 MPa, representative of a low Tg polymer [5], and the Poisson's ratio was estimated at 0.3 since the Poisson's ratio for most polymers range from 0.25 to 0.44 [5]. The etch barrier densification was 10% (v/v). The motion of the 7.6  $\mu\text{m}$  long centerline was analyzed at the base of the features for displacement motion in-plane with the substrate. This "in-plane" displacement magnitude was defined as shown below:

**Equation 7.24** 
$$D_{in-plane} = \sqrt{\delta_x^2 + \delta_y^2}$$

where  $\delta_x$  and  $\delta_y$  are orthogonal displacement vectors parallel to the substrate surface.

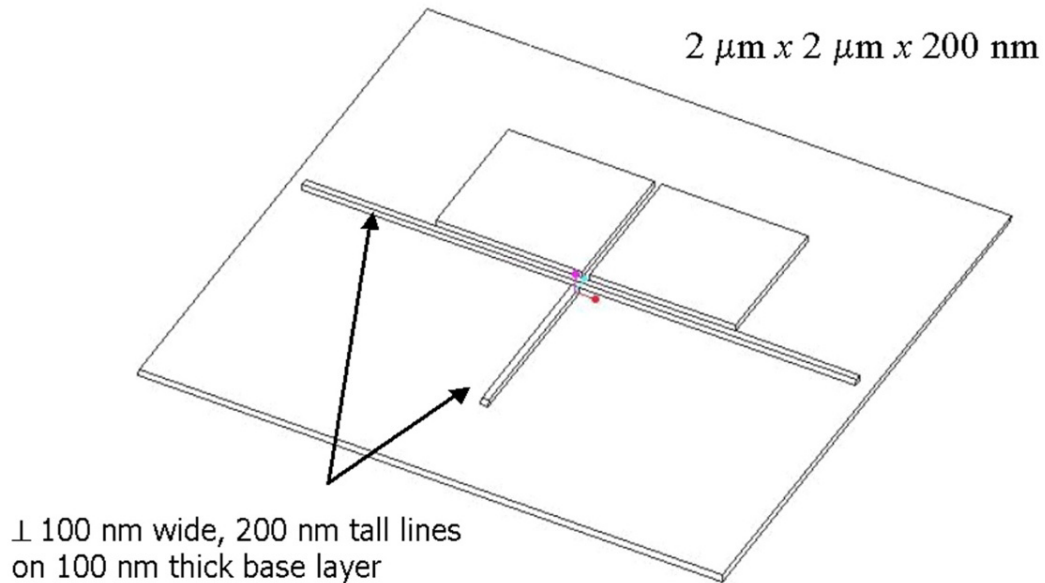


Figure 7.9. Pattern placement model.

The asymmetric pattern simulation was performed to assess whether catastrophic errors in pattern placement would result from the densification of the etch barrier. A color-coded image of the pattern motion resulting from densification is shown in Figure 7.10. The key point of interest is the pattern placement of the centerline as it runs along the asymmetric pattern. The displacement of the line in the plane of the surface was found to be less than 1nm from its original position. An independent simulation using COSMOS<sup>®</sup> corroborated this result. Neither computation predicts a local pattern density effect for the SFIL process.

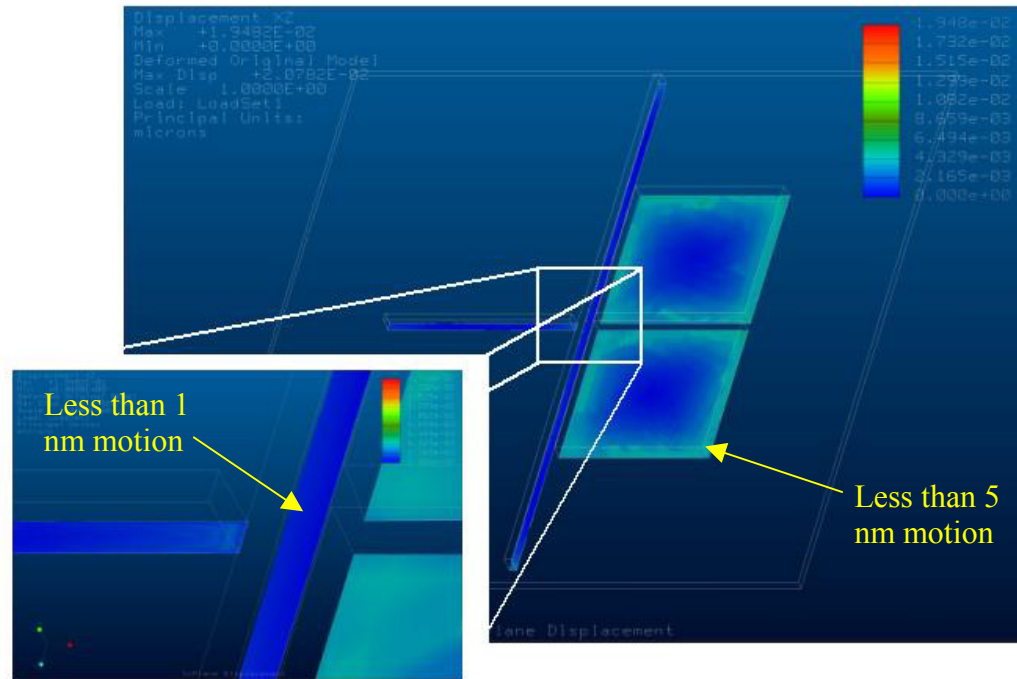


Figure 7.10. In-plane pattern motion measured just above the base layer predicts less than 1 nm displacement for the 100 nm wide line running parallel to the edge of the two  $\mu\text{m} \times 2 \mu\text{m}$  square features (color scale units are in  $\mu\text{m}$ ).

#### 7.4.4 Effect of Densification on Feature Geometry

Subsequent simulations explored the interaction of changes in density, aspect ratio, Poisson's ratio and elastic modulus on the geometry of features. The model system is shown in Figure 7.11. A rigid bottom surface was used to simulate a transfer layer with a modulus much greater than that of the etch barrier. The reference points are labeled *A* through *G*. The displacements of these points were used to calculate the changes in the length, height, and sidewall angle. The sidewall angles were determined as the dot product of the vectors defined by the

lines  $AE$  and  $AB$ , and lines  $AE$  and  $DE$ . A symmetric boundary condition was placed through the center of model, half way along the length of the features.

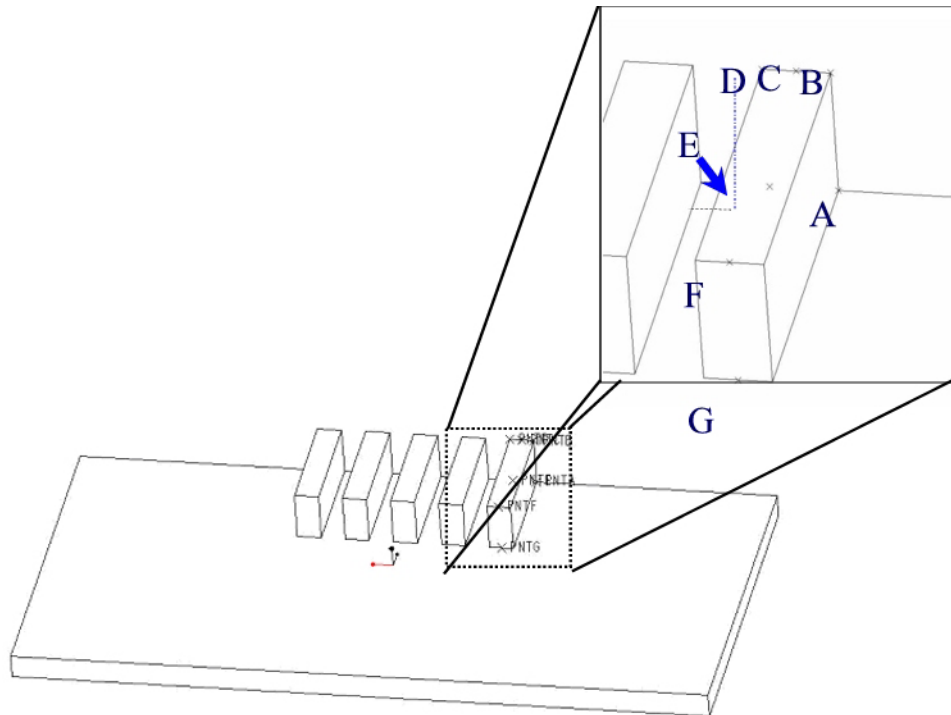


Figure 7.11. Parametric model used for densification simulations.

The simulations were performed using a full factorial design of experiment on 200 nm tall feature with line widths of 100 nm, 500 nm, 1  $\mu\text{m}$ , and 10  $\mu\text{m}$ , densifications of 3%, 6.0%, 11.5%, and 17%. The features had a length to width ratio of 10 and a 1:1 pitch (line width: line space) except for the 10  $\mu\text{m}$  features which had a length to width ratio of 1:1. The base layer was 100 nm. The elastic modulus and Poisson's ratio were 1 MPa and 0.5; respectively. In addition to the above simulations, Poisson's ratios of 0.3 and 0.4 were applied to models with densification of 6.0% and 11.5% and line widths of 100 nm, 500 nm,

and 1  $\mu\text{m}$  in order to quantify the effect of Poisson's ratio and 200 nm wide lines having a Poisson's ratio of 0.5 were simulated for densifications of 3% and 17%.

#### ***7.4.4.1 Effect of Elastic Modulus of Feature Shape***

A set of simulations was performed on 500 nm wide features, 200 nm tall features on a 100 nm base layer with a Poisson's ratio of 0.5. The modulus ranged from 1 MPa to 1 GPa. The simulations revealed that the tensile modulus of the photopolymerized material does not affect feature shape over the range studied. Densification fixes the strain at the etch barrier-transfer layer interface and Poisson's ratio dictates how the stress is translated in the direction normal to the applied strain. While the modulus may affect the separation process, it does not affect the feature profiles.

#### ***7.4.4.2 Vertical shrinkage***

The vertical shrinkage is an important property to understand. During the reactive ion etch (RIE) process, the height of a photopolymerized feature will limit the aspect ratio of the final transferred feature. Therefore, it must be accounted for in the design criterion of any SFIL template.

The influence of densification and Poisson's ratio on the cross section of features with width ranging from 100 nm to 10  $\mu\text{m}$  in width has been investigated. For the simulations, the vertical shrinkage was measured at the center of the feature (Point C in Figure 7.10) in a dense array. This height was subtracted from the average height of the feature base taken on the left (Point E in Figure 7.10) and right side (Point A in Figure 7.10). The ratio of this height to the original height, 200 nm, is reported in Figure 7.12. The densification of the monomer and

the Poisson's ratio both affect the vertical shrinkage significantly. The maximum vertical shrinkage predicted by the simulation is ~17% for a Poisson's ratio of 0.5 and 17% densification. This maximum occurs in the center of feature that experiences the greatest vertical shrinkage. This point represents the worst-case scenario for the replication process.

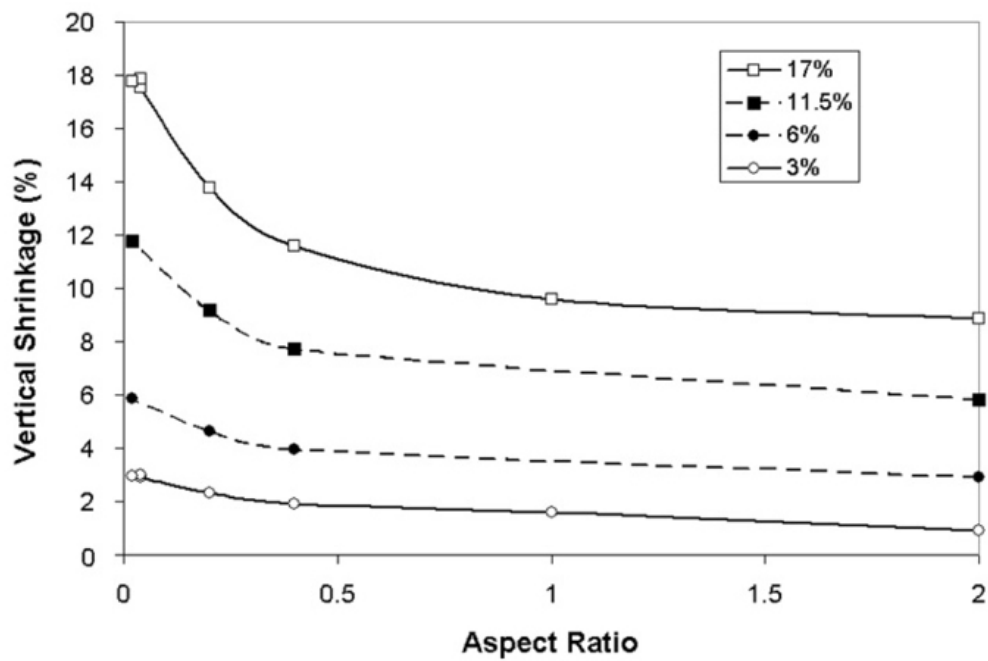


Figure 7.12. Vertical Shrinkage of etch barrier features.

Poisson's ratio translates a tensile stress in one direction into the strain in an orthogonal direction. The Poisson's ratio of typical polymers range from 0.3 to 0.45 so it is important to understand how the Poisson's ratio affects vertical shrinkage given the constraint of adhesive in-plane linkage with the rigid substrate. The ratios of the vertical shrinkage for a Poisson's ratio of 0.3 and 0.4

relative to the vertical shrinkage for a Poisson's ratio of 0.5 were compared as a function of feature aspect ratio and are shown in Figure 7.13. This ratio-aspect ratio curve was found to be independent of densification given a feature aspect ratio. Thus, these curves can be used to extrapolate the vertical shrinkage calculated for a Poisson's ratio of 0.5 to a vertical shrinkage for Poisson's ratios of 0.3 and 0.4.

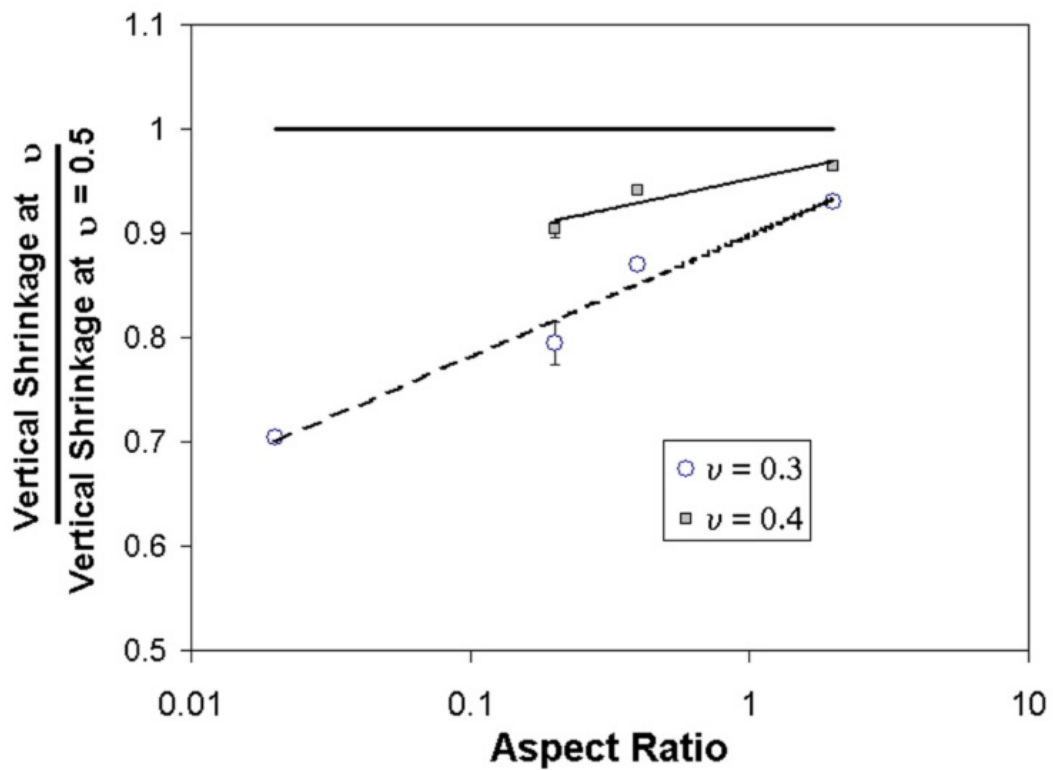


Figure 7.13. The ratio of the vertical shrinkage for a Poisson's ratio of 0.3 and 0.4 relative to the vertical shrinkage for a Poisson's ratio of 0.5 is independent of densification but is aspect ratio dependant.

#### 7.4.4.3 *Line Width Change*

As stated in Chapter 1, the minimization of the line width in MOSFET device and the control of that line width has been the driving force for lithographic research for the past 30 years. If there is any change in line width from the template to the substrate, it must be quantifiable and predictable. These simulations are an effort to defined the template feature-replicated feature bias.

The line width was measured at the top of the feature after densification and compared to the original width. The change in line width predicted by the simulation is shown in Figure 7.14. The plot indicates that densification plays the major role in line width shrinkage. The percent change decreases as features get wider but the absolute amount of line width change increases. In the worst case of densification ( 17% (v/v) ), the actual change in length at the top of the features approaches a limiting value of 80 nm for 200 nm tall features. The percent change in line width at the top of the feature associated with the densification is small; the worst case being 9.1% (or 20 nm of a 200 nm wide feature) for 17% densification and 0.5 Poisson's ratio.

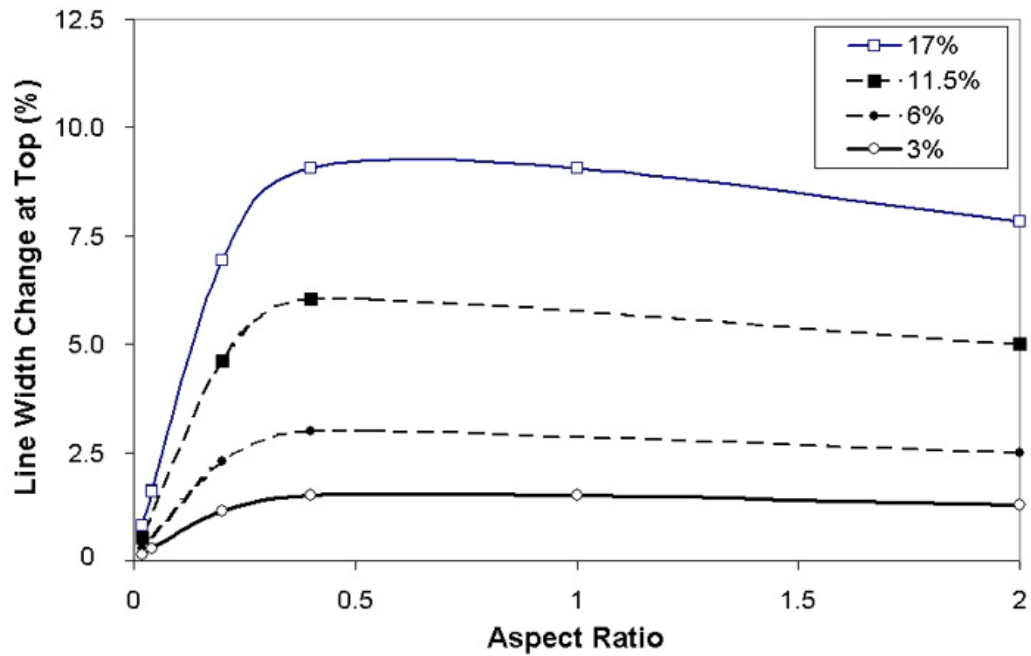


Figure 7.14. Effect of densification on line width at the top of the features.

The computed line width change at the base of the features was less than 2.3% for even the worst case. Figure 7.15 shows the absolute line end shrinkage resulting from densification as function of aspect ratio. The absolute line end motion is less than 20 nm even for 10  $\mu\text{m}$  long features. For materials similar to the etch barrier (1 MPa, 8.9% densification,  $\nu=0.4$ ), the line width change at the base of the feature was less than 0.3%.

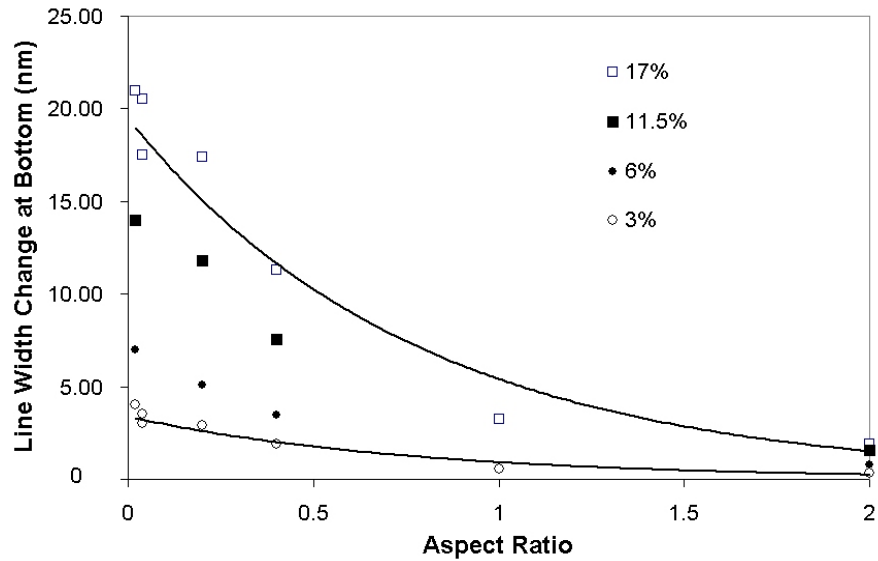


Figure 7.15. Effect of densification on line width at the bottom of the features.

#### 7.4.4.4 Sidewall Angle

The convolution of line width change and vertical shrinkage manifests itself in sidewall angle changes. While the amount of vertical shrinkage and line width change are important to characterize, sidewall angle will dictate how successful the RIE transfer will be. For a high volume manufacturing process, the sidewall angles should be no less than  $80^\circ$  and preferably as close to  $90^\circ$  as possible.

Analysis of the calculated sidewall angle data revealed dependence on aspect ratio. Figure 7.16 shows that the sidewall angle is closer to  $90^\circ$  for smaller features than for larger features and that the sidewall angle approaches  $80^\circ$  for small aspect ratio features with 17% densification and Poisson's ratio of 0.5. The line end angle was also studied as a function of aspect ratio; it follows a trend

similar to that of sidewall to aspect ratio. As the aspect ratio becomes small, the sidewall angle and line end angle both decrease approach the same value.

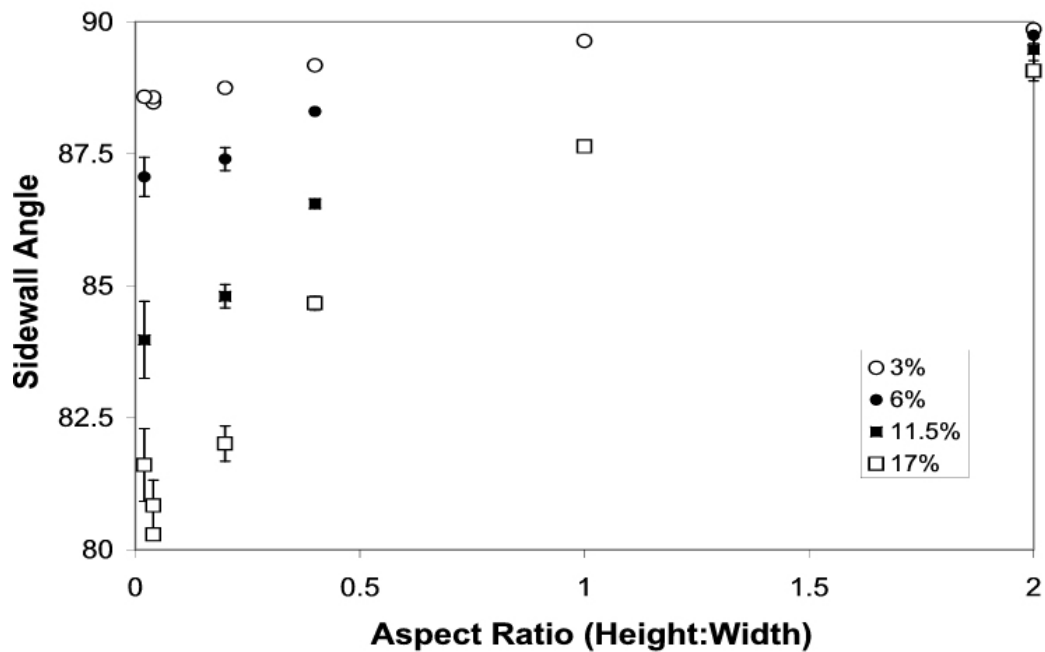


Figure 7.16. Effect of densification and Poisson’s ratio on sidewall angle.

#### 7.4.4.5 Line End Pullback

Since the preliminary simulations insinuate that the line end is susceptible to line end pull back, it is important to relate the template line length to the printed line length for reasons of process control and proper template design. The line end motion was quantified at the top and bottom of the features and is presented in Figure 7.17. Both the top and the bottom of the structures experience some line pullback. However, the maximum pullback for the top of the feature is 4.16% while the maximum pullback for the bottom of the feature is

0.94%; both for features with 17% shrinkage and an aspect ratio of 2. For materials that densify between 6% and 11.5%, the top and bottom shrinkage is approximately 1.4% to 2.8% and 0.18% and 0.37%, respectively. The effect of line end shrinkage is linearly related to the aspect ratio of the features for a given level of volumetric shrinkage and becomes negligible as the aspect ratio of the line becomes small. The maximum line end pull back at the top of the feature was 7.1 nm for a densification of 17% and line length of 10  $\mu\text{m}$ .

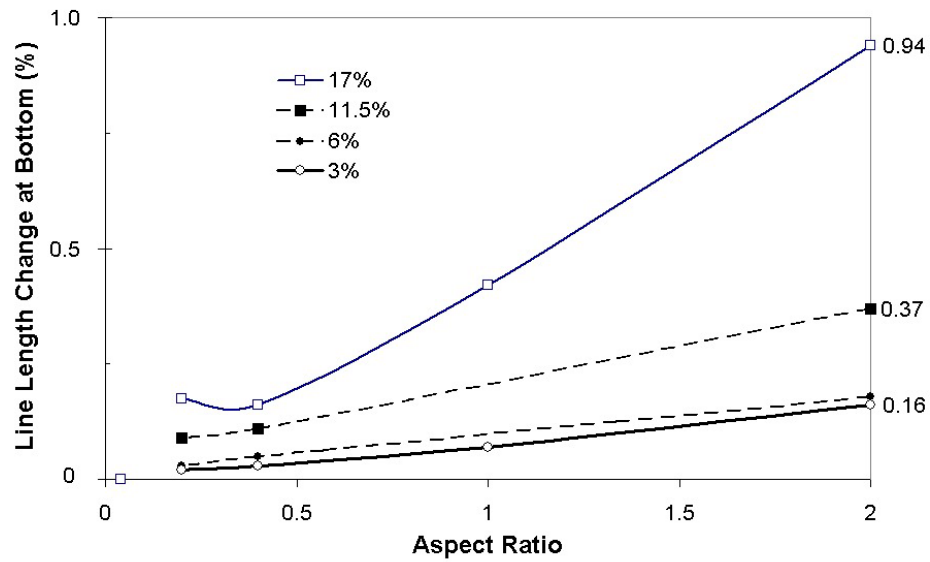
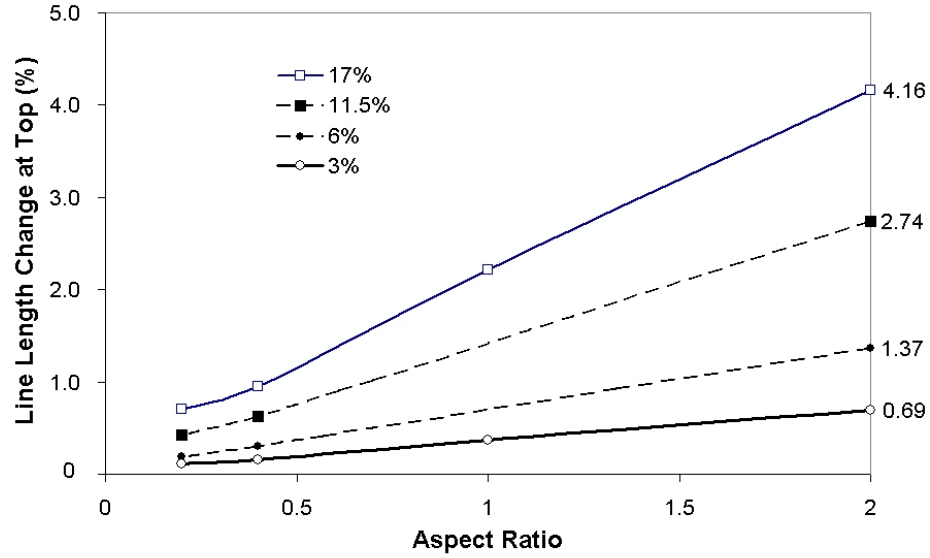


Figure 7.17. (Top) Top length shrinkage of etch barrier features as a function of aspect ratio and volumetric shrinkage. (Bottom) Top length shrinkage of etch barrier features as a function of aspect ratio, and volumetric shrinkage.

#### 7.4.5 Line Width Evaluation by SEM

The line widths of resist features are more easily characterized than line lengths or sidewall angles. Line lengths are too long to measure with the resolution necessary to identify small length changes. The sidewalls of the replicated features are too short to allow accurate measure angle for these features. Line width, however, can be measured with a degree of accuracy that provides some insight into the validity of the simulations. Using the oblique scanning mode on a Hitachi 4500 FESEM, the amplitude of the signal was overlaid the SEM image. The line widths were estimated using peak-to-peak measurements of these amplitudes for both replicated features and the template that generated them. Three measurements were taken peak-to-peak, middle-to-middle, and trough edge-to-trough edge (see Figure 7.18). A plot of the results is shown in Figure 7.19. The error bars represent  $1\sigma$ . Within experimental error, the template width and replicated widths are statistically identical. Qualitatively, these measurements do not contradict the simulation results since the measured line widths were less than the template widths. However, a more detailed experimental analysis is necessary to make any quantitative arguments.

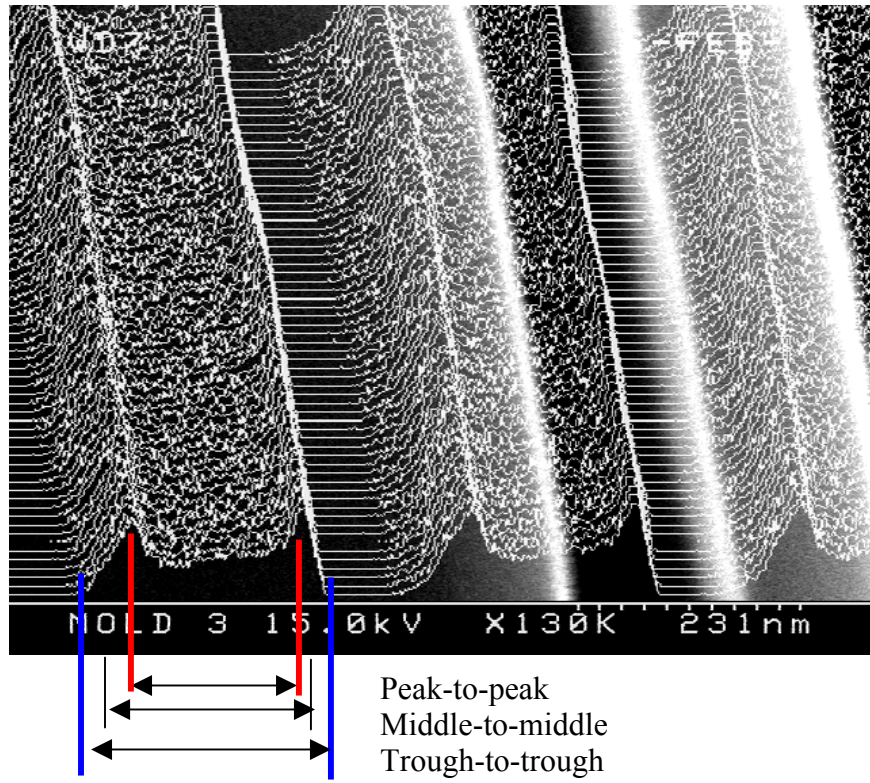


Figure 7.18. Top-down SEM of line width measured using oblique overlay to determine line edge position.

### Top-Down SEM Characterization of Line Width

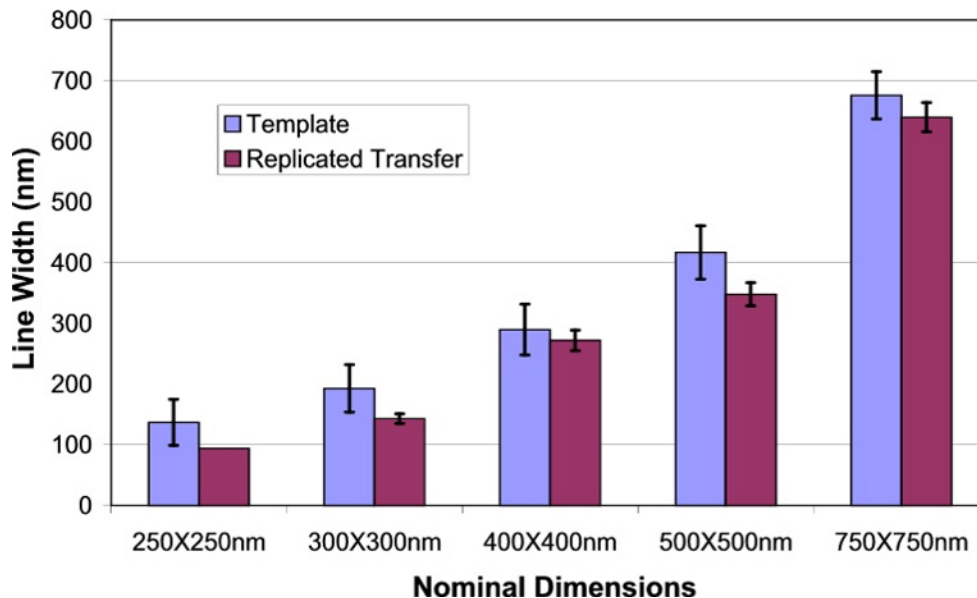


Figure 7.19. Line width measured by SEM for the template and the replicated features.

### 7.5 CONCLUSIONS

FEM has been proven to be a useful tool for analyzing the effects of densification on the SFIL replication process. Preliminary simulations provided the necessary incentive for continued analysis and provided a worst-case estimate of the effect that densification will have on 100 nm features in isolated lines, gratings, and *L*-structures. Detailed FEM analysis predicts that pattern placement will not be a problem for the current etch barrier formulation and that densification will manifest itself mainly in the direction normal to the substrate surface. Line width change is a small percentage of the original line width. Sidewall angle is aspect ratio and material property dependent. The effect of

densification will be most prominent in isolated trenches. The sidewall angle for the 10  $\mu\text{m}$  feature is greater than  $80^\circ$  for densification less than 17% and greater than  $85^\circ$  for densification less than 6.0%. These are reasonable profiles that allow etch transfer into the transfer layer with minimal bias. These simulations provide a good estimate of the effect that etch barrier properties have on the template-replica bias.

## **7.6 FUTURE WORK**

Future work should continue with FEM simulations of “L” structures such as those shown in Figure 7.3 with focus on the pattern placement at the vertex of the *L*-structure. A more advanced Pro/E solid model has been developed for this particular structure that includes a symmetry boundary condition along the diagonal to reduce computational time and reference points to measure distances and angles. Further, evaluation of strain energy resulting from densification could be performed to provide information on logical locations where crack propagation or delamination may originate. Ultimately, the modeling work must be compared to experiment and my colleagues will continue to work toward this goal.

References:

---

- 1 Colburn, M.; S. Johnson, M. Stewart, S. Damle, B. J. Jin, T. Bailey, M. Wedlake, T. Michaelson, S.V. Sreenivasan, J. Ekerdt, C.G. Willson; "Step and Flash Imprint Lithography: An alternative approach to high resolution patterning." *Proc. SPIE*. 3676, 379-389 (1999)
- 2 Colburn, M.; A. Grot, M. Amistoso, B.J. Choi, T. Bailey, J. G. Ekerdt S.V. Sreenivasan, J. Hollenhorst, C. G. Willson;"Step and Flash Imprint Lithography for sub-100nm Patterning." *Proc. SPIE*, 3676, 379-389 (2000)
- 3 Patel, S. Structural Mechanics with Introductions to Elasticity and Plasticity, McGraw, NY (1970)
- 4 Gupta, K.K.; J.L. Meek. Finite Element Multidisciplinary Analysis, American Institute of Aeronautics and Astronautics, Reston, VA (2000)
- 5 van Krevelen, D.W.; Properties of Polymers, 3<sup>rd</sup>, Elsevier, NY (1990)

## 8 Reactive Ion Etching

Wet chemical, reactive ion, and chemically-assisted ion beam are three variations of etching are utilized in the semiconductor manufacturing [1]. The depth, size, and shape of the desired feature dictates the type of etch to be used. Each method utilizes different chemistries, different mechanisms and different equipment that characterized by their selectivity and anisotropy that are defined in Equation 8.1 and Equation 8.2.

$$\text{Equation 8.1.} \quad \textit{Selectivity} = \frac{\textit{Etch Rate of Material 1}}{\textit{Etch Rate of Material 2}}$$

$$\text{Equation 8.2} \quad \textit{Anisotropy} = \frac{\textit{Vertical Etch Rate}}{\textit{Horizontal Etch Rate}}$$

If the etch preferentially removed one material over another it is highly selective and if the etch progresses in a preferred direction, which is usually parallel to an applied field, it is highly anisotropic.

Wet chemical etches are typically very selective but are isotropic. Ion milling is physical process with exceptional anisotropy but no selectivity [2]. RIE utilizes both physical sputtering and chemical reaction to etch a material. Physical sputtering of a surface is highly anisotropic but lacks selectivity while chemical reactions tend to be extremely selectivity but are isotropic. Combined they can offer a balance of selectivity and anisotropy.

## **8.1 BACKGROUND**

Reactive ion etching is a process in which a gas is dissociated by a glow discharge or plasma into reactive species that react with a substrate to form volatile products; effectively etching the surface of the substrate [1]. By definition, a plasma is a volume of electrically charged (ions) and neutral (free radicals) species that has no net charge. The mechanism of plasma generation and a simplified view of plasma chemistry can be understood using a capacitively coupled parallel plate etcher as an example.

### **8.1.1 Parallel-plate Capacitively Coupled Etcher.**

A schematic of a conventional parallel-plate capacitively-coupled etcher is shown in Figure 8.1. It consists of a driven lower electrode that serves as a substrate holder, an grounded upper electrode, a grounded chamber, a vacuum source, and process gas delivery port. The voltage on the lower electrode is driven by an AC power source modulated at 13.56 MHz (RF frequency) and referenced to ground. The blocking capacitor prevents current from flowing to ground through the driven electrode and large electrical discharges from being conducted across the electrode gap. When the RF power is applied, the plasma forms between the two electrodes and electrically charged regions called sheath forms between the plasma and the electrodes.

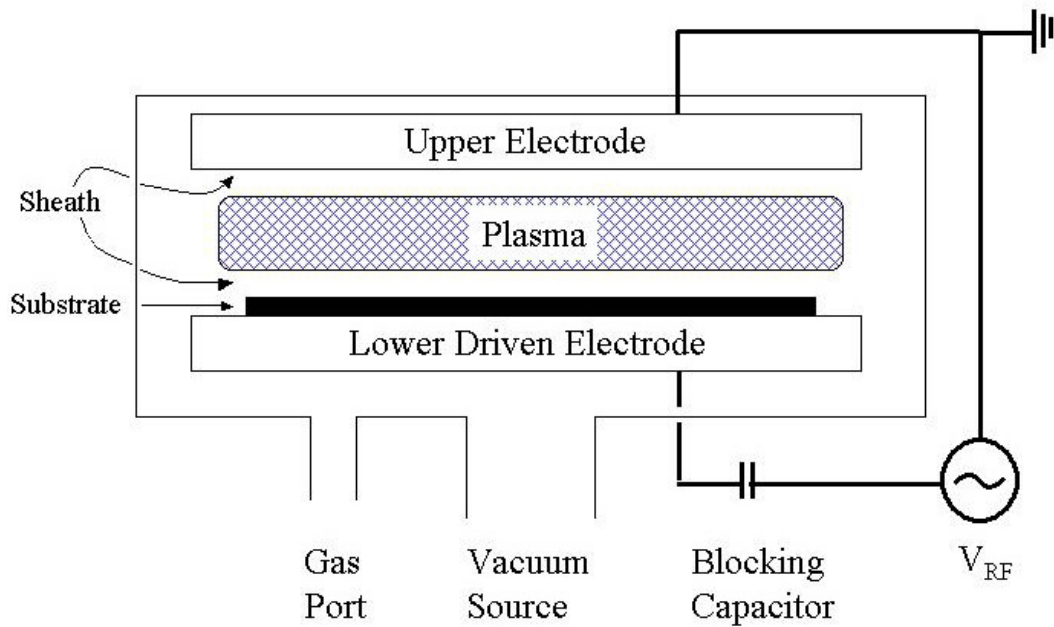


Figure 8.1. Parallel plate capacitively coupled etcher.

Prior to generating a plasma, the potential at the electrodes is zero since the upper electrode is grounded and the lower electrode has no average potential or dc-bias applied to it. Once the RF potential,  $V_{RF}$ , is applied, the gas dissociates into electrons, ions, and free radicals. The potential causes the electrons to flow toward the positive potential on the electrode which causes a deficiency of electrons in the sheath and generates a positive potential relative to ground in the plasma that serves to inhibit further electron current. The charged ions then migrate to the surface of the electrode. An equilibrium plasma potential,  $V_p$ , is established when the electron current and ion current are equal. The plasma potential is always positive since the mobility of electrons is greater than the

mobility of ions and allows for excess ions in the sheath regions over the course of an RF cycle.

As the RF potential is modulated, the plasma potential also oscillates since the electrons high mobility allows them to respond to high frequency RF signal. The ratio between the RF potential and the plasma potential is approximated by the following relationship [1]:

**Equation 8.3**

$$\frac{V_p}{V_{RF}} \cong \frac{A_D}{(A_D + A_G)}$$

where  $A_G$  is the area of the grounded electrode, and  $A_D$  is the area of the driven electrode. For a symmetric etcher with two equal sized electrodes,  $V_p$  is will be approximately half the  $V_{RF}$ , For an asymmetrical etcher with a large grounded electrode,  $V_p$  is much less than  $V_{RF}$ . Most RIE systems are asymmetric since more surfaces are grounded than driven.

Since no DC current is allowed to flow through the blocking capacitor, the electrons build up a negative charge on the blocking capacitor over a RF cycle, which creates a DC self-bias,  $V_{DC}$ , on the driven electrode. No bias develops on the grounded electrode since electrons are allowed to flow to the ground. Since the self-bias is always negative and the mobility of the ions only allow them to respond to time-averaged potentials, the self-bias affects the energy with which ions arrive at the surface of the driven electrode and thus the substrate. The potential across the electrodes is represented schematically in Figure 8.2 where  $V_p$ ,  $V_{DC}$ , and  $V_{RF}$  are referenced. The energy that ion impact the surface of the driven electrode is  $e(V_p+V_{DC})$  but is  $eV_p$  for the grounded electrode [3]. High-

energy ions bombard the surface causing physical sputtering of the surface, a decrease in selectivity, and an increase in anisotropy.

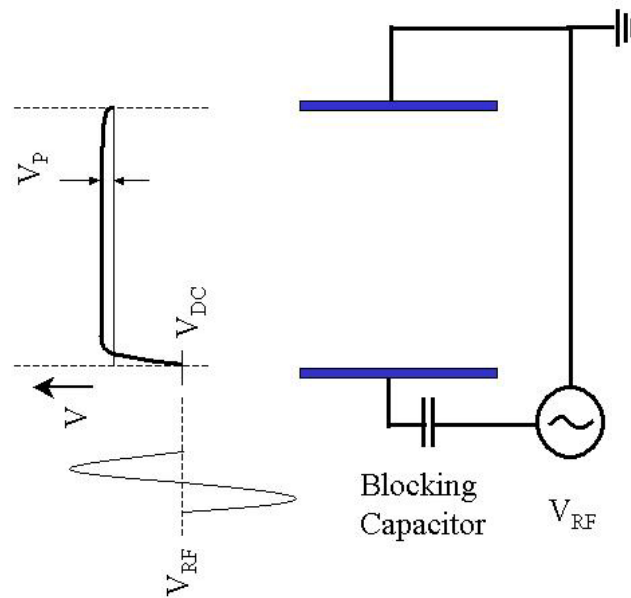
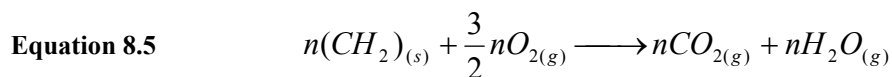


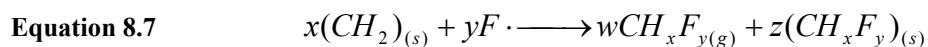
Figure 8.2. Time-averaged potential across the electrode gap with an applied RF voltage ( $V_{RF}$ ).

As stated above, the glow discharge forms charged species and neutral species. These species are accelerated toward the driven electrode to etch the substrate. There is always some degree of physical sputtering with RIE but the surface reactions of the radicals and ions play an important role in generating selectivity. In SFIL, both the break through etch and the amplification etch rely on RIE to pattern the underlying layer in an anisotropic and selective manner. The etch selectivity of the etch barrier during the amplification RIE is crucial to transferring a low aspect-ratio replica in the etch barrier through the transfer layer to the substrate. This is the defining characteristic of the Step and Flash process.

Both oxygen and halogen etch chemistries used in SFIL have been studied extensively [3]. For example, in the oxygen RIE, there are well over 54 second- and third-order reactions between electrons,  $O_2$ ,  $O_2^+$ ,  $O^-$ , and  $O_3$  [3] in the plasma alone. Additionally, surface reactions resulting from *chem*-absorption and *phys*-adsorption affect the etch rates. The source of the etch barrier's etch resistance during  $O_2$  RIE is the volatility of the organic transfer layer and the involatility of the silylated etch barrier during  $O_2$  RIE shown in Equation 8.4 and Equation 8.5. As a result the etch barrier acts as a mask to transfer the template's relief structure into the transfer layer.



During the halogen break-through etch, the feed gas decomposes into Fluorine radicals that react with the silicon in the etch barrier forming volatile fluorosilanes (Equation 8.6). Anisotropy of this etch is augmented by the redeposition of poly( $CH_yF_x$ ) films that passivate the sidewalls of the etch barrier features (Equation 8.7).



Since the etch barrier is an organosilicon solution, the etch barrier is susceptible to both the  $O_2$  RIE and halogen RIE. As a result it is critical that we understand the effect of silicon content on the etch rate and etch selectivity during both  $O_2$  etch and halogen etch relative to the transfer layer.

Since RIE is a chemical and physical process there are a wide variety of tunable parameters. As shown above, the most important parameter is the etch chemistry. Without the proper chemistry, a lack of selectivity may make the pattern transfer impossible. Once a proper chemistry is selected, parameters such as substrate temperature, pressure, flow rates, and concentration of species affect the etch rate and the selectivity [3]. The RF power, the electrode area, the electrode gap, and the applied DC-bias all affect the potential to which the plasma is subject and consequently the RIE characteristics. While some of the variables are fixed for a given equipment set, the number of variables can be overwhelming. For parallel-plate capacitively-coupled etchers discussed in the following chapters, only pressure, RF power, process gases, and gas flow rates were controllable.

## **8.2 EQUIPMENT**

### **8.2.1 Reactive Ion Etcher at Agilent Laboratories**

A Materials Research Corporation (MRC) parallel-plate capacitively-coupled RF reactive ion etcher with a 15.24 cm diameter grounded electrode, 15.24 cm driven lower electrode, and a 5.08 cm electrode gap was used for all of the etch work performed at Agilent Technologies (formerly Hewlett Packard Laboratories). Trifluoromethane, oxygen, argon, and helium were plumbed to the etcher. Mass flow controllers and pressure controller were set manually but controlled automatically. All valves were manually operated. The RF power was

tuned manually to maximize the power transferred from the source to the plasma.

The substrate rested on a 0.635 cm thick, 15.24 cm diameter quartz plate.

The etch rates were measured using *in situ* HeNe interferometry and were validated by both pre-etch and post-etch two-angle ellipsometry and profilometry measurements. Film thickness changes were estimated using wave theory which states that the intensity of the reflection,  $R$ , off a thin film can be modeled as [4]:

**Equation 8.8** 
$$R \propto \cos(4\pi nD / \lambda)$$

where  $\lambda$  is the wavelength of the normal incident probe light,  $n$  is the index of refraction of the material at  $\lambda$ , and  $D$  is the film thickness. Further the thickness change from the reflection maximum and minimum,  $\Delta T$ , can be described by:

**Equation 8.9** 
$$\Delta T_{\max-\min} = \frac{\lambda}{4n}$$

An example of the HeNe interferometer signal is shown in Figure 8.3 where (—) represents the signal during the halogen etch and (— · —) represents the signal during the oxygen etch. The time scales are relative.

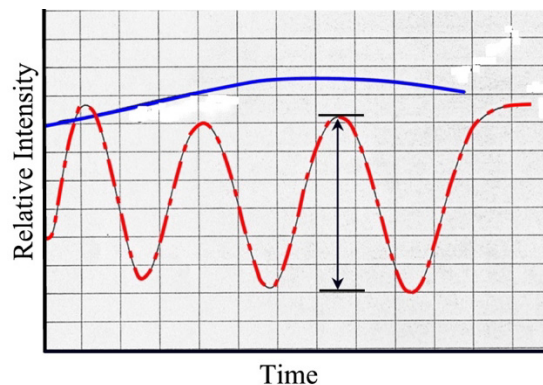


Figure 8.3. HeNe interferometry signal taken during O<sub>2</sub> RIE process.

### 8.2.2 UT Reactive Ion Etcher

A preliminary RIE process based on the RIE collaboration with Agilent Technologies has been used at The University of Texas at Austin with a quartz template process. This work was performed on an asymmetric Oxford Instruments Plasmatek  $\mu$ 80 parallel plate, capacitively coupled RF reactive ion etcher. It has a 15.24 cm diameter lower driven electrode, and a 30.48 cm diameter grounded upper electrode. The gap between the electrodes is 5.08 cm.

The RF power is controlled automatically via the Oxford Instruments' matching network. The pressure is controlled manually with a MTS pressure controller. Both a Pirani gauge and a Baratron gauge monitor the chamber pressure. Two thermocouple pressure gauges monitor the pressure just after the roughing pump and before the turbo pump. A gate valve and a chiller have been added to the system to improve the etch quality. A standard operating procedure for this etcher is found in the Appendices. Nitrogen, helium, tetrafluoromethane, and oxygen are plumbed to the etcher. Currently the system is controls three gases (He, CF<sub>4</sub>, and O<sub>2</sub>) but is capable of running up to four different etch gases and one purge gas. Nitrogen is used only during purge cycle.

There are two spare electrodes; one upper and one lower. The spare upper electrode has been retrofitted with a HeNe interferometry endpoint detection system. A simple acquisition and analysis software has been developed for use with this endpoint system. Trifluoromethane is also available but is not currently plumbed to the system. The spare lower electrode is ~300 mm in diameter and would result in a higher potential voltage.

## 8.3 RESULTS

### 8.3.1 Effect of Silicon Content on RIE Selectivity

The study was carried out to determine the weight percent of silicon that must be incorporated into the etch barrier in order to achieve an etch rate selectivity greater than 10 between the etch barrier and the transfer layer. The etch conditions for O<sub>2</sub> RIE were 40 standard cubic centimeters per minute (sccm) O<sub>2</sub>, and 200 V at 20 mTorr. This etch was approximately 80% anisotropic providing the degree of undercut necessary for subsequent additive metalization. The etch rate was measured using *in situ* HeNe interferometry and initial and final thickness were corroborated by both two angle ellipsometry and profilometry.

Formulations with varying silicon content were prepared by mixing cyclohexyl acrylate (Aldrich) and (3-acryloxypropyltrimethylsiloxy)silane (SIA 0210.0, Gelest) with a constant 5% (w/w) 1,3-bis(3-methacryloxypropyl)tetramethyldisiloxane (SIB 1402, Gelest). The mixtures ranged from 95% (w/w) cyclohexyl acrylate to 95% (w/w) (3-acryloxypropyltrimethylsiloxy)silane with the constant 5% (w/w) 1,3-bis(3-methacryloxypropyl)tetramethyldisiloxane. A 1:1 mixture of bis(2,4,6-trimethylbenzoyl)phenylphosphine oxide (Irgacure 819, Ciba) and 1-benzoyl-1-hydroxycyclohexane (Irgacure 184, Ciba) were added to the above solution at 3% (w/w) to initiate free radical polymerization upon UV illumination. For ~30% (w/w) silicon samples, low molecular weight poly(acryloxypropylmethylsiloxane-co-dimethylsiloxane) (UMS-182, Gelest) was used.

Two organic films were used as model transfer layer materials during the RIE studies: polystyrene and poly(methyl methacrylate) (PMMA). A 10% (w/w) solution of polystyrene (50,000 molecular weight) in toluene was spun at 4000 revolutions per minute (RPM) for 60 seconds and post-apply baked at 90 C for 90 seconds. A 10% (w/w) solution of PMMA (496,000 molecular weight) in chlorobenzene was spun at 4000 to 6000 RPM for 60 seconds depending on desired thickness then hard baked at 200 C for 4 minutes under vacuum.

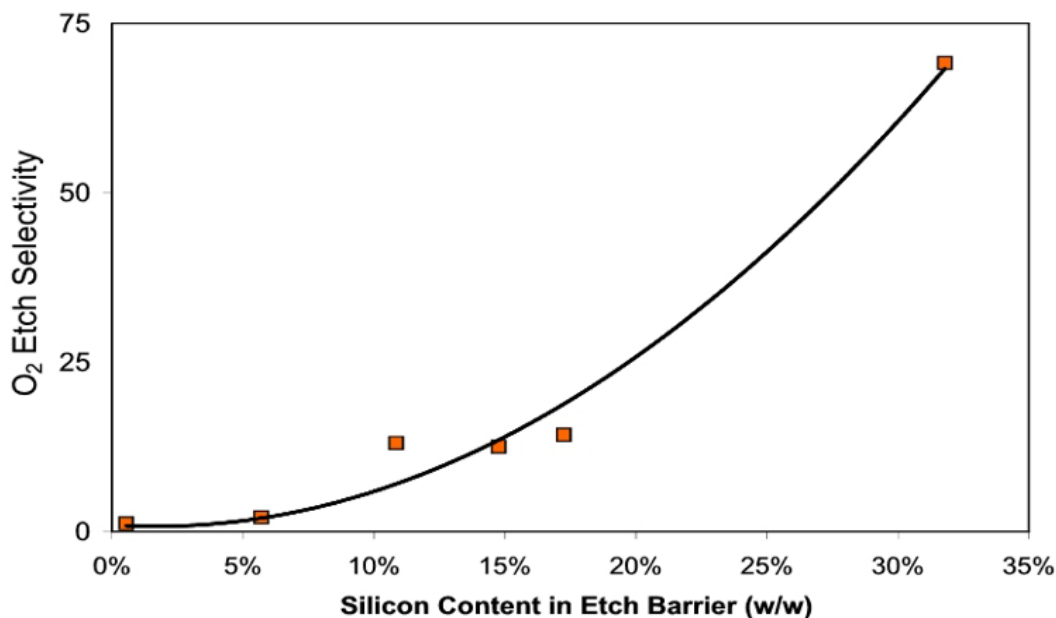


Figure 8.4. Effect of silicon content on O<sub>2</sub> etch selectivity between the etch barrier and a polystyrene film.

The O<sub>2</sub> etch selectivity starts at 1:1 and increases to 60:1 for 30% (w/w) silicon formulations. As the silicon weight percent increases past 11% (w/w) the

desired etch selectivity of 10:1 is achieved as shown in Figure 11. Therefore, etch barrier solutions currently used contain a minimum of 11% (w/w) silicon. The etch barrier formulation used at Agilent that was reformulated to spin coat was ~30% (w/w) silicon. The low viscosity etch barrier formulation used on the SFIL stepper has a silicon content of 13.5%(w/w). The original etch barrier solution has a 21% (w/w) silicon content.

### 8.3.2 Base Layer Study

While the etch rates of blank films provides insight into the proper etch conditions as well as the proper etch barrier formulation, they do not address the major concern of SFIL bilayer process. In order to transfer the replicated features, a uniform base layer must be achieved. Figure 8.5 illustrates the requirement that the variation (A, A') in the base layer must be smaller than the depth (B) of the replicated features.

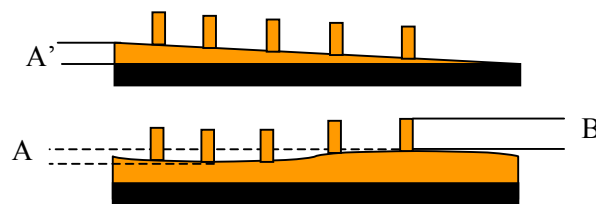


Figure 8.5. The variation in base layer thickness (A) across the imprint must be less than the feature height (B) if the RIE transfers function properly.

While this may not be difficult for deep features, replication techniques utilizing acrylate-methacrylate chemistries have been found experimentally to be limited to a 3:1 aspect ratio [5,6]. For sub-100 nm feature size of interest, this demands a uniformity of less than ~100nm if the features are to be transferred

reliably. Utilizing a compliant template and the Agilent imprint equipment, base layers as thin as 20 nm have been achieved. An SEM of a 55+ nm base layer is shown in Figure 8.6a. The base layer across a 1" x 1" imprint field, shown in Figure 8.6b, was characterized by two-angle ellipsometry and has a thickness and uniformity that is less than 100 nm.

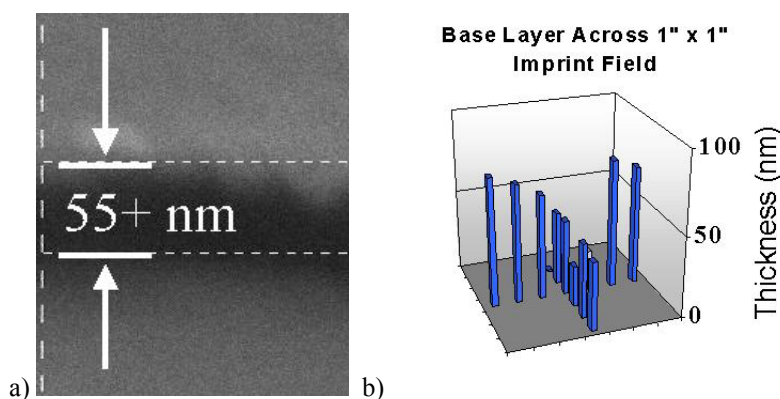


Figure 8.6. a) SEM of 55+nm base layer using polycarbonate template. b) Base layer across a 1" x 1" patterned region measured with ellipsometry.

### 8.3.3 Transfer Layer Etch Process

A full factorial design of experiment was performed on a PMMA transfer layer during O<sub>2</sub> RIE. The RF voltages were 150 V, 200 V, and 300 V and the pressures were 10 mTorr, 20 mTorr, and 40 mTorr. The vertical etch rate was measured by *in situ* interferometry and validated by pre-etch and post-etch ellipsometry. The horizontal etch rate was measured by cross sectional SEM.

The measured vertical etch rate of PMMA is shown in Figure 8.7. The etch rate more than doubles as the applied voltage rises from 150V to 250V and it

doubles as the pressure rises from 10mT to 40mT. A first order ANOVA fit of the vertical etch rate yields the following relation:

$$\text{Equation 8.10} \quad ER_{\text{vertical}} = -845 + 7.3V + 13.5P$$

where  $V$  is volts,  $P$  is pressure in mTorr, and  $ER_{\text{vertical}}$  is in  $\text{\AA}$  per minute. The intercept does not equal zero since the model is not based on the fundamental physics of the etch but just empirical analysis.

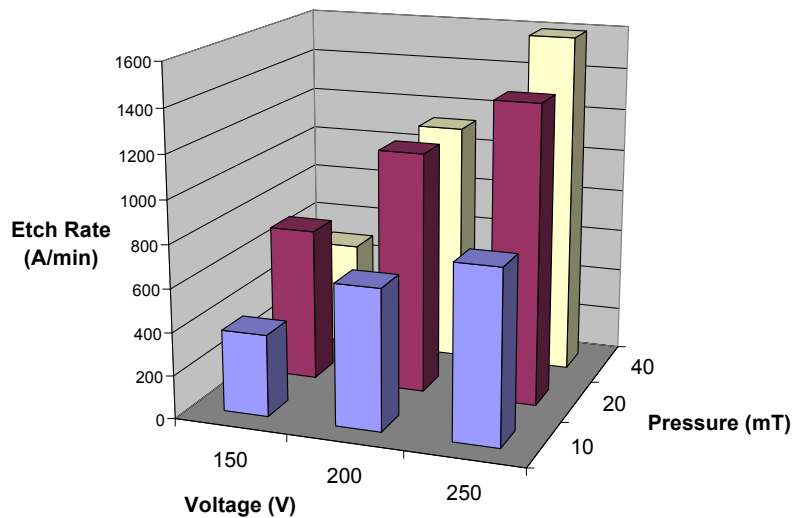


Figure 8.7. Etch Rate of 467k MW PMMA in O<sub>2</sub> RIE

An undercut analysis proved difficult due to the high degree of anisotropy for most of these etch conditions. Two extremes of undercut are shown in Figure 8.8 where the left is the 150 V, 40 mTorr sample while the right is a 10 mTorr, 250 V sample. The average horizontal etch rate is 15  $\text{\AA}$ /minute where the average vertical etch rate was 915  $\text{\AA}$ /minute which results in a degree of anisotropy of 60. While the effect of process conditions on undercut was statistically insignificant

at 95% confidence, the best results were achieved at low pressure. Consequently, for the sub-100 nm features the pressure was dropped to 6 mTorr, which is the lowest pressure the system could run stably.

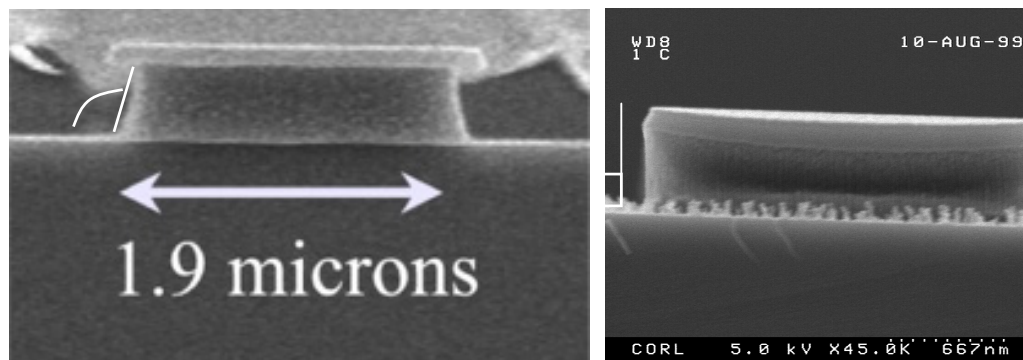


Figure 8.8. Undercut at 40 mTorr and 150 V (left), and 10 mTorr and 250 V (right).

PMMA was the primary transfer layer used during the development of the transfer etch since additive metalization was the next process step. However, the etch characteristics of PMMA are not the most desirable for etch transfer into silicon. Table 8.1 compares the etch rates for four other transfer layer candidates, which have higher etch selectivity relative to silicon under identical etch conditions. The  $O_2$  process conditions were 40 sccm  $O_2$ , 12, and 250 V at 20 mTorr while the halogen etch conditions were 56 sccm  $CHF_3$ , 12.5 sccm He, and 450 V at 6 mTorr. The etch rate of polystyrene is indicative of aromatic photoresists such as novolac or polyhydroxystyrene. The top two, polystyrene and PMMA, exhibit the faster etch rates in both  $O_2$  RIE and halogen RIE than the two crosslinked resists: poly(imide) and UV11. The  $O_2$  etch rates of the films are

quite high with respect to the etch barrier while the halogen selectivity is between  $\frac{1}{2}$  and 2.

Table 8.1. Screening of Transfer Layer Candidates (\* from Allcock [7])

Material	Tg (C)	O <sub>2</sub> Rate (A/s)	Halogen Rate (A/s)
Poly(styrene)	100*	12	3
PMMA	105*	11	4.4
Poly(imide)	>200	4.5	1
UV11	---	4.5	2.8
Etch Barrier	<-30	0.17	2.4

#### 8.3.4 Etch Stop Experiment

With the proper etch conditions for both high resolution RIE and slight undercut required for addition metalization transfer identified and a thin uniform base layer; the achievable aspect ratio and resolution of the entire SFIL process was investigated. An etch stop experiment was conducted in which the O<sub>2</sub> RIE was stopped after only partially penetrating the transfer layer. Using a wafer with 80 nm features replicated on 1.1  $\mu\text{m}$  of hard-baked PMMA, the O<sub>2</sub> RIE was halted after penetrating 300 nm into the PMMA transfer layer. The sample was characterized in cross-section by SEM (shown in Figure 12a).

After determining the features could structurally withstand both high aspect ratios and the etch conditions, another section of the same wafer was etched until the endpoint was determined by HeNe interferometry. A 20% overetch was performed to clear the resist at the base of the features. This sample was also characterized by SEM and is shown in Figure 12b. These features have a

remarkable aspect ratio of 14:1 and demonstrate a benefit of SFIL's silylated bilayer scheme over other imprint techniques.

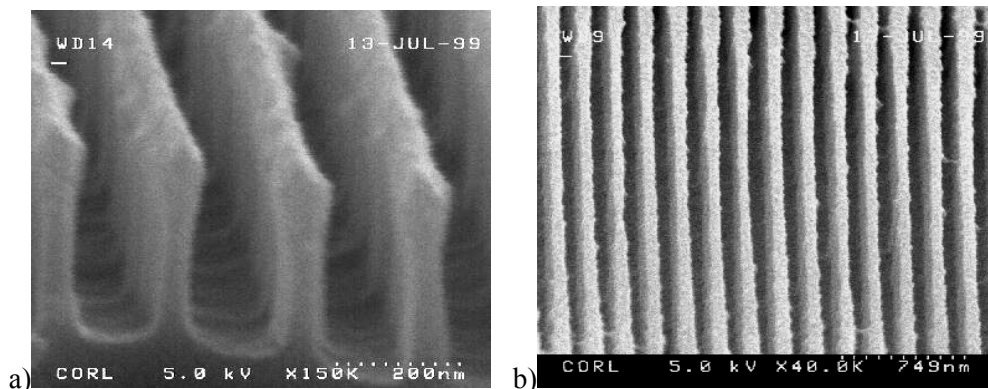


Figure 8.9. (a) 80 nm features etched 300 nm into the PMMA transfer layer, (b) 80 nm features etched through 1.4  $\mu\text{m}$  of PMMA.

### 8.3.5 High Resolution Etch Transfer

A high-resolution template was created using a single path electron beam exposure in 100 nm of PMMA. The master had 60 nm features etched 50 nm deep. A daughter template was replicated from this master onto a compliant polycarbonate sheet. Wafers were coated with 300 nm of hard baked PMMA and patterned with these 60 nm features. A short 20 second  $\text{CHF}_3\text{-O}_2\text{-He}$  breakthrough etch followed by an  $\text{O}_2$  transfer etch generated 60 nm features with 6:1 aspect ratio and a slight undercut demanded for additive metalization. These features are shown in Figure 13. These are the highest resolution features transferred through the transfer layer.

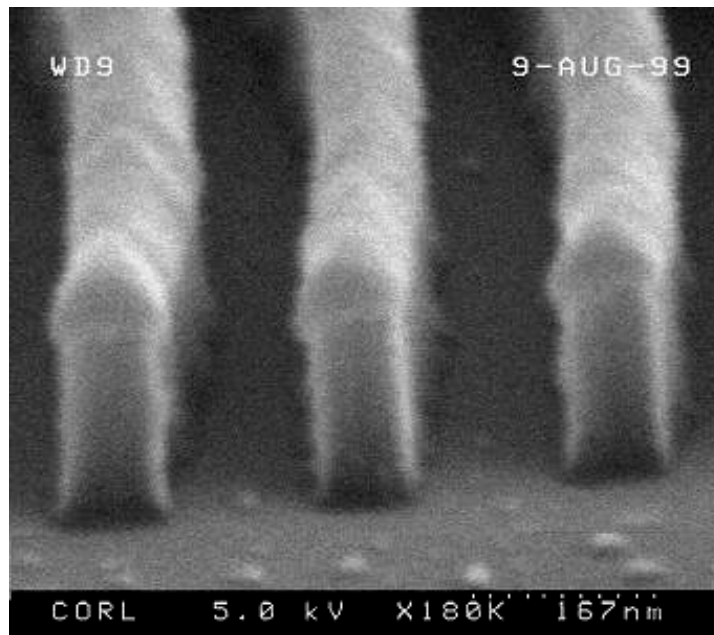


Figure 8.10. 70 nm features etch transferred through 300 nm of PMMA.

### 8.3.6 UT Stepper Base Layer

For the SFIL stepper, the ability to achieve a uniform base layer rests with the wafer uniformity under vacuum, the wafer chuck uniformity, the orientation of the template, and the volume of dispensed fluid. The uniformity of the wafer is specified by the semiconductor industry and less than 0.18 nm across the 300 mm diameter [8]. The uniformity of the wafer chuck is specified by the manufacturer and is truly limited only by economic factors. The current chuck has a uniformity of 1/10 wave across the 300 mm diameter. While the uniformity of the chuck may be specified, it has been found that the surface of a 300 mm diameter wafer may be deflected under vacuum if the wafer chuck is designed improperly [9].

An example of the nonuniformity in the etch barrier resulting from poor chuck design is shown below and exhibit a period of 5 mm, which is equal to the pin spacing for this chuck. For a pin-type vacuum chuck, the optimum diameter and spacing for minimized wafer deflection are 0.5 mm and 5 mm, respectively [9]. After resurfacing the current wafer chuck, the thinnest uniform base layer measured using the SFIL multi-imprint stepper was 138 nm (Figure 8.12).

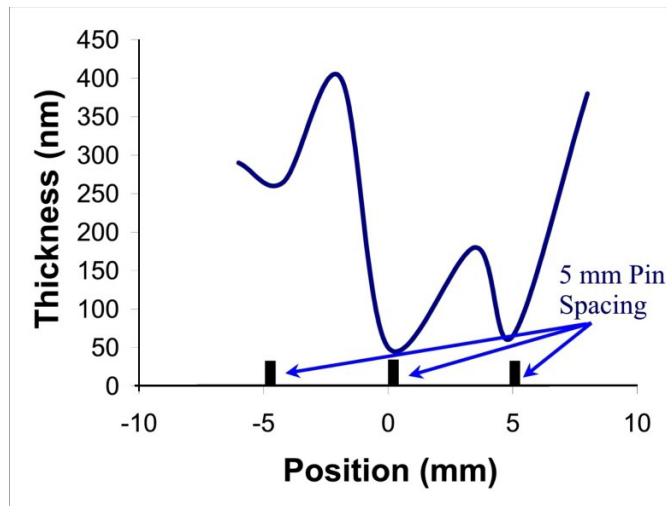
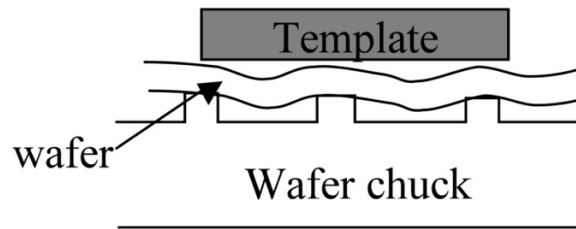


Figure 8.11. (Top) Schematic of wafer deflection under vacuum. (Bottom) Thickness of an imprinted film on a poor quality wafer chuck.

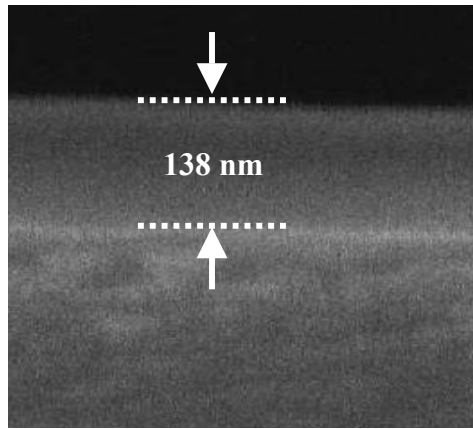


Figure 8.12. 138 nm base layer imprinted with a quartz template in the SFIL Stepper.

### 8.3.7 Etch Transfer with Rigid Template Replication

For these initial etch transfer investigations on the  $\mu$ 80 RIE, a transfer layer of PMMA was spin coated 100 nm thick and post-application baked at 200°C for 2+ hours. The etch barrier formulation was 47% (3-acryloxypropyltristrimethylsiloxy)silane, 47% butyl acrylate, 2.3% 1,3-bis(3-methacryloxypropyl) tetramethyldisiloxane, 1.85% bis(2,4,6-trimethylbenzoyl)-phenylphosphineoxide and 1.85% 1-benzoyl-1-hydroxycyclohexane, by weight. The O<sub>2</sub> RIE conditions were 10 sccm O<sub>2</sub>, and 215 W at 10 mTorr. The halogen RIE conditions were utilized; 28 sccm CF<sub>4</sub>, 8 sccm He, and 1 sccm O<sub>2</sub> with 215 W at 10 mTorr.

A template fabricated at IBM-Burlington was used to demonstrate the RIE process on substrates patterned on the multi-imprint stepper with a rigid quartz template. A series of the line-space dimensions on the template were characterized on the Hitachi 4500 FESEM. These features were then replicated

and etch transferred through the transfer layer. The base layer was approximately 250 nm thick but fairly uniform. The break-through etch was run for ~2 minutes while the oxygen amplification etch was run for 1 minute. The line-space dimensions of these features were characterized before and after RIE. A comparison of the line-space dimensions is shown in Figure 8.13.

An example of these features is shown in Figure 8.14. There is no detectable difference in line-space widths between the template and the replicated features; however, there is a significant bias between the line widths of the replicated features and etched images. Additional tilt-SEM images were taken and reveal little undercut of the etch barrier, which indicates the break-through etch is the primary source of the etch bias.

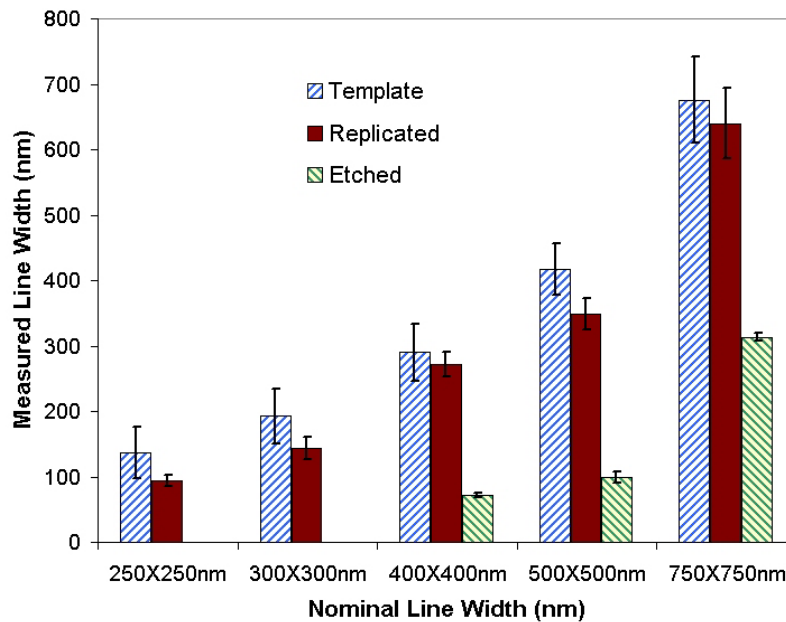


Figure 8.13. Line width characterized by SEM of a) the template, b) the replicated features, and c) the etch transferred features.

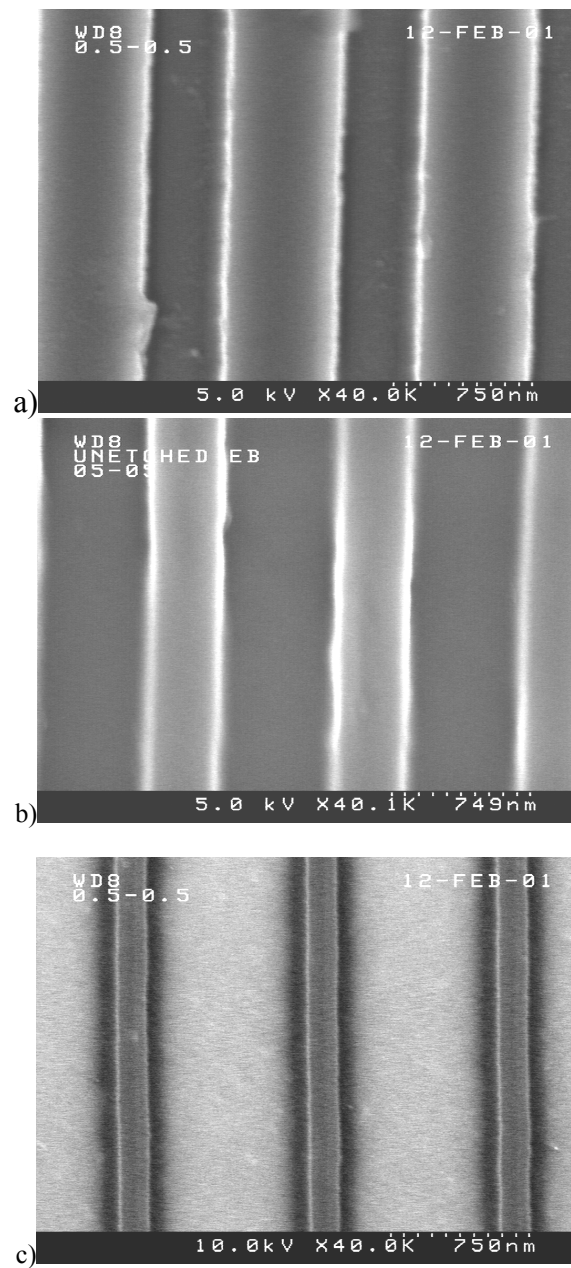


Figure 8.14. Comparison of Template (top), the replicated features (middle), and the etched features (bottom).

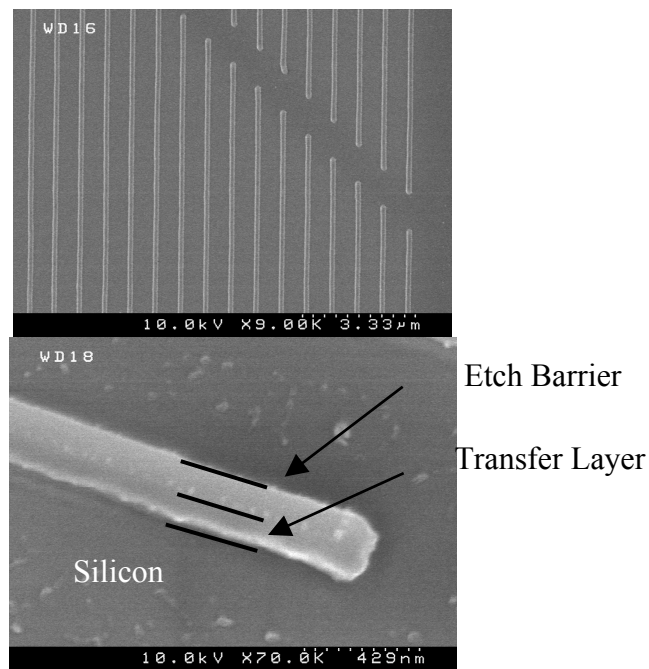


Figure 8.15. Top-Down and Tilt SEM of features etch transferred with the  $\mu$ 80 etcher.

#### 8.4 CONCLUSIONS

The bilayer reactive ion etch process has been developed on two separate parallel-plate, capacitively-coupled reactive ion etchers. The process on the MRC etcher had a tremendous degree of anisotropy as well as excellent etch selectivity between the etch barrier and the transfer layer. The smallest 60 nm features on the compliant were faithfully replicated and transferred through the transfer layer with little undercut. The smallest features on the IBM template (60 nm) were faithfully replicated. However, the smallest features remaining features were  $\sim$ 60 nm after etch but were originally  $\sim$ 300 nm prior to etch. The Oxford instruments  $\mu$ 80 RIE successfully transferred images but only with significant lateral etch rate

resulting in etch bias on the order of 300 nm. The SFIL process has proven to have high resolution replication capability but is dependent on the RIE quality for final image transfer.

## **8.5 FUTURE WORK**

Significant effort has been put forth transferring the etch developed at Agilent to The University of Texas at Austin laboratories. Any further improvement in the RIE process must be performed on an etcher that is designed for sub-100 nm features. According to the RIE theorist, low density plasmas such as a parallel-plate, capacitively-coupled etcher should not be able to achieve sufficient anisotropy for reliable sub-300 nm transfer [10]. Advanced RIE tools have been designed for sub-100 nm RIE [1,3] and are capable of independent control of ion bombardment energy and plasma density, which makes control of the RIE conditions less difficult.

An oxygen RIE process developed for Top Surface Imaging [11] on a LAM 9400 TCP reactive ion etcher should be well suited for the SFIL O<sub>2</sub> RIE. Several attempts to perform preliminary etch transfer experiments on the LAM 9400 TCP etcher were pre-emptly stopped due to backside particle contamination that prevented the wafers from seating on the LAM electrostatic chuck. In a control experiment, two wafers were loaded onto the etcher. One was imprinted and the other was only loaded onto the SFIL stepper wafer chuck; both failed to form a seal with the electrostatic chuck due to backside particles.

Several steps were taken to address this issue. The addition of new vacuum wafer wands, a new wafer chuck, and wafers precoated with a transfer layer did not eliminate the particles from contaminating the backside of the wafer. There are several potential sources of particles. Transportation in the wafer boats and particles from the wafer chuck are two primary suspects; however, during the initial phases of the defect susceptibility, particle contamination due to transportation was found to be minimal [12]. With a new wafer chuck, the wafers should be able to be loaded into the LAM 9400 TCP RIE for process development.

While an advance RIE tool is ideal for SFIL, inevitably some users will be limited to less sophisticated etchers. For these users, there are several potential equipment improvements to consider. If DC-bias is not available, an applied DC bias could be installed or the self-bias of the driven electrode modified by changing the surface area of the driven electrode relative to the grounded surface area. Reducing the DC bias minimizes sputtering while increasing DC-bias will improve anisotropy. Also, an interferometric endpoint detection system is quite useful for proper control and characterization of the RIE process. Chilling the driven electrode also improves the anisotropy of the RIE [11]. Additional improvements may be made to the RIE chemistry. By adding hydrogen into the Halogen RIE, the etch selectivity between the etch barrier and the transfer layer will increase dramatically [13]. With these suggestions, further progress toward a universally, reliable RIE process is feasible.

References:

---

- 1 Coburn, J; "Plasma Etching and Reactive Ion Etching," *SPIE Short Course*. (2001)
- 2 Hartley, F; C. K. Malek, J. Neogi, "Sub-optical lithography with Nanometer Definition Masks," *43rd International Conference EIPBN*, Marco Island, FL, U.S.A. (1998)
- 3 Lieberman, M.A.; A.J. Lichtenberg, *Principles of Plasma Discharges and Materials Processing*, Wiley, NY (1994)
- 4 Thompson, L.F.; C.G. Willson, M.J. Bowden, Introduction to Microlithography, ACS, Washington. p.153 (1994)
- 5 Haisma, J.; M.Verheijen, K. van der Huevel, J. van den Berg, "Template-assisted nanolithography: A process for reliable pattern replication," *J. Vac. Sci. Technol. B* **14**(6), 4124-29 (1996)
- 6 H-C Scheer, H. Schults, F. Gottschalch, T. Hoffmann, C.M. Torres, Sotomayor "Problems of the Nanoimprint Technique for nm-scale Pattern Definition," *J. Vac. Sci. and Technol. B.* **16**(6), 3917-3921 (1998)
- 7 Allock, H. R.; F.W. Lampe. Contemporary Polymer Chemistry, 2<sup>nd</sup>. Prentices, NJ (1990)
- 8 *International Technology Roadmap for Semiconductors*. Semiconductor Industry Association (1999)
- 9 Une, A.; Y. Kai, M. Mochida, S. Matsui, F. Ohira, "Influence of Wafer Chucking on Focus Margin for Resolving Fine Patterns in Optical Lithography," *Microelectronic Engineering*, 53, 137-140 (2000).
- 10 Hallock, G; Class notes from "Plasma Processing of Semiconductors – I," The University of Texas at Austin (1999)
- 11 Somervell, M. "Top Surface Imaging," Ph.D Thesis, The University of Texas at Austin, (2000)
- 12 Bailey, T.; B. Smith, B.J. Choi, M. Colburn, M. Meissl, S.V. Sreenivasan, J.G. Ekerdt, C.G. Willson, "Step and Flash Imprint Lithography: Defect Analysis," *J. Vac. Sci. Technol. B.* [submitted]

---

13 Heinecke, R; *J. Electrochem. Soc.* 129. 2282 (1982)

## 9 Spectral Reflectometry for *Real-time* Gap Sensing and Other Applications

### 9.1 INTRODUCTION

Over the course of the SFIL development, it became evident that an actively controlled template stage would provide several advantages over the current passive stage. An active stage with feedback control is one step toward a stage capable of performing high resolution layer-to-layer alignment and would provide a controlled mechanism of separation whether by wedging or by coplanar z-separation (stud pull). This stage also enables quantification of separation forces in a more rigorously controlled manner than is possible with the current configuration.

An absolute gap sensing system must be incorporated into the control system for such an active stage. Four principle techniques were originally considered as potential solutions to the gap sensing system: i) capacitance sensing, ii) interferometry (single and multiwavelength), iii) ellipsometry, and iv) spectral reflectometry.

Capacitance measurement is one of the most accurate methods of gap measurement available and is capable of high bandwidth signal generation (1+ kHz). The only characteristic that could be an issue for this application is the requirement of placing an electrode on the surface of the template and on the surface of the substrate. While the electrode on the template may not be difficult to manufacture, it would be opaque to the UV light that initiates the free radical

polymerization. This may generate problems with subsequent imprints if any of the etch barrier remains unpolymerized. The electrode on the substrate is also impractical. Capacitive sensing may be useful for some applications of imprint lithography but it is generally not applicable.

Single wavelength interferometry measures relative displacement by measuring the phase of an intensity signal. For a system in which the gap may be oscillating in an up and down manner at high frequencies with a magnitude on the order of the wavelength, single wavelength interferometry is impractical. It does however provide a high bandwidth means of measuring relative displacement. This method may be useful if combined with a technique that can calibrate the signal to an initial absolute gap and periodically monitor the absolute gap, but has been eliminated as a possible option for our stand alone device [1].

Multiwavelength interferometry utilizes two or more single wavelength interferometers. This system provides relative displacements just as single wavelength interferometry but if the system is designed properly, it may provide a gap measurement with a period of repetition that much larger than the single wavelength interferometry. For example, the period of a two-wavelength interferometer using 500 nm and 600 nm light is 3000 nm if the index of refraction is assumed to be 1. Over the 3000 nm period, there are unique combinations of the cosine of the phase difference ( $\Delta$ ) and cosine of the phase sum ( $\Sigma$ ) as shown in Figure 9.1. The sensitivity of  $\cos(\Delta)$  and  $\cos(\Sigma)$  are complimentary; each having distinct ranges over which the change in their signal amplitude is large for a given change in thickness. The phase is defined in

Equation 9.1. An initial calibration would still be required to determine the initial gap thickness since the template travel is greater than 3 microns.

**Equation 9.1** 
$$\phi_i = \frac{2\pi nD}{\lambda_i}$$

**Equation 9.2** 
$$\Sigma = \phi_1 + \phi_2 = 2\pi nD \frac{\lambda_1 + \lambda_2}{\lambda_1 \lambda_2}$$

**Equation 9.3** 
$$\Delta = \phi_1 - \phi_2 = 2\pi nD \frac{\lambda_1 - \lambda_2}{\lambda_1 \lambda_2}$$

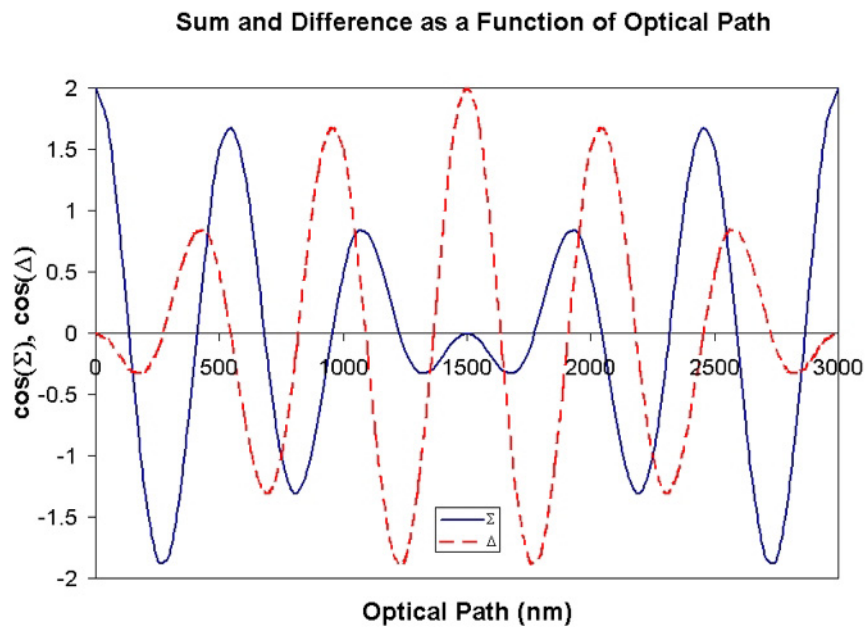


Figure 9.1. Plot of  $\cos(\Sigma)$  and  $\cos(\Delta)$  for optical path lengths ( $nD$ ) ranging from 0 nm to 3000 nm for wavelengths of 500 nm and 600 nm.

Ellipsometry, particularly spectral ellipsometry, is a sophisticated technique that provides accurate film thickness measurements from essentially zero thickness ( $<10\text{\AA}$ ) to several microns. This technique utilizes off axis illumination ( $65^\circ$ - $75^\circ$  from normal) of a sample with circularly polarized light having a beam cross-section that is several millimeters long by 1 to 2 mm wide. The polarized light interacts with the film on the substrate and experiences a phase change ( $\Delta$ ) and a polarization change ( $\Psi$ ); both of which are used to calculate the film properties [2]. Off-axis illumination and the large cross-section characteristics pose difficulties for sensing through a 2.54 cm x 2.54 cm template that resides in a recessed housing. The ellipsometer also requires a large footprint relative to the size of the template stage and is relatively expensive.

Spectral reflectometry is used extensively for dissolution rate characterization of thin lithographic films and several analysis algorithms exist [2,3,4,5]. In dissolution rate monitoring (DRM), spectral data is collected in real time and later analyzed using these algorithms to extract the thickness of the film as a function of time. All these techniques are based on advanced curve fitting algorithms similar in nature to the algorithm detailed in “Spectroscopic Reflectometry” [2]. The basic components of the instrument are detailed in the following sections. The implementation can be operated in a normal or off-axis configuration. As with ellipsometry, the analysis of the spectral reflection yields absolute film thickness if the index of refraction is known. The challenge that remains is developing an algorithm that allows for real time analysis rather than post-processing analysis.

## 9.2 SPECTRAL REFLECTION

In order to develop the algorithm, one must understand the nature of the signal to be analyzed. For spectral reflectometry to be applied, there must exist some constructive-destructive interference. A simplified example of the SFIL template-gap-substrate system is shown in Figure 9.2. Incident light of energy,  $E_I$ , is reflected off the template-gap interface ( $E_0$ ) and transmitted into the gap and is in turn reflected off the gap-substrate interface. The light that is reflected off the gap-substrate interface is then partially transmitted through the gap-template interface ( $E_1$ ) and partially reflected back into the gap for the gap-template interface.

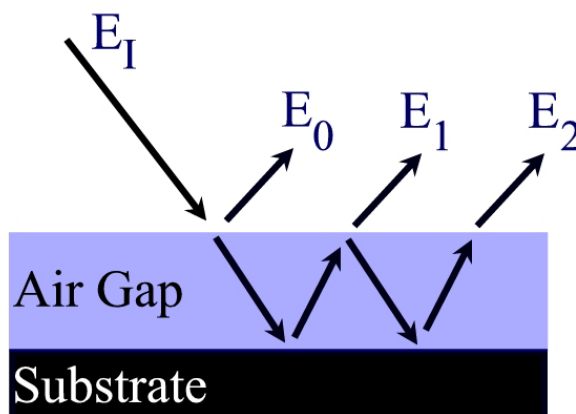


Figure 9.2. Simplified SFIL system consisting of a template, gap, and substrate.

This reflection and transmission of the light within the film continues infinitely. With each additional pass, more energy is absorbed by the film. This series of reflection/transmission events, depicted in Figure 9.2, can be mathematically described based on the refractive index ( $\tilde{n}$ ), the reflectivity ( $\rho_{ij}$ ) of

the interfaces, absorption coefficient ( $\alpha_{ij}$ ), and the transmission coefficient ( $\tau_{ij}$ ) for the interfaces; the definitions of which are stated below:

**Equation 9.4**

$$\tilde{n} = n - i\kappa$$

**Equation 9.5**

$$\rho_{ij} = \frac{\tilde{n}_i - \tilde{n}_j}{\tilde{n}_i + \tilde{n}_j} = X + iY = \text{Re}^{i\theta}$$

**Equation 9.6**

$$|\rho_{ij}^2| = X^2 + Y^2$$

**Equation 9.7**

$$\tan^{-1}\left(\frac{Y}{X}\right) = \theta$$

**Equation 9.8**

$$\alpha_i = \frac{4\pi\kappa}{\lambda}$$

**Equation 9.9**

$$\tau_{ij} = \frac{2\tilde{n}_i}{\tilde{n}_i + \tilde{n}_j}$$

**Equation 9.10**

$$k = \frac{2\pi\tilde{n}}{\lambda}$$

where  $X$ ,  $Y$ , and  $\theta$ , are the real and imaginary components of the reflectivity, and the phase change upon reflection off the gap-substrate interface, and  $i$  and  $j$  refer to the  $i^{\text{th}}$  and  $j^{\text{th}}$  material.

For the derivation below, it was assumed that the substrate exhibited perfect reflection and no absorption. As a result, the phase change ( $\theta$ ) is  $90^\circ$  and  $\rho_{\text{gap-substrate}}$  is 1. If the energy of incident light reflected off the first interface is given by  $\rho_{\text{template-gap}}E_I$  and the transmitted energy ( $\tau_{\text{template-gap}}E_I$ ) is absorbed along the path length,  $D$ , reflected off the gap-template interface, then the transmitted energy ( $E_{RI}$ ) through the gap-template interface as result of the first reflection off the substrate is  $\tau_{\text{template-gap}}E_I\tau_D\rho_{\text{gap-substrate}}\tau_D\tau_{\text{gap-template}}$ ; where  $\tau_D$  is the absorbance along the path length (shown below).

**Equation 9.11**  $\tau_D = e^{-ik2D} = e^{-i4\pi mD/\lambda} e^{-4\pi\kappa D/\lambda}$

**Equation 9.12**  $\text{Re}(\tau_D) = e^{-\alpha D} \cos\left(\frac{4\pi mD}{\lambda}\right)$

Since the light transmitted through the template-gap interface travels through the path length twice,  $\tau_D$  appears twice. If this same approach is applied to all the internally reflected light, the following equation is developed [6]:

**Equation 9.13**

$$\begin{aligned} E_R &= \sum_{i=0}^{\infty} E_i = E_0 + E_1 + E_2 + \dots = \rho_{tg} E_I + \tau_{tg} E_I \tau_D \rho_{gs} \tau_D \tau_{gt} \\ &\quad + \tau_{tg} \tau_D \rho_{gs} \tau_D \tau_{gt} E_1 + \tau_{tg} \tau_D \rho_{gs} \tau_D \tau_{gt} E_2 \\ &= \rho_{tg} E_I + \tau_{tg} \tau_{gt} (\tau_D^2 \rho_{gs}) E_I + (\tau_D^2 \rho_{gs} \rho_{gt}) E_1 + (\tau_D^2 \rho_{gs} \rho_{gt}) E_2 \end{aligned}$$

where  $t$  refers to the template,  $g$  refers to the gap and  $s$  refers to the substrate.

This can be simplified to the following relationship [5].

**Equation 9.14**  $\frac{E_R}{E_I} = \left( \rho_{tg} + \frac{\tau_{tg} \tau_{gt} \tau_D^2 \rho_{gs}}{1 + \tau_D^2 \rho_{gs} \rho_{gt}} \right)$

The intensity of light is equal to the square of the energy. If the relation in Equation 9.12 is substituted in to Equation 9.14 and the equation is squared, the spectral reflectivity is derived as a function of gap thickness,  $D$ . The relative reflectivity,  $R$ , of a single optical thin film is described by the following equation:

**Equation 9.15**  $R = \frac{\rho_{t,g}^2 + \rho_{g,s}^2 e^{-\alpha 2D} - 2\rho_{t,g} \rho_{g,s} e^{-\alpha D} \cos(4\pi mD/\lambda)}{1 - (\rho_{t,g} \rho_{g,s})^2 e^{-\alpha 2D} + 2(\rho_{t,g} \rho_{g,s}) e^{-\alpha D} \cos(4\pi mD/\lambda)}$

where  $\rho_{i,j}$  is the reflectivity of the  $i$ - $j$  interface,  $n$  is the real component of the refraction index [7].

### 9.3 BACKGROUND

Sakuraio *et.al.* showed that for small values of the reflectivity,  $R$ , x-rays oscillate in thin film stacks according to the following equation where  $F_{ij}$  are the Fresnel coefficients at the interface of the  $j-1$  and  $j$  interface, and  $\gamma=(4\pi/\lambda)\sqrt{(\theta_2-\theta_{c2})}$  [8].

$$R = \frac{F_{1,2}^2 + F_{2,3}^2 - 2F_{1,2}F_{2,3} \cos(\gamma d)}{1 - F_{1,2}^2 - F_{2,3}^2 + F_{1,2}^2 F_{2,3}^2}$$

**Equation 9.16**

A recently published work by Bouldin *et.al.* demonstrated the use of Fourier analysis on x-ray reflectivity (XRR) data collected during the characterization of the thermal expansion coefficient of a low  $k$  dielectric [9]. This work, developed independently from ours, validates the use of Fast Fourier Transforms (FFTs) as an analytical technique in thin film characterization. Their work is based on the analysis of conducting thin film stacks illuminated with x-ray radiation at grazing angles between 0.011 to 12 mrad in vacuum. The index of refraction for x-rays passing through a thin film is:

$$n = 1 - \frac{N}{2\pi} r_o \lambda^2 \sum \frac{\rho_j}{A_j} f_i$$

**Equation 9.17**

where  $N$  is Avogadros number,  $r_o$  is the electron radius,  $\lambda$  is the x-ray wavelength.

The sum is over the elements in the material; the  $\rho$ ,  $A$  and  $f$  are the density, atomic mass and form factor of that element, respectively.

One interesting aspect and key difference between the method used by Bouldin *et.al.* for XRR and the FFT UV-VIS spectral reflectometry, detailed in the following sections, is the mechanism in which the spectral information is generated. We use a broadband source to illuminate over a range of wavelengths ( $\lambda$ ). The XRR method uses changes in incidence angle ( $\theta$ ) which results in an effective change in wavelength since  $\gamma$  is changing. This requires extremely accurate control of motion between 0.011 and 12 mrad relative to the sample surface.

Equation 9.18 
$$\gamma \propto \sqrt{(\theta^2 - \theta_c^2)}$$

#### 9.4 APPLICATION OF SPECTRAL REFLECTIVITY TO GAP SENSING

The gap between the template and substrate generates thin film interference that follows the relationship described in Equation 9.15. Two types of gaps were considered when developing the technique. The first is an air gap and the second a gap filled with etch barrier. For the air gap the index of refraction is assumed to be constant over wavelength. For the etch barrier filled gap, the dispersion can be defined by the Cauchy coefficients. In both cases, the absorbance in the visible spectrum is assumed insignificant. So, the absorbance terms ( $e^{-\alpha D}$  and  $e^{-2\alpha D}$ ) in Equation 9.15 can be neglected. The reflectivity of the template-gap interface ( $\rho_{ij}$ ) is much less than the reflectivity of the gap-substrate

reflectivity in our system. The signal from the transfer layer is removed from the total reflection by collecting and storing a background signal with the transfer layer present. In this way, the spectral reflectivity of the system can be reduced to a “model” system described in Equation 9.20 that oscillates at the frequency,  $4\pi nD$ , in wavenumber space.

The assumptions and substitutions (1-5) shown below can simplify Equation 9.15 to Equation 9.19 which can be separated into two fractions,  $\Xi$  and  $\Phi$ , where

$$\Phi = \frac{A}{\xi + 2B \cos(4\pi nD w_n)} \text{ and } \Xi = \frac{2B \cos(4\pi nD w_n)}{\xi + 2B \cos(4\pi nD w_n)}. \text{ Both } \Phi \text{ and the}$$

$\Xi$  oscillate at the same frequency as the cosine of  $4\pi nD/\lambda$ .

- 1)  $A = \rho_{1,2}^2 + \rho_{2,3}^2$
- 2)  $B = \rho_{1,2}\rho_{2,3}$
- 3)  $\xi = 1 - B^2$
- 4) if  $\alpha D \ll 1$ ,  $e^{-\alpha D} \rightarrow 1$
- 5)  $\rho_{1,2} < \rho_{2,3} < 1$ ;  $\rho_{1,2}\rho_{2,3} < 1$

$$\text{Equation 9.19} \quad R = \frac{A}{\xi + 2B \cos(4\pi nD / \lambda)} - \frac{2B \cos(4\pi nD / \lambda)}{\xi + 2B \cos(4\pi nD / \lambda)}$$

$$\text{Equation 9.20} \quad R = \Phi - \Xi \propto \cos(2\pi(nD / \lambda))$$

## 9.5 FOURIER TRANSFORM

In both techniques, the spectral reflectivity oscillates periodically according to the wavenumber ( $w_n=1/\lambda$ ) not the wavelength. Fourier analysis is a mathematical transformation based on the principle that periodic signals can be broken down into a series of sinusoidal functions of different frequencies and amplitudes. The Fast Fourier transform (FFT) is a computationally efficient technique in which the Fourier transform of a discrete signal having  $2^N$  points can be calculated with a drastically reduced set of data manipulations. This facilitates real time characterization.

Application of Fourier analysis requires a seemingly unusual approach to the definition of frequency. Traditionally, frequency is defined either temporally or spatially in terms of Hertz (1/second) or inverse distance (1/meter). However, since the oscillations are periodic in wavenumber (1/nm) not wavelength (nm), the mathematical space to which the Fourier is applied is the wavenumber domain. Consequently, the frequency is expressed in inverse spatial dimension or length (nm).

By definition, the Fourier transform,  $F(\omega)$ , of a function,  $f(t)$ , is defined as follows:

Equation 9.21 
$$F(\omega) = \int_{-\infty}^{\infty} f(t)e^{i\omega t} dt$$

where  $t$  is time, and  $\omega$  is the frequency. For example, if  $f(t)$  equals  $\cos(2\pi nt)$  for the range  $t_1$  to  $t_2$  and zero everywhere else, the Fourier transform becomes:

$$\text{Equation 9.22} \quad F(\omega) = \int_{t_1}^{t_2} \cos(2\pi nt) e^{i\omega t} dt$$

Substituting the complex definition of cosine into the equation yields:

$$\text{Equation 9.23} \quad F(\omega) = \int_{t_1}^{t_2} \frac{e^{i(2\pi nt)} - e^{-i(2\pi nt)}}{2} e^{i\omega t} dt$$

Evaluation of this integral,  $F(\omega)$ , yields a pair of sinc functions at the characteristic frequencies  $\pm 1/2\pi n$ . If the function were equal to  $\cos(2\pi nt)$  for the range  $-\infty$  to  $+\infty$ ,  $F(\omega)$  would be a pair of Dirac delta functions at the characteristic frequencies  $\pm 1/2\pi n$ .

Since the FFT is performed on discrete points, there is a finite frequency resolution. The fast Fourier transform of a signal, such as the intensity of spectral reflection, generates an array containing the Fourier coefficients (the amplitudes) of the signal at corresponding discrete frequencies. The frequency with the dominant amplitude is proportional to film thickness ( $D$ ) just as in the Fourier transform shown above. The frequency resolution is dependent on the number of sampled points, the FFT points and the spectral range. Each discrete frequency has an associated index ( $i$ ). The ratio of the sampled points (*sample*) taken at even intervals over a spectral range ( $\Delta w_n$ ), to the number of points in the FFT defines the magnification factor (*Mag*) for the FFT analysis. The number of

oscillations over the given spectral range is defined as the index of the FFT divided by the magnification factor. The calculation of film thickness is trivial once the index of the FFT maximum ( $i_{FFT}$ ) is determined. The film thickness calculation for a film with constant index of refraction ( $n$ ) then becomes:

**Equation 9.24** 
$$D = \frac{i_{FFT} \cdot Mag}{2n \cdot (\Delta w_n)}$$

## 9.6 EXPERIMENTAL SETUP

The spectral reflectometer, shown in Figure 9.3, consists of a 600 MHz computer running Labview 6i<sup>®</sup>, an Ocean Optics<sup>®</sup> S2000 single channel UV-VIS spectrometer containing a 25  $\mu$ m slit, a 600 line grating blazed at 500nm, and 2048 pixel CCD array, a Tungsten-Halogen illuminator connected to a bifurcated illumination-sampling fiber optic, and a fiber optic holder containing collimation lens that projects light onto a sample and collects light for transmission to the spectrometer. The control software utilizes the OOIbase32 driver from Ocean Optics for spectra acquisition and the built-in FFT algorithm from MATLAB<sup>®</sup>. The system has a maximum spectrum acquisition rate of 10 Hz. This can be improved to ~40 Hz with the Ocean Optics High Speed driver (Ooihspl.dll). Normal, 15, 30, and 45 degree incident illumination is accommodated by a custom fiber optic holder designed for multi-angle spectral reflectometry measurements.

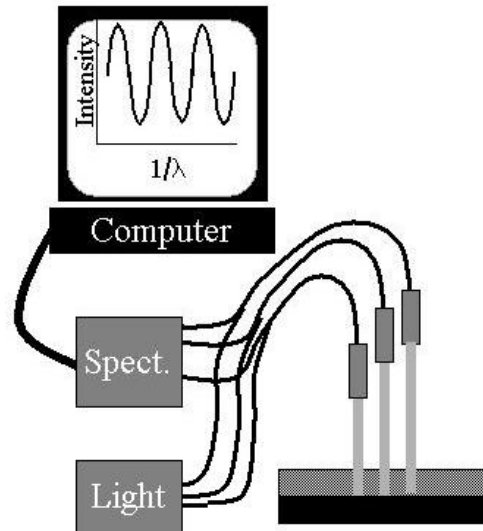


Figure 9.3. *In situ* Spectral Reflectometry System.

The particular application of interest for Step and Flash Imprint Lithography is gap control during actuation of the transparent template toward the silicon substrate coated by the transfer layer. This technique can monitor the orientation of the template with respect to the substrate by acquiring data from a set of three probes spaced at known positions across the surface of the template. The three distances ( $D1$ ,  $D2$ ,  $D3$ ) define the orientation of the template surface with respect to the substrate surface as shown in Figure 9.4.

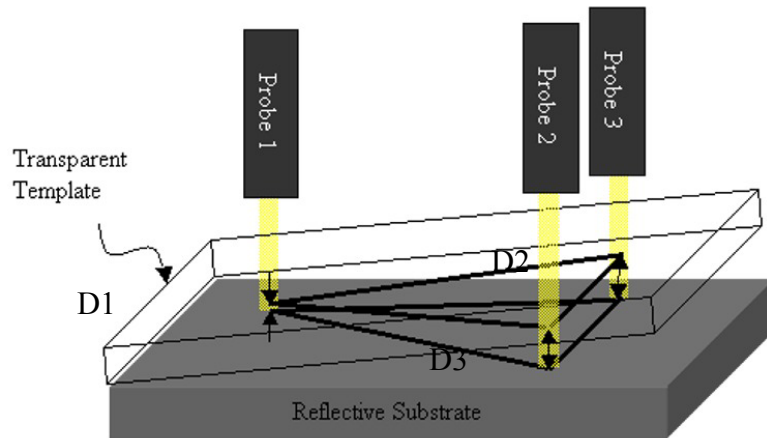


Figure 9.4. Gap Sensing Orientation Measurement.

## 9.7 FFT ANALYSIS SIMULATION

A set of “model” films was simulated and analyzed using the FFT algorithm built into MATLAB® prior to implementation for gap control. The goal of these studies was to determine the conditions under which the FFT analysis would fail to detect the proper thin film thickness. The “model” film thickness ranged from 1000 nm to 25 nm. An incident light had a wavelength from 322 nm to 1064 nm. The film had an index of refraction of 1.5. An example of the resulting signal is shown in Figure 9.5 where (a) is the Intensity vs wavelength, (b) is the Intensity vs wavenumber, and (c) is the FFT of (b). The periodicity of reflectivity in wavenumber is evident in Figure 9.5b and its resulting FFT maximum is easily detected as is shown in Figure 9.5c.

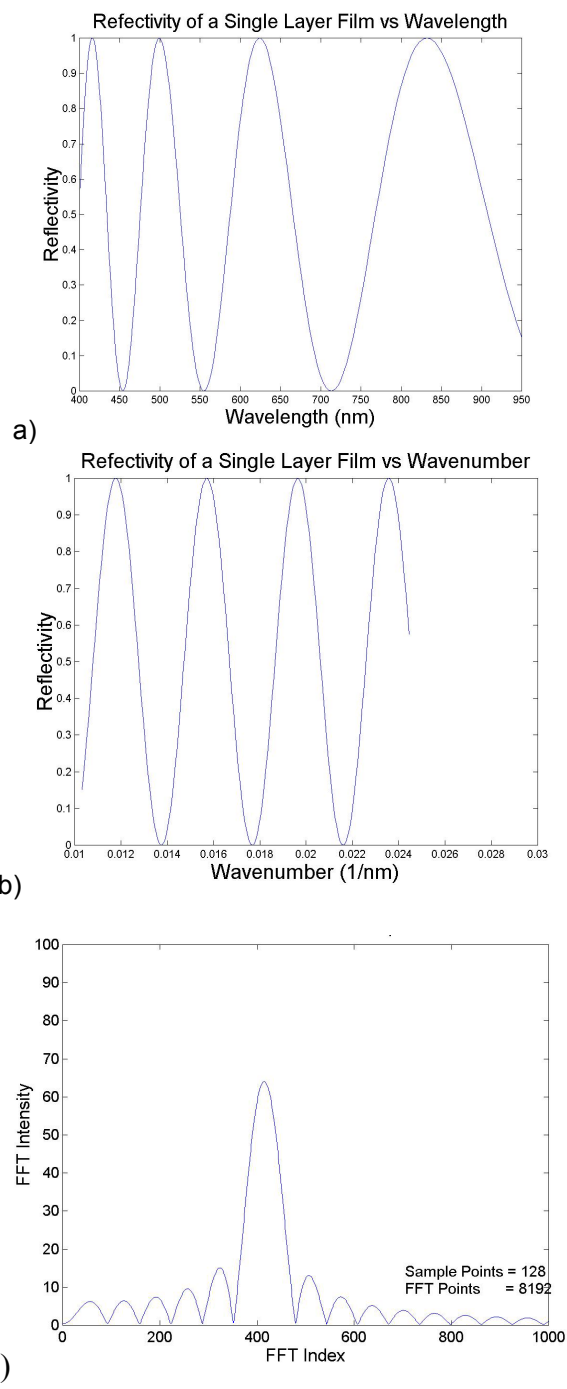


Figure 9.5. Example of Simulated Signal for (a) relative intensity vs wavelength, (b) relative intensity vs wavenumber, and (c) FFT of (b).

Figure 9.6 shows the error in the calculation of thickness as a function of simulated film thickness. The FFT was performed with  $2^{13}$  points and sample sizes of 128. Theoretically, the Fourier transform should fail at an optical path ( $nD$ ) of  $(2 \Delta w_n)^{-1}$ ; at which point there is less than one full period within the sampled wavenumber region ( $\Delta w_n$ ). For this particular simulation, the theoretical minimum optical path length is 231 nm. The results indicate that the FFT failed to detect the proper film thickness within 5% for films less than 250 nm or an optical path length of 375 nm. The spectrometer has a variable wavelength range so smaller gaps could be detected. The lower limit of the detectable optical path length for a spectrometer that samples from 400 nm to 800 nm light is 400 nm. If the film has an index of refractive of 1.6, typical of photoresists, the minimum detectable thickness is 267 nm.

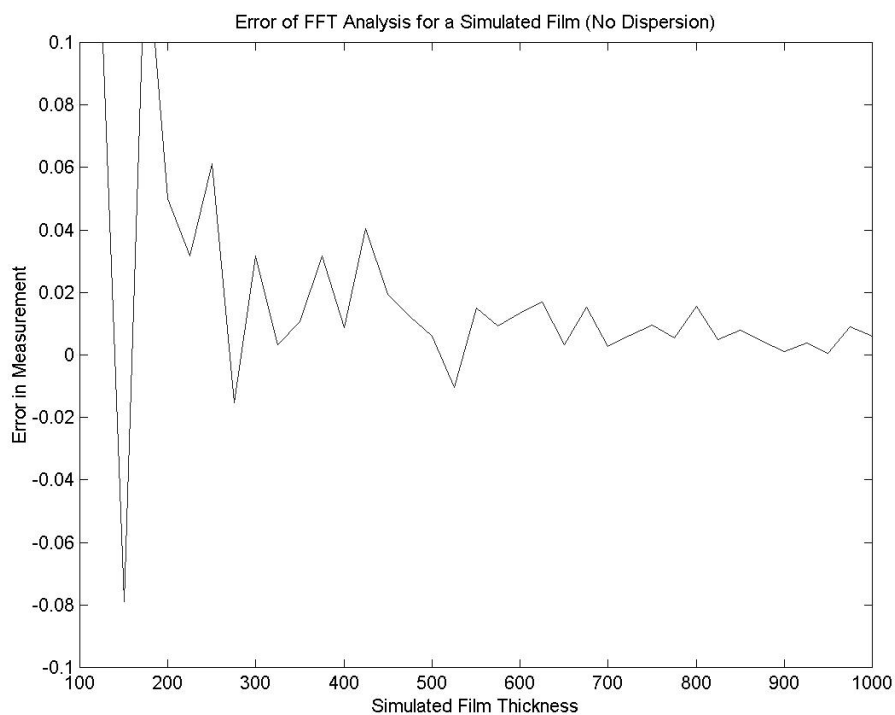


Figure 9.6. Error associated with calculated thin film for a set of ideal films.

The *in situ* FFT analysis of a dissolving film is shown Figure 9.7. The  $2^{13}$  FFT was performed on  $2^7$  sampled points over a wavelength range of 400 nm to 800 nm. The film thickness calculation breaks down at  $\sim 300$  nm. The theoretical minimum is 267 nm; so the experimentally observed minimum thickness accurately measured by the FFT analysis during dissolution rate monitoring is only 10% larger than the theoretical limit.

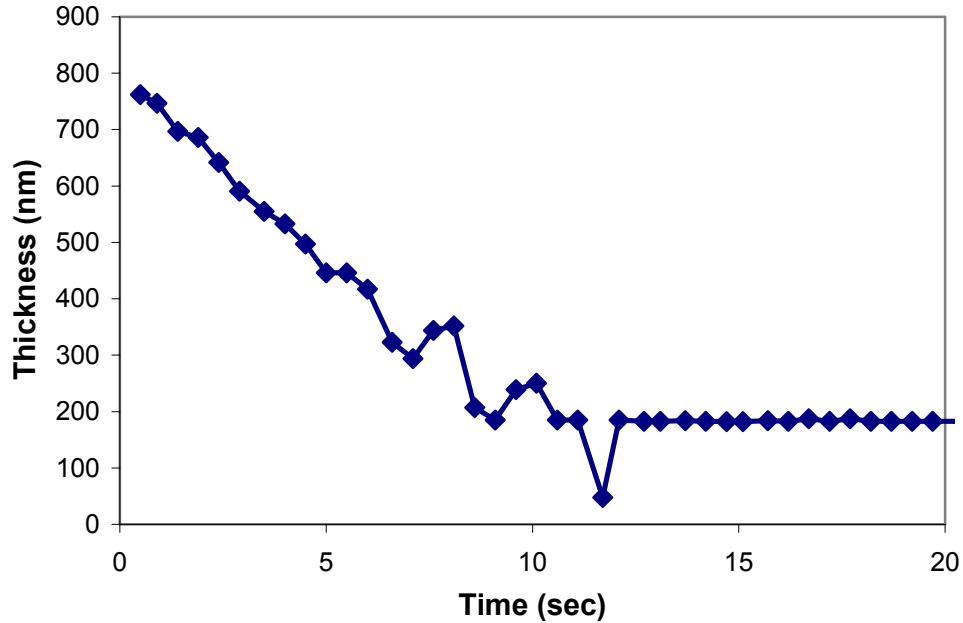


Figure 9.7. Film Thickness of a dissolving film calculated by FFT analysis alone.

### 9.8 EFFECT OF DISPERSION ON FFT ANALYSIS

The simulations described above were performed with a constant index of refraction. However, many films have an index of refraction that is a function of wavelength in the Ultraviolet (UV) to Visible (VIS) wavelength range. The real component of the refractive index is typically modeled using the Cauchy coefficients (A, B, and C) that describe the dispersion of  $n(\lambda)$  as a series expansion.

Equation 9.25 
$$n(\lambda) = A + \frac{B}{\lambda^2} + \frac{C}{\lambda^4}$$

Here,  $A$ ,  $B$ , and  $C$  are derived from least squared regression applied to data collected over a specific wavelength range. The effect of dispersion is important to understand if the gap sensing technique is to be applied to a variety of films.

A set of simulations was run on films where the index of refraction for the FFT analysis was set to  $1.5 + B/\lambda^2$  and  $B$  was set to 0,  $0.001 \mu\text{m}^2$ ,  $0.005 \mu\text{m}^2$ ,  $0.01 \mu\text{m}^2$ , and  $0.02 \mu\text{m}^2$ . The  $C$  parameter is usually quite small and has been neglected for these simulations. The results of these simulations are shown in

Table 9.1. Incorporating the second Cauchy coefficient has a significant effect on the calculated film thickness when  $B$  is greater than  $0.001 \mu\text{m}^2$ . This value resulted in calculated thickness errors greater than 5% of the films true value.

Fortunately, the index of refraction relevant to a FFT analysis of wavenumber linearly sampled data can be calibrated based on a single film of known thickness or the dispersion can be measured by spectral ellipsometry. An example of the linear calibration is shown in Table 9.2. Five films were spin coated with a photoresist. A single film was calibrated by measuring its film thickness by ellipsometry. The error in measurement is also shown. It should be noted that the characteristic index can also be calibrated by profilometry. Thus, the measurement is valid without knowing the Cauchy coefficients and can be extrapolated to all films of the sample composition.

Table 9.1. Error Associated with FFT analysis using different estimates of indices.

<i>Case</i>	$n(\lambda)$	<i>Slope (nm)</i>	$\langle n_{wn} \rangle$	<i>Error</i>	$n_{max}$	<i>Error</i>
A	$1.5 + 0.0001/\lambda^2$	1.508	1.5005	0.5%	1.501	0.71%
B	$1.5 + 0.001/\lambda^2$	1.528	1.5053	1.5%	1.510	1.52%
C	$1.5 + 0.01/\lambda^2$	1.621	1.5264	6.2%	1.548	5.05%
D	$1.5 + 0.005/\lambda^2$	1.740	1.5529	12.1%	1.596	9.37%
E	$1.5 + 0.02/\lambda^2$	1.991	1.6057	24.0%	1.693	17.99%

Table 9.2. Error associated with single thickness calibration.

Ellipsometry (nm)	Reflectometry (nm)	Error (%)
1022.6	1051	3%
840.6	841	Calibration
735.7	689	-6%
591.7	572	-3%

To improve the accuracy of the calculation for films for which the Cauchy coefficients are known, the sampled data sent to the FFT algorithm can be linearly sampled from the spectrum defined by  $2n(\lambda)/\lambda$  rather than  $1/\lambda$ . This results in a FFT maximum that is directly proportional to the thickness by the Equation 9.26 when  $\Delta w_n$  is defined by  $2n(\lambda)/\lambda$ . The error associated with this analytical technique was less than 0.3% for first Cauchy coefficients of 1.5, 1.6, and 2.0 and a second Cauchy coefficient of  $0.02 \mu\text{m}^2$ . This is shown in Table 9.3. This method was shown to be more robust if the Cauchy coefficients are known accurately. It should be noted that for the application of sensing an air gap, this method is not necessary since the index of air is constant over the wavelengths of

interest. In fact, this method was developed independently by Filmetrics and is now incorporated in their commercially available tool [10].

**Equation 9.26** 
$$T = \frac{Mag}{\Delta w_n} i_{FFT}$$

Table 9.3. Error associated with the  $n(\lambda)/\lambda$  sampling method for a range of Cauchy coefficients.

<i>Case</i>	$n(\lambda)/\lambda$	<i>Slope (nm)</i>	<i>Error</i>
F	$1.5/\lambda + 0.02/\lambda^3$	1.0030	0.31%
G	$1.6/\lambda + 0.02/\lambda^3$	1.0028	0.35%
H	$2.0/\lambda + 0.02/\lambda^3$	1.0022	0.24%

## 9.9 EFFECT OF FFT PARAMETERS ON ANALYSIS

The quality of the signal, the number of sampling points, and the number of points in the FFT directly affect the resolution, sensitivity, accuracy, precision and speed of the analysis. In an effort to understand these tradeoffs, statistical data on the mean and standard deviation of the FFT peak was determined for films with different thicknesses. The signal strength, processing time, precision and resolution of the FFT technique were evaluated as a function of sample size and FFT points. The sample size ranged from  $2^4$  to  $2^{10}$ . The FFT points ranged from  $2^{12}$  to  $2^{16}$ .

The following observations were made. The signal strength improves with the sample size but is independent of FFT points. The process time is strongly dependent on the number of points in the FFT since the FFT performs ( $N$

$\log N$ ) data manipulations. The precision of the measurement improves with sample size but is weakly affected by FFT points over the range tested. The resolution ( $R$ ) of frequency improves with the ratio of FFT points to sample size and is described by the following relationship.

**Equation 9.27** 
$$R = \frac{Mag}{\Delta w_n}$$

According to these observations, there is a trade-off among speed, precision, signal strength, and resolution. Consequently, an optimum solution must be designed for the particular application. In the case of gap sensing, a 128 sample size and  $2^{14}$  FFT points provides a measurement that operates at the limiting speed of the spectral data acquisition ( $\sim 10$  Hz), a precision better than 0.5%, a signal-to-noise ratio of 100:1, and resolution of 6.25 nm. The resolution can be improved by reducing the sampling or increasing the number of FFT points. The analysis time for  $2^7$  samples and  $2^{14}$  FFT points on a 600 MHz computer with 128 MB of RAM ranges from 20 to 50 milliseconds with the average less than 30 milliseconds.

### **9.10 INFLECTION-MAXIMUM-MINIMUM ANALYSIS (IMMA)**

The FFT algorithm analysis is quite robust but it does have a lower limit. It fails to accurately measure a gap when the oscillation of the reflectivity has less than one full period within the sampled wavenumber range. In order to overcome this problem and extend the lower limit of the measurable film thickness, it is

possible to implement a simple regression to find a local minimum ( $w_1$ ) or maximum point ( $w_2$ ) in the reflectivity between  $w_{n,min}$  and  $w_{n,max}$  and thereby compute the period information. The slope of reflectivity is zero at  $w_1$  and  $w_2$ . The reflectivity of Equation 9.15 has its maximum at  $w_n$  equal to 0 (infinite wavelength). This point is not physically significant but it is important from the point of analysis because it allows the film thickness to be calculated from a single extrema or inflection point within the sampled spectral range.

Inflection-Maximum-Minimum-Analysis (IMMA) is based on the calculation of the period ( $P$ ) of the spectral reflectivity oscillation. The period is most easily defined by the inflection points or extrema (maximum, minimum) points. From the simplified reflectivity, the period,  $P$ , is defined by the following equation.

**Equation 9.28** 
$$P = \frac{\theta}{2\pi} = \frac{2\pi(2nD\Delta w_n)}{2\pi} = 2nD\Delta w_n$$

Further, if the wavenumber range ( $\Delta w_n$ ) of the spectrometer is larger than  $w_{min}$ , the oscillation length of the reflectivity data between 0 -  $w_{min}$  is smaller than that of  $\Delta w_n$ . Certain inferences can be made regarding the reflectivity. These are detailed in Table 9.4. If multiple points (extrema or inflections) are detected, each can be utilized to calculate the film thickness and provide an estimate of the error in the calculation.

The description above is based on constant index of refraction, the  $n(\lambda)/\lambda$  sampling is again valid for IMMA. Since IMMA works on the same fundamental principle of periodicity as the FFT analysis, IMMA will also be unaffected by the  $n(\lambda)/\lambda$ . The output of the analysis, as with the FFT, is thickness rather than optical path.

Table 9.4. Logic used to calculate optical path (nD). (I<sub>down</sub> = negative inflection point, I<sub>up</sub> = positive inflection point, Min = minimum point, Max = maximum point,  $\phi$  = one full period)

	<b>IMMA Results</b>	<b>Calculation of wavelength</b>
1	I <sub>down</sub>	I <sub>down</sub> = $\frac{1}{4} \phi$
2	I <sub>down</sub> , Min	I <sub>down</sub> = $\frac{1}{4} \phi$ , Min = $\frac{1}{2} \phi$
3	Min	Min = $\frac{1}{2} \phi$
4	Min, I <sub>up</sub>	Min = $\frac{1}{2} \phi$ , I <sub>up</sub> = $\frac{3}{4} \phi$
5	Min, I <sub>up</sub> , Max	Min = $\frac{1}{2} \phi$ , I <sub>up</sub> = $\frac{3}{4} \phi$ , Max = $\phi$
6	I <sub>up</sub> , Max	I <sub>up</sub> = $\frac{3}{4} \phi$ , Max = $\phi$
7	I <sub>up</sub> , Max, I <sub>down</sub> (I <sub>down</sub> > I <sub>up</sub> )	I <sub>up</sub> = $\frac{3}{4} \phi$ , Max = $\phi$ , I <sub>up</sub> = $\frac{5}{4} \phi$
8	All	I <sub>up</sub> = $\frac{3}{4} \phi$ , Max = $\phi$ , I <sub>up</sub> = $\frac{5}{4} \phi$ , Min = $\frac{3}{2} \phi$
9	Max, I <sub>down</sub> , Min (Min > Max)	Max = $\phi$ , I <sub>up</sub> = $\frac{5}{4} \phi$ , Min = $\frac{3}{2} \phi$
10	All ( I <sub>up</sub> > I <sub>down</sub> )	Max = $\phi$ , I <sub>up</sub> = $\frac{5}{4} \phi$ , Min = $\frac{3}{2} \phi$ , I <sub>down</sub> = $\frac{7}{4} \phi$
11	Multiple I <sub>up</sub> , I <sub>down</sub> , Min, or Max	$\Delta$ Max = $\phi$ , $\Delta$ I <sub>up</sub> = $\phi$ , $\Delta$ Min = $\phi$ , $\Delta$ I <sub>down</sub> = $\phi$

## 9.11 PHASE ANGLE CALCULATION (PAC)

Like the FFT analysis, IMMA has a lower limit. It is initiated when the thickness and the optical density can no longer be reliably calculated using FFT analysis, which occurs at an optical path length of 400 nm for the current spectrometer configuration. However, IMMA requires at least one inflection point from which the wavelength of the signal can be calculated. So, IMMA can theoretically measure the optical path down to the point at which only an inflexion point with a negative slope can be detected within the sampled spectral region. Assuming a constant index, this occurs when  $\frac{8nD}{\lambda}$  equal 1. For a spectrometer with a spectral range of 400 nm to 800 nm, the lower detectable optical path length for IMMA is 50 nm.

In the SFIL application, a template starts at several microns from a substrate and is lowered into direct contact with the substrate. Measurement of gaps that have an optical path length less than 50 nm requires another technique that was developed, called **Phase-Angle-Calculations (PAC)**. This analysis is based on monitoring the phase angle to determine the thickness of the film. The technique uses monochromatic reflectivity data from measurements of wider gaps to extend the calculations to thickness less than 50 nm. We can calculate the phase angle values and directly determine the absolute film thickness from the equation below where  $I_{\lambda}$  is the intensity at the wavelength,  $\lambda$ .  $I_{min}$  and  $I_{max}$  are the

minimum and maximum of the intensity at the wavelength,  $\lambda$ , over the time frame of the measurements. Since PAC utilizes monochromatic light, the effect of dispersion is not applicable. However, the index of refraction at  $\lambda_{\min}$  must be known prior to implementation of PAC. Otherwise, back calculations can be used to calibrate PAC to a given film. It should be noted that PAC performs like a single wavelength interferometer and must be used in a “scanning” mode in order to collect the required Intensity information and to calculate the phase properly.

**Equation 9.29**

$$Phase = \cos^{-1}\left(\frac{I_{\lambda} - I_{\min}}{I_{\max} - I_{\min}}\right) = \frac{2nD}{\lambda}$$

## 9.12 EXPERIMENTAL RESULTS

### 9.12.1 Dissolution Rate Monitor (DRM)

The FFT-IMMA-PAC analysis technique is well suited for monitoring the dissolution of a photoresist. In a demonstration, a wafer was spin coated with PFI88a5 resist for 30 seconds at 2000 RPM, post-application baked at 90°C for 90 seconds, exposed to 100 mJ/cm<sup>2</sup> with 365 nm ultraviolet light, and post exposure baked at 110°C for 90 seconds. The wafer was developed in 0.26 N TMAH (AZ 300 MIF) developer while the film thickness was monitored by spectral reflectivity. Figure 9.8 shows the thickness of a rapidly dissolving photoresist film calculated in real time by the FFT-IMMA-PAC algorithms. The average time required to analyze each spectral data was 20 mseconds.

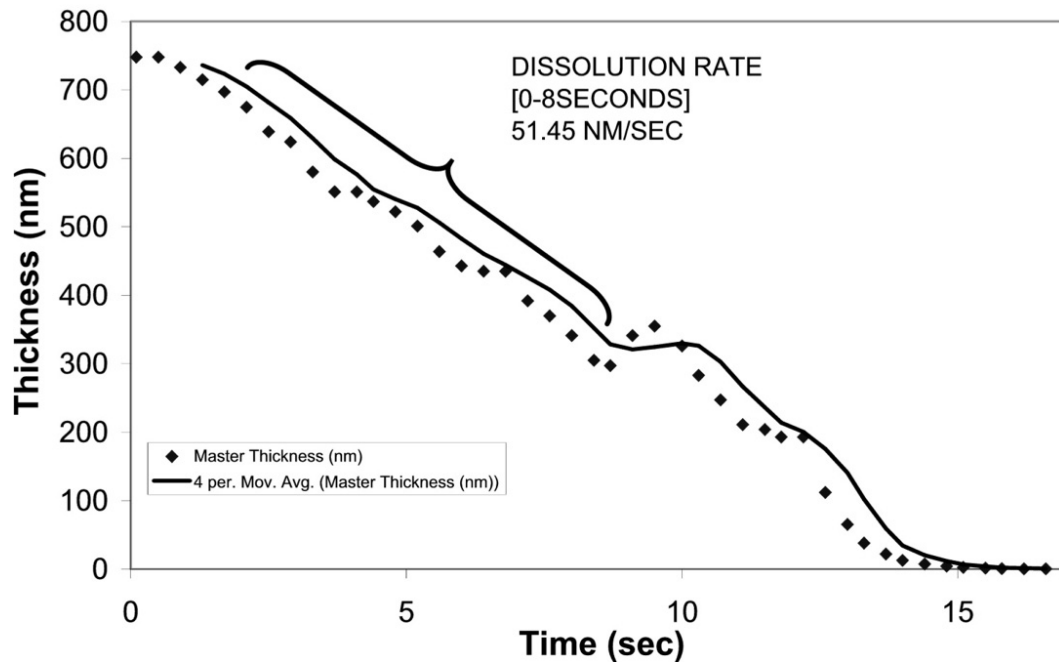


Figure 9.8. Thickness of a dissolving film was calculated *in situ* analysis.

### 9.12.2 Static Film Thickness Characterization

A set of i-120 photoresist films were cast by spin coating at 500, 1000, 1500, 2000, and 3000 RPM for 30 seconds. The films were baked at 90°C for 90 seconds to drive off excess solvent. A second set of BARLi antireflective coatings was cast by spin coating diluted at 2000 RPM for 30 seconds. These films were baked, according to the manufacturer's recommended coating procedure, at 170°C for 4 minutes to remove solvent and to crosslink the film. The thickness of the films were measured by profilometry, ellipsometry, and the

real time reflectometry (using Cauchy coefficients measured by the spectral ellipsometer).

Table 9.5 displays the corresponding thickness measurements. These indicate that the FFT-IMMA technique offers both precision and accuracy and can be implemented with comparably inexpensive hardware. The real time FFT method measures the average film thickness even with a large degree of film non-uniformity. Films of i120-500 RPM and BARLi-E were highly non-uniform due to the low spin speed and as a result abnormal measurements of film thickness by ellipsometry.

Table 9.5. Static film thicknesses (nm) measured by FFT-IMMA combined algorithm.

Film	Spectral Ellipsometry (nm)	Profilometry (nm)	Real Time Reflectometry (nm)
i120 – 1000 RPM	1022.6	1090	1098
i120 – 1500 RPM	840.56	850.5	878
i120 – 2000 RPM	735.68	747	720
i120 – 3000 RPM	591.66	1619	598
i120 – 4000 RPM	552	563	624
PMMA	192.03	205	221.2
PS	219.46	271.5	252.8
BARLi – A	192.03	197.5	221.2
BARLi – B	142.65	173.5	164.3
BARLi – C	301.76	316.5	347.6
BARLi – D	274.32	330	316.0

### 9.12.3 Active Test Bed Gap Sensing

The gap between the template and the substrate has been successfully measured using the FFT analysis. A template held in a 2-degree of freedom ( $Z, \alpha$ ) stage was actuated through both an air gap and a water filled gap [11]. Two probes positioned on opposite side of the tilt axis were monitored. The gap height in air and in water is shown in Figure 9.9 a) and b) respectively. The air gap starts at approximately  $2.5 \mu\text{m}$  and decreases over the course of 1.2 seconds to a level of 500 nm. For the water gap, the two sides of the template start at approximately  $2.5 \mu\text{m}$  and  $5.0 \mu\text{m}$  and decrease over the course of 1.2 seconds to a level of  $1.5 \mu\text{m}$  and  $2.5 \mu\text{m}$ , respectively. The force measured during actuation through air is plotted against the measured thickness in Figure 9.9c. The force increased significantly before the template-substrate gap approached zero. This indicates either particle contamination or template tilt in the  $\beta$ -direction. Either situation would cause a portion of the template to come in contact with the substrate prior closing the gap.

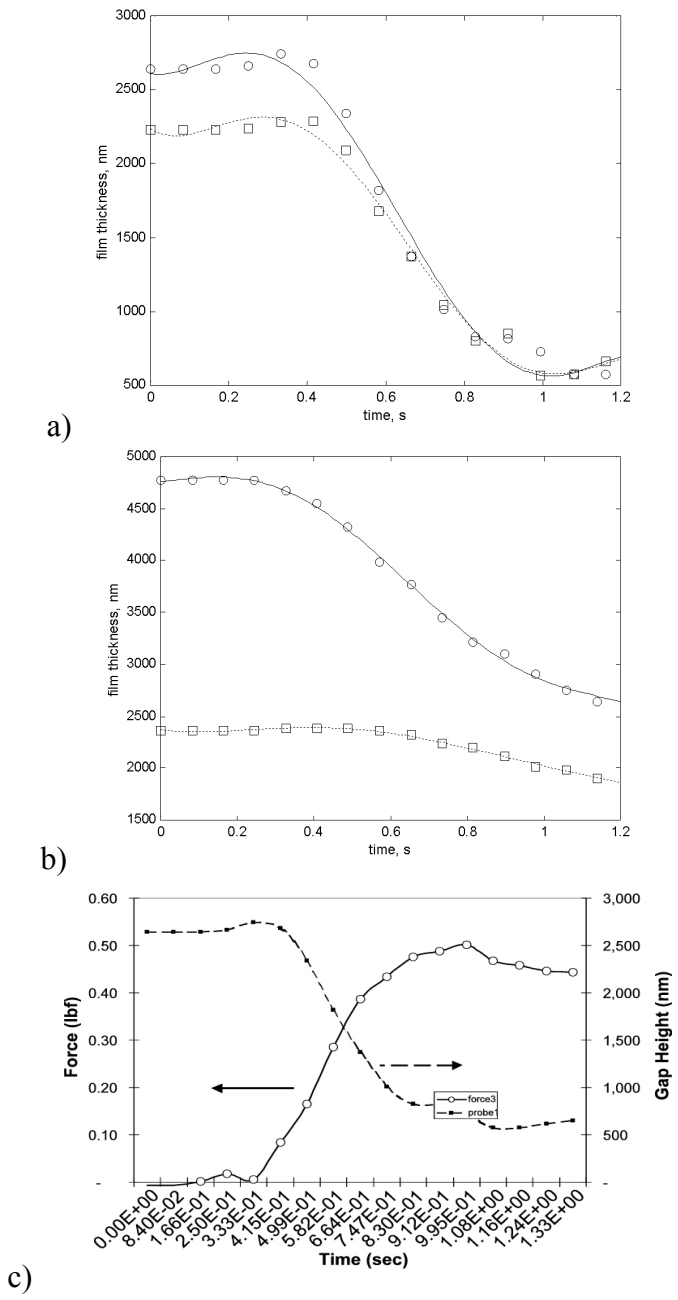


Figure 9.9. Gap measurement through a transparent template. a) Air Gap, b) Water Gap, and c) Overlay of measured force and gap height.

### 9.13 CONCLUSIONS

The real time film thickness method based on an FFT algorithm has proved useful for XRR [9] and now for UV-VIS reflectometry as well. The technique has been successfully applied to static film measurements, the DRM, and gap sensing. The IMMA algorithm successfully determined the thickness of a film that was below the intrinsic resolution of the FFT algorithm. The PAC algorithm was successfully used to measure the thickness of a dissolving film in the region below 50 nm. The three algorithms, FFT, IMMA, and PAC, combine to form a valuable gap-sensing instrument. The useful range for each algorithm is shown in Table 9.6 for constant index of refraction and in Table 9.7 for materials of known dispersion.

Table 9.6. Optical Path (nD) over which each algorithm is utilized if the index is constant.

Algorithm	Maximum Optical Path Length (nm)	Minimum Optical Path Length (nm)
FFT	$\frac{Sample}{10\Delta w_n}$	$\frac{1}{2\Delta w_n}$
IMMA	$\frac{9\lambda_{min}}{8}$	$\frac{\lambda_{min}}{8}$
PAC	$\frac{\lambda_{min}}{4}$	0

Table 9.7. Optical Path (nD) over which each algorithm is utilized if the film exhibits dispersion.  $\Delta w_n$  is defined at  $\left( \frac{n(\lambda_{\min})}{\lambda_{\min}} - \frac{n(\lambda_{\max})}{\lambda_{\max}} \right)$ .

Algorithm	Maximum Thickness (nm)	Minimum Thickness (nm)
FFT	$\frac{\text{Sample}}{10\Delta w_n}$	$\frac{1}{2\Delta w_n}$
IMMA	$\frac{9\lambda_{\min}}{8n(\lambda_{\min})}$	$\frac{\lambda_{\min}}{8n(\lambda_{\min})}$
PAC	$\frac{\lambda_{\min}}{4n(\lambda_{\min})}$	0

#### 9.14 FUTURE WORK

While the proof-of-concept for the real time gap sensing device is complete, much improvement and advancement is possible. The stability of the dissolution rate calculation can be improved. Namely, the transitions between the IMMA and FFT, and IMMA and PAC should be improved. While the gap measurement tool appears to be successful in determining the gap thickness greater than 500 nm, additional experiments must be performed on sample that approach a gap of zero.

The speed of the spectral reflectometry while not rate limited by the analysis is limited by the data acquisition. A high-speed driver (OOIHSP.dll) available from Ocean Optics enables high-speed acquisition speed of 40+ Hz. A preliminary version of this software has been developed. Unfortunately, due to the method in which the acquisition software stores the spectra, this driver can only be used for post-acquisition analysis.

Advanced features such as the multiangle analysis (See Appendix 10) would eliminate the need for knowledge of the Cauchy coefficients and decreases the minimum thickness that can be measured by FFT and IMMA. Further adaptation of this system could be incorporate into a dual-mode gap sensing system in which high speed relative displacement monitoring is performed by an interferometer and the absolute position is periodically verified by spectral reflectometry [12]. Such a system would be useful for deposition or etch rate monitoring applications.

The Fourier analysis is also ideal for monitoring the thicknesses of individual films in a multilayer stack. Below is an example of a bilayer film analyzed by FFT in the wavenumber domain. The bottom film is an antireflective coating and the top film is a novolak photoresist. The position of the FFT maxima indicate that the novolak is approximately 8 times thicker than the BARLi film. The ability to break out the thickness of the two films may be quite valuable.

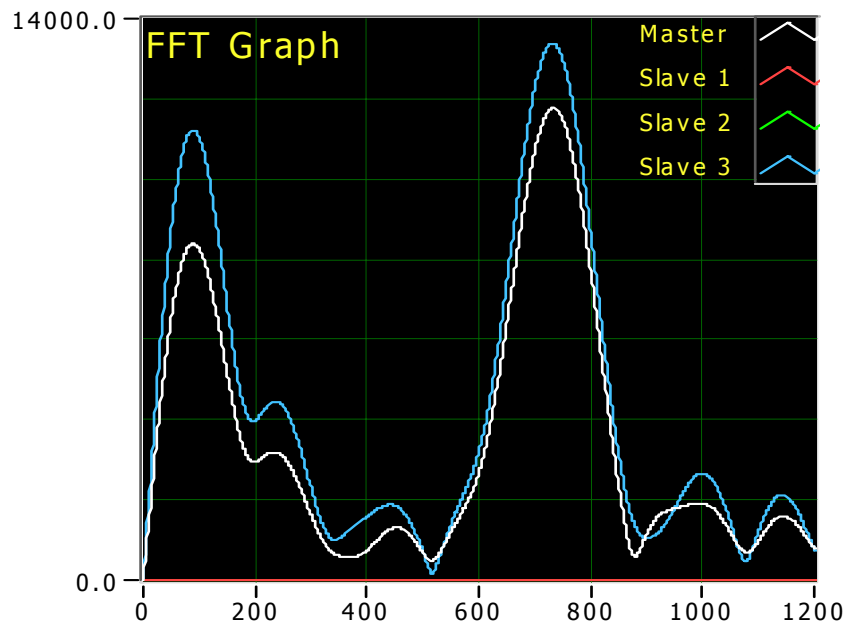


Figure 9.10. FFT of the spectral reflection from a bilayer film stack.

## References

---

- 1 Francon, M.; Optical Interferometry. Academic Press, NY (1966)
- 2 Tompkins, H.G.; W. A. McGahan. Spectroscopic Ellipsometry and Reflectometry, A User's Guide. Wiley, NY (1999)
- 3 Tsairtas, P. C.; *Dissolution Behavior of Phenolic Polymers Used in Positive Tone Semiconductor Microlithography*. The University of Texas at Austin (1998)
- 4 Scheer, S.; *Development of a multiwavelength dissolution rate analysis tool*. The University of Texas at Austin (2000)
- 5 Konnerth, K. L.; Dill, F. H. "In-Situ Measurement of Dielectric Thickness During Etching and Developing Processes," *IEEE Trans. Electron Devices*, ED-22, No. 7, 452-456 (1975)
- 6 Mack, C. A.; Lecture Notes from "Semiconductor Microlithography," The University of Texas at Austin. (2001)
- 7 Konnerth, K.L; F.H. Dill. *Solid-State Electronics*, 15, 371-380 (1972)
- 8 Sakurao, K.; A. Itada. "Fourier Analysis of Interference Structure in R-ray Specular Reflection From Thin Films," *Jap. J. Appl. Phys. 2 Let.* **31**(2A) L113-5, (1992)
- 9 Bouldin, C. E.; W. E. Wallace, G.W. Lynn, S.C. Lynn, S.C. Roth, W.L. Wu. "Thermal expansion coefficients of low-k dielectric films from Fourier analysis of x-ray reflectivity," *J. Appl. Physics.* **88**(2) 691-695 (2000)
- 10 Chambers, C.; "Rapid and accurate thin film measurement of individual layers in a multilayered or patterned sample," *U.S. Patent No.* 6,204,922. March (2001)
- 11 Nguyen. A. Q.; "Asymmetric Fluid-Structure Dynamics in Nanoscale Imprint Lithography," MS. Thesis. The University of Texas at Austin, August (2001)
- 12 Kerwick, M.; "Real-time gap sensing by multiwavelength interferometry," MS Thesis. The University of Texas at Austin (2001)

## 10 Patterning Results and Conclusions

### 10.1 PATTERNING RESULTS

The SFIL process has been developed based on experimental validation of theoretical considerations. Using etch barrier formulations that exhibit tremendous etch selectivity, preferential release from the template, rapid displacement under applied pressure, and mechanical properties consistent with faithful replication, several examples of SFIL's patterning capabilities are presented below.

#### 10.1.1 Replication Resolution

First, an example of the resolution capability of the replication process is shown in Figure 10.1 [1]. These features were replicated onto a transfer layer of HR100 (Olin) using the original single imprint apparatus. The template was manufactured using a process similar to that described in Chapter 2. The etch barrier composition for this sample was 50% poly(acryloxypropylmethylsiloxane-co-dimethyl siloxane) (UMS-U22, Gelest), 25% (3-acryloxypropyl-trimethylsiloxane)silane (SIA0210, Gelest), 25% *n*-butyl acrylate to which 3% of a 1:1 mixture of bis(2,4,6-trimethylbenzoyl)phenylphosphine oxide (Irgacure 819, Ciba) and 1-benzoyl-1-hydroxycyclohexane (Irgacure 184, Ciba) were added by weight and it was exposed for ~60 seconds (~60 mJ/cm<sup>2</sup>). Close evaluation of this cross section reveals that sub-25 nm defects in the template that resulted from field-to-field stitching errors were replicated faithfully in the etch

barrier. So, while the features shown here are ~150 nm wide, the fidelity of the process is shown to be even higher.

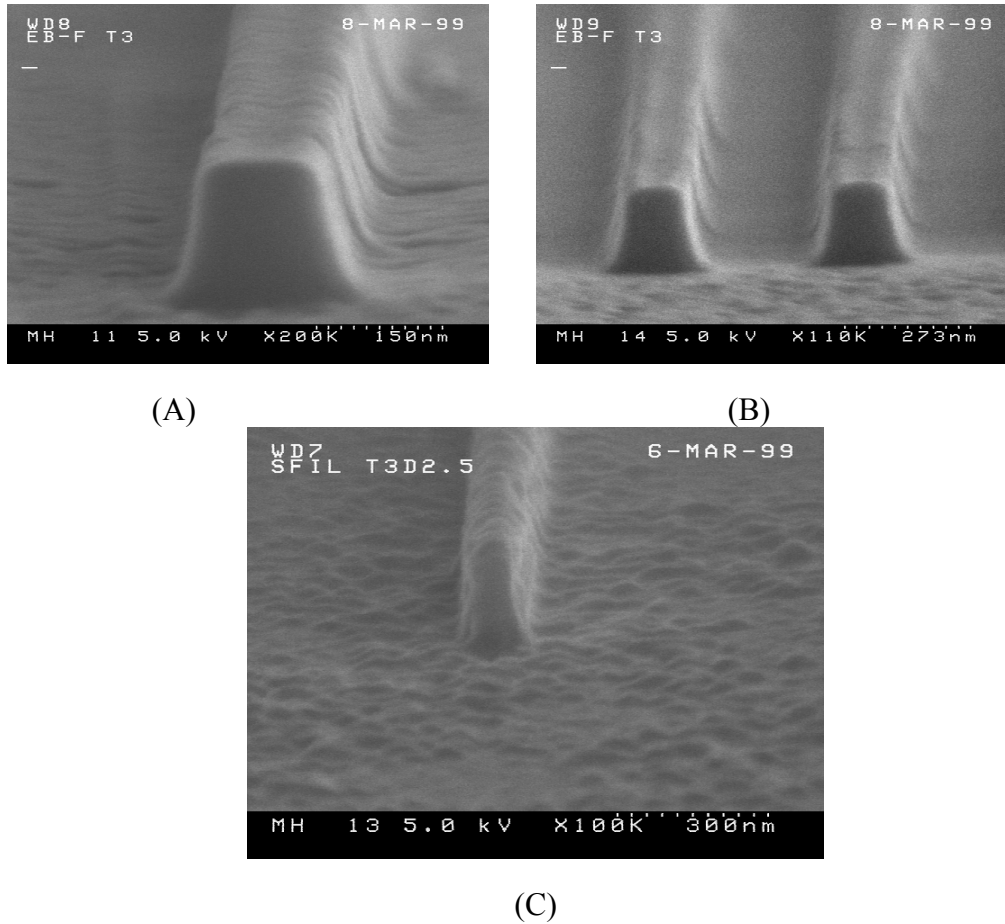


Figure 10.1. Replication resolution demonstration. (A) 135 nm wide feature replicated in the etch barrier. (B) Lower resolution of (A) shown the repeating stitching error that demonstrate sub-25 nm fidelity of the replication process. (C) 60 nm feature that is ~190 nm tall replicated in the etch barrier. All samples were coated with Au for imaging by SEM.

### 10.1.2 Etch Transfer Resolution

Once the replication resolution was completed with this template, the collaboration with Agilent Technologies began for the RIE process development. With the etch barrier reformulated for the Agilent imprint equipment, an 100 nm deep 100 nm line-and-space template was replicated on a 1.4 micron thick PMMA layer during the etch-stop experiment. The 14:1 aspect ratio features remain the highest aspect ratio features produced by SFIL. While the bottom of the features was not perfectly etched, it does demonstrate the benefit of the SFIL bilayer process for creating high aspect ratio features.

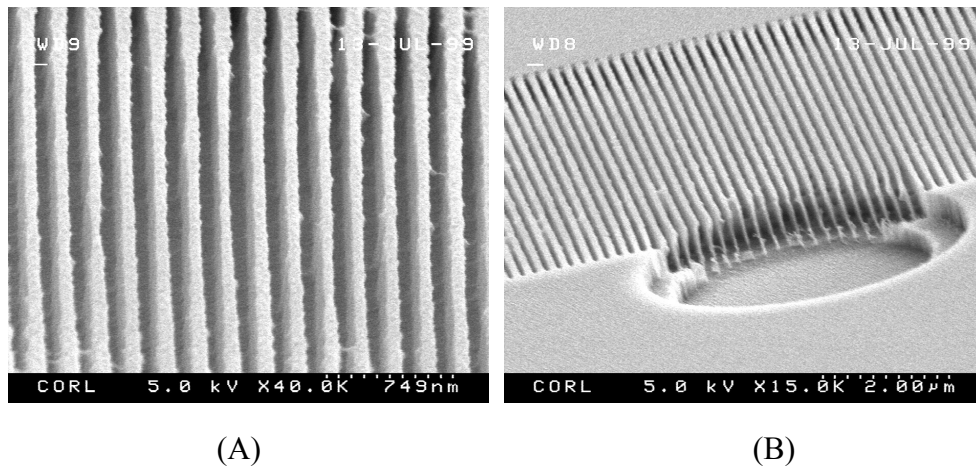


Figure 10.2. (A) Top-down SEM of 14:1 aspect ratio features etch transferred through 1.4 micron thick PMMA. (B) Tilt SEM of a defect region that shows the aspect ratio more clearly [2].

A high-resolution template was made in GaAs that consists of 90 nm deep 60 nm wide lines on a 200 nm pitch. The shape of the lines in the daughter template was nearly triangular as is shown in Figure 10.3. The etch transferred

features, which were shown in Chapter 8, are shown again in cross-section in Figure 10.4. The features have an aspect ratio of  $\sim 6:1$ .

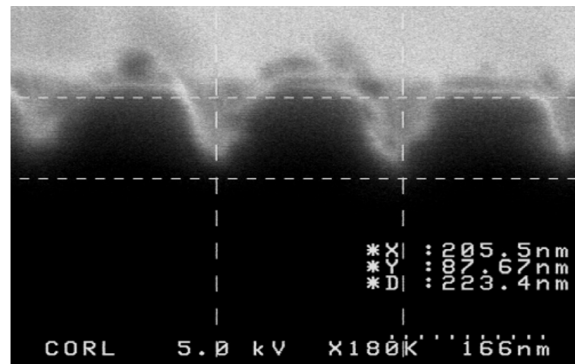


Figure 10.3. Cross-section of the GaAs template.

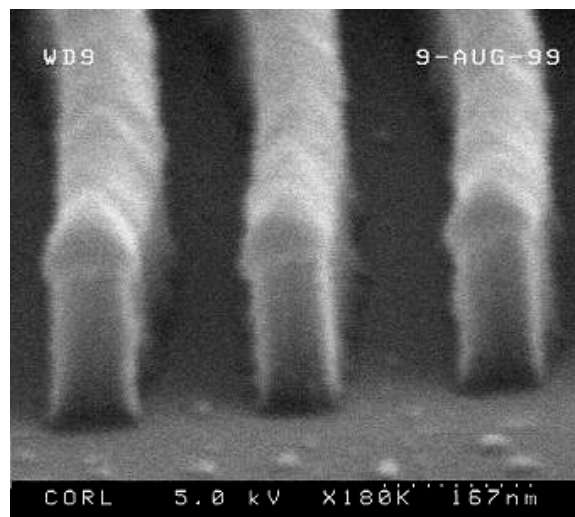


Figure 10.4. Cross-section of the transferred structure.

Additive metalization was then performed on features similar to those shown above. In this process, the features are covered with a layer of metal in an

anisotropic way such that the feature side remain free of metal and are subject to dissolution. This process is shown schematically in Figure 10.5.

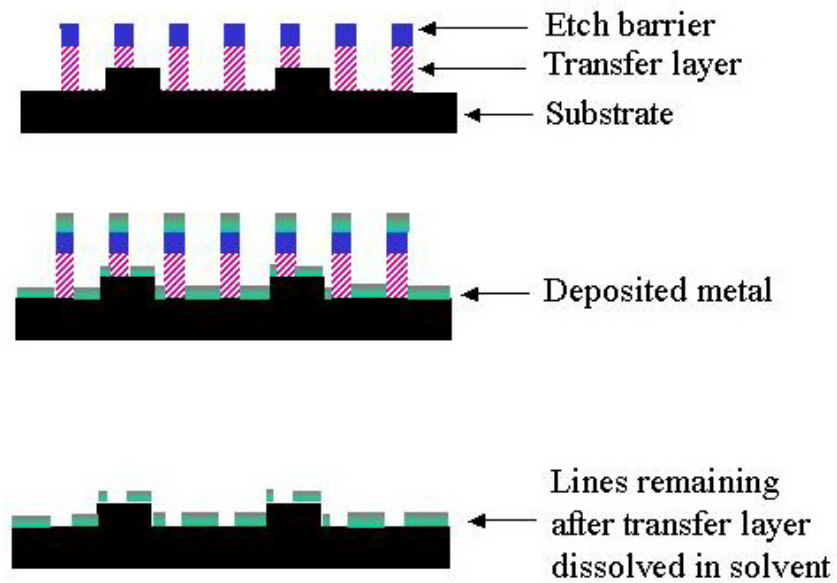


Figure 10.5. Additive metalization process.

Using this process on an array of 100 nm lines that were 100  $\mu\text{m}$  in length and supported every 20  $\mu\text{m}$  by 5  $\mu\text{m}$  support struts produced the micropolarizer array shown in Figure 10.6.

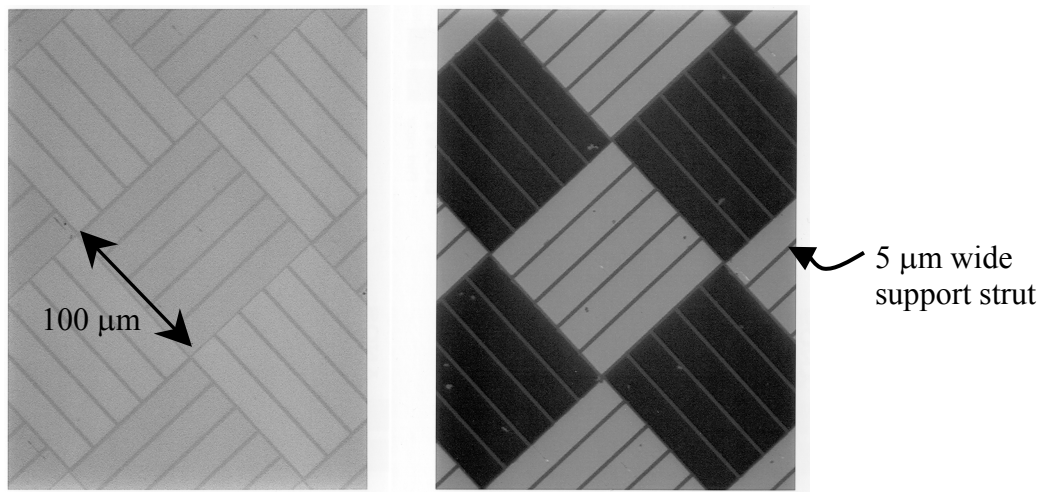


Figure 10.6. Micropolarizer array consisting of orthogonal 100 nm lines and spaces shown illuminated with non-polarized light (left) and polarized light (right).

The SFIL process is useful to fabrication of other optoelectronic devices as well. More recently, Dr. Annette Grot of Agilent Laboratories applied the SFIL process to the fabrication of a photonic crystal shown in Figure 10.7 [3]. Other potential applications include diffractive grating, waveguides, and dense wavelength division multiplexors (DWDMs).

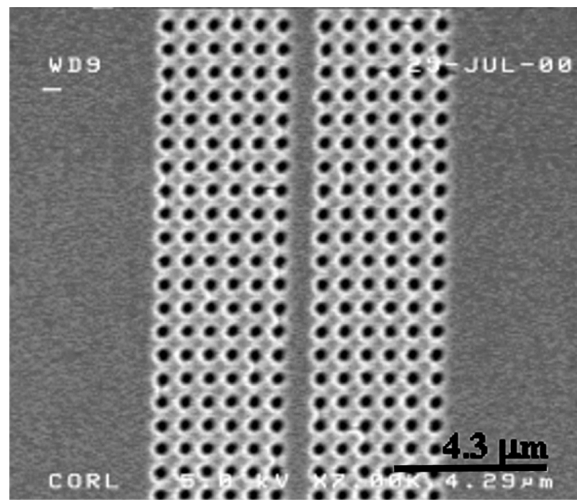


Figure 10.7. Photonic crystal fabricated by SFIL at Agilent Technologies.

### 10.1.3 Non-flat patterning

Two types of non-flat patterning have been performed with SFIL. In the first method, developed in collaboration with Agilent, a layer of PMMA was spin coated on substrates bearing a topography and hard-baked at 200°C for 2-4 minutes. A UV crosslinkable organic film was coated on the substrate and cured through the backside of a *featureless* (flat) template. This process planarizes the substrate. The planarized substrate is then patterned using the standard SFIL process using a template with topography. Finally, this relief structure is etch transferred through the imprinted planarization layer, the transfer layer.

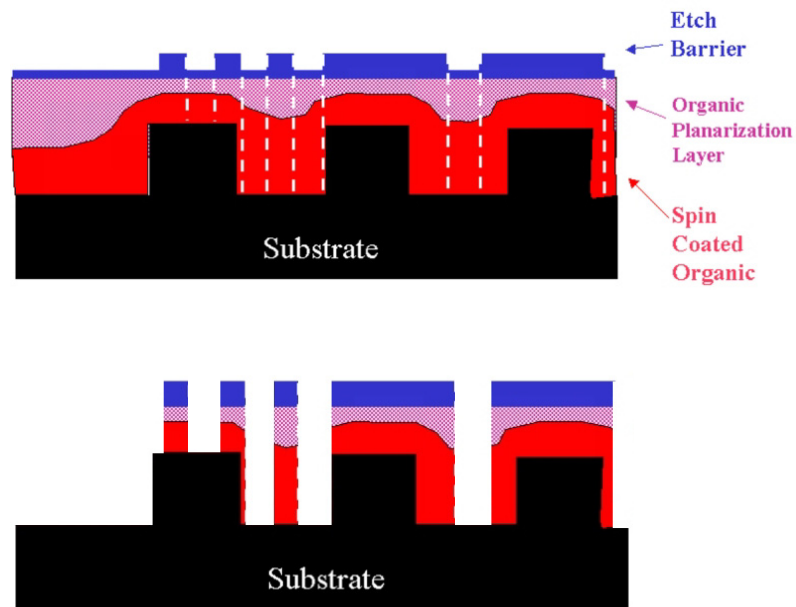
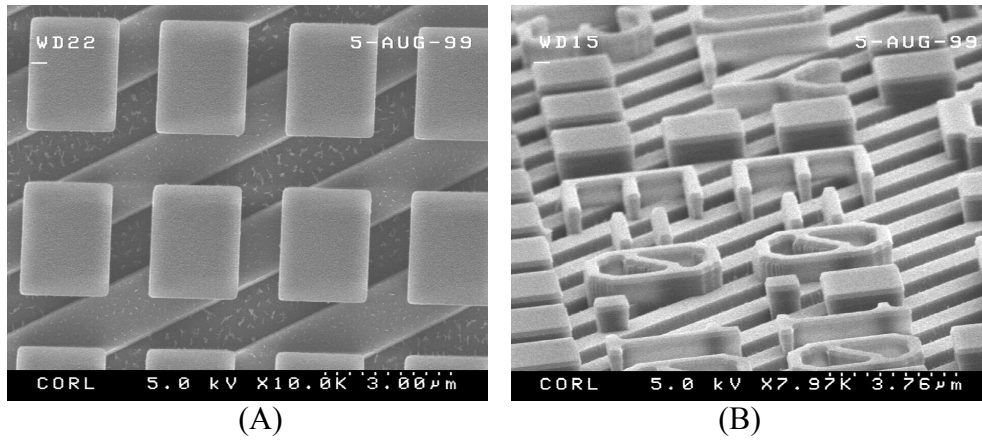


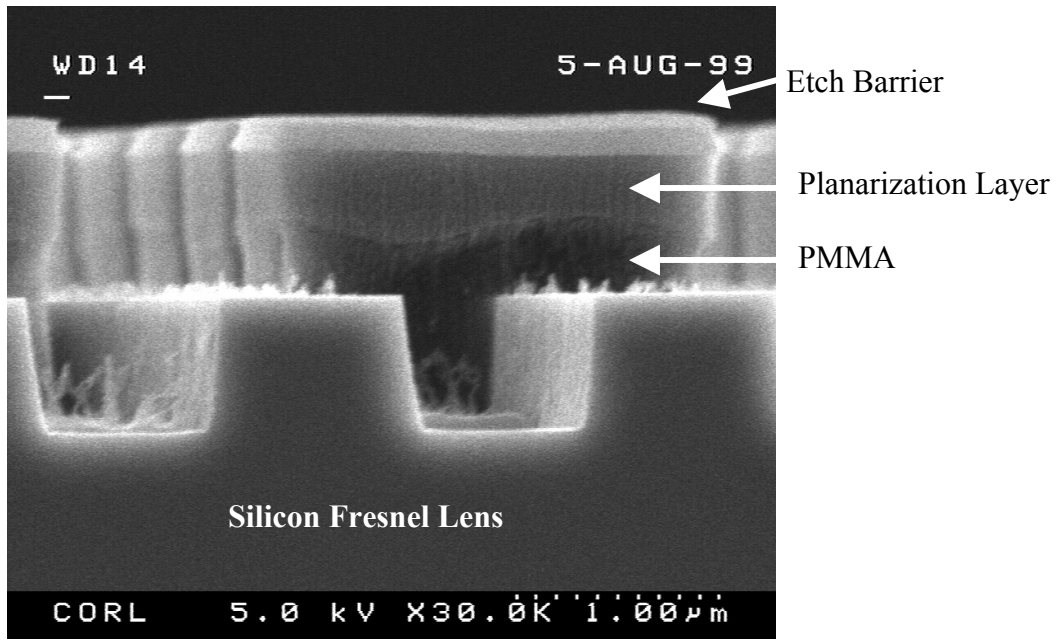
Figure 10.8. A schematic of an SFIL non-flat patterned cross section (top) prior to etch transfer and (bottom) after etch transfer [4].

The planarization layer consisted of 95% cyclohexyl acrylate and 5% SIB 1402 to which 3% of a 1:1 mixture of Irgacure 819 and Irgacure 184 were added. An example of the surfaces that were patterned is shown in Figure 10.9



(A)

(B)

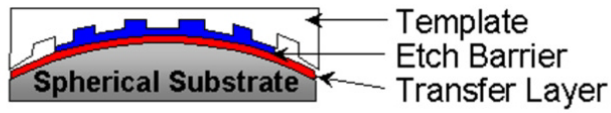


(C)

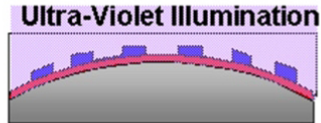
Figure 10.9. (A) Top-down SEM of non-flat patterning process. The lines are part of a 700 nm tall Fresnel lens. (B) 250+ nm features were transferred through 1.1 mm of PMMA and the planarization layer over the 700 nm tall Fresnel lens. (C) Cross-section SEM shown the silicon substrate, the spincoated PMMA layer, the planarization layer, and the etch barrier

## 10.2 CURVED SURFACE PATTERNING

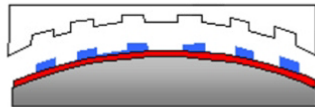
The relief structure of a convex template was replicated on a concave substrate that was coated with a 1.4  $\mu\text{m}$  organic transfer layer [5]. In this process shown in Figure 10.10, the curved template was closely aligned over the coated substrate and a drop of a low viscosity, photopolymerizable, organosilicon solution was introduced into the gap by capillary action. The etch barrier contained 47 % (w/w) poly(acryloxypropylmethylsiloxane-co-dimethylsiloxane) (UMS-U22, Gelest), 3.5 % (w/w) Irgacure 184, 1.5 % (w/w) Irgacure 819, 24 % (w/w) (3-acryloxypropyltrimethylsiloxy)silane, and 24 % (w/w) *n*-butyl acrylate. The gap was closed by vertical translation of the template toward the substrate until it made contact with the transfer layer and then irradiated with ultraviolet light through the backside of the template. Once the photocuring was complete, the template was separated from the substrate leaving a relief image on the surface of the transfer layer. An  $\text{O}_2$  RIE etch through the transfer layer can be used to create a high aspect ratio image on the substrate.



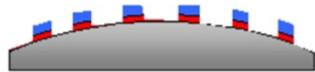
(A) Bring template into proximity of a coated curved substrate and dispense etch barrier.



(B) Bring into contact with substrate and expose with UV.

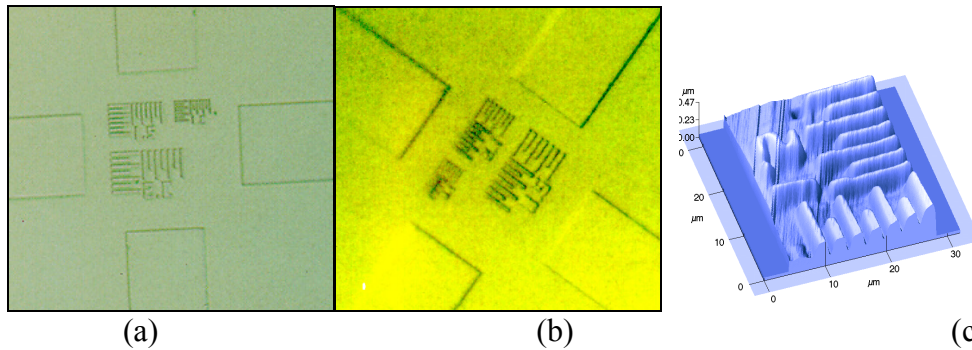


(C) Remove Template.



(D) Transfer Pattern with RIE

Figure 10.10. Curved surface replication process flow.



(a) (b) (c)  
 Figure 10.11. (a) Optical micrograph shows features etched into the template generated by ion-proximity lithography. (b) Optical micrograph shows a relief pattern in the etch barrier. (c) AFM image of topography patterned in etch barrier [5].

### 10.3 CONCLUSION

The goal of the Step and Flash Imprint Lithography development program is to pattern a substrate with sub-100 nm features at room temperature and with minimal applied pressure. Three methods of fluid delivery were analyzed theoretically and tested experimentally. Droplet compression has proven to be the most effective method of fluid delivery using the rigid quartz template, while spincoating was applied successfully to roller imprint equipment. The interfaces of the SFIL system have been tailored to provide for preferential release at the template-etch barrier interface and this is observed experimentally. In a rudimentary study of imprint reliability, a field of ~1000 features were replicated faithfully and reliably over the course of 10 consecutive imprints without one visible defects [6]. Further, during a preliminary study of defect susceptibility [7], it was shown that particles contaminating the template were entrained in the

etch barrier upon photopolymerization and that after just 8 imprints a contaminated template was cleaned. While the investigation of SFIL's reliability continues, the quality of the replicated features was studied using FEM techniques based on the etch barrier's experimentally determined elastic modulus of 4.2 MPa and its 9.3 % (v/v) volumetric contraction. The FEM results indicate that no pattern motions or major geometric distortion will occur for materials similar to the current etch barrier formulation. The etch selectivity of the etch barrier has been ensured by incorporating greater than 11% (w/w) silicon into the polymer precursors. In fact, the three etch barrier formulations detailed in Chapter 8 exhibit O<sub>2</sub> etch selectivity between 20:1 and 60:1. With these outstanding etch properties, high resolution features with width as small as 60 nm have been transferred through a 300 nm thick transfer layer. Further, aspect ratios of 14:1 have been achieved with 100 nm equal line-space patterns. Similar features were utilized as additive metalization mask to form a large area micropolarizer array that consisted of 20 micron long, 100 nm thick, Ti equal line-space on a 200 nm pitch. The advantage of the SFIL chemistry was also demonstrated by etch transfer of features over 700 nm topography. The design of SFIL materials is consistent with the requirements of high-volume manufacturing and SFIL takes advantage of several existing semiconductor processes such as phase-shift reticle technology, reactive ion etching, and optical overlay methodologies [1,2,3,6,7,8]. The Step and Flash Imprint Lithography process has been proven to be a high-resolution technique capable of patterning a wide variety of substrates at room temperature, under low applied pressure, and in a reliable, cost-effective manner.

## References

---

- 1 Colburn, M.; S. Johnson, M. Stewart, S. Damle, B. J. Jin, T. Bailey, M. Wedlake, T. Michaelson, S.V. Sreenivasan, J. Ekerdt, C.G. Willson. "Step and Flash Imprint Lithography: An alternative approach to high resolution patterning." *Proc. SPIE*. 3676, 379-389 (1999)
- 2 Colburn, M.; A. Grot, M. N. Amistoso, B. J. Choi, T. C. Bailey, J. G. Ekerdt, S.V. Sreenivasan, J. Hollenhorst, C.G. Willson. *Proc. SPIE*. 3997, 453-457 (2000)
- 3 Colburn, M.; A. Grot, T. Bailey, B.J. Choi, M. Stewart, L. Wills, M. Amistoso, S.V. Sreenivasan, J.G. Ekerdt, C.G. Willson, "High Resolution Patterning with Step and Flash Imprint Lithography," *Trends in Nanotechnology*, Toledo, Spain, (2000)
- 4 Colburn, M.; A. Grot, B. J. Choi, M. Amistoso, T. Bailey, S.V. Sreenivasan, J. G. Ekerdt, C. G. Willson. "Patterning non-flat substrates with a low pressure, room temperature imprint lithography process," *J. Vac. Sci. Technol. B*. (2001) [submitted]
- 5 Ruchhoeft, P.; M. Colburn, B. J. Choi, H. Nounu, S. Johnson, T. Bailey, S. Damle, M. Stewart, J. Ekerdt, S.V. Sreenivasan, J. C. Wolfe, C. G. Willson, *J. Vac. Sci. Technol. B*, **17**(6), 2965-2969 (1999)
- 6 Bailey, T; B. Smith, B.J. Choi, M. Colburn, M. Meissl, S.V. Sreenivasan, J.G. Ekerdt, C.G. Willson, "Step and Flash Imprint Lithography: Defect Analysis," *J. Vac. Sci. Technol. B*. [submitted]
- 7 Bailey, T.; B. J. Choi, M. Colburn, M. Meissl, S. Shaya, J. G. Ekerdt, S.V. Sreenivasan, C. G. Willson. "Step and Flash Imprint Lithography: Template Surface Treatment and Defect Analysis," *J. Vac. Sci. Technol. B*, **18**(6), 3572-3577 (2000).
- 8 Choi, B. J.; M. Meissl, M. Colburn, T. Bailey, P. Ruchhoeft, S.V. Sreenivasan, F. Prins, S. Banerjee, J.G. Ekerdt and C.G. Willson; "Layer-to-Layer Alignment for Step and Flash Imprint Lithography," *Proc. SPIE's 26th Intl. Symp. Microlithography: Emerging Lithographic Technologies*, Santa Clara, CA. (2001)

## **Appendix**

### **APPENDIX A: SFIL STEPPER OPERATION**

#### **A.1 Start-Up**

The system is controlled via custom-built Labview graphic users interface. Therefore, the control computer must first be turned on and Labview running multiimprint.vi; the control software front-end. The house vacuum and nitrogen must be turned on. The fluid dispense system must contain sufficient etch barrier not only to dispense on the wafer but also to fill the deposition line that leads from the etch barrier vial to the micro-actuator that dispensing the fluid. The stepper must be turned on to ensure power to DAQ board, force transducers, stepper motor, the X-Y stage motors and encoders. The lamp and its power supply must be powered and the lamp ignited. The shutter should be closed (by default) and the house water supply open to cool the IR water filter. The house vacuum must be on to hold the wafer to the wafer chuck. If dose control is desired, the inline amplifier must be turned on as well.

The template must be installed. To install a 1" x 1" template, remove four-bar flexure stage, which is held in place by 4 Allen head screws. Loosen the 8 set screws that press against the aluminum template fitting (the square bracket that fits just around the 1" x 1" templates). Remove the template fitting, and place around a template, which is face-up on a clean room nap. Place the

template with the fitting face-up in the flexure stage. Tighten gently the setscrews being careful not to apply too much pressure. Once secure, reinstall the flexure stage on the template calibration stage using the 8 Allen head screws. After installation, the system is ready for calibration.

### **A.2 Wafer Calibration Procedure**

Before any imprinting can occur, the X-Y stage must be parallel to the template. To accomplish this, a calibration is performed on a test wafer that is installed on the wafer stage. The template is lowered the identical amount in three corners defined by the micrometers on the wafer calibration stage. The force is read. The state is leveled relative to the template by adjusting the three micrometers. Once equal the wafer calibration stage is parallel to the template.

### **A.3 Template Calibration Procedure**

After the wafer stage is calibrated, the template stage must be calibrated relative to the wafer. The template is lowered until contact is just observed by the force transducers. The template orientation relative to the wafer is inferred from the Fizeau Fringes that result from the misorientation of the template. The template is leveled relative to the wafer using the three micrometers on the template orientation stage that change the orientation of the attached template. Once no fringes are observed, the system is co parallel and is ready to imprint.

### **A.4 Imprint Procedure**

After the template is installed and calibrations are performed, imprint can begin. A wafer spin coated with an organic transfer layer is loaded onto the steppers wafer stage. The system is initialized and homed. The desired exposure

length (or expose dose) is entered into the exposure time field (exposure dose field). The file to which data is saved is entered into the “Save Data” field. The volume or number of drops is entered into the volume dispense field. The imprint field size and the desired distance between imprint fields are entered. X-Y Stage velocity is specified. The system can be moved in manual mode to the desired location, fluid dispensed, template pressed, illumination initiated, separation performed. In automatic mode such as that used in the defect studies, the above information is entered and the entire process is repeated across the wafer automatically.

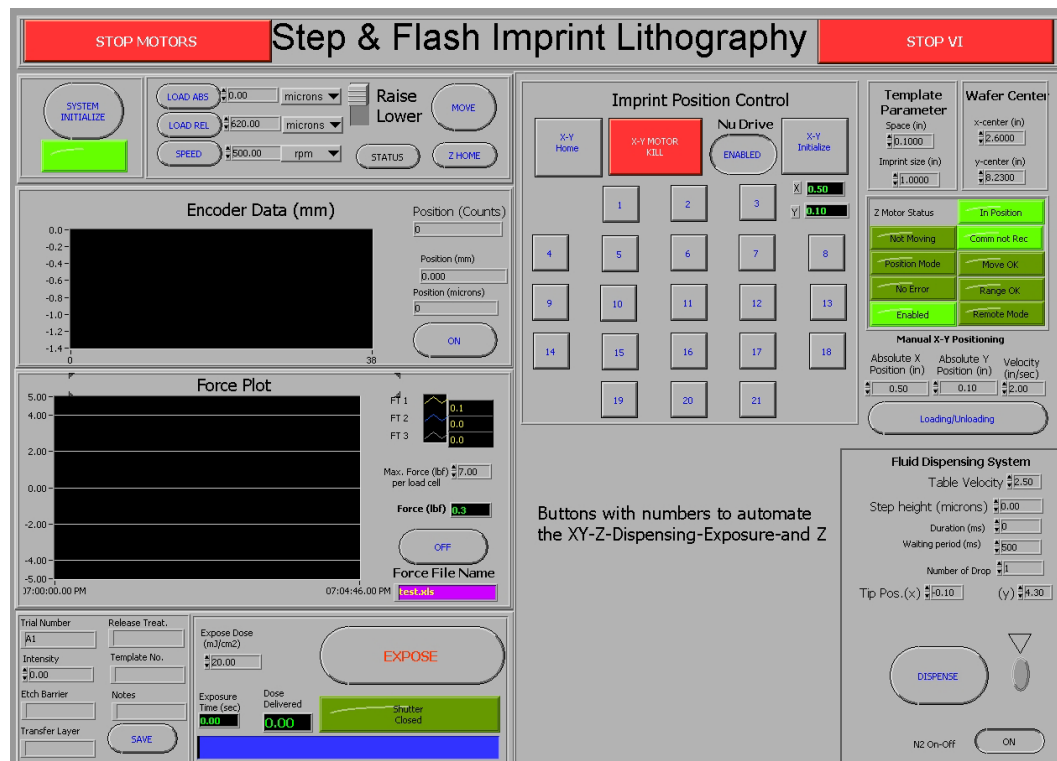


Figure A.1. SFIL Stepper Graphic User Interface.

## APPENDIX B: POWER METER DESIGN

The multi-imprint stepper is equipped with a custom-made low profile power meter consisting of a thermopile (Oriel, 71751), a 45° tilt mirror, a protective housing that blocks stray light from entering the detector, and an inline instrumental amplifier to increase the signal strength. A picture of the power meter is shown in Figure B.1

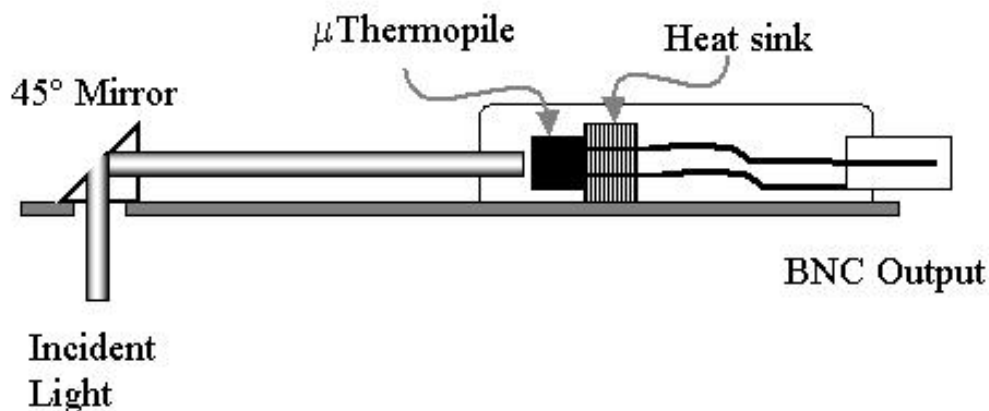


Figure B.1 Power meter and inline instrumental amplifier.

The thermopile is glued to an aluminum heat sink within the housing. The thermopile has a sapphire crystal for enhanced UV sensitivity. The thermopile voltage output is connected to the BNC connector on the back of the housing. The output of the thermopile is a voltage on the order of 40mV/mW. The signal is sent to an inline instrumental amplifier based on the Texas

Instruments INA 110 DIP. The circuit layout for the system is shown in Figure B.2. The amplification is set to 500 V/V. The response time of the amplifier is 4  $\mu$ seconds. A table of the amplifier components is listed in Table B.1. The output signal from the amplifier is sent to the National Instrument's data acquisition board.

The instantaneous single can be used to monitor the delivered dose using the PowerMeter.vi program. Given a calibration constant between the signal and the dose, the power meter vi integrates the dose until the desired dose is exceed. At that point, the program outputs a signal to the multi-imprint stepper main program to close the shutter.

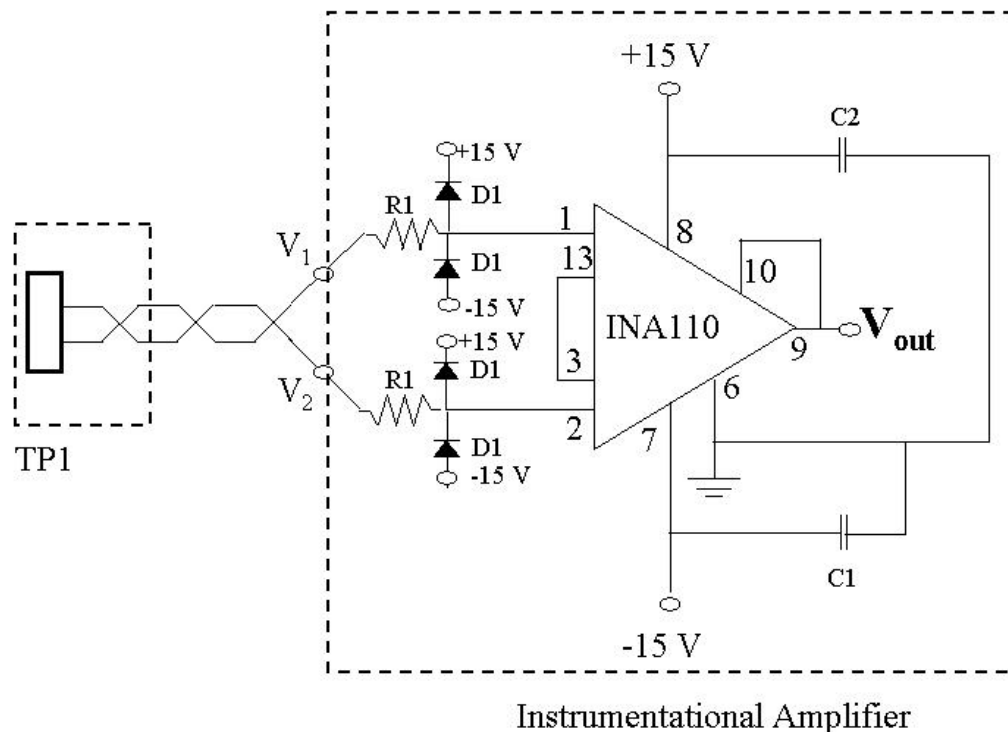


Figure B.2. Instrumental Amplifier Circuit Diagram.

Table B.1. Amplifier components.

Component	Type	Manufacturer / Part No.
TP1	Thermopile (photo detector)	Oriel / 71767
INA110	Amplifier	Texas Instrument / INA 110
R1	Resistor	Physics Shop / 20k $\Omega$
D1	Diode	Physics Shop / FDH300
C1	Capacitor	Physics Shop / 0.1 $\mu$ F
C2	Capacitor	Physics Shop / 1.0 $\mu$ F

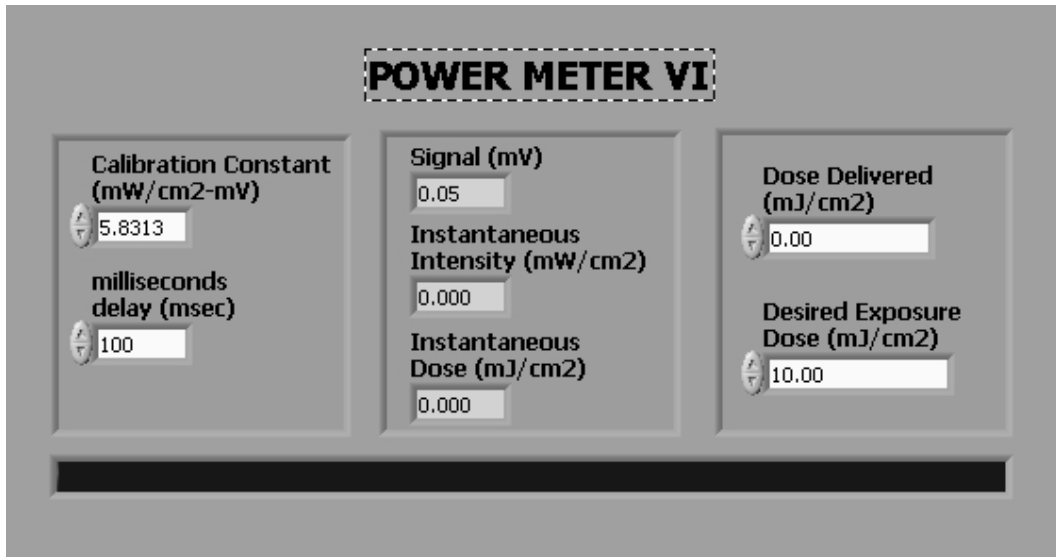
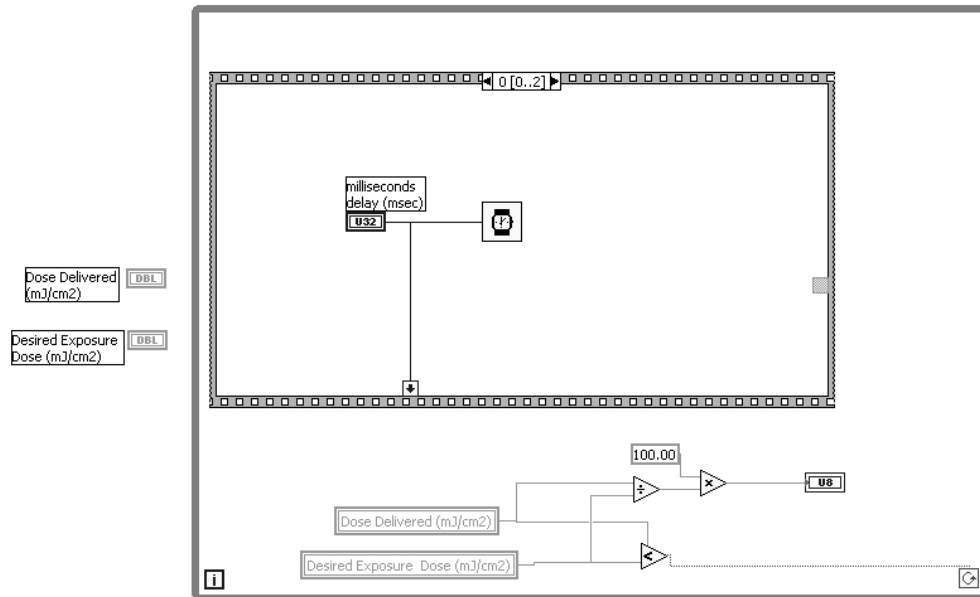
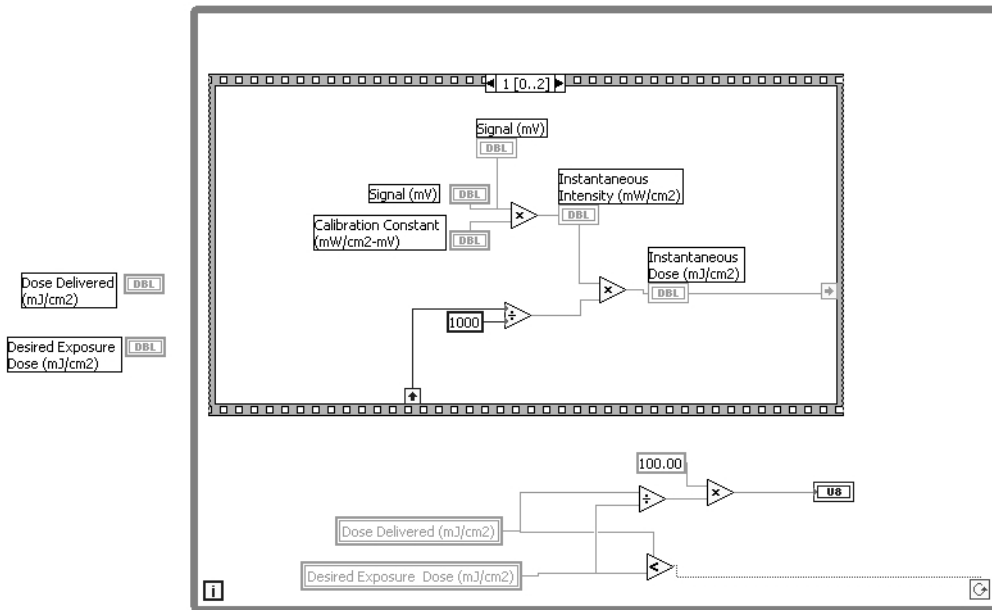


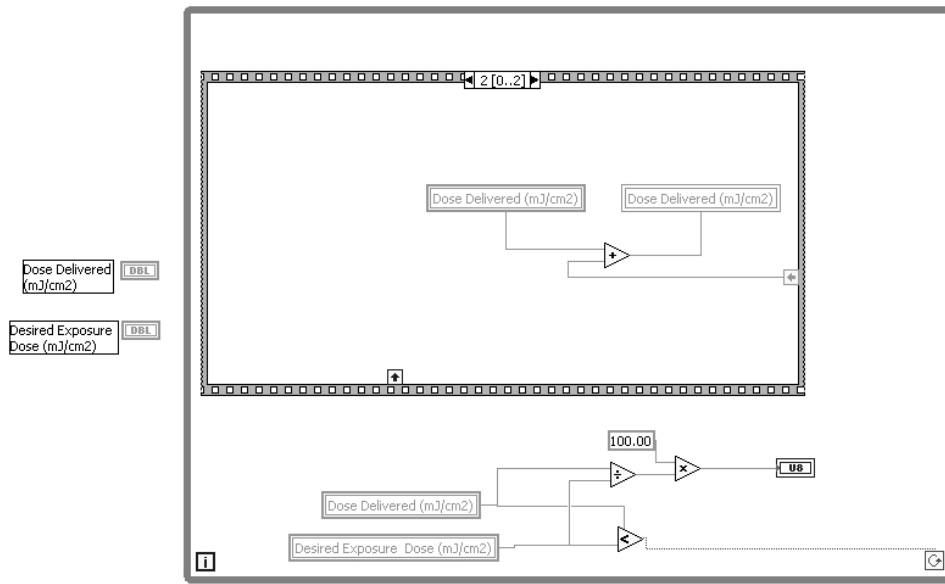
Figure B.3. PowerMeter.vi Front End.



a)



b)



c)

Figure B.4. Power meter algorithm (Steps 1 through 3)

## APPENDIX C: MULTIANGLE SPECTRAL REFLECTOMETRY

Off-axis illumination extends the lower limit of this analysis technique. As shown in Figure C.1, the path length of the incident light increases according to Snell's law by non-normal illumination. The detected path length is directly correlated to the film thickness as shown in the equations below. This analysis is valid for thin films that do not exhibit birefringence ( $n_{\perp} \neq n_{\parallel}$ ). Imaging films such as photoresists used in semiconductor manufacturing generally fall in this category.

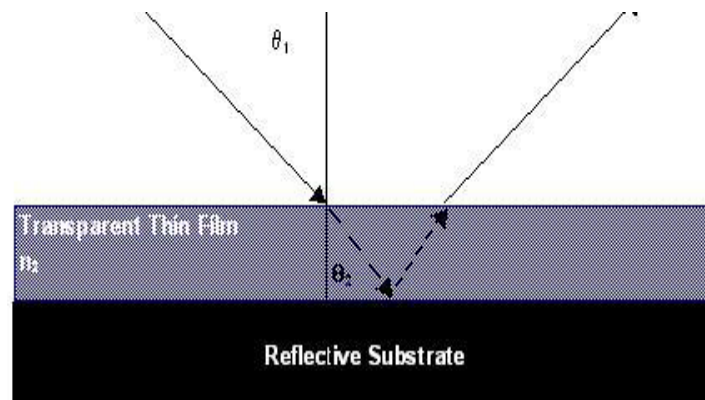
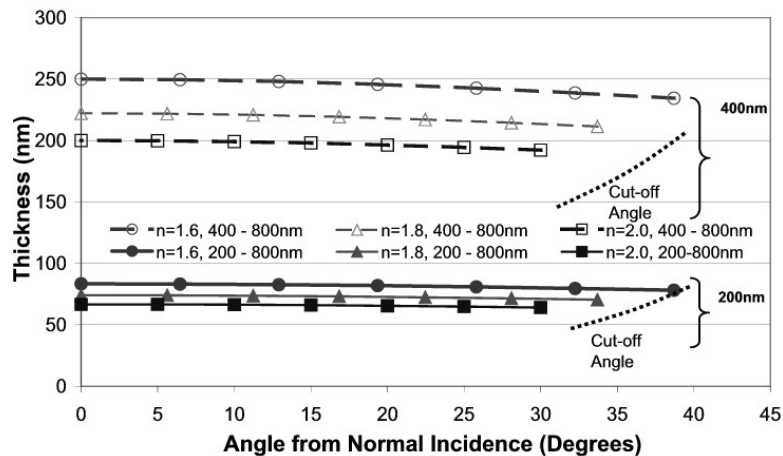


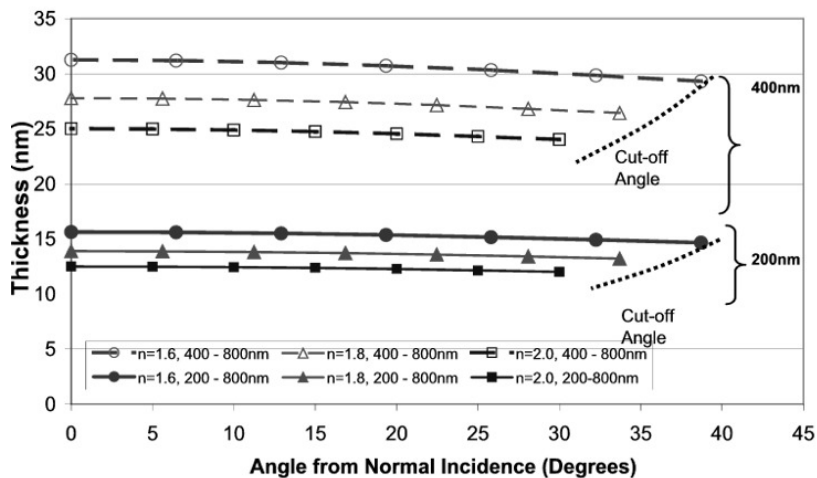
Figure C.1. Path length of the probe light is increased by non-normal illuminations

Since the FFT analysis is based on the optical path, the minimum observable film thickness can be extrapolate to other refractive indices and other spectral ranges using the dimensionless optical thickness ( $2nD\Delta w_{n,min}$ ). Figure C.2 shows the estimated minimum film thickness that can be accurately measured for three indices of refraction (1.6, 1.8, 2.0) and for spectral ranges of 200 nm to

800 nm, and 400 nm to 800 nm. The effect of wavelength range is greatest but the off-axis illumination allows for additional information about the film to be retrieved.



a)



b)

Figure C.2 Effect of Incident Angle and Spectral Range on the Minimum Detectable Thickness for a) FFT algorithm, and b) the IMMA algorithm.

For the case where the index of refraction of a material is unknown over the sampled spectral range, a multiangle analysis yields a system of equations based on Snell's Law, shown in Equation C.1 through Equation C.3 that once solved simultaneously give both the film thickness ( $T$ ) and a characteristic index of refraction ( $n_2$ ) of the material. In the system of equations,  $n_1$  is the index of refraction for the material above the thin film,  $\theta_1$  is the incident angle at which the light is approaching the thin film,  $\theta_2$  is the angle at which the light is approaching the bottom of the film, and  $D$  is the path length of the non-normal light.

$$\text{Equation C.1} \quad n_1 \sin(\theta_1) = n_2 \sin(\theta_2)$$

$$\text{Equation C.2} \quad \theta_2 = \sin^{-1}\left(\frac{n_1}{n_2} \sin(\theta_1)\right)$$

$$\text{Equation C.3} \quad T = D \cos(\theta_2)$$

Two particularly useful applications of this method may be (i) thickness monitoring when both index of refraction and thickness are changing due to evaporation of solvent, and (ii) phase transition characterization when a film is undergoing a transition from glass to rubber. One well-known characteristic of a secondary phase change such as glass transition temperature of a polymer is that its thermal expansion coefficient slowly changes. Another property that changes is its dielectric constant. Given that the index of refraction is related to the square root of the dielectric constant, the multi-angle real time analysis theoretically can be used to detect the glass transition temperature of a transparent thin film.

### APPENDIX D: PRIMARY ETCH BARRIER FORMULATIONS

There are four primary etch barrier formulations that have been found to perform satisfactory: the original etch barrier (O-EB), the Agilent etch barrier (-EB), the low viscosity etch barrier (Low- $\mu$  EB), and the liquid initiator low viscosity etch barrier (LI Low- $\mu$  EB). Their formulations are shown in Table D.1. Also listed is the composition of the organic planarization layer. The solution mass is defined by the organic and silylated monomers.

Table D.1. Primary Etch Barrier Formulations

Function	Component	O-EB	A-EB	Low- $\mu$ EB	LI Low- $\mu$ EB	PL
Organic and Silylated Monomers	SIA0210 (Gelest)	24.3		46.3	46.4	
	Butyl Acrylate (Aldrich)	24.3		46.3	46.4	
	UMS-U22 (Gelest)	48.5	97.1			
	Cyclohexyl Acrylate					92.6
Crosslinker	SIB 1402 (Gelest)			4.6	4.6	4.6
Free Radical Initiator	1:1 Irgacure 819: Irgacure 184 (Ciba)	2.9	2.9	2.8		3.8
	Darocure 4263				2.6	

## Bibliography

1. "3rd International SEMATECH Next Generation Lithography Workshop." (Semiconductor Industry Association, ).
2. Fundamentals of Adhesion. L. H. Lee, Ed. (Plenum, NY, 1991).
3. "Rame-Hart m100 Goniometer Standard Operating Procedure" (Rame-Hart, 1998).
4. Official Methods and Recommended Practices of AOCS (AOCS, ed. 5th, 1998).
5. "User's Guide to AutoProbe CP" (Park Scientific Instruments, 1998).
6. "International Technology Roadmap for Semiconductors" (Semiconductor Industry Association, 1999).
7. H. R. Allock, F. W. Lampe., Contemporary Polymer Chemistry (Prentice, NJ, ed. 2nd, 1990).
8. B. Ameduri, R. Bongiovanni, G. Malucelli, A. Pollucino, A. Priola, J. Poly. Sci. A **37**, 77-87 (1999).
9. J. M. Andreas, E. A. Hauser, W. B. Tucler, J. Phys. Chem. **42**, 1001 (1938).
10. B. Arkles, Chemtech **7**, 766-778 (1977).
11. W. J. Bailey, et al., Polym. Prepr. **26**, 50-1 (1985).
12. T. Bailey, et al., J. Vac. Sci. Technol. B **18**, 3572-3577 (2000).
13. T. Bailey, et al., J. Vac. Sci. Technol. B. (2001 [submitted]).
14. F. Bashforth, J. C. Adams, , Cambridge University Press (1883).
15. C. E. Bouldin, et al., J. Appl. Physics. **88**, 691-695 (2000).
16. G. Bouwhuis, et al., Principles of optical disc systems. (Adam Hilger,, Bristol, UK, 1985).
17. S. D. Burns, et al., Determining Free Volume Changes During PAB and PEB of a Chemically Amplified Resist, Retech 12th International Conference on Photopolymers, NJ (2000).
18. C. Chambers, . (2001).
19. B. J. Choi, S. Johnson, M. Colburn, S. V. Sreenivasan, C. G. Willson, J. Precision Engineering. (2000 [accepted]).
20. B. J. Choi, et al., Proc. SPIE: Emerging Lithographic Technologies. (2001 [accepted]).
21. S. Y. Chou, P.R.Krauss, P. R. Renstrom, J. Vac. Sci. Technol. B **14**, 4129-33 (1996).
22. S. Y. Chou, L. Zhuang., J. Vac. Sci. Technol. B. **17**, 3197-3202 (1999).
23. J. Coburn, (2001).
24. M. Colburn, et al., Proc. SPIE. **3676**, 379-389 (1999).
25. M. Colburn, et al., Proc. SPIE. **3997**, 453-457 (2000).

26. M. Colburn, et al., High Resolution Patterning with Step and Flash Imprint Lithography, Trends in Nanotechnology, Toledo, Spain (2000).
27. M. Colburn, et al., J. Vac. Sci. Technol. B. (2001 [submitted]).
29. M. Colburn, et al., J. Vac. Sci. Technol. B. (2001 [submitted]).
30. C. Constantine, L. Heckerd., Proc. SPIE **3412**, 220-227 (1998).
31. W. M. Deen, Analysis of Transport Phenomena, Oxford Press, NY (1998)
32. J. Domke, M. Radmacher, Langmuir **14**, 3320-3325 (1998).
33. F. M. Fowkes, Ind. Eng. Chem. **55**, 28 (1964).
34. M. Francon, Optical Interferometry (Academic Press, NY, 1966).
35. M. Goken, M. Kempf, W. D. Nix, Acta Mater. , 903-911 (2001).
36. J. I. Goldstein, et al., Scanning Electron Microscopy and X-Ray Microanalysis: A text for biologist, material scientists, and geologists (Plenum, NY, 1992).
37. L. L. Guo, P. R. Krauss, S. Y. Chou., Appl. Phys. Lett. **17**, 1881-1883 (1987).
38. K. K. Gupta, J. L. Meek., Finite Element Multidisciplinary Analysis (American Institute of Aeronautics and Astronomics, Reston, VA, 2000).
39. J. Haisma, M. Verheijen, K. van der Huevel, J. v. d. Berg., J. Vac. Sci. Technol. B. **14**, 4124-29 (1996).
40. G. Hallock, Class Note from Plasma Processing. (The University of Texas at Austin, 2000).
41. F. Hartley, C. K. Malek, J. Neogi, Sub-optical lithography with Nanometer Definition Masks, 43rd International Conference EIPBN,, Marco Island, FL (1998).
42. R. Heinecke, J. Electrochem. Soc. **129**, 2282 (1982).
43. H. J. Hertz, J. Riene Angew. Mathematik , 156-171 (1882).
44. J. Isrealachvili, Intermolecular & Surface Forces (Academic Press, San Diego, ed. 2nd, 1991).
45. B. W. J., ACS Symp **559**, 38-59 (1977).
46. R. W. Jaszewski, H. Schiff, J. Gobrecht, P. Smith., Microelectronic Engin. , 575-578 (1998).
47. K. L. Johnson, Contact Mechanics (University Press,, Cambridge, 1987).
48. S. Johnson, MS Thesis, The University of Texas at Austin (1999).
49. S. A. Joyce, J. E. Houston, Rev. Sci. Instrum. **62**, 710-715 (1991).
50. M. Kerwick, MS Thesis, The University of Texas at Austin (2001).
51. E. Kim, Y. Xia, G. M. Whitesides, Adv. Mater. , 581-584 (1995).
52. E. Kim, Y. Xia, G. M. Whitesides, Adv. Mater. **9**, 651-654 (1997).
53. K. L. Konnerth, F. H. Dill., Solid-State Electronics **15**, 371-380 (1972).
54. K. L. Konnerth, F. H. Dill, IEEE Trans. Electron Devices **ED-22**, 452-456 (1975).
55. A. Kumar, G. M. Whitesides., Appl. Physics Lett. **63**, 2002-2004 (1993).
56. L. H. Lee, Ed., Fundamentals of Adhesion (Plenum, NY, 1991).

57. M. A. Lieberman, A. J. Lichtenberg, Principles of Plasma Discharges and Materials Processing (Wiley, NY, 1994).
58. G. M. Loudon, Organic Chemistry (Redwood City, CA, 1995).
59. C. A. Mack, Lecture Notes from Semiconductor Microlithography. (The University of Texas at Austin, 2000).
60. C. A. Mack, M. Ercken, M. Moelants., Proc. SPIE. **3679** (1999).
61. K. L. Mittle, Ed., Adhesion and Wettability .
62. G. Moore, Electronics **38**, 114-117 (1965).
63. A. Q. Nguyen, MS. Thesis, The University of Texas at Austin (2001).
64. S. Okazaki, J. Vac. Sci. Technol. B **9**, 2829-2833 (1991).
65. W. C. Oliver, G. M. Pharr, J. Mater. Res. **1**, 601 (1992).
66. D. K. Owens, R. C. Wendt, J. Appl. Poly. Sci. **13**, 1741-1747 (1969).
67. S. Patel, Structural Mechanics with Introductions to Elasticity and Plasticity (McGraw-Hill, NY, 1970).
68. K. Patterson, et al., Proc. SPIE. , 425-437 (1998).
69. D. R. Paul, D. W. Fowler, J. Applied Polymer Sci. **19**, 281-301 (1975).
70. E. M. Pearce, W. C.E., B. K. Bordoloi, in Educational Modulus for Material Science and Engineering Projects . (1982).
71. E. Pitts, J. of Fluid Mechanics **59**, 753-767 (1973).
72. E. P. Plueddemann, Silane Coupling Agents (Plenum, NY, 1992).
73. J. D. Plummer, M. D. Deal, P. B. Griffin., Silicon VLSI Technology: Fundamentals, Practice, and Modeling. (Prentice, NJ, 2000).
74. E. Reichmanis, G. Smolinsky, J. Electrochem. Soc. **132** (1985).
75. P. Ruchhoeft, et al., J. Vac. Sci. Technol. B. **17**, 2965-2969 (1999).
76. K. Sakurao, A. Itda, Jap. J. Appl. Phys. 2 Let. **31**, L113-5 (1992).
77. H.-C. Scheer, H. Schults, F. Gottschalch, T. Hoffmann, C. M. S. Torres, J. Vac. Sci. and Technol. B. **16**, 3917-3921 (1998).
78. S. Scheer, MS Thesis, The University of Texas at Austin (2001).
79. H. H.-C. S. Schultz, T. Hoffmann, C. M. Sotomayor Torres, K. Pfeiffer, G. Bleidiessel, G. Grützner, Ch. Cardinaud, F. Gaboriau, M.-C. Peignon, J. Ahopelto, and B. Heidari, J. Vac. Sci. Technol. B. **18**, 1861 (2000).
80. J. Shaw, E. Babich, M. Hatzakis, J. Paraszczak., Solid State Technology. **30**, 83-89 (1987).
81. I. N. Sneddon, Int J. Eng. Sci. **2**, 47-57 (1965).
82. M. Somervell, Ph.D Thesis, The University of Texas at Austin (2000).
83. B. G. Streetman, Solid State Electronic Devices (Prentice, NJ, ed. 4th Ed, 1995).
84. L. F. Thompson, C. G. Willson, M. J. Bowden, Introduction to Microlithography (ACS, Washington, 1994).
85. T. Thurn-Albrecht, et al., Science **290**, 2126-2129 (2000).
86. H. G. Tompkins, W. A. McGahan, Spectroscopic Ellipsometry and Reflectometry, A User's Guide (Wiley, NY, 1999).

87. P. C. Tsairtas, Ph.D Thesis, The University of Texas at Austin.
88. A. Une, Y. Kai, M. Mochida, S. Matsui, F. Ohira, *Microelectronic Engineering* **53**, 137-140 (2000).
89. D. W. van Krevelen, *Properties of Polymers* (Elsevier, NY, ed. 3rd, 1990).
90. C. J. van Oss, R. J. Chaudury, M. K. Goode, *Langmuir* **4**, 884-891 (1988).
91. K. van Workum, J. J. d. Pablo, P. F. Nealy, K. Yoshimoto, *Glass Transition and Mechanical Properties of Thin Polymer Films and Nano-scale Structures*, EIPBN, Resists I: Properties and Processing, Washington, D.C. (2001).
92. J. L. Wilbur, E. Kim, G. M. Whitesides, *Adv. Mater.* **6**, 600-604 (1994).
93. S. Wu, *J. Adhesion* **5** (1973).
94. S. Wu, *Polymer Interface and Adhesion* (Marcel Dekker, NY, 1982).
95. S. Wu, *Polymer Handbook*. (Wiley, 1989) pp. 411-432.
96. Y. Xia, G. M. Whitesides, *Angew. Chem. Int.* **37**, 550-575 (1998).
97. W. Zhang, S. Y. Chou, *Multilevel nanoimprint lithography with submicron alignment on 4" wafers*, EIPBN, Palm Springs, CA (2000).
98. L. Zhuang, Personal Communication. (2000).

## **Vita**

Matthew Earl Colburn was born on February 8, 1974 in West Allis, Wisconsin, the youngest son of Paul and Carol Colburn, and was raised in Waukesha, Wisconsin where he attended elementary and secondary school. He graduated from Catholic Memorial high school in 1992 and enrolled in Purdue University where he graduated with Distinction with a Bachelor's of Science degree in Chemical Engineering. After working for a year for Intel in Phoenix, Arizona, he enrolled in the Chemical Engineering graduate program at The University of Texas at Austin and began his doctoral work under the guidance of Professor C. Grant Willson. During his graduate studies, he was received a summer internship at Agilent Technologies (formerly, Hewlett Packard Laboratories) in Palo Alto, California and received the Richard W. Moncrief Endowed Engineering fellowship. On June 17, 2000, he married Jennifer L. Schmitz in Lafayette, Indiana. After completing his doctorate, he will be employed by IBM at their Watson Research facility in Yorktown Heights, New York.

Permanent address: 808 Sweetbriar Court, Waukesha, Wisconsin, 53186

This dissertation was typed by the author.

